



HAL
open science

Fabrication of Large Bulk YBaCuO Superconductor Single Domains for Application to Flux Trapping, Current Transport and Energy Storage at 77K

Cui Ping Zhang

► **To cite this version:**

Cui Ping Zhang. Fabrication of Large Bulk YBaCuO Superconductor Single Domains for Application to Flux Trapping, Current Transport and Energy Storage at 77K. Physics [physics]. Université de Grenoble, 2009. English. NNT: . tel-00616678

HAL Id: tel-00616678

<https://theses.hal.science/tel-00616678>

Submitted on 23 Aug 2011

HAL is a multi-disciplinary open access archive for the deposit and dissemination of scientific research documents, whether they are published or not. The documents may come from teaching and research institutions in France or abroad, or from public or private research centers.

L'archive ouverte pluridisciplinaire **HAL**, est destinée au dépôt et à la diffusion de documents scientifiques de niveau recherche, publiés ou non, émanant des établissements d'enseignement et de recherche français ou étrangers, des laboratoires publics ou privés.

Université Joseph Fourier – Grenoble
Northwestern Polytechnical University – Xi'an

PhD Thesis

To obtain the grades of

Doctor of the Université Joseph Fourier, Spécialité Physique des Matériaux
Doctor of the Northwestern Polytechnical University

Presented by

ZHANG Cui Ping

Fabrication of Large Bulk YBaCuO Superconductor Single Domains for Application to Flux Trapping, Current Transport and Energy Storage at 77K

Elaboration de larges monodomaines de supraconducteurs YBaCuO pour application au piégeage de champ magnétique, au transport de courant et au stockage d'énergie à 77 K

The 18 th of November 2009

Jury :

YAN Guo	Vice Director of the NIN Superconductivity laboratory	Reporter
NOUDEM Jacques	Senior Lecturer at CRISMAT, Caen	Reporter
ZHANG Pingxiang	Professor, vice-president of NIN	Examinator
LI Yulong	Professor, dean of Graduate School at NPU	Examinator
TOURNIER Robert	Emeritus Research director at CRETA	Examinator
ZHOU Lian	Professor NPU, Doctor Honoris Causa UJF	Supervisor
BEAUGNON Eric	Professor UJF and director of CRETA	Supervisor
CHAUD Xavier	Research Engineer at CRETA	Co-supervisor

PhD thesis prepared at the CRETA, CNRS Grenoble, France
and at the Northwestern Institut for Non-ferrous Metal Research, Xi'an, China
in the framework of the French-Chinese International Associated Laboratory LAS2M.

Résumé

Une série de résultats fructueux ont été obtenus au cours de notre étude sur la fabrication de supraconducteur YBCO monodomaine à partir d'un procédé par fusion de poudre (PMP). Premièrement, grâce à une balance de Faraday à haute température, nous avons révélé les transitions de phase dynamiques pendant la croissance de monodomaine YBCO par le procédé PMP, ce qui est un travail de recherche original dans ce domaine. Ces résultats sur les transitions de phase ont contribué à une meilleure compréhension de la fabrication des monodomaines PMP-YBCO. Deuxièmement, nous avons étudié la dynamique de croissance des monodomaines PMP-YBCO. L'effet de la diffusion de l'oxygène sur le taux de croissance des monodomaines YBCO est démontré. De la relation entre les taux de croissance et l'étude de la surfusion, nous déduisons que la croissance de cristaux d'YBCO dépend de deux types de diffusion. L'une a trait au transport des ions yttrium, baryum et cuivre vers l'interface de croissance de la phase 123 à travers la phase liquide fondue par diffusion en solution et interfaciale comme dans un système liquide fondu-solide. L'autre concerne la diffusion de l'oxygène qui repose sur la diffusion interfaciale à partir de l'air comme dans un système vapeur-solide. Enfin, nous avons été les premiers à fabriquer par lot avec succès des monodomaines YBCO par procédé PMP de taille $\Phi 30\text{mm} \times 15\text{mm}$. Un champ magnétique important de 739 mT a pu être piégé par un monodomaine YBCO à parois minces de $\Phi 15\text{mm}$. Une mesure magnétique record de la densité de courant critique $J_{cm} \sim 1,2 \times 10^5 \text{A/cm}^2$ (77K) a été atteinte. Les résultats obtenus nous donnent plus de confiance pour fabriquer des échantillons YBCO monodomaine de haute qualité.

Mots clefs : Supraconductivité, $\text{YBa}_2\text{Cu}_3\text{O}_x$, Monodomaine, Croissance cristalline, Oxygénation, Applications

Abstract

A series of fruitful results were achieved in the course of our study on the fabrication of superconductor YBCO single domain by Powder Melting Process (PMP). First, by the high temperature Faraday Balance, we revealed the dynamic phase transition in the growth of YBCO single domain in PMP process, which is an original research work in this field. The clear phase transition results build a fundamental understanding for fabricating YBCO single domain by the PMP process. Second, we studied the growth dynamics of PMP-YBCO single domain. The effect of oxygen diffusion is underlined on the growth rate of YBCO single domain. From the relationship of growth rate and the undercooling study, we deduce that the YBCO crystal growth depends on two types of diffusion. One relates to the yttrium, barium and copper ions transport to the 123 growth interface through the melt liquid by solution diffusion and interfacial diffusion as in melt-solid system. The other one concerns the oxygen diffusion which relies on interfacial diffusion from air as in vapor-solid system. Finally, we were first to successfully fabricate the $\Phi 30\text{mm} \times 15\text{mm}$ YBCO single domain in batch with PMP process. A large trapped magnetic field value of $B_{tr}=739\text{mT}$ was obtained in a $\Phi 15\text{mm}$ hole YBCO single domain. A record magnetic critical current density $J_{cm} \sim 1.2 \times 10^5 \text{A/cm}^2$ (77K) was achieved. The obtained results give us more confidence to fabricate high quality YBCO single domain samples.

Keywords: Superconductivity, $\text{YBa}_2\text{Cu}_3\text{O}_x$, Single domain, Crystal growth, Oxygen annealing, Applications

Acknowledgement

I am grateful to my director Prof. Zhou Lian for his thoughtful advices and encouragements firstly. In the period of his striving to the serious illness, he persists in working to listen to our research presentation and gives me more important advices. His persistent spirit and active attitude inspire me to improve myself and do my best for my works.

Secondly, I am grateful to my director Eric Beaugnon and Xavier Chaud for their profitable advices, physics materials knowledge and equipmental skills. I have obtained much more helpful discussions from Xavier Chaud; he gives me more detail advices for experiments process, equipments operation and paper rewriting skills. My thankful expression is endless. And I should thank the people of UJF University and Adum in CNRS for their helps.

I am appreciation for the Chinese colleagues, professors and directors in NIN, Xi'an, for their helps and supports. I thank my colleagues and director Li Chenshan in SMRC, thank Madame Xu Xiaoyan for her assists in our works, thank Prof. Wang Jingrong for his directions, and thank Dr.Chen Shaokai in Analysis department for his important advices. I should thank the people in CRETA/CNRS, who give me much more helps for my work when I was in Grenoble. I want to thank Prof. Touriner, technician engineer Pierre-Frederic, researcher Laureline, Particia, Sophie, Patricia and Secretary Marie-Dominique for their helps.

I should thank my professors in NWPU University for their concerns. I thank Prof. Fu Hengzhi for his directions, Prof. Li Jinshan for his arrangement of my courses and works. I thank my classmates in State key solidification lab, Dr. Cao Haitao and Dr. Zhou Shengyin for their detail assists. I thank the Graduate Student College for the helping.

I must thank the Science and Technology Department of French Embassy at Beijing for their scholarship for PhD student. I thank the Chinese NFSC organization (50432050) and the project "863" (2007aa03z241) for the research financial support. I should thank the CNRS/NIN international associated laboratory LAS2M (Laboratory of Applied Superconducting and Magnetic Materials) for their support. Especially I thank Prof. A Sulpice, owh provides much more particular attention to me and helps.

In the end, I should thank my husband Mr. Liang Zhaohui for his continuous encourages and supports, thank my daughter for her cheering words. I should thank my father, brothers and sister for their assists. In my heart sincerely, I thank all my friends, professors, classmates, colleagues and who help me in sometime and somewhere ever. Thanks !

Physical Term and Physical Unit Notation

YBCO	$\text{YBa}_2\text{Cu}_3\text{O}_{7-\delta}$
123	$\text{YBa}_2\text{Cu}_3\text{O}_{7-\delta}$
211	Y_2BaCuO_5
011	BaCuO_2
L	Liquid phase
Sm123	$\text{SmBa}_2\text{Cu}_3\text{O}_{7-\delta}$
Yb123	$\text{YbBa}_2\text{Cu}_3\text{O}_{7-\delta}$
PMP	Powder melting process
MTG	Melted Textured Growth
MPMG	Melting Powder Melted Process
T_c	<i>Superconducting transition temperature</i>
$7-\delta$	<i>Oxygen content of $\text{YBa}_2\text{Cu}_3\text{O}_{7-\delta}$</i>
ξ	<i>Coherence length</i>
F	<i>Levitation force</i>
$F(\chi)$	<i>Magnetic force</i>
χ	<i>Susceptibility</i>
m	<i>Magnetization</i>
dH/dz	<i>Magnetic field gradient</i>
B_{tr}	<i>Trapped magnetic field</i>
B, H	<i>Applied magnetic field</i>
B_{irr}, H_{irr}	<i>Irreversibility magnetic field</i>
J_c	<i>Superconducting critical current density</i>
J_{cm}	<i>Magnetism superconducting critical current density</i>
J_{ct}	<i>Transport superconducting critical current density</i>
α	<i>Jackson Factor</i>
σ	<i>Solution supersaturation</i>
R	<i>Growth rate of crystal</i>
R_a	<i>Growth rate on ab plane</i>
R_c	<i>Growth rate of c-axis</i>
ΔT	<i>Undercooling</i>
T_m	<i>Melting temperature</i>
ΔG	<i>Free energy difference</i>

Résumé détaillé de la thèse en français

Le travail de recherche de cette thèse s'inscrit dans le cadre de l'effort de développement entrepris au CRETA pour produire des monodomains d'YBaCuO en vue de leur utilisation dans des applications électrotechniques. Les monodomains sont des sortes de monocristaux dans lesquels des défauts sont introduits volontairement (phase secondaire pour le piégeage des vortex) ou non (défauts de croissance). L'objectif de la thèse est de croître des monodomains d'YBaCuO supraconducteur de haute qualité en utilisant le meilleur précurseur et le procédé PMP (Powder Melt Process, une technique de croissance à partir d'un germe sur une préforme d'un mélange de poudres d'oxydes précurseurs compacté). Les travaux de recherche sont effectués dans le cadre Laboratoire International Associé français-chinois LAS2M (Laboratoire pour l'application des supraconducteurs et des matériaux magnétiques) et ont été soutenus par une bourse de doctorat en alternance de l'ambassade de France à Pékin ainsi que par le projet chinois NFSC (50432050) et le projet chinois 863 (2007aa03z241).

Les monodomains de supraconducteur YBCO seront utilisés pour des paliers magnétiques (volants d'inertie pour le stockage de l'énergie, les systèmes de translation linéaire sans frottement), pour la production de champ magnétique élevé (moteurs, aimants permanents supraconducteurs). Les applications nécessitent une densité de courant critique J_c améliorée et des monodomains d'YBCO de plus grande taille. Le laboratoire CRETA a développé une technique originale de caractérisation in situ pour étudier les transitions de phase en mesurant la susceptibilité magnétique en temps réel sous champ magnétique à haute température par une balance de Faraday. Des monodomains allant jusqu'à 10 cm de diamètre ont été obtenus grâce à une approche originale de surveillance vidéo in situ de la croissance en surface. Le NIN (Northwest Institute for Non-Ferrous Metal Research, Xi'an, Chine) a une expertise dans la production de poudres supraconductrices et de superconducteurs massifs de haute qualité. Le matériau YBCO fabriqué par le procédé original de la fusion de poudres (PMP), inventé et développé par le NIN, est caractérisé par une distribution homogène de fines particules Y211 (phase secondaire améliorant les propriétés supra) et par une densité de courant J_c élevée. L'élaboration de monodomains d'YBCO par la méthode PMP doit permettre d'obtenir des J_c élevées. Donc, notre objectif est d'étudier le procédé PMP et de fabriquer des monodomains d'YBCO de haute qualité par cette méthode. Le travail de recherche est mené dans ces deux laboratoires, le CRETA et le NIN en utilisant la balance de Faraday à haute température sur le procédé PMP. Ce travail est décrit en 4 chapitres principaux, outre les chapitres d'introduction et de conclusions.

Dans le chapitre d'introduction, nous présentons l'état de l'art nécessaire pour poser les objectifs de cette thèse. Les différentes applications envisagées nécessitent d'importants courants capables de circuler sur une grande boucle, d'où le besoin d'étudier les mécanismes de croissance pour obtenir les cristaux les plus larges et de corrélérer microstructure et propriétés pour optimiser les densités de courant dans l'état supraconducteur.

Dans le chapitre 2, les transitions de phases lors de l'élaboration de massifs d'YBCO par le procédé PMP sont étudiées in situ par une balance de Faraday à haute température. C'est la première fois que sont révélées les principales transitions de phase ayant lieu au cours de la fabrication de massifs PMP-YBCO, incluant la formation et la fusion de la phase Y123, la fusion de la phase 011, la décomposition et la recombinaison du CuO en Cu₂O, et la solidification du cristal d'YBCO (Y123). L'effet de la vitesse de chauffe sur la transition de phase du massif PMP-YBCO est étudié par la mesure de susceptibilité. Celle-ci montre que la formation de 123 est évitée dans un massif PMP-YBCO à parois minces au-dessus d'une vitesse de chauffe critique de 120 ° C / h. Elle révèle aussi la manière dont la température de surchauffe et la surface spécifique influencent les transitions de phase dans les massifs PMP-YBCO.

Dans le chapitre 3, nous étudions la dynamique de croissance de monodomaines PMP-YBCO à parois minces. La vidéo haute-température in-situ du front de croissance permet de démontrer que la croissance du monodomaine a lieu dans une fenêtre étroite de températures comprises entre 1000°C et 980°C. En utilisant ces observations, nous avons réussi à fabriquer des monodomaines YBCO $\Phi 30\text{mm} \times 15\text{mm}$ par lot par le procédé PMP. Cette contribution est importante pour aborder la fabrication pratique de monodomaines YBCO de haute qualité.

Les résultats expérimentaux montrent que le taux de croissance suivant l'axe c, R_c , est directement proportionnel à la vitesse de diffusion de l'oxygène V_{O_2} : $R_c \propto V_{O_2}$. Ce résultat prouve que la diffusion de l'oxygène domine la croissance des monodomaines PMP-YBCO. De l'étude de la dynamique de la croissance, nous déduisons que la croissance dans l'air de monodomaines PMP-YBCO à parois minces repose sur deux systèmes de croissance: un système liquide fondu-solide et un système vapeur-solide. Dans le système de croissance liquide fondu-solide, le taux de croissance est proportionnel au carré de la surfusion ΔT , comme $R \propto \Delta T^2$. Dans le système vapeur-solide, le taux de croissance est lié à la vitesse de transport massique de l'oxygène $R_c \propto V_{O_2}$. Et la croissance du cristal d' Y123 est dépendante de deux types de diffusion: 1) les ions d'yttrium, de barium et de cuivre sont transportés dans le liquide fondu jusqu'à l'interface de croissance de la phase Y123 par diffusion en solution et

diffusion interfaciale comme un système liquide fondu-solide ; 2) la diffusion de l'oxygène dépend de la diffusion interfaciale à partir de l'air comme dans un système vapeur-solide. Les deux diffusions agissent sur la croissance cristalline de l'Y123 en même temps. Nous montrons qu'une surface spécifique augmentée par des trous artificiels dans le massif fournit un tunnel efficace de diffusion de l'oxygène pour la croissance du cristal d'Y123.

Dans le chapitre 4, les relations entre la microstructure et la densité de courant critique J_c , le champ magnétique piégé B_{tr} et la force de lévitation F des monodomains PMP-YBCO sont étudiées. Les monodomains PMP-YBCO à parois minces ont une morphologie typique de cristal carré (croissance d'une phase tétragonale) et une distribution de particules d'Y211 inhomogène à l'échelle macroscopique à cause du phénomène de pushing-trapping. A l'échelle microscopique, les particules d'Y211 sont fines, sphériques et distribuées de manière homogène conformément au procédé PMP. Le piégeage de flux n'est pas seulement lié aux particules d'Y211, mais aussi à la température critique de transition supraconductrice T_c (liée au taux d'oxygène dans le matériau). La densité de courant critique magnétique J_{cm} atteint $\sim 1,2 \times 10^5 \text{ A/cm}^2$ (77K, 0T) dans les monodomains PMP-YBCO, ce qui rejoint les meilleurs résultats à l'heure actuelle. La densité de courant critique de transport J_{ct} atteint $\sim 7,5 \times 10^3 \text{ A/cm}^2$ (78.5K), mais la différence avec J_{cm} montre qu'il existe encore beaucoup de pores et de fissures dans le matériau. Nous montrons qu'un traitement à haute pression d'oxygène permet d'améliorer le flux magnétique piégé B_{tr} à 739 mT à 77K pour un monodomaine PMP-YBCO à parois minces de 15 mm de diamètre.

Dans le chapitre 5, nous nous sommes intéressés à l'effet du taux de chauffe sur la taille des particules Y211 et la densité de courant critique magnétique J_{cm} des massifs PMP-YBCO. Le taux de chauffe le plus rapide ou le plus lent affine les particules d'Y211 et une densité de courant critique magnétique J_{cm} de 10^5 A/cm^2 (77K, 0T) est atteinte. Un taux de chauffe raisonnable est nécessaire pour la croissance des monodomains PMP-YBCO.

Le chapitre de conclusion reprend les résultats énoncés ci-dessus et propose en perspective une approche plus quantitative des mesures de susceptibilité pour l'analyse des transition de phase, de continuer à explorer le rôle de l'oxygène dans la croissance des monodomains et d'optimiser l'oxygénation sous pression.

Contents

Résumé.....	3
Abstract.....	3
Acknowledgement.....	5
Physical Term and Physical Unit Notation.....	7
Résumé détaillé de la thèse en français.....	9
Contents.....	13
Introduction.....	17
Chapter 1 State of Art.....	19
1.1 Application of bulk HT _c superconductor YBCO.....	19
1.2 Phase diagram and susceptibility transition of YBCO.....	20
1.3 Growth theory of YBCO single domain.....	22
1.3.1 Solidification Theory.....	22
1.3.2 Thermal Undercooling and Constitutional Undercooling.....	23
1.3.3 Smooth surface and nucleation.....	24
1.3.4 Y diffusion growth model.....	25
1.3.5 Interface growth model.....	25
1.4 Microstructure of YBCO single domain.....	26
1.5 The critical current density J_c and flux pinning of YBCO.....	28
1.5.1 The critical current density J_c	28
1.5.2 Vortex Phase Diagram.....	28
1.5.3 Flux pinning mechanism and effective pinning sites.....	31
1.6 Our study purpose and contents.....	32
References.....	34
Chapter 2 Phase transition of bulk PMP-YBC.....	37
2.1 High temperature Faraday Balance.....	37
2.2 Phase transition of bulk PMP-YBCO.....	38
2.2.1 Experimental.....	38
2.2.2 Phase transitions in bulk PMP-YBCO.....	40
2.3 Effect of heating rate on phase transition.....	51
2.3.1 Experimental.....	51
2.3.2 Effect of heating rate on phase transition of plain samples.....	52
2.3.3 Effect of heating rate on phase transition of hole samples.....	53
2.4 Effect of reduced diffusion path on phase transition.....	54
2.5 Effect of overheating-temperature on phase transition.....	55
2.6 Summary.....	58
References.....	60
Chapter 3 Growth of PMP-YBCO single domain.....	61
3.1 YBCO single domain fabrication by Powder Melting Process.....	61
3.2 Nucleation.....	62
3.2.1 Screw nucleation.....	62
3.2.2 Nucleating temperature.....	63
3.3 Growth of plain PMP-YBCO single domain.....	64
3.3.1 High temperature furnace with in situ video monitoring.....	64
3.3.2 The solidification window of PMP-YBCO.....	65

3.3.3 Batch fabrication of PMP-YBCO single domain	66
3.4 Oxygen diffusion effect to the growth	67
3.5 Dynamics of the hole PMP-YBCO single domain growth	71
3.5.1 Growth of hole PMP-YBCO single domains	71
3.5.2 Growth rate R_a	71
3.5.3 Experimental	73
3.5.4 Growth rates R_{ab} and R_c determined from quench experiments.....	75
3.5.5 Effect of oxygen diffusion on growth rate R_c	76
3.5.6 Hole PMP-YBCO Single domain growth in flowing air	78
3.5.7 Constitutional undercooling in the growth.....	79
3.5.8 Effect of reduced diffusion path on growth	80
3.6 Growth mechanism of hole PMP-YBCO single domains.....	82
3.6.1 Faceted growth, Surface and nucleation of 123 crystals.....	82
3.6.2 Yttrium diffusion.....	83
3.6.3 Oxygen diffusion.....	84
3.6.4 Solution diffusion and growth system.....	85
3.7 Summary	87
References	89
Chapter 4 Microstructure and properties of PMP-YBCO single domain	91
4.1 Microstructure of PMP-YBCO single domain.....	91
4.2 High pressure oxygen treatment and low pressure flowing oxygen treatment	98
4.3 T_c and oxygen content	99
4.4 Comparison of trapped magnetic field B_{tr} of PMP-YBCO treated in HO_2 and LO_2	101
4.5 Trapped magnetic field B_{tr} and levitation force F of PMP-YBCO single domain ..	103
4.6 Magnetic critical current density J_{cm}	105
4.7 Flux pinning in PMP-YBCO single domain	108
4.7.1 Irreversibility line B_{irr}	108
4.7.2 Flux pinning and vortex phase diagram of PMP-YBCO	109
4.8 Transport critical current density J_{ct}	111
4.9 Summary	115
References:.....	116
Chapter 5 Effect of the heating rate on PMP-YBCO single domain	117
5.1 Experimental	117
5.2 Effect on the phase transition.....	117
5.3 Effect on the 211 particles.....	118
5.4 Effect on the magnetism critical current density J_{cm}	122
5.5 Summary	127
References	127
Chapter 6 Conclusion and prospect.....	129
Annex 1: Magnetic field character parameter and the temperature distribution measurement	133
Annex 2 : Susceptibility and oxygen lost calculation of PMP-YBCO sample	139
Annex 3 : Effect of changing heating rate on the measured signal.....	147
Annex 4 : The susceptibility measured signal of 011 phase	151
Annex 5 : Porosity Calculation	153
Published Papers and Conferences.....	157

Résumé	3
Abstract	3
Acknowledgement	5
Physical Term and Physical Unit Notation	7
Résumé détaillé de la thèse en français	9
Contents	13
Introduction	17
Chapter 1 State of Art.....	19
1.1 Application of bulk HT _c superconductor YBCO	19
1.2 Phase diagram and susceptibility transition of YBCO.....	20
1.3 Growth theory of YBCO single domain	22
1.3.1 Solidification Theory.....	22
1.3.2 Thermal Undercooling and Constitutional Undercooling.....	23
1.3.3 Smooth surface and nucleation	24
1.3.4 Y diffusion growth model	25
1.3.5 Interface growth model	25
1.4 Microstructure of YBCO single domain	26
1.5 The critical current density J_c and flux pinning of YBCO.....	28
1.5.1 The critical current density J_c	28
1.5.2 Vortex Phase Diagram	28
1.5.3 Flux pinning mechanism and effective pinning sites	31
1.6 Our study purpose and contents	32
References	34
Chapter 2 Phase transition of bulk PMP-YBC	37
2.1 High temperature Faraday Balance	37
2.2 Phase transition of bulk PMP-YBCO.....	38
2.2.1 Experimental	38
2.2.2 Phase transitions in bulk PMP-YBCO	40
2.3 Effect of heating rate on phase transition.....	51
2.3.1 Experimental	51
2.3.2 Effect of heating rate on phase transition of plain samples.....	52
2.3.3 Effect of heating rate on phase transition of hole samples.....	53
2.4 Effect of reduced diffusion path on phase transition.....	54
2.5 Effect of overheating-temperature on phase transition	55
2.6 Summary	58
References	60
Chapter 3 Growth of PMP-YBCO single domain.....	61
3.1 YBCO single domain fabrication by Powder Melting Process.....	61
3.2 Nucleation	62
3.2.1 Screw nucleation	62
3.2.2 Nucleating temperature	63
3.3 Growth of plain PMP-YBCO single domain	64
3.3.1 High temperature furnace with in situ video monitoring	64
3.3.2 The solidification window of PMP-YBCO.....	65
3.3.3 Batch fabrication of PMP-YBCO single domain.....	66
3.4 Oxygen diffusion effect to the growth	67
3.5 Dynamics of the hole PMP-YBCO single domain growth	71
3.5.1 Growth of hole PMP-YBCO single domains.....	71
3.5.2 Growth rate R_a	71
3.5.3 Experimental	73
3.5.4 Growth rates R_{ab} and R_c determined from quench experiments.....	75

3.5.5 Effect of oxygen diffusion on growth rate R_c	76
3.5.6 Hole PMP-YBCO Single domain growth in flowing air	78
3.5.7 Constitutional undercooling in the growth.....	79
3.5.8 Effect of reduced diffusion path on growth	80
3.6 Growth mechanism of hole PMP-YBCO single domains.....	82
3.6.1 Faceted growth, Surface and nucleation of 123 crystals.....	82
3.6.2 Yttrium diffusion.....	83
3.6.3 Oxygen diffusion.....	84
3.6.4 Solution diffusion and growth system.....	85
3.7 Summary	87
References	89
Chapter 4 Microstructure and properties of PMP-YBCO single domain	91
4.1 Microstructure of PMP-YBCO single domain.....	91
4.2 High pressure oxygen treatment and low pressure flowing oxygen treatment	98
4.3 T_c and oxygen content	99
4.4 Comparison of trapped magnetic field B_{tr} of PMP-YBCO treated in HO_2 and LO_2	101
4.5 Trapped magnetic field B_{tr} and levitation force F of PMP-YBCO single domain ..	103
4.6 Magnetic critical current density J_{cm}	105
4.7 Flux pinning in PMP-YBCO single domain	108
4.7.1 Irreversibility line B_{irr}	108
4.7.2 Flux pinning and vortex phase diagram of PMP-YBCO	109
4.8 Transport critical current density J_{ct}	111
4.9 Summary	115
References:	116
Chapter 5 Effect of the heating rate on PMP-YBCO single domain	117
5.1 Experimental	117
5.2 Effect on the phase transition	117
5.3 Effect on the 211 particles.....	118
5.4 Effect on the magnetism critical current density J_{cm}	122
5.5 Summary	127
References	127
Chapter 6 Conclusion and prospect.....	129
Annex 1: Magnetic field character parameter and the temperature distribution measurement	133
Annex 2 : Susceptibility and oxygen lost calculation of PMP-YBCO sample	139
Annex 3 : Effect of changing heating rate on the measured signal.....	147
Annex 4 : The susceptibility measured signal of 011 phase	151
Annex 5 : Porosity Calculation	153
Published Papers and Conferences.....	157

Introduction

The research work of this thesis is part of the development effort undertaken at CRETA to produce YBaCuO single domain for using in electrotechnical applications. The aim of the thesis is to grow high quality single domain YBaCuO superconductor using the best raw material and PMP process. The research works are performed under the frame of the French-Chinese International Associated Laboratory LAS2M and supported by the French Embassy at Beijing as an alternating PhD grant, by the Chinese NFSC Project (50432050) and the Chinese 863 project (2007aa03z241).

Superconductor YBCO single domain will be used for magnetic bearings (flywheels for energy storage, frictionless linear translation systems), for producing high magnetic field (motors, superconducting pseudo permanent magnets). The engineering application requires an improved J_c and a larger size YBCO single domain. The CRETA laboratory has developed an original in situ characterization technique for phase transition studying by measuring the magnetic susceptibility in real time under magnetic field– high temperature Faraday Balance. Single domains up to 10 cm have been obtained thanks to an original approach using in situ video monitoring of the surface growth. NIN (Northwest Institute for Non-ferrous Metal Research, Xi'an, China) has expertise in producing high quality superconducting powder and bulk material. The YBCO material fabricated by the original powder melting process (PMP) has the character of well distributed refined 211 particles and high J_c which invented in NIN. If the large single domain YBCO is prepared by the PMP method, it will obtain high J_c . So our purpose is to study the PMP process and fabricate the high quality YBCO single domain by PMP process. The research work is conducted at both CRETA and NIN by using the high temperature Faraday Balance under the PMP process. This research works includes mainly four different chapters.

In the chapter 2, the phase transition of PMP-YBCO bulk is investigated by the high temperature Faraday Balance. It is the first time to reveal the main phase transitions happening during the PMP-YBCO bulk fabrication including 123 formation and melting, 011 melting, CuO decomposing, CuO composing and the 123 crystal solidification. The effect of the heating rate on the phase transition of PMP-YBCO bulk is investigated by the susceptibility measurement. The critical heating rate 120°C/h is found to avoid the 123 formation in hole PMP-YBCO single domain fabrication. It reveals the laws how the overheating temperature and the specific surface area influence the phase transition of PMP-YBCO.

In the chapter 3, the dynamics of hole PMP-YBCO single domain growth is studied. It is found the single domain growth window is in 1000°C-980°C investigated by the high

temperature video in-situ. The experimental result shows the c-axis growth rate R_c is directly proportional to the oxygen diffusion velocity V_{O_2} : $R_c \propto V_{O_2}$. The result proves the oxygen diffusion dominating the growth of PMP-YBCO single-domain. By the dynamics studying, we consider the holed PMP-YBCO single domain growth in air depending on two growth systems: the melt-solid system and the vapour-solid system. In the melt-solid growth system, the growth rate is proportional to the square of the undercooling ΔT , as $R \propto \Delta T^2$. In the vapour-solid system, the growth rate is related to the oxygen mass transport velocity $R_c \propto V_{O_2}$. And the 123 growth is depended on two diffusion classes: 1) the yttrium, barium and copper ion diffuse in melt liquid transport to the 123 growth interface from the solution diffusion and interfacial diffusion as in melt-solid system. 2) The oxygen diffusion depends on interfacial diffusion from air as in vapour-solid system. The two diffusions act in the 123 crystal growth at the same time. A large specific surface area with artificial holes provides an effective tunnel for oxygen diffusion in the 123 crystal growth.

In chapter 4, the relationship of microstructure and the properties of critical current density J_c , trapped magnetic field B_{tr} and levitation force F of a PMP-YBCO single domain are studied. The thin walled PMP-YBCO single domain has a typical morphology of square single domain and presents a macrodistribution of the 211 particles characteristic of the pushing-trapping phenomenon during growth. Locally, it has a homogenous microdistribution of fined and round 211 particles as expected from PMP process. The flux pinning is related not only to the 211 particles but also to the superconducting transition temperature T_c (oxygen content). The magnetism critical current density J_{cm} is achieved as $\sim 1.2 \times 10^5 \text{ A/cm}^2$ (77K, 0T) in the PMP-YBCO single domain which reaches the best record at present. The transport critical current density J_{ct} is measured to $\sim 7.5 \times 10^3 \text{ A/cm}^2$ (78.5K). The high pressure oxygen treatment is proved to improve the trapped magnetic field B_{tr} of hole PMP-YBCO single domain to 739mT in diameter of $\Phi 15\text{mm}$ at 77K.

In the chapter 5, the effect of heating rate on the size of 211 particles and the magnetic critical current density J_{cm} of PMP-YBCO bulk is studied. The faster or the slower heating rate will refine the 211 particles and a high magnetism critical current density J_{cm} as 10^5 A/cm^2 (77K, 0T) is achieved. The feasible heating rate is necessary to the PMP-YBCO single domain growth.

In PMP process the author has successful fabricated the batch of PMP-YBCO single-domain $\Phi 30\text{mm} \times 15\text{mm}$. It gives a important contribution for practical fabrication of high quality YBCO single domain.

Chapter 1 State of Art

1.1 Application of bulk HT_c superconductor YBCO

HT_c superconductor Y₁Ba₂Cu₃O_{7-δ} (as also referred to as YBCO or 123) is associated to trapped magnetic field, high critical current and levitation properties. Based on these properties, the superconductor YBCO single domain can find applications in the Maglev train [1.1], flywheel energy storage system [1.2], superconductor bearing [1.3], superconducting permanent magnet [1.4]. And it is expected to represent a valuable share in the further superconducting material's market. The superconducting Maglev can benefit from the levitation properties and the superconducting permanent magnet from the trapped magnetic field. At present, the best record of the levitation force F for a YBCO single domain is up to $16 \text{ N}\cdot\text{cm}^{-2}$ at 77K [1.5]. The maximum trapped field B_{tr} at 77K is 2.1 T for a U-irradiated $\text{Ø}20\text{mm}$ sample, and is 1.6T for a $\text{Ø}33\text{mm}$ YBCO sample without irradiation prepared at ISTECH (International Superconductivity Technology Centre) by MPMG [1.6]. The trapped magnetic field distribution of the latter is shown in figure 1-1. Since the levitation force F and the trapped magnetic field B_{tr} are proportional to the critical current density J_c and the superconducting current loop radius r , the properties are improved by enhancing J_c and enlarging the size of the single domain.

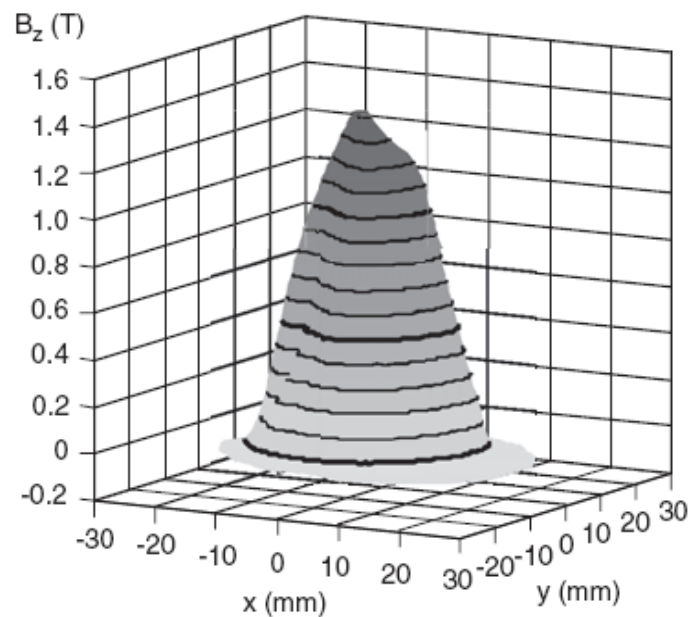


Figure 1-1 Trapped magnetic field of a MTG-YBCO at 77K [1.6]

1.2 Phase diagram and susceptibility transition of YBCO

It is necessary to fabricate large YBCO single domains. But the continuous directional growth of large size crystal domain is not easy to control. The chemical reaction of 123 crystal formation is a peritectic reaction where the solid Y_2BaCuO_5 (short for 211) reacts with liquid phase according to the following description:



Figure 1-2 is a section of the phase diagram in the Y_2O_3 -BaO-CuO system [1.7]. The thermal equilibrium temperature of forming 123 crystal is given at 1002°C . The principle of the peritectic reaction is clear but the dynamic phase transition is very complicated so that the 123 crystal directional solidification is not easy.

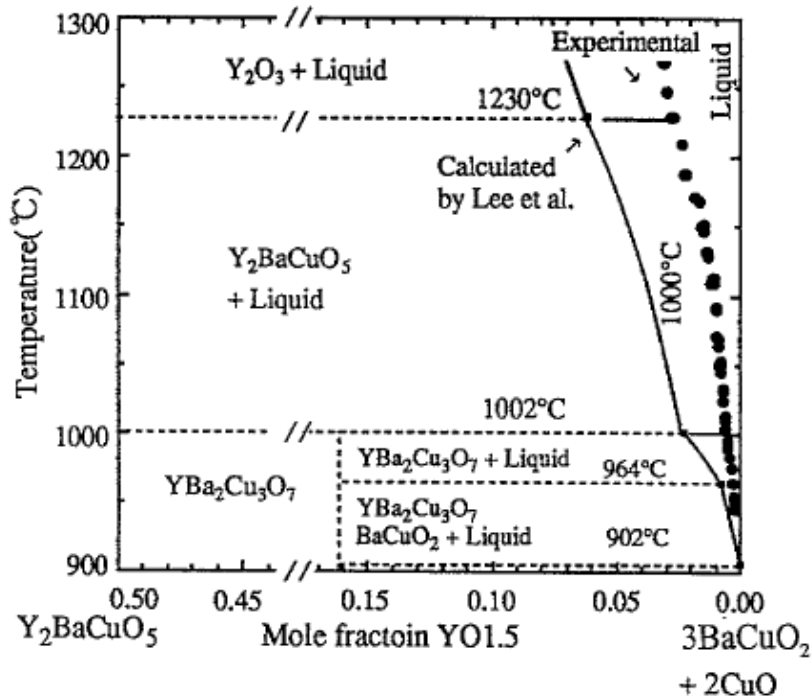


Figure 1-2 Phase diagram of YBCO in Y_2O_3 -BaO-CuO system at 0.21atm oxygen pressure [7]

In order to investigate the dynamic phase transition of a YBCO single domain growth, Eric Beaunon et al. used the high temperature Faraday Balance for studying the solidification of bulk YBCO superconductor in MTG process firstly [1.8, 1.9]. The YBCO has a paramagnetic behavior and its susceptibility decreases as the temperature increases abiding a Curie-Weiss law. However, at high temperature, the susceptibility also changes according to the Cu valence or to phase transformation when the liquid-solid transition occurs

[1.10, 1.11]. So the susceptibility variation could reveal the phase transitions in bulk YBCO sample such as melting and solidification. As shown in figure 1-3, the measured susceptibility transition curve displays the practical melting range and solidification window of bulk MTG-YBCO in situ. This phase transition information helped to the fabrication of large YBCO single domains [1.12]. Figure 1-4 shows the largest YBCO single domain (93mm in diameter) prepared up to now at the CRETA/CNRS laboratory by a top seeding technique.

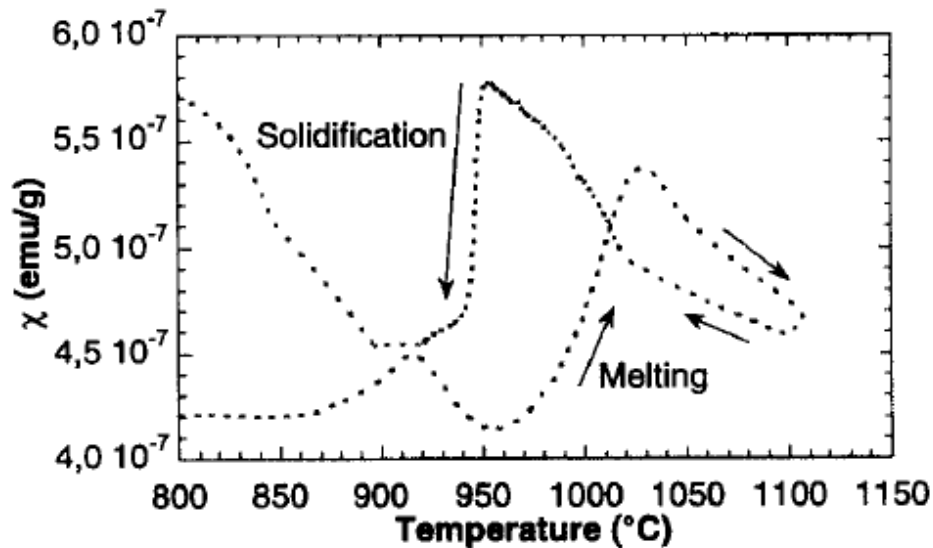


Figure1-3 Melting and solidification of MTG-YBCO investigated by the magnetic susceptibility transition^[1.9]



Figure 1-4 A YBCO single domain of 93 mm in diameter.

After the discovery of the superconductor YBCO, the process of fabricating YBCO material was developed from the primary solid-state sintering method to the MTG (melt textured growth) (1988), QMG (quench and melt growth) (1990), and PMP (powder melt textured growth) (1990) methods used at present [1.13]. Practically, these methods consist in bringing a pellet at high temperature to melt precursors and then in slow cooling so that crystals can appear and grow. To control the nucleation and the growth direction, these

methods are associated with a seeding technique, cold or hot depending whether the seed is placed prior the treatment or after the melting step, using one or multiple seeds. Depending on the modified process, the structure of the bulk YBCO becomes more textured with well linked boundaries, eventually with no more boundaries. The aim of texturation is to get rid of weak links which are boundaries weakening drastically the superconducting properties. Strongly disoriented grain boundaries are weak links. The critical current density J_c has been improved by two orders of magnitude. Furthermore, with the multi-seeding technique, large YBCO single domains of 50mm×30mm could be prepared as shown in figure 1-5. However, growing large size and high quality single domain is still a key issue in the bulk YBCO fabrication. Firstly, it is not easy to control the “large” YBCO single domain solidification since random nucleation may occur at the front of the growth interface. Secondly, the growth mechanism of the YBCO single domain is not completely understood. Thirdly, the critical current density determined by magnetic measurement is no more than 10^4 A.cm^{-2} (77K) in bulk YBCO although the theoretical J_c value is up to 10^8 A.cm^{-2} (77K) and is the J_c tested in YBCO films can reach up to 10^6 A.cm^{-2} (77K). How to improve the critical current density J_c and to make the bulk YBCO single domain fabrication process robust and reproducible become the key problems.

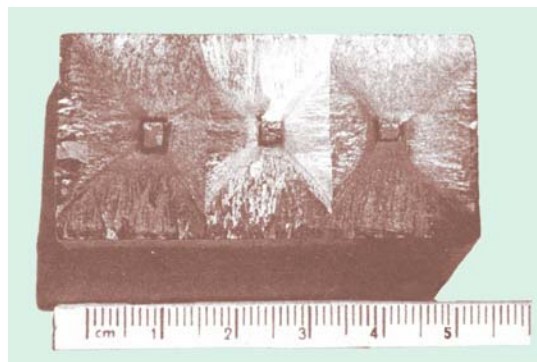


Figure 1-5 A large YBCO single domain of 50mm×30mm prepared by multi-seeding technique

1.3 Growth theory of YBCO single domain

1.3.1 Solidification Theory

The growth mechanism of the directional solidification of large size YBCO single domain could be described by the crystal solidification theory. Based on the metal solidification theory created by Gibbs and Turnbull et al. [1.14], in pure metal, if the temperature is decreased below the melting point, the Gibbs free energy G of the system will

decrease to bring the nucleation in the liquid metal system. The decreasing Gibbs free energy ΔG_m is proportional to the undercooling ΔT :

$$\Delta G_m \approx \frac{\Delta H_0 \cdot \Delta T}{T_m} \quad (1-2)$$

Here, ΔH_0 is the enthalpy of fusion, ΔT the undercooling, T_m the melting point.

The metal solidification theory is extended to the crystal growth system. A thermodynamic driving force of crystallization comes from the negative difference ($\Delta G < 0$) between the free energies of the liquid and the solid. According to the solidification theory, the driving force of 123 crystal nucleation and growth comes from the undercooling ΔT yielding a Gibbs free energy ΔG decrease.

1.3.2 Thermal Undercooling and Constitutional Undercooling

The driving force for the growth of 123 crystals is provided by an undercooling which can be thermal or associated with concentration variation at the solid-liquid interface. The undercooling near 123 crystal growth interface is analyzed by Michael J Cima as shown in figure 1-6 [1.15]. The actual undercooling ΔT_p which implies the material is brought to a temperature below the peritectic one includes three aspects as follows:

$$\Delta T_p = \Delta T_G + \Delta T_s + \Delta T_c \quad (1-3)$$

Here, ΔT_G is the depression of the integrated temperature resulting from the temperature gradient G , ΔT_s the maximum “constitutional supercooling” ahead of the interface, and ΔT_c the temperature depression resulting from the deviation in solute concentration at the 211 interface from that of the peritectic liquid composition, C_{LP} .

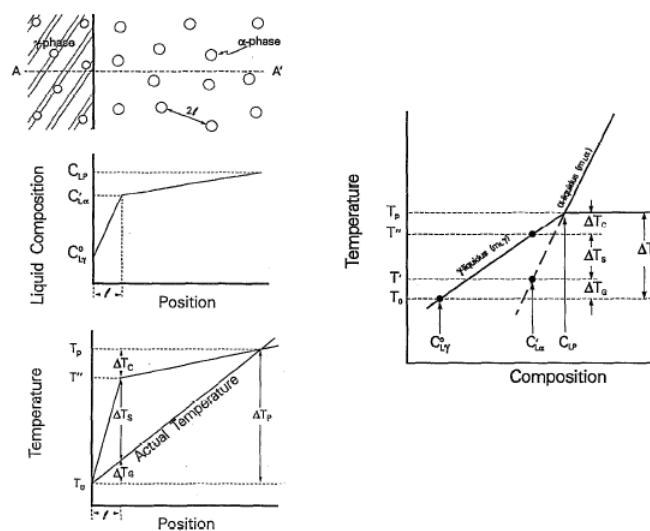


Figure 1-6 The ΔT_G , ΔT_s and ΔT_c undercooling components at the interface of the 123 crystal growth front [1.15]

1.3.3 Smooth surface and nucleation

The solidification theory tells us the essential condition of nucleation and growth in the system. It informs us about the possibility of the material's solidification. In 1951, Burton, Cabrera and Frank published "the growth of crystals and the equilibrium structure of their surfaces" and built the **BCF** interface growth theory [1.16]. Following the BCF theory, K A Jackson brought forward a criterion of crystal surface as smoothness or roughness, identifying the nucleation type in one atom layer model [1.17]. He analyzed the atom occupied fraction of surface sites on the growth interface from the thermodynamics and statistics, obtained the Jackson parameter α described as follows:

$$\alpha = \frac{\Delta H_0}{kT_m} \left(\frac{\eta}{\nu} \right) \quad (1-4)$$

The parameters are the following ones: η - the number of neighbors atoms at interface, ν - the number of neighbors atoms in crystal lattice, $\frac{\Delta H_0}{kT_m}$ - the entropy of phase transition, $\frac{\eta}{\nu}$ - the crystallographic anisotropy factor, which depends on the crystal structure and the facial index.

The Jackson parameter α is related to the entropy and the crystal structure. When $\alpha \geq 5$, the crystal surface is smooth; when $\alpha \leq 5$, the surface is rough. Based on the BCF theory, the surface structure in equilibrium controls the growth mechanism of crystal. For smooth surfaces, the crystal grows layer by layer. It grows by two-dimensional nucleation or screw dislocation. For rough surfaces, it grows by continuous growth. The growth rates in both growth types are determined by the super-saturation σ or kinetic undercooling ΔT_k .

C. Klemenz calculated the Jackson parameter α of YBCO crystal [1.18] and found a value between 9 and 13. So the 123 crystal surfaces are smooth and the nucleation should be two dimensional or screw nucleation. Otherwise, it becomes continuous growth if the surface roughness increased. B. N. Sun and other several groups investigated nucleation on (001) plane [1.19] and found that the YBCO crystal grows by the screw dislocation. However, the 123 growth in the case of the screw dislocation depends on the supersaturation σ and the thermal kinetic undercooling ΔT_k . If the supersaturation is very high, the rate of screw dislocation will approach the continuous growth law as an upper limit which is similar to two-dimensional nucleation growth.

The Gibbs's solidification theory lays the possible condition of nucleation and crystal growth. The BCF theory predicts the intrinsic crystal growth structure and the growth law. We think it is better to discuss the growth mechanism of YBCO by a combination of both theories.

1.3.4 Y diffusion growth model

In 1992, Izumi, Cima and Mori presented a 123 growth model based on yttrium diffusion [1.20, 1.21, 1.22]. They assumed the 123 crystal growth rate is limited by the yttrium diffusion. In a classical peritectic reaction, once the 123 occurred, the 211 particles would be wrapped by 123 phase and yttrium would have to diffuse through the 123 solid towards the liquid phase. As the 123 shell would become larger, it would more difficult for yttrium to reach the 123 solid-liquid interface. The resulting microstructure would be an assembly of 123 grains with a 211 core. This is not what is experimentally observed. On the contrary large 123 grains are obtained trapping many 211 particles.

To solve this inconsistency, a new mechanism has been proposed which is illustrated in figure 1-7. In this model, the 211 particles dissolves partially in the melt and the yttrium is transported to the growing 123 interface by diffusion in the melt. Once the 123 nucleation happened, the yttrium necessary for the 123 growth front is provided by the neighbouring 211 particles. As the liquid phase is depleted in yttrium by the growth front, these particles partially melt to compensate the yttrium depletion. The dissolved yttrium ions travel across the liquid to the 123 growth interface front - driven by the yttrium gradient - for feeding the 123 crystal continuous growth. Thus, the growth rate is controlled by the yttrium diffusion rate.

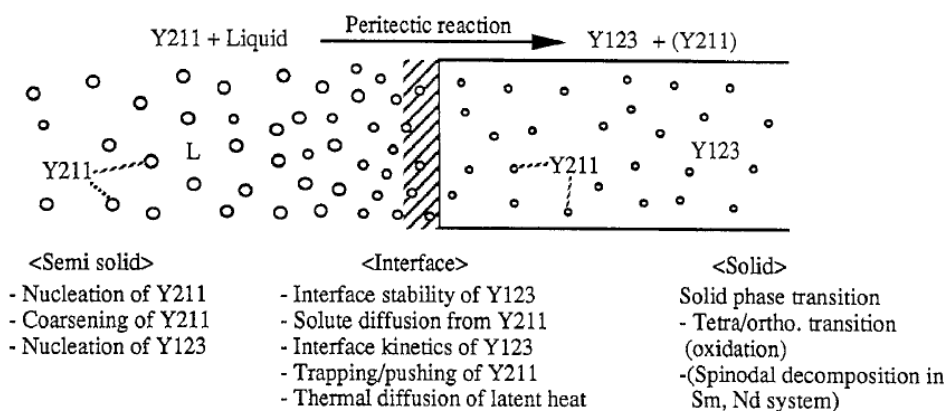


Figure 1-7 The interface at the front of the 123 crystal growth. It shows the growth problems related to the 123 crystal growth process.

1.3.5 Interface growth model

It is noticed that the faceted growth of 123 crystals is related to surface smoothness [1.7]. Because of the small yttrium solubility in liquid and low atom diffusion velocity at the interface, the growth rate is lower than 10^{-5} mm/s [1.23]. Y. Shiohara and A. Endo considered that the interfacial kinetics follows the BCF theory. They assumed the 123 crystal growth is

related to the solution supersaturation σ . The relationship between the growth rate R on ab-plane and the yttrium supersaturation σ was investigated by Kanamori and Y. Shiohara by the SRL-CP (Solute Rich Liquid-Crystal Pulling) method which is a modified pulling method to grow single crystal. Their experimental result is in accordance with the law $R \propto \sigma^2$ when the yttrium supersaturation is sufficiently small, $\sigma < \sigma_1$ [1.7].

The two models above can explain the problem of low growth rate. But there are still further problems impeding the practical growth such as which solution diffusion control the growth rate, how to increase the solution diffusion in the growth, how to control the 211 particles coarsening, etc. Only a good understanding of the 123 crystal growth can help us to solve these problems. They are summarized in figure 1-7 [1.7]. They are addressed in our research works.

1.4 Microstructure of YBCO single domain

The property such as the J_c of YBCO single domain depends on its microstructure. The lattice of YBCO crystal is the perovskite structure as shown in figure 1-8. The physical properties and structure are changed with the oxygen content. When the oxygen content is as $7-\delta < 6.5$, $YBa_2Cu_3O_{7-\delta}$ is a non superconducting tetragonal phase. When it is as $6.5 < 7-\delta < 7.0$, the $YBa_2Cu_3O_{7-\delta}$ phase becomes a superconducting orthorhombic phase.

The typical morphology of MTG-YBCO sample displays an anisotropic platelet structure inside a 123 grain, as shown in figure 1-9. This platelet structure appears in a grain after oxygenation has induced an intensive cracking along the ab-plane. Thus the visible cracks are also indicating the ab-plane. High-angle grain boundaries act as weak links limiting the current flow. Therefore, the YBCO grains should be well oriented to diminish this weak link behavior. The optimum is to get only one large 123 crystal in a pellet.

One can notice the presence of a relatively well distributed secondary phase in fig 1-9. Partly because of this secondary phase which are 211 particles and partly because of alignment defects, the term of domain is preferred to that of crystal. In 123 crystal growth, inhomogeneous size and distribution of 211 particles is induced by the 123 solidification process. The 211 particles have a trend to grow larger to minimize interfacial energy since smaller size 211 particles have higher interface energy than larger size 211 particles. This is called Ostwald ripening mechanism. Depending on their size, the 211 particles are “trapped” behind the growth front during the peritectic recombination, or others are “pushed” in the front of the growth interface. This is called the “**pushing-trapping**” phenomenon [1.7]. The finer the particles, the more chance it has to be “pushed” ahead by the growth front.

Other special characters of the microstructure are twins and cracks. The cracks are clearly visible in figure 1-9a. The twin structure appears in figure 1-9b as parallel traces along the vertical face of the layers. Twinning is created by a symmetrical exchange of the a and b lattice parameters. Twin and crack formations are mostly triggered by the tetragonal-to-orthorhombic (**T-O**) phase transition process. After an oxygen treatment at 350°C-750°C, oxygen atoms fill the O_1 sites which results in the shrinking of the lattice parameter c and a , as well as in the extending of b . It yields a shear stress in the 123 matrix that generates twinning and cracking. These typical microstructure characters have an influence on the critical current density J_c of YBCO single domain.

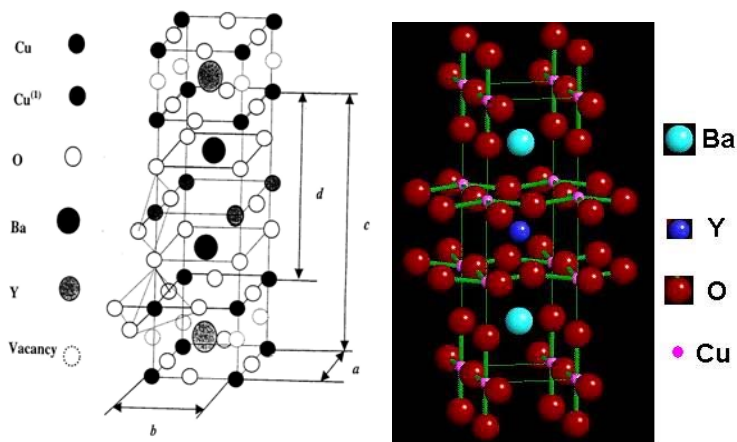


Fig1-8 The lattice of YBCO superconductor crystal (R=Yttrium)

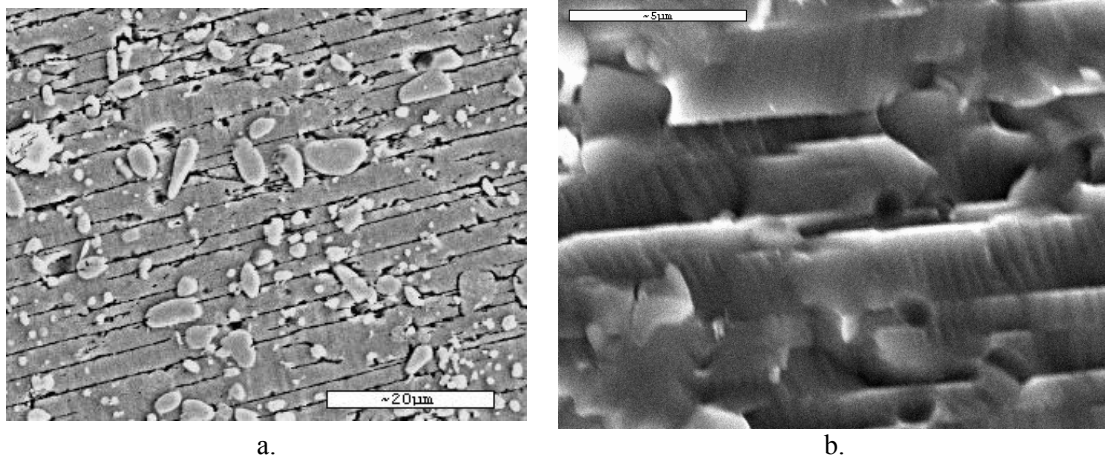


Figure 1-9 Typical microstructure of YBCO. On the left is the 123 grain layered structure and ab cracks, on the right the twins structure are visible on the fractured section of the 123 grain layered structure. The particles visible on left are the 211 phase. They left holes on the right picture.

1.5 The critical current density J_c and flux pinning of YBCO

1.5.1 The critical current density J_c

The critical intrinsic current in superconductor is the de-pairing critical current j_c^{dep} . It is estimated to be the order of H_c/λ , if $H_c=0.1T$ and $\lambda=100nm$, the j_c^{dep} is given as [1.13]:

$$j_c^{dep} = H_c/\lambda \approx 10^8 \text{ A.cm}^{-2} \quad (1-5)$$

This value is four (4) orders of magnitude higher than the experimental value. As the superconducting current flows in crystal and through grain boundary, the critical current density J_c of bulk YBCO can be divided due to defects, imperfections and cracks. There are two type of J_c measurement: the magnetization current density J_{cm} and the transport current density J_{ct} . The magnetization current density J_{cm} is intra-grain current (inside grain). It is measured by the magnetic irreversibility line. This measurement depends on the pinning force and requires the grain size or the scale at which the current is flowing to be known. The transport current density J_{ct} is the inter-grain current (from one grain to another through grain boundary). It is measured directly by the four point method. Because of low flux pinning, of weak links at the boundary and of cracks, the practical current density J_c is usually much lower than the theoretical value.

In MTG-YBCO single domain, the maximum transport critical current density J_{ct} so far is around $\sim 2.5 \times 10^4 \text{ A.cm}^{-2}$ (77K, 1.5T) (figure 1-10) [1.24], its mean value is around $\sim 10^3 \text{ A.cm}^{-2}$ (77K). A maximum magnetism critical current density J_{cm} is $\sim 1.1 \times 10^5 \text{ A.cm}^{-2}$ (77K, 0T) (figure 1-11) [1.25], its mean value is around $\sim 10^4 \text{ A.cm}^{-2}$ (77K). The transport critical current density J_{ct} and the magnetism critical current density J_{cm} of small PMP-YBCO samples are over $\sim 10^5 \text{ A.cm}^{-2}$ (77K, 0T). The higher J_{cm} is a benefit of refined 211 particles while J_{ct} is increased by well connected 123 crystal boundaries in PMP-YBCO sample.

1.5.2 Vortex Phase Diagram

The superconducting magnetism critical current density J_{cm} is related closely to the flux pinning. Being a type II superconductor, the YBCO has the following characters: 1) higher critical transition temperature, $T_c \sim 90K$; 2) short coherence length ξ , $\xi_{ab} = 2.7nm$ (77K), $\xi_c = 0.3nm$ (77K); 3) strong anisotropy, $\xi_{ab}(0)/\xi_c(0) = 5 \sim 8$. When the superconductor is in the mixed state, the flux lines are pinned. A flux line contains one quantum of magnetic flux $\Phi_0 = h/2e$. It is composed of a normal conducting core of radius ξ (**coherence length**) and a surrounding supercurrent, as shown in figure 1-12. In order to improve the critical current J_{cm}

the size of the pinning centers should be nanometric, of the same order as to the coherence length ξ .

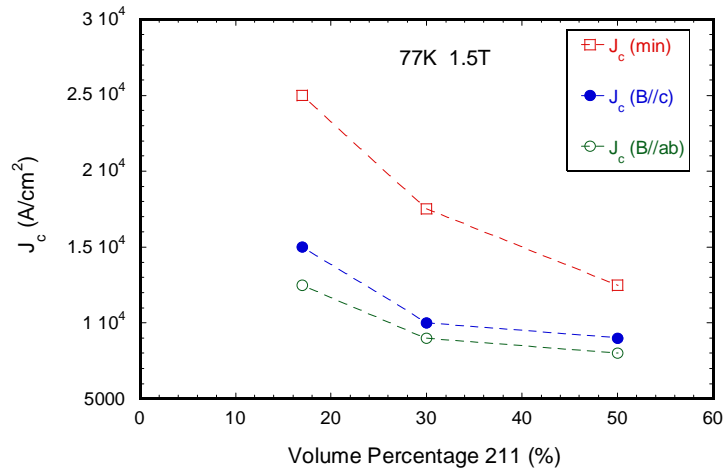


Figure 1-10 The transport critical current density J_{ct} of YBCO crystal with 211 content [1.24]

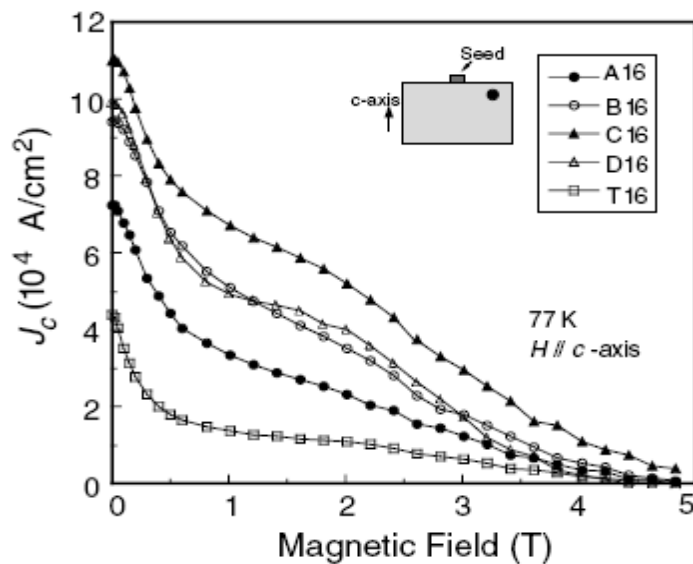


Figure 1-11 The magnetization critical current density J_{cm} of bulk YBCO vs. magnetic field [1.25]

Flux (or vortex) state in YBCO has a different behaviour at different temperatures T or field H as shown in the vortex phase diagram of the figure 1-13 [1.26]. The vortex phases are divided into flux liquid, vortex glass and Bragg glass/vortex lattice. In the vortex liquid state, the superconducting current is zero. Only below the irreversibility field B_{irr} , the flux is pinned and provides a current. If the irreversibility field B_{irr} is increased, the magnetic current density J_{cm} will be improved. Different mechanisms of flux pinning exist in different region of the diagram (low field/high field for instance). Only a good understanding of the different pinning mechanism could provide us an effective way to increase the pinning force. The vortex glass

phase corresponds to a region where the flux is strong. The Bragg glass phase corresponds to a weak pinning state. It should be noted that the temperature of 77K envisaged for most of the applications of YBCO corresponds to a weak pinning state for flux line. Thus, at 77K, the flux trapping capability of bulk YBCO is not optimal. The record is about 1.6T at 77K for a $\Phi 33\text{mm}$ sample. Therefore, moving the irreversibility line B_{irr} to a higher field or to decrease the application temperature is necessary for improving the limited trapped magnetic field of bulk YBCO.

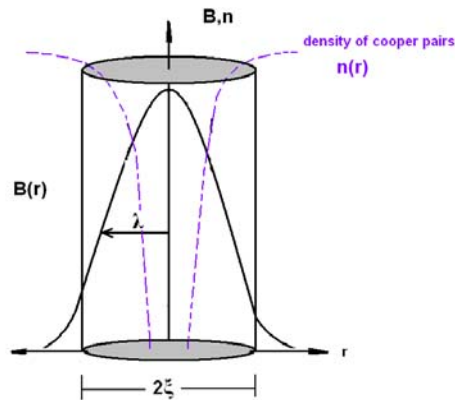


Figure 1-12 A flux core showing the Cooper pairs density and the flux core distributed over 2ξ distance

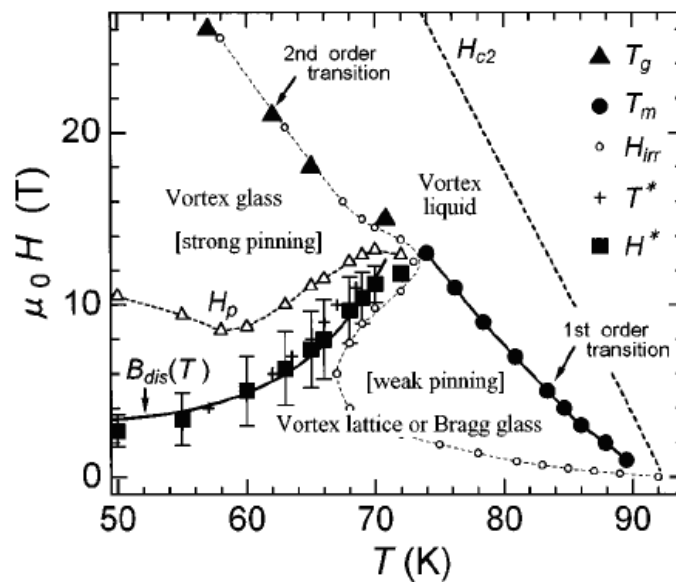


Figure 1-13 Magnetic field versus temperature phase diagram. Transition lines $T_m(H)$, $T_g(H)$ and $H^*(T)$ terminate at the multi-critical point and divide into three different phases of the vortex liquid, the vortex glass, and the Bragg glass. The solid curve is a fit to the field-driven transition line $B_{dis}(T)$ [1.26]

1.5.3 Flux pinning mechanism and effective pinning sites

In the vortex phase diagram of YBCO, there is no universal pinning mechanism to explain the vortex behaviour over the whole temperature and field range. According to Blatter's reviews [1.27], there are two fundamental pinning mechanisms describing the flux pinning in superconductor: 1) *δl -pinning*, the scattering of the electron mean free path; 2) *δT -pinning*, the spatial scatter of the superconducting transition temperature T_c .

In YBCO material, there are several co-existing pinning sites related to the *δl -pinning* mechanism such as: 211/123 interfaces, twin boundaries, dislocations, stacking faults, oxygen vacancies. Here, the dominant pinning mechanism in the different field regions should be identified so as to design an optimized procedure to increase the critical magnetic current J_{cm} , especially at 77K.

M. Murakami found that the critical current density J_c is increased by 211 addition. It is proved that the 211/123 interfaces are effective pinning sites in YBCO [1.28]. B. Martinez investigated the pinning mechanism in 123-211 (38vol%211+1%CeO₂) composites [1.29]. He found a pinning behaviour divided into four parts in the vortex phase diagram estimated from the pinning effects of various defects in the 123-211 composites. Aside the 211/123 interface, many results identify the twin boundaries also as effective pinning sites in YBCO. A high twin density improves the critical current density J_c [1.30]. If an ideal twin structure could be realized, the trapped magnetic field would reach 4.8T [1.31]. Stack dislocations of nanometer size are also considered to be active pinning sites.

Oxygen vacancies have a wide influence on the phase diagram. The pinning mechanism is supposed to be related to the *δT -pinning* mechanism. In pure twin-free YBa₂Cu₃O_{7- δ} single crystal ($\delta=0.003$) [1.32], the irreversible line is moved to higher magnetic field and higher temperature. The irreversibility field B_{irr} with oxygen content 6.97 at 77K is near 7T. With an oxygen content of 6.90, the irreversibility field B_{irr} is lowered to 3T at 77K. It reveals that the phase diagram changes with the random disorder from oxygen reduction. The pinning by oxygen vacancies raises the B_{irr} line limitation in the phase diagram at 77K, making the possibility of higher trapped magnetic field B_{tr} . So the oxygen vacancy is also one of the important pinning sites of YBCO.

Active flux pinning sites are 211/123 interface, oxygen vacancies and twins. Therefore, it is possible to increase the critical current density J_c from two parts: 1) optimising the oxygen content to raise the irreversibility field B_{irr} ; 2) introducing more active pinning sites into sample, such as 211/123 interfaces.

1.6 Our study purpose and contents

We have recognized that the magnetism critical current density J_{cm} is improved by optimising oxygen content, increasing the irreversibility line B_{irr} and introducing effective pinning sites such as 211/123 boundaries.

Presently, the most common fabrication process is the top seed melted textured growth (TSMTG) derived from Jin's MTG method [1.33]. It can be used to grow large size YBCO single domain up to 10 cm in diameter. The MTG process use 123 and 211 powder as precursors. The pressed bulk is heated to a semi-melted state where 123 decomposes into 211 solid particles and a liquid phase. With the seed directing, the sample grows into a single crystal domain by the thermal undercooling. The 211 particles have a trend to grow larger during the 123 melting and solidification By the Ostwald ripening mechanism [1.34]. The resulting inhomogeneous size (1-5 μ m) and distribution of 211 particles is not optimal for pinning, so that the transport critical current density J_{ct} is no more than $10^3\sim 10^4$ A.cm⁻²(77K, 0T).

PMP (Powder Melting Process) uses 211, BaCuO₂, CuO as precursor powders to fabricate bulk YBCO [1.35]. As the 211 particles will be consumed in the peritectic reaction, refined and homogeneous 211 particles (0.4 μ m) will be distributed in 123 matrix, so as to contribute to the flux pinning improvement. Small bars cut out of PMP-YBCO samples with homogenous distribution of fine 211 particles show a high critical current up to 10^5 Acm⁻² (77K, 0T). It is a one order of magnitude improvement compared to MTG-YBCO sample.

If the YBCO single domain is fabricated by the PMP method, it will achieve higher property thanks to the peculiarities of refined 211 particles and higher transport critical current density J_{ct} . Therefore our purpose is to study the PMP process and use the PMP method to fabricate high property YBCO single domains taking advantage of the improved J_c property. We will study the phase transition and the growth dynamics of the PMP-YBCO single domain as well as the microstructure and the properties. The research works includes three aspects as follows:

- 1) Studying the dynamic phase transition of PMP-YBCO. We will investigate the phase transition of the YBCO growth in situ by a high temperature Faraday Balance. To find the real melting and solidification window from the susceptibility transition. To study the effect of heating rate on the phase transition, on the microstructure, and especially on the 211 particles during bulk PMP-YBCO growth. To study the effect of the overheating temperature on the random nucleation. To study the effect of the specific surface area on the phase transition of the bulk PMP-YBCO.

- 2) Studying the growth dynamics of PMP-YBCO single domain. We will study the nucleation and growth rate with the high temperature Faraday Balance to reveal the practical growth window of PMP-YBCO single domain. We will study the relationship of the growth rate and the undercooling by quenching method. We will study the relationship of the solution diffusion and the growth rate by thermogravimetry experiment. We will study the effect of the specific surface area on the growth. And we will try to build a practical growth model to describe the mechanism of the growth of PMP-YBCO single domain.
- 3) Studying the microstructure, the critical current J_{cm} , the trapped magnetic field B_{tr} and their relationship. We will investigate the 211 particles shape and distribution, the effect of the artificial hole on the growth texture, the cracks and the porosity in the PMP-YBCO single domain by optical microscopy and the scanning electron microscopy (SEM). We will investigate the oxygen constant from comparing the sample prepared in high pressure oxygen and in low pressure oxygen treatment. We will study the relationship of the magnetism critical current density J_{cm} and the 211 particles, as well as the relation of the trapped magnetic field B_{tr} and the oxygen constant. We will analysis the flux pinning mechanism in PMP-YBCO sample. We will raise the irreversibility line B_{irr} and increase the properties by refining the 211 particles, increasing the surface area ratio and applying the high pressure oxygen treatment to improve the 211/123 interface density and to increase the twins density as well as the oxygen vacancies.

References

- [1.1] J.S.Wang, S.Y.Wang et al, “Experiment results of high temperature superconducting Maglev vehicle”, *Physica C*, 2003, 386, 431-437.
- [1.2] A C Day, M Strasik, K E McCrary, P E Johnson, J W Gabrys, J R Schindler, R A Hawkins, D L Carlson, M D Higgins and J R Hull, “Design and testing of the HTS bearing for a 10 kWh flywheel system”, *Supercond. Sci. Technol.* 2002, 15, p838–841.
- [1.3] Koji Matsunaga, Masaru Tomita, et al., “YBCO bulk of the superconducting bearing for a 10kWh flywheel”, *Supercond. Sci. Technol.* 2002, 15, p842–845.
- [1.4] M Sander, U Sutter, M Adam and M Klaser, “Comparison of pulsed magnetization processes for HTS bulk parts”, *Supercond.Sci.Technol.*, 2002, 15 p748-753.
- [1.5] H T Ren, L Xiao, Y L Jiao, M H Zheng, “Processing and characterization of YBCO superconductors by top-seeded melt growth method in batch process”, *Physica C*, 2004, 412-414, p597-601.
- [1.6] S Nariki, N Sakai, M Murakami and I Hirabayashi, “High critical current density in Y-Ba-Cu-O bulk superconductors with very Y211 particles”, *Supercond. Sci. Technol.* 2004, 17, S30–S35.
- [1.7] Y. Shiohara, A. Endo, “Crystal growth of bulk high-Tc superconducting oxide materials”, *Materials Science and Engineering, Materials Science and Engineering*, 1997, R19 p1-86.
- [1.8] Beaugnon E, Chaud X, De Rango P in Masuhiro Yamaguchi, Yoshifumi Tanimoto 2006 *Magneto-Science/ Magnetic Field Effects on Materials: Fundamentals and Applications* (Berlin: Kodansha Springer), 2006, p179.
- [1.9] Xavier Chaud, E. Beaugnon, R. Tournier, “Magnetic susceptibility during the peritectic recombination of YBaCuO”, *Physica C*, 1997, 282-287, p525-526.
- [1.10] T C Shields, I R Harris, J S Abell, “Magnetic properties of high Tc superconductors”, *Physica C*, 1988, 153-155, p1535-1536.
- [1.11] Takao Ishii, Tomoaki Yamada, “The origin of Curie-Weiss susceptibility in Ba₂YCu₃O_y”, *Physica C*, 1990, 165, p139-142.
- [1.12] Xavier Chaud, D Isfort, E Beaugnon and R Tournie, “Isothermal growth of large YBa₂Cu₃O_{7-x} single domain up to 93mm”, *Physica C*, 2000, 341-348, p2413.
- [1.13] G Krabbes, G Fuchs, W-R Canders, H May, R Palka, “High Temperature Superconductor Bulk Materials”, WILEY-VCH VERLAG GmbH&Co.KGaA, 2006.
- [1.14] 闵乃本, 《晶体生长的物理基础》, 上海科学技术出版社, 1982年1月.

- [1.15] Michael J.Cima, Merton C Flemings, Anacleto M Figueredo, et al, "Semisolid solidification of high temperature superconducting oxides", *J.Appl.Phys.* 1992, 72, p179.
- [1.16] W K Burton, N Cabrera and F C Frank, The growth of crystals and the equilibrium structure of their surfaces, *Phil.Trans.Roy.Soc.A*, 1951, 243, P299-358.
- [1.17] K A Jackson, "Growth and Perfection of Crystals, Proceedings of an International Conference on Crystal Growth held at Cooperslown, New York on August 27-29,1958", edited by R H Doremus, B W Roberts, David Turnbull, (New York. John Wiley & sons, Inc. London. Chapman and Hall Limited), p319.
- [1.18] C.Klemenz, H.J.Scheel, "Flat $\text{YBa}_2\text{Cu}_3\text{O}_{7-\delta}$ layers for planar tunnel-device technology", *Physica C* 1996, 265, p126.
- [1.19] B N SUN, R BOUTELLIER and H SCHMID, "Growth spiral on single crystal of $\text{YBa}_2\text{Cu}_3\text{O}_{7-\delta}$ ", *Physica C* 1989, 157, 189-191.
- [1.20] T Izumi, Y. Nakamura, and Y. Shiohara, "Crystal growth mechanism of $\text{YBa}_2\text{Cu}_3\text{O}_y$ Superconductors with Peritectic reaction", *J.Crystal.Growth*, 1993, 128, p757-961.
- [1.21] M J Cima, Merton C.Flemings, Anacleto M.Figueredo, Masahiko Nakade,Hideo Ishii, Harold D.Brody, John S.Haggerty, "Semisolid solidification of high temperature superconducting oxides", *J.Appl.Phys.* 1992, 72, 179-190.
- [1.22] N Mori, H Hata, K Ogi, "Growth mechanism of $\text{YBa}_2\text{Cu}_3\text{O}_y$ material", *J Jpn.Inst.Mat*, 1992, 6, p648.
- [1.23] A Endo, H S Chauhan, Y Nakamura, Y Shiohara, "Relationship between growth rate and undercooling in Pt-added $\text{YBa}_2\text{Cu}_3\text{O}_{7-\delta}$ ", *J Mater Res*, 1996 11 1114-1119.
- [1.24] D F Lee, V Selvamanickam and K Salama, "Influences of Y_2BaCuO_5 particels size and content on the transport critical current density of $\text{YBa}_2\text{Cu}_3\text{O}_x$ superconductor", *Physica C*, 1992, 202, p83.
- [1.25] T Nishizaki, T Naito and N Kobayashi, "Anomalous magnetization and field-driven disordering transition of a vortex lattice in untwinned $\text{YBa}_2\text{Cu}_3\text{O}_y$ ", *Physical Review B*, 1998, 58, 11169.
- [1.26] Blatter G, Feigel'man M V, Geshkenbein V B, Larkin A I and Vinokur V M, "Vortices in high-temperature superconductors", *Rev.Mod.Phys.* 1994, 66, 1125.
- [1.27] M Murakami,H Fujimoto, "Flux pinning due to nonsuperconductoing particles in melt processed YBaCuO superconductors", *Physica C*, 1991, 185-189, 321.
- [1.28] B.Martinez, X Obradors, A Gou, V.Gomis, S.Pinol and J.Fontcuberta, "Critical currents and pinning mechanisms in directionally solidified $\text{YBa}_2\text{Cu}_3\text{O}_7\text{-Y}_2\text{BaCuO}_5$ composites", *Physical Review B*, 1996, 53, p2797.

- [1.29] Linfeng Mei, V S Boyko, Siu-Wai Chan, “Twin engineering for high critical current densities in bulk $\text{YBa}_2\text{Cu}_3\text{O}_{7-\delta}$ ”, *Physica C*, 2006, 439, 78-84.
- [1.30] V.S.Boyko, “Microstructure design by twinning in high-temperature superconductor $\text{YBa}_2\text{Cu}_3\text{O}_{7-\delta}$ for enhanced J_c at high magnetic fields”, *Physica C*, 2007, 466, p56-60.
- [1.31] H Kupfer, Th Wolf, R Meier-Hirmer, A A Zhukov, “Peak effect and vortex phase diagram in twin-free $\text{YBa}_2\text{Cu}_3\text{O}_{7-\delta}$ single crystals”, *Physica C*, 2000, 332, p80-85.
- [1.32] S Jin, T H Tiefel, R C Sherwood et al., “Melt-textured growth of polycrystalline $\text{YBa}_2\text{Cu}_3\text{O}_{7-\delta}$ with high transport J_c at 77K”, *Physical Review B*, 1988, 37, p7850.
- [1.33] M T Gonzalez, S Vidal, J Vina, M R Osorio,et al., “Electric field versus current density curves in melt-textured samples of $\text{YBa}_2\text{Cu}_3\text{O}_{7-\delta}$ under currents well above the critical current”, *Physica C*, 2002, 372-376 p1852-1854.
- [1.34] Zhou Lian, Zhang Pingxiang, Ji Ping, Wang Keguang, Wang Jingrong, “The properties of YBCO superconductors prepared by a new approach: the ‘powder melting process’”, *Supercond. Sci. Technol*, 1990, 3, p490-492.
- [1.35] F Gaucherand, E Beaugnon, “Magnetic susceptibility of high-Curie-temperature alloys near their melting point”, *Physica B*, 2001, 294-295, p96-101.

Chapter 2 Phase transition of bulk PMP-YBC

2.1 High temperature Faraday Balance

The crystalline phase transition of paramagnetic material is related to the susceptibility transition. In the melting and solidification, the susceptibility of the material will be transformed due to its volume or its valence changing. An effective method of studying the crystalline phase transition of paramagnetic material has been proposed by measuring the susceptibility variation during thermal cycle. Gaucherand et al. and Reutzel (reference missing in the reference part) successfully investigated the solid-liquid phase transition in cobalt alloy by measuring the susceptibility at high temperature [2.1, 2.2]. They obtained the melting and solidification temperature window of Co-S alloy in supercooling process. Eric Beaugnon and Xavier Chaud used the high temperature Faraday Balance for studying the phase transition of bulk YBCO superconductor in MTG process firstly [2.3, 2.4]. They revealed the practical melting range and solidification window of bulk MTG-YBCO in situ. Classical phase diagrams give information about transition at equilibrium (the change are supposed reversible). This method gives information about transition during real heat treatment and so includes out of equilibrium process, effect of diffusion, and so on... The phase transition information realized the possibility of fabricating Ø 40 mm and up to 90 mm YBCO single domains.

The susceptibility can be measured by the Faraday Balance. For instance, R A Faraday designed in 1930 an instrument to measure the susceptibility of a material by putting a small sample in a magnetic field gradient [2.5, 2.6, 2.7]. The magnetic susceptibility is derived from measuring by a weighting device the magnetic force exerted on the magnetic material placed in a field gradient. The sample susceptibility can be calculated from this measured magnetic force, as follows:

$$\chi = F / (m \cdot H \cdot dH/dz). \quad (2-1)$$

Here F represents the force of the material in the magnetic field gradient, χ the susceptibility, m the mass of sample, H the applied magnetic field strength, and dH/dz the magnetic field gradient.

In this work, a special furnace is used that has been designed to fit and to work inside the room temperature bore of a magnetic coil. Hence, the Faraday balance is improved by the high magnet field gradient generated by a superconducting coil and by the possibility to work at high temperature up to 1200°C. It is called as “the in situ high temperature Faraday

balance”, the schematic is shown in figure 2-1. The magnetic force is measured by using an electronic balance with a 1 mg resolution, which means in term of susceptibility a resolution of 1010 emu/g or 106 SI because of the high value of HdH/dz ($2.8 \cdot 10^8 \text{ T}^2/\text{m}$) made available by the use of a superconducting coil. The in situ high temperature Faraday balance in our experiments has been set up by the researchers at the CNRS/CRETA laboratory (Grenoble – France), as shown in figure 2-2. An 8 Tesla magnetic field is produced by a superconducting coil of a classical Oxford RMN cryostat. The magnetic field distribution and the temperature distribution are shown in Annex 1.

In zero magnetic field, the apparatus provides thermogravimetric measurements that can be subtracted to the measurements under field to keep the true magnetic part of the signal.

2.2 Phase transition of bulk PMP-YBCO

2.2.1 Experimental

We investigate the crystalline phase transition of bulk PMP-YBCO during the fabricating process by in situ magnetic susceptibility measurement. PMP means powder melt processed. The Y_2BaCuO_5 (211) , BaCuO_2 (011), CuO are used as precursors for PMP route whereas already reacted YBCO powders are used in a classical route such as MTG (melt textured growth). The stoichiometric composition is $\text{Y}_{1.8}\text{Ba}_{2.4}\text{Cu}_{3.6}\text{O}_{7-\delta}$ with 1%wt CeO_2 addition for 211 particles refinement [2.8]. The mean size of the mixed powder is 1-2 μm after ball milling. The mixed powder is uni-axially pressed at 60 MPa into a $\Phi 20\text{mm} \times 18\text{mm}$ pellet (about 20 g). There are two superposed substrates under the sample avoiding bulk YBCO reaction with Al_2O_3 crucible. One is a layer of Y123/Yb123 mixture (about 4g with a 1:0.2 weight ratio). Another is an Y_2O_3 layer (about 2.5g). The sample with substrates in its alumina crucible is put into the vertical furnace which is inserted in the bore of magnetic coil, as shown in figure 2-3.

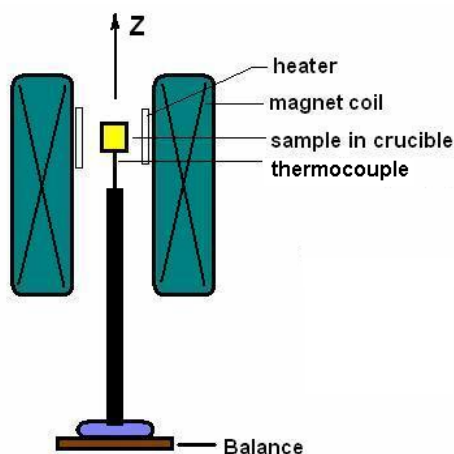


Figure 2-1: Schematic of high-temperature Faraday balance for in situ susceptibility measurement.



Figure 2-2: High-temperature Faraday Balance with Oxford superconducting coil in the CNRS/CRETA laboratory.

Theoretically, the susceptibility of bulk PMP-YBCO is best obtained by measuring its magnetic force without substrate and crucible. But in our experiment, the crucible and substrates are necessary to support the sample. We tried to measure the susceptibility of the PMP-YBCO sample without substrates, but we were facing a serious reaction between the PMP-YBCO pellet and the alumina crucible. The Y123 crystal was not growing because of the lost of an important quantity of liquid phase. Hence, the measured data of PMP-YBCO without substrates did not display the real solidification of the PMP-YBCO compound. So we used the configuration with substrates to study the phase transition of PMP-YBCO in all experiments.

The heat treatment used while measuring the susceptibility of bulk PMP-YBCO is shown in figure 2-4. The bulk PMP-YBCO is heated to 900°C at 240°C/h, up to 1060°C at 60°C/h, kept two hours at 1060°C, then cooled down to 1020°C at 60°C/h, to 980°C at 1°C/h. During the experiment, we observe the nucleation on the sample surface with eyes and camera at the same time. For identifying the phases at different stages of the heat treatment, a quench experiment was conducted using the same temperature profile in a box furnace. Ten samples were processed in one batch. At each chosen quenching temperature, one sample is taken out of the furnace quickly (about 20 seconds) and quenched on a copper plate at room temperature. The quenching temperatures were 900°C, 925°C, 980°C, 1020°C and 1040°C during heating, and 1040°C, 1010°C, 1000°C and 970°C during cooling. X-ray diffraction analysis were performed to detect the crystalline phases.

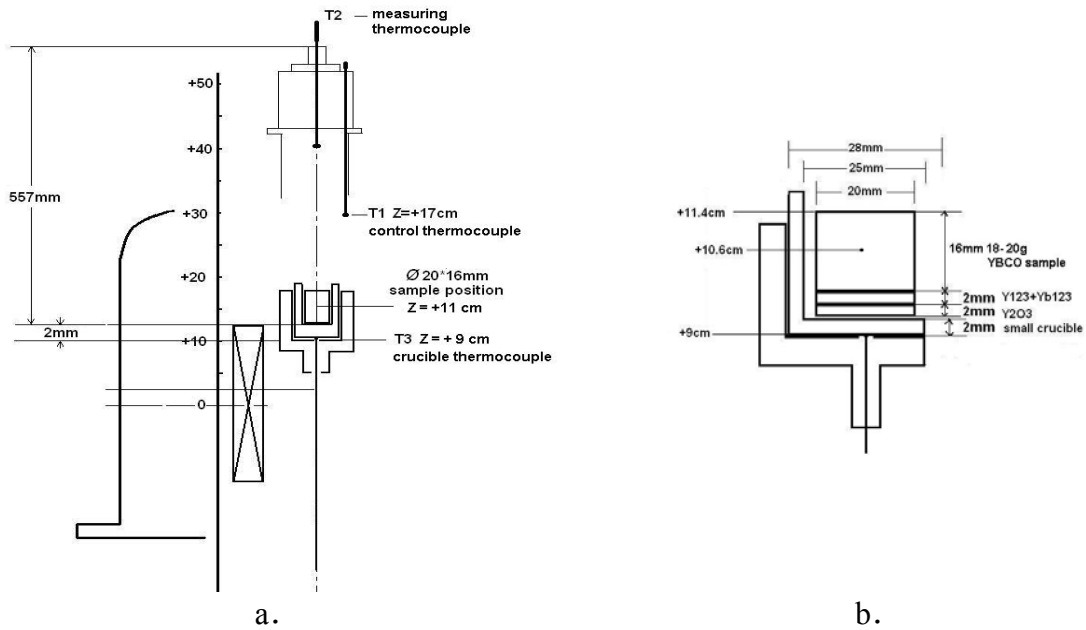


Figure 2-3 The placement of the sample in furnace (vs. temperature profile) and in magnetic coil (vs. magnetic gradient). The sample is placed on the substrates of Y123-Yb123 and Y₂O₃ layer, in an Al₂O₃ crucible as shown in inset.

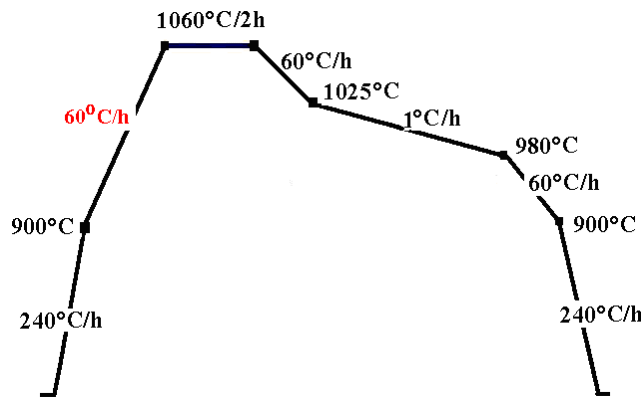


Figure 2-4 Temperature profile applied to PMP-YBCO pellets for susceptibility measurement.

2.2.2 Phase transitions in bulk PMP-YBCO

In the high temperature susceptibility measurement, the measured force signal F includes two parts: one from the magnetic force; the other from the weight loss of the sample which is caused by the oxygen released out at high temperature. The measured force signal F is described as follows:

$$F = F_i(\chi) + \Delta G_i \quad (2-2)$$

where $F_i(\chi)$ is the “magnetic force” and ΔG_i the gravitational weight. We assumed that the reaction between PMP-YBCO and substrates is neglected. Therefore, the measured force signal F includes the magnetic force $F_1(\chi)$ related to the susceptibility χ contribution of the PMP-YBCO bulk, the magnetic force $F_2(\chi)$ related to the susceptibility of the ensemble

substrates (Yb123+Y123, Y2O3) and Al2O3 crucible, the weight ΔG_1 coming from the weight variation of PMP-YBCO bulk itself, the weight ΔG_2 from the weight loss of the ensemble substrates (Yb123+Y123, Y2O3) and Al2O3 crucible. The different force contributions are illustrated in figure 2-5. The measured force F could be described by the following equation (2-3):

$$F = F_1(\chi) + F_2(\chi) + \Delta G_1 + \Delta G_2 \quad (2-3)$$

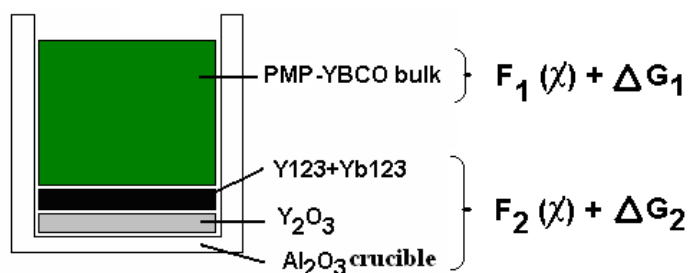


Figure 2-5 The PMP-YBCO bulk is placed on the substrate made of layers of Y123/Yb123 and Y₂O₃, the set is put into an Al₂O₃ crucible. $F_1(\chi) + \Delta G_1$ is related to the PMP-YBCO bulk; $F_2(\chi) + \Delta G_2$ is related to the ensemble crucible and substrates provided by the Y123/Yb123 and Y₂O₃ layers .

After removing the force signal $F_2(\chi)$, ΔG_1 and ΔG_2 from the total force signal (F), the susceptibility of PMP-YBCO sample can be derived from $F_1(\chi)$ by using the equation (2-1). In order to remove the signals which are not contributing to the susceptibility of bulk PMP-YBCO from the overall signal, we performed four kinds of measurements to obtain the susceptibility of bulk PMP-YBCO itself. The detailed description of the experiments is in Annex 2.

The unit of susceptibility emu/g used here is to comparing the data in literature [2.12], instead of using the SI unit. The susceptibility χ of bulk PMP-YBCO versus temperature corresponding to the temperature profile given in figure 2-4 is shown in figure 2-6. This result has a good repeatable measurement as shown in the section 2.3 which in room temperature to 900°C. As the temperature varies, the magnetic susceptibility curve transforms obviously at the following temperature points: 900°C, 1000°C and 1012°C on heating and at 1020°C, 1004°C, 980°C on cooling. The crystalline phases at different temperatures were identified by X-ray diffraction performed on quenched samples, as shown in figure 2-7. Based on the susceptibility transition, the X-ray diffraction results and the thermogravimetric measurements, we analyze the phase transitions of the PMP-YBCO in the fabricating process in-situ (see fig. 2-8).

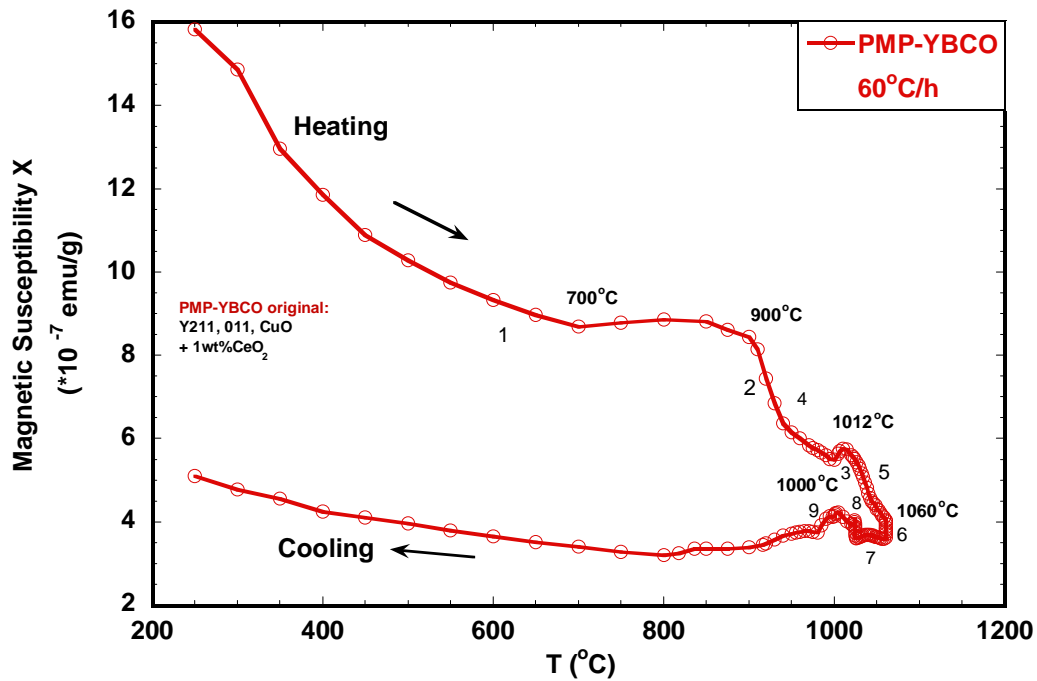


Figure 2-6 The susceptibility curve of the bulk PMP-YBCO in fabricating process. The marks 1 to 9 on the plot are guidelines for the explanation.

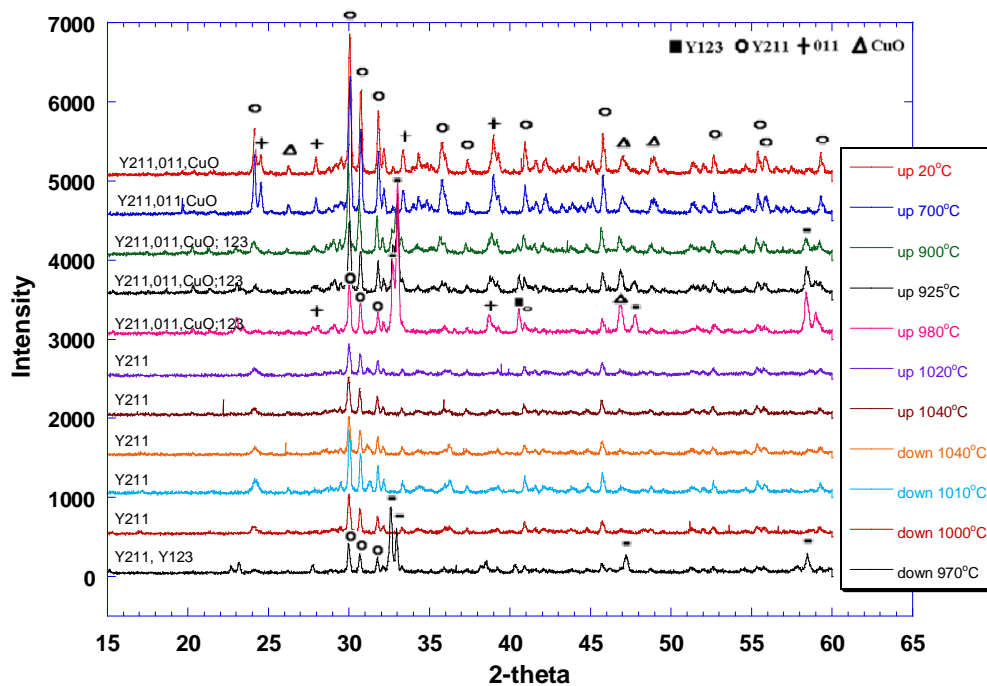


Figure 2-7 The X-ray diffraction patterns of quenched samples show the phases existing at different temperatures. The Y123 phase appeared from 900°C and disappeared at 1020°C. BaCuO₂ and CuO decomposed after 900°C until 1020°C where they melted into a liquid phase. The Y123 phase appeared again at 970°C during the cooling stage.

In order to understand the relationship between the phase transition and the susceptibility transition of PMP-YBCO bulk, we should understand the magnetism of various phases in the bulk PMP-YBCO. The material magnetism depends on the magnetic elements in the

compound and of the way they combined (orbital hybridation). The PMP-YBCO route uses 211, BaCuO₂ and CuO as precursors. The valence of the different ions in 211, 011 and CuO are the nonmagnetic Y³⁺, Ba²⁺ and O²⁻, and the paramagnetic Cu²⁺. Therefore, the 211, 011 and CuO are paramagnetic so that the susceptibility abides by a Curie-Weiss law when there is no phase transition.

However, the copper valence is very complicated in YBa₂Cu₃O_{7-δ} and changes with variation of the oxygen content 7-δ. Noburu Fukushima tested the copper valence as Cu²⁺ and Cu³⁺ in YBa₂Cu₃O_{7-δ} (7-δ<5.8) with titration method [2.9]. W. M. Temmerman analyzed the divalent (d9) /magnetic Cu²⁺ and trivalent (d8)/nonmagnetic Cu³⁺ in YBa₂Cu₃O_{6.0} and YBa₂Cu₃O_{6.5} [2.10]. S. Scheurell used the method of abrasive stripping voltammetry to show that the Cu³⁺ → Cu²⁺ and Cu⁺ → Cu⁰ (or Cu²⁺ → Cu⁰) transitions exist in YBa₂Cu₃O_{6.3} [2.11]. Thus it is proved that the Cu valences Cu⁺, Cu²⁺, Cu³⁺ exist in YBa₂Cu₃O_{7-δ}, and that Cu⁺ and Cu³⁺ are nonmagnetic, while Cu²⁺ is paramagnetic. Shields et al. have pinpointed a strong dependence of the susceptibility on temperature and oxygen content in YBa₂Cu₃O_{7-δ} (<850°C) [2.12]. They indicated the susceptibility of YBa₂Cu₃O_{6.0-6.87} looks like an Curie-Weiss behaviour versus temperature. Its paramagnetic property comes from copper divalent Cu²⁺. If there is no Cu²⁺ ↔ Cu³⁺ or Cu²⁺ ↔ Cu⁺ transition, the susceptibility of PMP-YBCO will abide by a Curie-Weiss law, $\chi=C/(T-\theta)$. Once a crystalline phase transition occurs, the Cu²⁺ ion quantity varies and affects the susceptibility of the PMP-YBCO material. From this viewpoint, the susceptibility transition of PMP-YBCO bulk comes from the Cu ion valence changing.

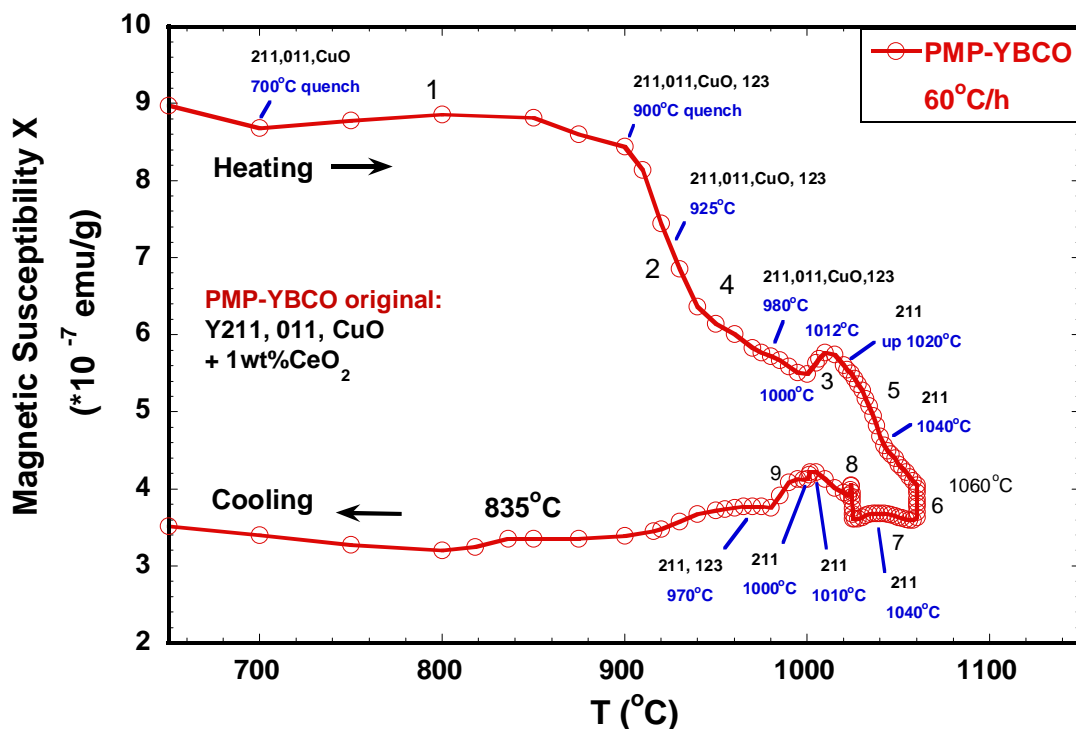


Figure 2-8: The susceptibility curve of PMP-YBCO versus temperature with a 60°C/h heating rate. It reveals the crystalline phase transitions of bulk PMP-YBCO in the fabrication. 123 phase formation and melting process take place in the 900°C-1012°C (step 2, 3). 123 crystal solidification is found in the 1004°C-980°C temperature window (step 9).

Heating stage

(step 1) 200°C-900°C

In figure 2-6, the susceptibility behavior varies inversely to the temperature from 200°C to 900°C. Between 20°C and 700°C, the crystalline phases which are detected in the X-ray diffraction patterns are the 211, 011 and CuO phases. A little quantity of the 123 phase appears at 900°C. From 200°C to 900°C, the phases found in bulk PMP-YBCO are 211, 011 and CuO without any phase transition. Because 211, 011 and CuO are paramagnetic, the resulting susceptibility is decreasing as the temperature increases and abides by a Curie-Weiss law, as follows:

$$\chi = C/(T-\theta) \quad (2-4)$$

From the susceptibility data taken below 750°C, the Curie constant C and Curie temperature θ are calculated as $C=6.8 \times 10^{-4} \text{ K} \cdot \text{emu/g/Oe}$, $\theta=93\text{K}$. Here the constant C and θ represent a behaviour of a compound not a simple phase.

(step 2) 900°C-1000°C

Figure 2-8 is a zoom up of figure 2-6 on the high temperatures region. It shows that the susceptibility decreases sharply from 900°C to 1000°C. At 900°C some quantity of the 123 phase is already formed as shown in the X-ray diffraction pattern. The intensity of peaks related to the 123 phase increases from the X-ray diffraction patterns taken at 900°C, 925°C and 980°C, while the 211 peaks are reducing. It is obvious that the 123 phase continue to form during this temperature range. Observing the susceptibility curve, the susceptibility is abruptly decreasing from 900°C to 1000°C. The slope is larger than expected from the paramagnetic behaviour of a Curie-Weiss law. The 123 phase formation implies here the following recombination: $211+011+\text{CuO} \rightarrow 123$, and that some of the Cu^{2+} ion in 211, 011, CuO phases should change to Cu^{3+} ions in the $\text{YBa}_2\text{Cu}_3\text{O}_{6.0-6.5}$ phase. Hence, the total amount of magnetic Cu^{2+} ion decreases and causes the drop of susceptibility that is observed. Here the in situ susceptibility measurement provides a clear temperature range for the 123 phase formation.

It is emphasized that every inflection in the susceptibility curve could be influenced by both the nature of the susceptibility transition and the heating/cooling rate which can affect time based transformation (implying diffusion for instance). In order to understand how much the heating/cooling rate affects the susceptibility, we investigate the susceptibility signal for

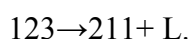
different heating rate. We found that an increase of the heating/cooling rate delays the phase equilibrium. By changing the heating rate from 240°C/h to 60°C/h at 900°C, the reaction has more time to proceed in a definite temperature range. At 900°C this phenomenon is few, at 1025°C in cooling stage, For every temperature point of changing cooling rate, the changing cooling rate has a less influence on the susceptibility signal except at 1025°C there is one hour delaying to equilibrium. The susceptibility is ultimately determined by the temperature changing and the phase transition. The detailed analysis is shown in [Annex 3](#).

Furthermore, in other experiments, we have shown that the 123 phase formation depends on the heating rate (10°C/h, 60°C/h, 120°C/h, 240°C/h) in the 900°C-1060°C temperature range of the heating stage. When the heating rate is faster than 120°C/h, we found there is no 123 phase formation. That points out that the recombination of 123 requires enough time and will not form if the time spent when in the 900°C-1000°C temperature range is less than an hour. In this paragraph, we just consider a heating rate of 60°C/h. The effect of heating rate on the PMP-YBCO phase transition is discussed more in details in section 2.3.

(step 3) 1000°C-1012°C

At 980°C, the phases detected are 123, 011 and CuO in the X-Ray diffraction spectra. At 1020°C and above, only the 211 phase remains. This indicates that the 123 phase decomposed as 123→211+L. The 011, CuO phases melt to liquid phase.

The susceptibility is increasing from 1000°C to 1012°C as shown in figure 2-8. It relates to the transformation of some nonmagnetic trivalent Cu³⁺ into paramagnetic divalent Cu²⁺. As we have seen above, the 123 forms in the 900°C-1000°C temperature range and has disappeared from the X-Ray spectra at 1020°C. The 123 melting occurs between 1000°C and 1020°C. The YBaCuO melting in the literature is given at 1015°C. So we can attribute consistently the susceptibility increase in the 1000°C-1012°C temperature range to the YBCO melting as:



(step 4) 900°C-1016°C

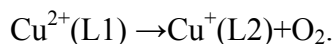
At 900°C, 925°C, 980°C and 1020°C, as shown in the X-ray diffraction patterns, the intensity of 011 and CuO phases reduced until they disappear at 1020°C as the temperature is increasing. We found in a separate susceptibility measurement that the melting point of 011 phase occurs around 1016°, as referred in Annex 4. Observing the present PMP-YBCO susceptibility curve in the 900°C-1020°C temperature range, there is no obvious transition for

the 011 and CuO melting point. According to this result, the melting point of 011 phase in the bulk PMP-YBCO is possibly covered and superposed to the melting of 123 phase (1012°).

(step 5) 1012°C-1060°C.

After the 123 peritectic melting at 1012°C as analysed in step 3, only the 211 phase is detected at 1020°C and 1040°C in the X-ray diffraction patterns. The 211 phase is a paramagnetic and stable phase up to 1270°C, so the susceptibility should decrease as the temperature increases up to 1060°C according to a Curie-Weiss law. However, it has been shown for MTG compounds that the change of susceptibility cannot be explained just by a Curie-Weiss law [2.3, 2.4]. According to the thermogravimetry curve in figure 2-9, a weight loss is taking place during heating with an increase of the loss rate around 900°C and a second change of rate for the 1012°C-1060°C temperature range. This phenomenon is analyzed further in section 3.4 of chapter 3.

Considering the Ba-CuO and Y123-CuO phase diagrams [2.13, 2.14], the CuO decomposes into Cu₂O and releases oxygen at 1022°C. Based on the X-ray diffraction patterns, CuO and Cu₂O should be existed as liquid phase as Cu²⁺(L1) and Cu⁺(L2). As the Cu²⁺(L1) valence change to Cu⁺(L2), releasing oxygen out. The magnetic Cu²⁺ ion transforms to nonmagnetic Cu⁺ ion, this reaction brings the susceptibility to decrease. Summing up the variation of susceptibility, the weight loss and the information of the phase diagram, the phase transition during 1022°C-1060°C is attributed to the following reaction:



(step 6) Dwell at 1060°C

At 1060°C, the thermogravimetry curve in figure 2-9 shows that the weight keeps decreasing; the susceptibility is also decreasing in figure 2-10 for a compound which has to be some 211 phase within a melted liquid. Considering the reaction $\text{Cu}^{2+}(\text{L1}) \rightarrow \text{Cu}^{+}(\text{L2}) + \text{O}_2$ in the 1022°C-1060°C temperature range, it is supposed that the CuO decomposition keeps going during the dwell at 1060°C. In order to confirm the phase transition $\text{Cu}^{2+}(\text{L1}) \rightarrow \text{Cu}^{+}(\text{L2}) + \text{O}_2$ at 1060°C, we deal with the measured susceptibility signal data and the thermogravimetry value and here we just show the result.

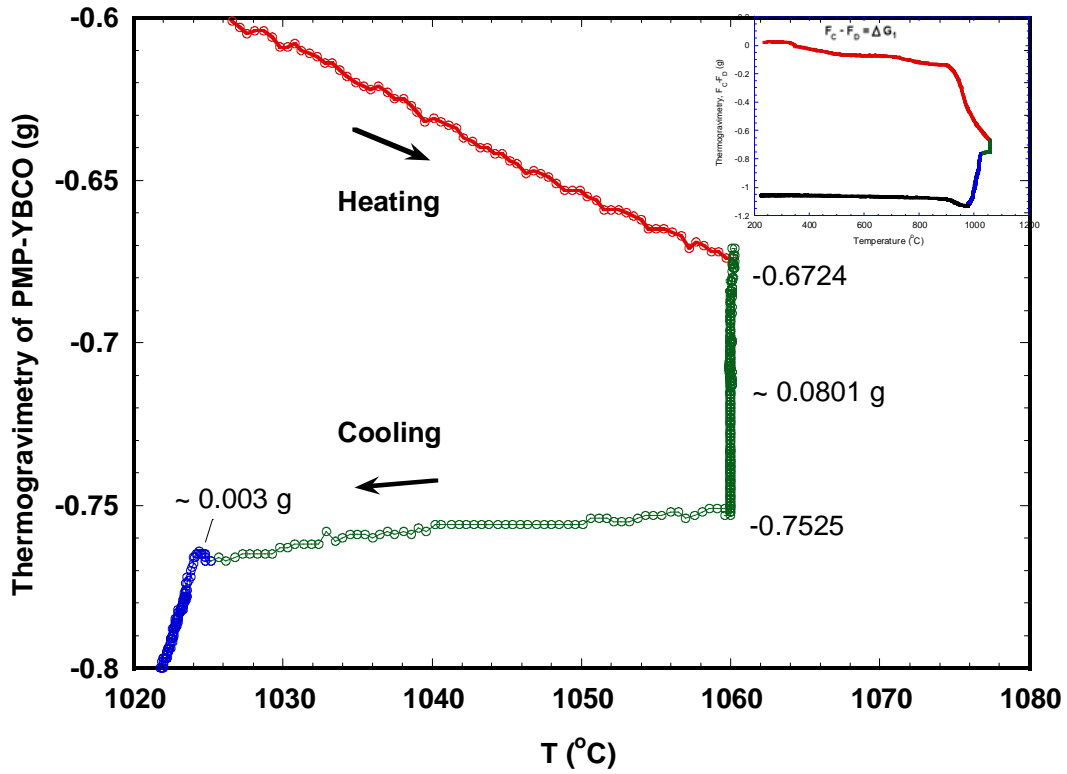


Figure 2-9 Thermogravimetric curve of PMP-YBCO bulk in similar conditions as those used for the susceptibility measurements.

In the bulk PMP-YBCO sample at 1060°C, the calculation of the magnetic force based on the mass of released oxygen (see fig 2-9), $\Delta G_{CuO} = 0.0801\text{g}$, by the reaction $\text{Cu}^{2+}(\text{L1}) \rightarrow \text{Cu}^+(\text{L2}) + \text{O}_2$, referred in Annex 2 yielding:

$$F1(\chi) + \Delta G_{CuO} = 0.9692\text{g} \quad (2-5)$$

The experimental data of magnetic force with released oxygen mass at 1060°C, as the measured signal is $F1(\chi) + \Delta G1 = 0.3347\text{g}$. Comparing both of the calculating data and the experimental data:

$$0.9692\text{g} > 0.3347\text{g} \quad (2-6)$$

Here the error for the calculation is as same as the measured value, as $\Delta G/G = 10^{-5}$.

Obviously, the calculated data is larger than the measured experimental data. The result suggests that there is other oxygen released in other reason except CuO decomposition, which is suggested as the oxygen dissolved in the sample. We name this dissolved oxygen as $\Delta G'$. Basing on the analysis, the released oxygen is dissolved in the sample, when the temperature is increasing the dissolved oxygen will release off. It contributes the oxygen lost $\Delta G'$.

Summarizing above, the main phase transitions were identified in the bulk PMP-YBCO during the heating process: 1) 123 formation, $211 + 011 + \text{CuO} \rightarrow 123$ (900°C-1000°C). 2) 123 melting, $123 \rightarrow 211 + \text{L} + \text{O}_2$ (1000°C-1012°C). 3) 011 and CuO melting, $011 + \text{CuO} \rightarrow \text{L}$ (900°C-1020°C). 4) Cu^{2+} valence changing, $\text{Cu}^{2+}(\text{L1}) \rightarrow \text{Cu}^+(\text{L2}) + \text{O}_2$ (1022°C-1060°C, at 1060°C).

There are two important phenomena not found before. The first one is the 123 phase forming at 900°C and then decomposing after 1012°C. This reaction is displayed clearly in the susceptibility transition. The second one is the oxygen released at high temperature. The released oxygen has a significant influence on the interpretation of the compound susceptibility as well as on the YBCO single domain growth because of its participation to the 123 solidification. Oxygen diffusion in the material has to be taken into account in the interpretation of the susceptibility curve.

Cooling stage

(step 7) 1060°C -1025°C.

Figure 2-10 shows the susceptibility of bulk PMP-YBCO measured during the heat treatment displayed on [fig 2-3](#) for the 930°C-1060°C temperature range. When the temperature is decreasing from 1060°C to 1041°C, the susceptibility is observed to increase to 1041°C. Then the curve turns down around 1041°C and the susceptibility is decreasing until the temperature reaches 1025°C. Considering the paramagnetic 211 phase existence at high temperature, the susceptibility should increase while the temperature is decreasing. So the susceptibility rise from 1060°C to 1041°C could be explained on the basis of a paramagnetic behavior, but not the change of the susceptibility variation observed at 1041°C. However, if there is still some CuO present in the sample above 1025°C, it will continue to decompose to Cu₂O and O₂, making the susceptibility to decrease again. If this influence is stronger than the paramagnetic contribution of the 211 phase to the susceptibility, we could observe the susceptibility signal decreasing again as seen at 1041°C on [figure 2-10](#).

The fact that the thermogravimetry (see [fig 2-9](#)) shows the weight keeps to decrease, even if lightly, in the concerned temperature range could support this assumption. So we attribute the strange behavior in step 7 to the juxtaposition of two effects: the paramagnetic behaviour of 211 and the $\text{Cu}^{2+}(\text{L1}) \rightarrow \text{Cu}^{+}(\text{L2}) + \text{O}_2$ transition above 1025°C.

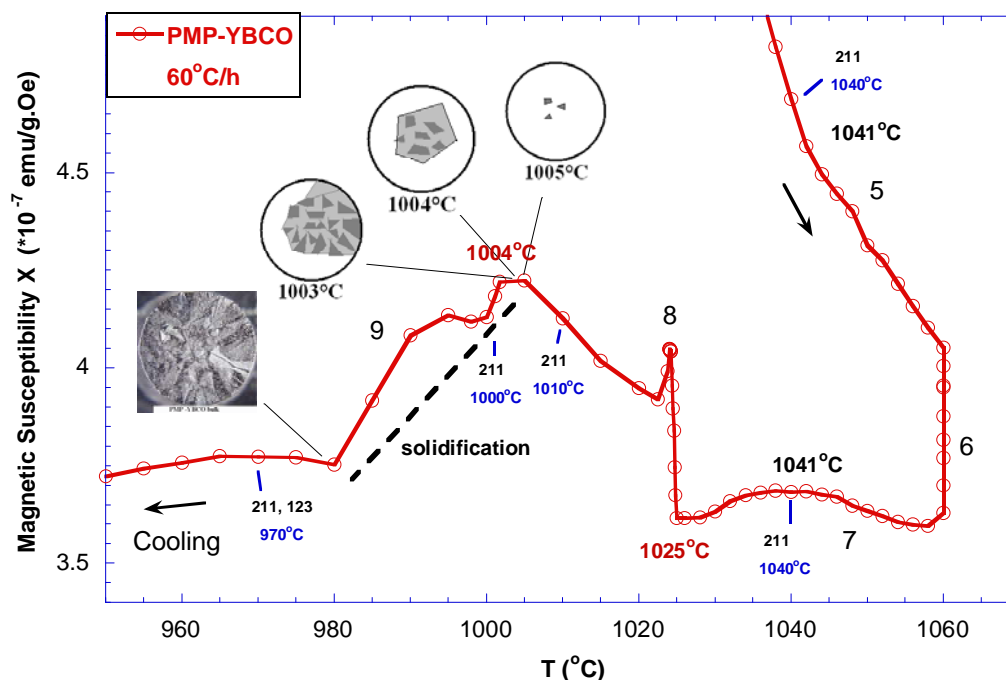


Figure 2-10 Zoom-in of the susceptibility of bulk PMP-YBCO in the 930°C-1060°C temperature range. Nucleation on the surface of PMP-YBCO bulk is observed with eyes and camera as drawn on the figure. It shows that the solidification of some 123 crystals starts at 1004°C (first visible nuclei). The crystals then grow until 980°C.

(Step 8) At 1025°C

At 1025°C the cooling rate is changed from 60°C/h to 1°C/h. The susceptibility increases around 1025°C in a rather short time (1 hour), as shown in figure 2-10. This indicates the amount of magnetic Cu^{2+} ion increased. At the same time, a weight increase of 0.003g is observed at 1025°C (see thermogravimetry curve in figure 2-9). It is supposed that the reaction $\text{Cu}^+(\text{L2}) + \text{O}_2 \rightarrow \text{Cu}^{2+}(\text{L1})$ is reversed at 1025°C. To confirm this reaction by similar analysis similar to the one proposed in step 6, we calculate the magnetic force and the released oxygen mass at 1025°C. Supposed the oxygen mass is up 0.003g, the increased signal is calculated as 0.0372g, but the measured signal increased 0.2578g. The detailed calculation is shown in Annex 2. It shows the experimental value is larger one magnitude than the calculated data:

$$0.2578\text{g} \gg 0.0372\text{g} \quad (2-7)$$

The result pinpoints discrepancies that we could explain only by the following assumption: the magnetic force increase comes from oxygen provided by the bulk of the sample instead from outside oxygen uptake. As analysis in step 6 there is a dissolved oxygen as $\Delta G'$ in the sample.

After 1025°C, the susceptibility decreases sharply in a few degrees then increases with the temperature decreasing. This phenomenon reveals that the amount of Cu^{2+} ion is not stable.

Following the cooling rate change, the system is out of equilibrium. After enough time for balancing, the susceptibility decreases until the amount of Cu^{2+} ion keeps stable, then the susceptibility signal gets to the equilibrium. From this equilibrium point, the susceptibility signal follows a Curie-Weiss law. It is considered the heating rate change delays the equilibrium.

From 1060°C to 1005°C , according to the Y123-CuO phase diagram, the paramagnetic 211 phase is present and detected in the X-ray diffraction spectrum at 1040°C and 1010°C . By the Curie-Weiss law, the susceptibility of paramagnetic PMP-YBCO increases as the temperature decreases, as shown in [figure 2-10](#).

(step 9) 1004°C - 980°C

In [figure 2-10](#), the susceptibility decreases in the 1004°C - 980°C temperature range. During the experiment, we observed the 123 nucleation on the surface once per hour and drew the morphology picture. The first 123 nuclei appeared at 1005°C as show by the drawing. One hour later or 1°C below, the number of 123 nuclei has increased and the 123 crystals have grown larger. Until 980°C the 123 crystals keep growing until they have covered all the top surface of the bulk PMP-YBCO.

When 123 is forming, the magnetic divalent Cu^{2+} transforms to nonmagnetic trivalent Cu^{3+} . According to the observation of the 123 crystal growth and to the X-Ray diffraction spectra, the decrease of susceptibility in the 1004°C - 980°C temperature range is related to the peritectic reaction $211+L\rightarrow 123$ proceeds.

We see first the nuclei on the surface, before to see a sharp decrease of the susceptibility. It should be noted that the susceptibility is a volume measurement. Whereas it is a very good tool to follow the bulk transition, we see in the case of the nuclei occurrence a limit of this measure. We have the visual information first, because the volume of nuclei at the surface is very small at the first nucleation stage.

Similarly, the 211 phase is detected at 1000°C but not the 123 phase in the X-ray diffraction spectrum. This result seems to be inconsistent with our observation of 123 nucleation around 1005°C and of the susceptibility decreasing after 1004°C . The reason why 123 phase is detected in susceptibility transition but not in X-ray diffraction spectrum at 1000°C is a resolution problem. Normally, the resolution of X-ray diffraction is about 5% in volume of material. In our experiment, we calculate the resolution of measured signal with 123 volume in Faraday balance. It is less than 1% by following estimation on the volume percent of 123 in total. Therefore, the Faraday balance can detect a very small susceptibility signal as 1%, but the X-ray diffraction system just detect 5% signal at best. To summarize, the

appearance of nuclei is best monitored visual control, then by the high resolution susceptibility measurement, and finally by X-ray diffraction.

As shown in figure 2-8, when cooling from 980°C to 200°C, 123 and 211 phase are detected at 970°C in X-ray diffraction spectrum. Because of the paramagnetism of 123 and 211, the susceptibility should increase when the temperature decreases. The susceptibility decreases slightly to 800°C then increases again when cooled down to 200°C. The concave peak at 800°C is not consistent.

Summarizing above, six remarkable crystalline transitions are taking place in bulk PMP-YBCO fabricating process. They are:

1. $211+011+CuO \rightarrow 123$ (900°C-1000°C);
2. $123 \rightarrow 211+L + O_2 \uparrow$ (1000°C-1012°C);
3. $BaCuO_2+CuO \rightarrow L$ (900°C-1020°C);
4. $Cu^{2+}(L1) \rightarrow Cu^+(L2)+O_2 \uparrow$ (1022°C-1060°C, at 1060°C, 1060°C-1025°C);
5. $Cu^+(L2) + O_2 \rightarrow Cu^{2+}(L1)$ (at 1025°C);
6. $211+L \rightarrow 123$ (1004°C- 980°C).

The susceptibility transition of bulk PMP-YBCO reveals that 123 phase forms and melts in the 900°C-1012°C and solidify in the 1004°C-980°C temperature ranges.

2.3 Effect of heating rate on phase transition

2.3.1 Experimental

We measured the susceptibility of some plain samples without seed. The samples are treated in the same process except changing different heating rate of 10°C/hr, 60°C/hr, 100°C/hr, 240°C/hr during 900°C-1060°C, then dwelling 2 hours at 1060°C, cooling to 1025°C by 60°C/hr, with slow cooling rate of 1°C/hr to 980°C, in the end cooling to room temperature, as shown in [figure 2.13](#).

The hole technique was proposed to diminish cracks in YBCO single domain [\[2.15\]](#). In the fact, the diffusion path in such samples is reduced. The susceptibility of such hole PMP-YBCO sample was measured with the same process as the plain samples mentioned above as shown in [figure 2-12](#). The layout of a hole sample is shown in insert. During the heating stage and in the temperature interval 900°C-1060°C, the following different heating rate were run: 10°C/h, 60°C/h, 90°C/h, 120°C/h, 240 °C/h. The hole samples were fabricated with a Sm123 seed placed on top prior to the process. The seed effect has an effect on the phase transition triggering, but it has no real influence for the present discussion. The susceptibility transition of bulk with seed and without seed is discussed in chapter 3.

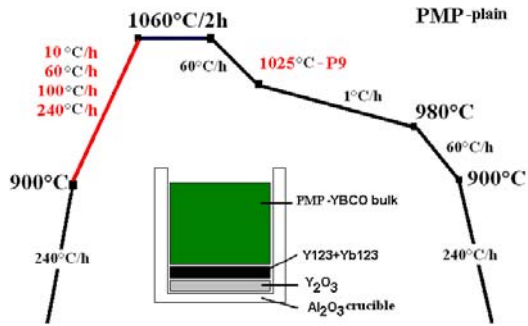


Figure 2-11 Layout and temperature profil for the susceptibility measurement of plain- PMP-YBCO samples in with different heating rates (10°C/h, 60°C/h, 100°C/h, 240 °C/h).

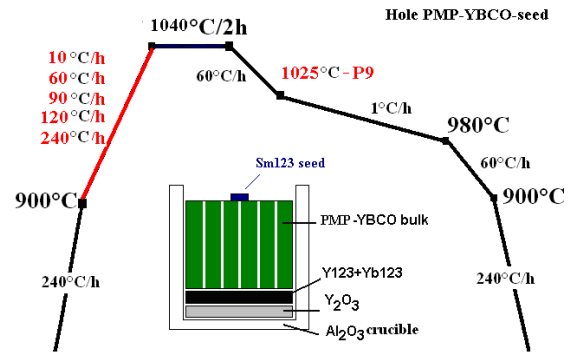


Figure 2-12 Layout and temperature profil for the susceptibility measurement of hole PMP-YBCO samples in with different heating rates (10°C/h, 60°C/h, 90°C/h, 120°C/h, 240 °C/h).

2.3.2 Effect of heating rate on phase transition of plain samples

When plain samples are heated with different heating rates, we found that the phase transition is different and we assume this is because there is a different amount of 123 phase formed in samples. The susceptibility curves for plain samples without seed using different heating rates are plotted together in figure 2.13.

Fig. 2-13a shows the representation of the susceptibility for the totality of the temperature range, whereas fig 2-13b shows only the part above 900°C. All the curves superpose on heating from 200°C to 900°C.

Between 900°C and 1060°C the susceptibility decreases when the temperature increases. If we consider the curve corresponding to the 60°C/h heating rate, we have attributed the variation from 900 to 1000°C to the formation of the 123 phase, and the increase just after to the 123 melting. If the heating rate is even lower, the formation of 123 is marked to the point that the curve can be superposed to an MTG curve, ie when the precursor is 123. We see also that the melting occurs at a lower temperature, which we can explain by the better temperature diffusion. The lower the rate, the better the thermalization of the sample will be.

When accelerating the heating rate, we observed that the small bump around 100°C we attributed to the 123 melting is smoothed and even disappears for heating rates above 100°/h. Due to the heating rate increase, we also observed that this bump is translating toward the higher temperature. From this observation, we consider that above an heating rate of 100°C/h, the 123 has no more time to form. We consider that this can have a technological importance since it may be easier to control the 123 nuclei formation with a low overheating if this phase has not been formed on the heating stage.

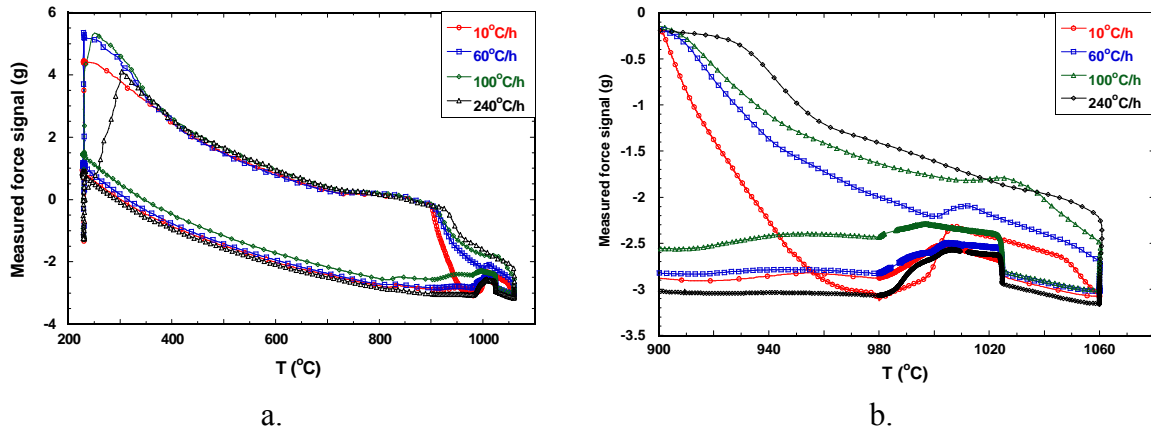


Figure 2-13 Magnetic force curves (proportional to susceptibility) versus temperature of PMP-YBCO plain samples heated at different rate. a. in the totality of the curves in the 200°C -1100°C temperature range. b. A zoom-in of the magnetic force curves above 900°C.

2.3.3 Effect of heating rate on phase transition of hole samples

Similarly to the plain samples, a quicker heating rate over the 900°C-1060°C temperature range also let less time to the 123 phase to form in hole sample, as shown in figure 2-14. It is found that the 123 phase melting transition is smoothed out when the heating rate is above 120°C/hr. The heating rate of 120°C/h becomes the critical heating rate for forming 123 phase in hole- PMP-YBCO bulk.

For plain samples, the specific surface area is less than the one of the hole samples. Therefore, the thermal and oxygen diffusion in hole samples are faster than in plain samples. It is easier to form 123 phase in hole sample so that the critical heating rate in hole samples is larger than it in plain sample. From this information, the heating rate of process for fabricating hole PMP-YBCO single domain is held at 120°C/hr in our single domain PMP-YBCO growth in the next step.

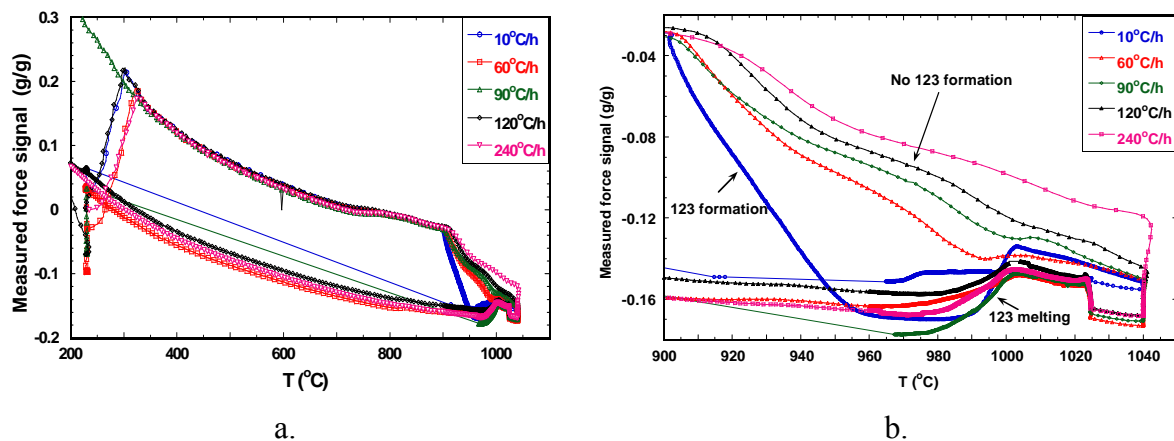


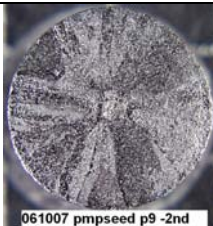
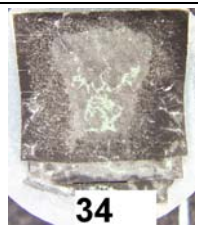
Figure 2-14 The magnetic force curve versus temperature of hole- PMP-YBCO-seed samples shows the effect of heating rate on the phase transition (totality of the curve - a, zoom-in above 900°C – b)

2.4 Effect of reduced diffusion path on phase transition

In order to investigate the effect of the hole shape on the single domain growth, we study the susceptibility transition of plain and hole samples. The process is as the one shown in figure 2-13 with a heating rate of 60°C/h, the grown samples are shown in table 2-1. The specific surface area σ of the plain sample and of the hole sample are 72 mm²/g and 275 mm²/g respectively. The susceptibility curves are superposed in figure 2-15. Comparing the susceptibility line of plain and hole samples, for the same heating rate, the decrease of susceptibility we attributed to the 123 phase formation is more pronounced for the hole sample. The large specific surface area of hole sample seems to improve the phase reaction. The increase of the specific surface area is a direct consequence of the holes and is associated to a drastic reduction of the diffusion path. The surface area is multiply by about a factor 4, whereas the diffusion path are reduced by about a factor 6.

There are two obvious differences in the susceptibility curve of plain and hole samples. One is happening during the 123 phase formation, the other is happening during the 123 solidification. After 900°C, the 123 phase starts forming and then melts. It is no obvious in plain sample but is distinct in the hole sample. It is concluded that the large specific surface area provides more oxygen transport into the bulk of the hole sample, improving the 123 phase formation as well as the 123 phase melting. The observation of the section morphology of plain and hole samples brings even a more striking information. For the same process, it is difficult to grow a single domain YBCO in the plain sample, whereas a single domain has grown through the entire bulk of the hole sample almost down to the substrate. As a collateral effect of the **hole technique**, we observed that the crystal growth is much improved. This phenomenon will be discussed further in chapter 3.

Table 2-1 The morphology on surface and cross-section of the plain sample and the hole sample in the susceptibility measurement.

PMP-YBCO	specific surface area σ (mm ² /g)	Surface	Section
Plain sample	72		

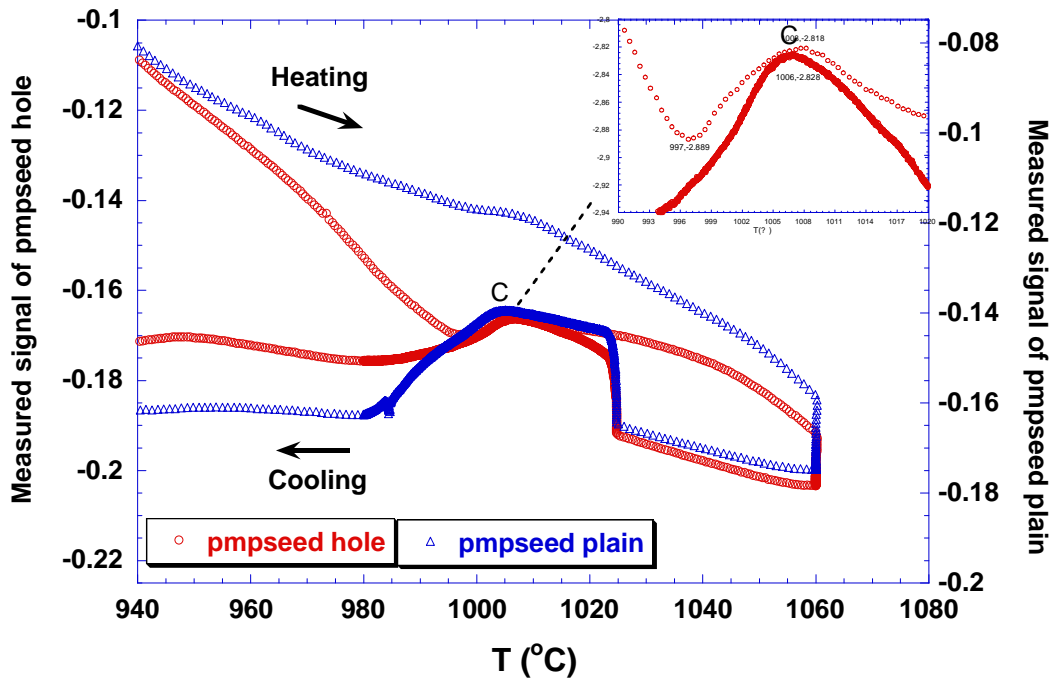
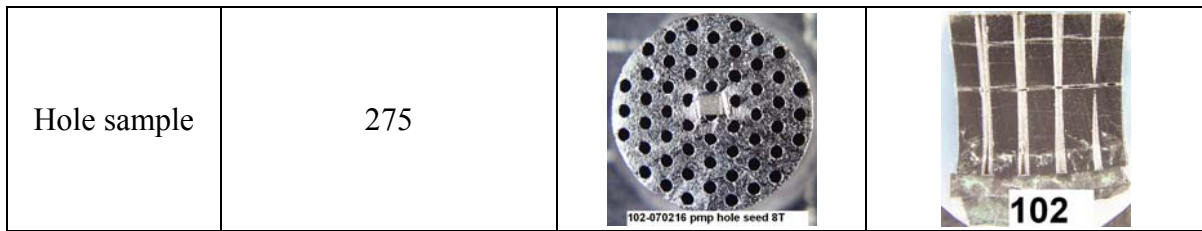


Figure 2-15 The measured magnetic force curves of plain and hole PMP-YBCO samples

2.5 Effect of overheating-temperature on phase transition

The overheating temperature T_o is the maximum temperature reached during the heat treatment, which is over the melting temperature T_m . We fixed different overheating temperature T_o in the process to study its effect on the nucleation. Three samples were prepared and processed in the same manner expect the overheating temperature T_o which was set at the following different values: 1060°C, 1100°C, 1150°C. The heating rate between 900°C and 1060°C was kept at 60°C/h. The surface nucleation was observed for every sample. The observed nucleation morphology on surface of sample with the overheating temperature T_o set at 1150°C is shown in figure 2-17.

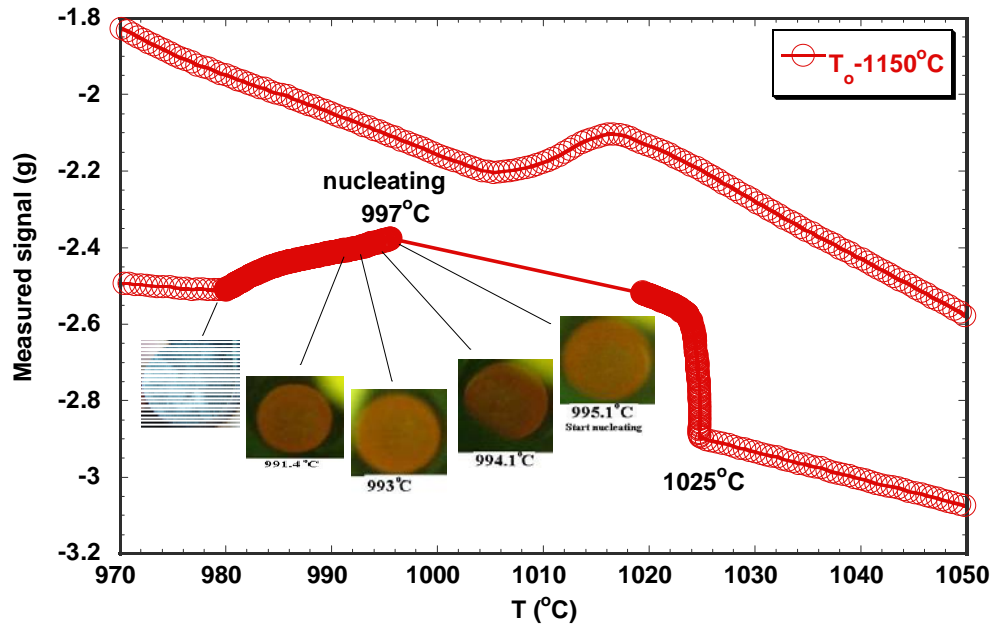


Figure 2-17 The nucleation and the measured force curve of PMP-YBCO sample, nucleating at 997°C.

When overheating temperature T_0 is 1060°C, the nucleating temperature T_n is 1004°C. As the overheating temperature T_0 is higher, 1150°C, the nucleating temperature T_n is starting at 997°C. As analyse in section 2.2, the susceptibility decreases after the nucleation starting, so the nucleating temperature T_n is easily identified. The nucleating temperature T_n of the sample with higher overheating temperature T_0 is lower than the one for sample with lower overheating temperature T_0 . Figure 2-18 shows the susceptibility curves of the samples with the overheating temperature T_0 as 1060°C, 1100°C, 1150°C. The nucleating temperature T_n is observed at 1004°C, 1000°C and 997°C respectively. The dependence of the nucleating temperature T_n on the overheating temperature T_0 is plotted in figure 2-19. It displays the shifting of the nucleating temperature down to lower temperature with an increasing overheating temperature.

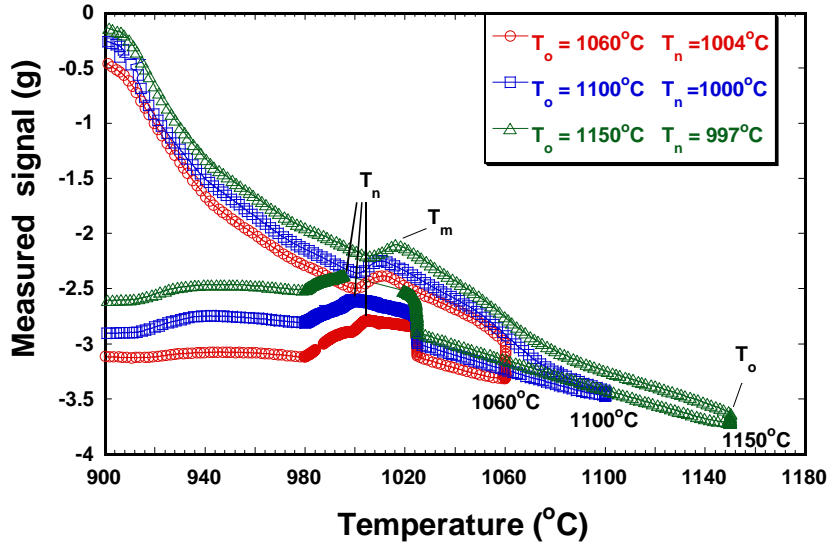


Figure 2-18 The measured susceptibility curves of the PMP-YBCO sample at different overheating temperature 1060°C, 1100°C, 1150°C.

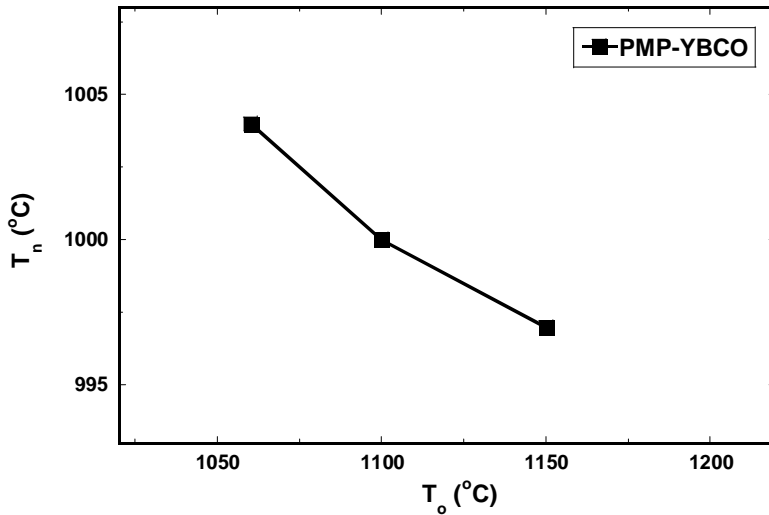


Figure 2-19 Dependence of nucleating temperature T_n on the overheating temperature T_o .

In 1950, D. Turnbull described the effect of overheating temperature T_o on the nucleating temperature T_n of metal in heterogeneous nucleation system. For the experimental nucleating data in various liquid-solid bulk material, he concluded the result of the effect of thermal history on nucleating temperature as shown in figure 2-20. The difference of overheating temperature T_o and the nucleating temperature T_n is marked as ΔT_+ , $\Delta T_+ = T_o - T_n$. The difference of melting temperature T_m and the nucleating temperature T_n is marked as ΔT_- , $\Delta T_- = T_n - T_m$. D. Turnbull assumed the pre-nuclei in melted phase at an overheating temperature is existing stably in solid in a concave. This solid pre-nuclei becomes a nuclei when passing the phase transition. As the overheating temperature T_o increases, the size of spheres reduces and the nuclei size decreases. It makes the critical nuclei size so small that the

random nucleating temperature T_n is reduced. This theory is successful to explain the effect of the overheating temperature T_o on the nucleating temperature T_n in PMP-YBCO nucleation. When the overheating temperature T_o increases, the size of 123 nuclei reduces. A greater undercooling degree ΔT is required to stabilize 123 nuclei and to provide a growth driving force. Therefore the nucleating temperature T_n is reduced.

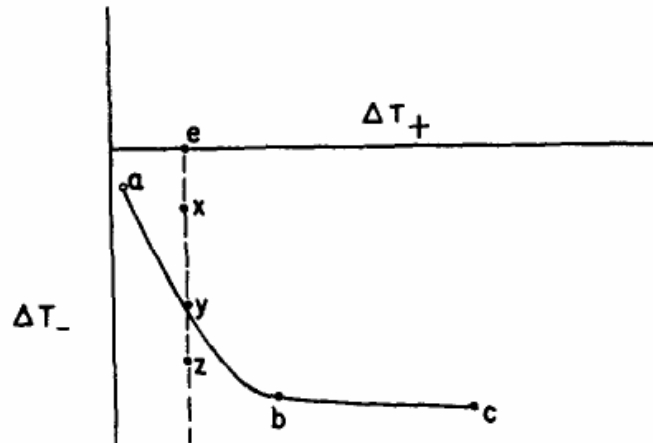


Figure 2-20 “Effect of thermal history on temperature of rapid nucleation in liquid-solid transformations.” by D. Turnbull.

2.6 Summary

We have shown that in situ susceptibility measurement at high temperature during processing of PMP-YBCO gives valuable information for the processing of the material.

1) We investigated the crystalline phase transitions of bulk PMP-YBCO by high-temperature Faraday Balance and quenching experiments. It was found that six remarkable crystalline transitions take place during the fabrication process of bulk PMP-YBCO. They are:

- 1) $211+011+\text{CuO} \rightarrow 123$ ($900^\circ\text{C}-1000^\circ\text{C}$);
- 2) $123 \rightarrow 211+\text{L} + \text{O}_2\uparrow$ ($1000^\circ\text{C}-1012^\circ\text{C}$);
- 3) $\text{BaCuO}_2+\text{CuO} \rightarrow \text{L}$ ($900^\circ\text{C}-1020^\circ\text{C}$);
- 4) $\text{Cu}^{2+}(\text{L1}) \rightarrow \text{Cu}^+(\text{L2})+\text{O}_2\uparrow$ ($1022^\circ\text{C}-1060^\circ\text{C}$, at 1060°C , $1060^\circ\text{C}-1025^\circ\text{C}$);
- 5). $\text{Cu}^+(\text{L2}) + \text{O}_2 \rightarrow \text{Cu}^{2+}(\text{L1})$ (at 1025°C);
- 6) $211+\text{L} \rightarrow 123$ ($1004^\circ\text{C}-980^\circ\text{C}$).

It reveals that 123 phase formed and melted in the $900^\circ\text{C}-1012^\circ\text{C}$ temperature range and solidified in the $1004^\circ\text{C}-980^\circ\text{C}$ temperature range.

2) We studied the effect of different heating rates on the phase transition of PMP-YBCO by high temperature Faraday Balance. When the heating rate is higher than 120°C/h, there is no more 123 phase formation in hole sample. The critical heating rate is 120°C/h in hole sample and 100°C/h in plain sample.

3) We investigated the effect of specific surface area on the phase transition. A large specific surface area provides an effective oxygen diffusion for the 123 crystal growth and improves the 123 phase formation as well as the 123 phase melting.

4) We studied the effect of the overheating temperature T_o on the nucleating temperature T_n in PMP-YBCO nucleation. When the overheating temperature T_o increasing the 123 nucleating temperature T_n reduced. As the overheating temperature T_o decreased from 1150°C to 1060°C, the 123 nucleating temperature T_n reduced from 1004°C to 997°C. This phenomenon is in accordance with the Turnbull's heterogeneous nucleation theory.

References

- [2.1] F. Gaucherand, E. Beaugnon. "Magnetic susceptibility of high-Curie-temperature alloys near their melting point". *Physica B*. 2001, 294-295, 96-101
- [2.2] F Gaucherand, E Beaugnon. "Magnetic texturing in ferromagnetic cobalt alloys". *Physica B*. 2004, 346-347, 262-266
- S. Reutzler, D. M. Herlach. "[Magnetic properties of undercooled Co-based alloys](#)". *Materials Science and Engineering A*. 2004, 375-377, 552-555
- [2.3] Beaugnon E, Chaud X, De Rango P. "Control of the solidification process by high static magnetic field : Application to YBaCuO superconductors" in "2006 Magneto-Science/ Magnetic Field Effects on Materials: Fundamentals and Applications", 2006, Masuhiro Yamaguchi, Yoshifumi Tanimoto, (Berlin: Kodansha Springer), 179-189
- [2.4] X. Chaud, E. Beaugnon, R. Tournier. "Magnetic susceptibility during the peritectic recombination of YBaCuO". *Physica C*. 1997, 282-287, 525-526
- [2.5] R A Fereday. "A method of comparing small magnetic susceptibilities". *Pros.Phys.Soc.*1930, 42, 251-263
- [2.6] R A Fereday. "An improved method for the comparison of small magnetic susceptibility". *Pros.Phys.Soc.* 1931, 43, 381-393
- [2.7] R D Heyding. "Four-Inch Shaped Pole Caps for Susceptibility Measurements by the Curie Method". *Review Scientific Instruments*. 1961, 32, 161-163
- [2.8] S K Chen, L Zhou, K G Wang. *Physica C*. 2002, 366, 190.
- [2.9] Noburu Fukushima, Hisashi Yoshino, Hiromi Niu, Masaru Hayashi, Hideyuki Sasaki. *Japanese Journal of Applied Physics*. 1987, 26, 719-720
- [2.10] W.M.Temmerman, H.Winter, Z.Szotek, and A.Svane. *Physical Review letters*. 2001, 86, 2435- 2438
- [2.11] S Scheurell, F Scholz, Tolesch and E Kemnitz. *Supercond.Sci.Technol*. 1992, 5, 303-305
- [2.12] A J Twin, J S Abell, I R Harris. *Journal Less-common Metals*. 1990, 164-165, 1136-1141
- [2.13] T B Lindemer, E D Specht. *Physica C*. 1995, 255, 81-94
- [2.14] T B Lindemer, F A Washburn, C S MacDougall, R Feenstra, and O B Cavin. *Physica C*. 1991, 178, 93-104
- [2.15] X. Chaud, D. Isfort , L. Porcar, R. Tournier, Growth of YBCO single domains through an array of holes for FCL c-axis superconducting elements. *J. Europ. Ceram. Soc*. 2005, 25, 2955

Chapter 3 Growth of PMP-YBCO single domain

3.1 YBCO single domain fabrication by Powder Melting Process

The process of fabricating single domain YBCO by powder melting process and the properties for application is outlined in figure 3-1. The process includes five steps: powder preparation, moulding, nucleation, growth and oxygen treatment.

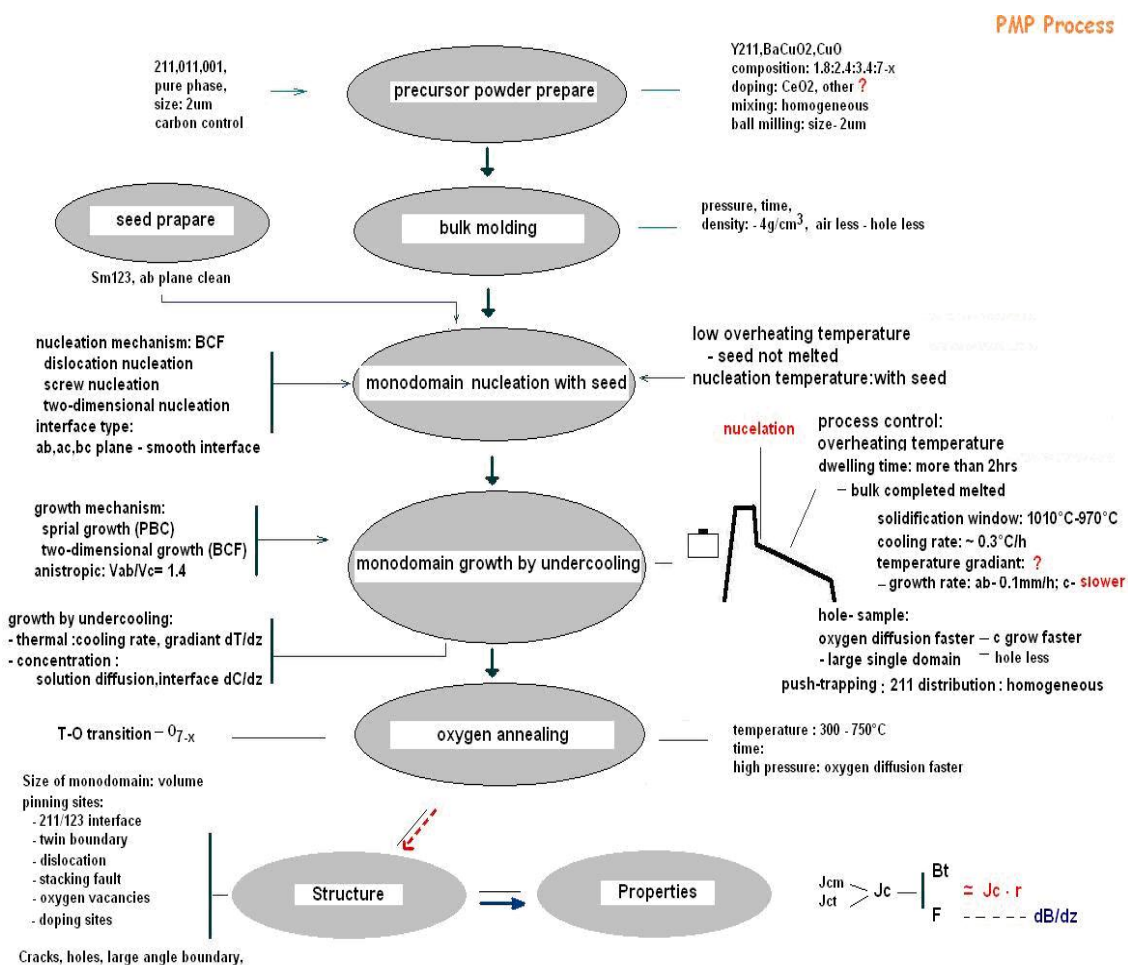


Figure 3-1 Flow chart of fabrication of bulk PMP-YBCO

The precursor powder is a mixture of Y₂BaCuO₅ (211), BaCuO₂ (011) and CuO. The 211 and 011 powders are prepared by co-precipitation in NIN. They are standard powder in terms of purity phase, the carbon content is lower than 800ppm and the mean size of powder is around 2µm. The stoichiometric composition of the mixture is Y_{1.8}Ba_{2.4}Cu_{3.6}O_{7-δ} with 1%wt CeO₂ addition for 211 particles refinement. The mean size of the mixed powder is 1-2 µm

after ball milling. The mixed powder is uni-axially pressed at 60 MPa into a $\Phi 20\text{mm} \times 18\text{mm}$ pellet (about 20 g). Sm123 seed is used to direct the nucleation and the $\text{YBa}_2\text{Cu}_3\text{O}_{6.5}$ (123) crystal is grown to a YBCO single domain with slow cooling rate. We refer to this YBCO single domain as “PMP-YBCO”. The PMP-YBCO single domain is treated in oxygen at temperatures between 750°C and 400°C to have the T-O phase transition and to obtain the superconducting phase $\text{YBa}_2\text{Cu}_3\text{O}_{6.9}$. In this chapter, we will study the growth dynamics of PMP-YBCO single domain.

3.2 Nucleation

3.2.1 Screw nucleation

Based on the Jackson’s single atom layer theory in crystal growth, the interface of 123 crystal could be identified as smooth or rough [3.1]. The Jackson factor α is calculated according to the equation (3-1).

$$\alpha = (L_0/kTE) \cdot (\eta/v) \quad (3-1)$$

C.Klemenz calculated the Jackson factor α of (100), (010) and (001) plane of 123 crystal [3.2] :

$$\alpha_{(001)} = 13.25, \alpha_{(100)/(010)} = 9.96 \quad (3-2)$$

If the Jackson factor $\alpha > 5$, the surface is smooth. So, the (100),(010) and (001) plane of 123 crystal are smooth surfaces. If the crystal surface is smooth, the crystal nucleation is abided by two-dimensional nucleation, dislocation nucleation or screw nucleation according to the BCF theory. B. N. SUN observed a spiral nucleation on (001) face of YBCO crystal [3.3]. In the observation of PMP-YBCO sample, the screw nucleation is also observed on (001) plane as shown in figure 3-2. The minimum screw nucleation size is observed to be around $3\mu\text{m}$.

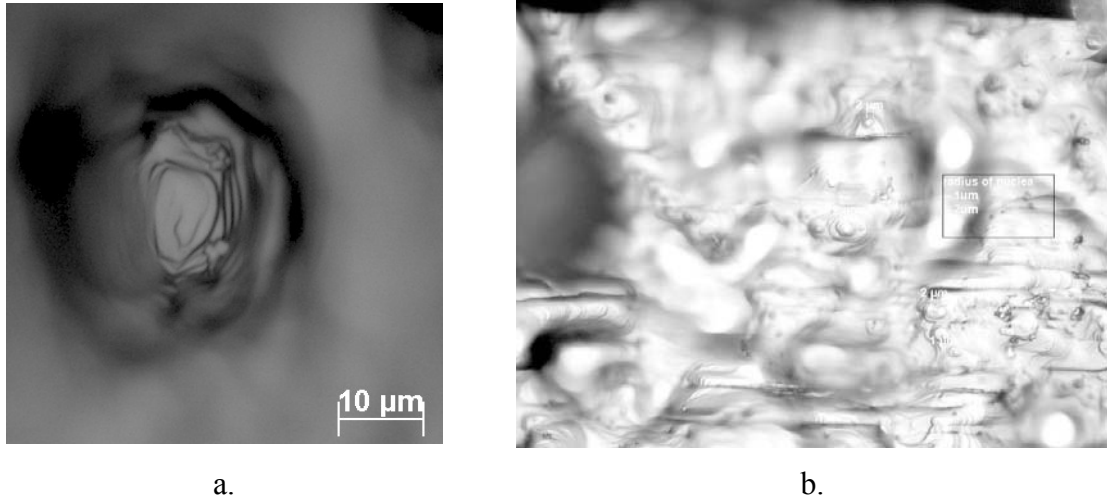


Figure 3-2 Screw nucleation on (001) plane are observed in PMP-YBCO single domain.

3.2.2 Nucleating temperature

In order to grow the single domain, it is necessary to prevent the random nucleation at the front of the growth interface. We compare the susceptibility transition of PMP-YBCO with seed and without seed, as shown in figure 3-3 (the magnetic signal is more or less reflecting the susceptibility. Curves measured in the same condition can be compared without calculating the susceptibility.) The Y123 nucleation is found to start at 1011 K with seed. The Y123 nucleation started at 1004 K without seed. The Y123 nucleating temperature with seed is 5 K higher than the nucleating temperature without seed, because the seed provides an already solid surface for nucleation and so allows to decrease the nucleation energy required. So using a seed, if we keep the sample temperature in the 1011 K-1006 K temperature range, the random nucleation can be prevented and a single domain can be grown. The Y123 single domain growth will be controlled by heterogeneous nucleation from the seed.

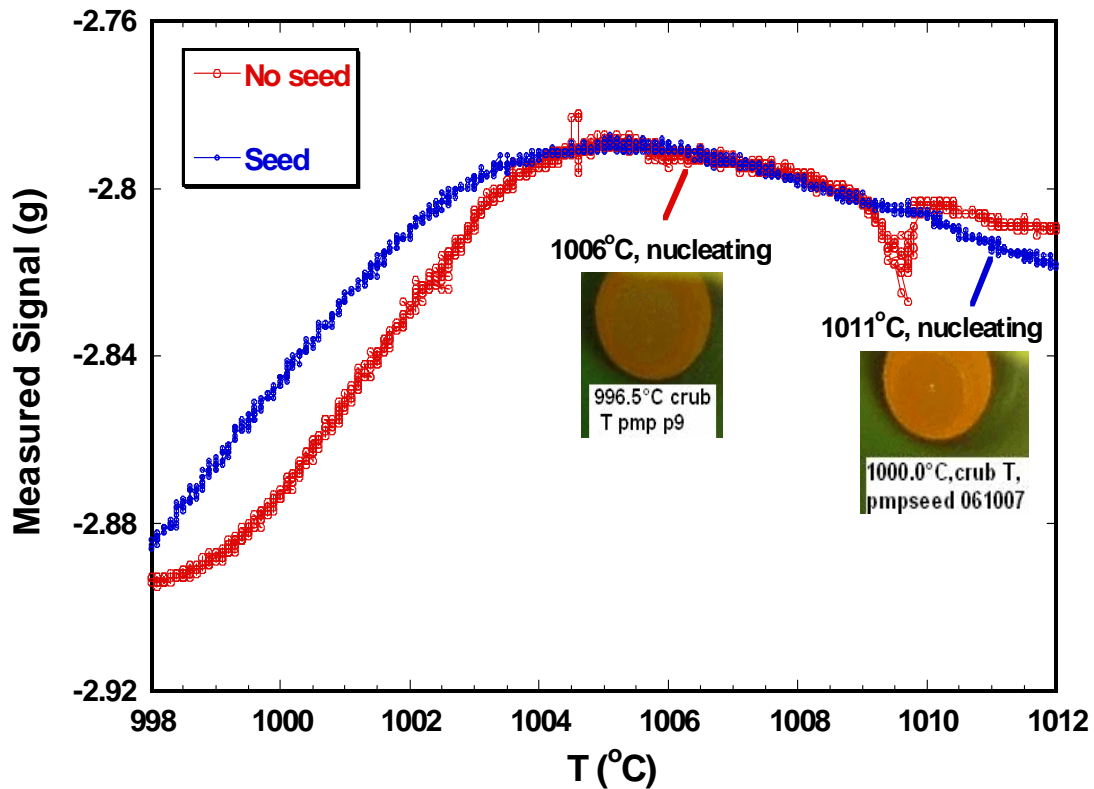


Figure 3-3 Nucleation of PMP-YBCO sample with seed or no seed in magnetic susceptibility measurement. The nature nucleation starts at 1006°C, the nucleation with seed is at 1011°C.

3.3 Growth of plain PMP-YBCO single domain

3.3.1 High temperature furnace with in situ video monitoring

Based on the information from susceptibility transition results in chapter 2, the process of PMP-YBCO single domain with Sm123 seed is established. PMP-YBCO bulk is prepared in the high temperature furnace with in situ video monitoring. This set-up is illustrated in figure 3-4 with an installed camera over the furnace. To get an exploitable picture, a contrast is created by illuminating the surface of the sample with a vertical light beam provided by some halogen lamps. The camera takes the pictures of the whole growth process on the sample's surface. One picture is recorded every hour, so that a movie of the growth can be built. From this recorded observation we can measure the growth rate R_a on the ab plane. The muffle furnaces M1(left) and M2(right) which are classical furnaces transformed at CRETA/CNRS lab are used to fabricate the YBCO single domain as shown in figure 3-5.

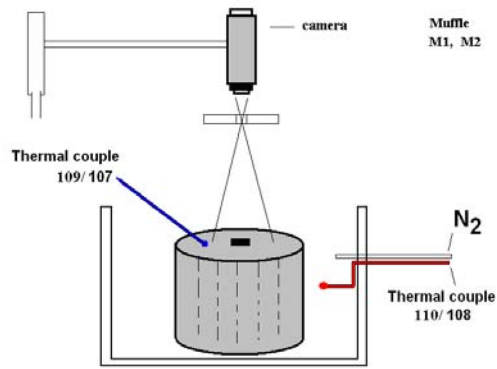


Figure 3-4 Sketch of muffle with camera.

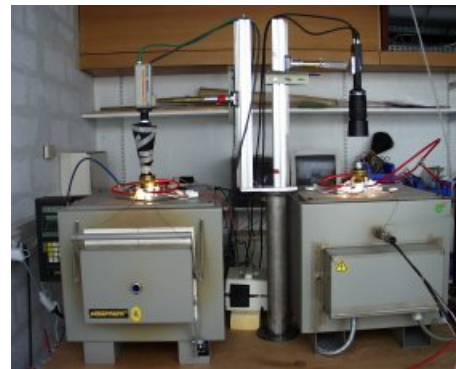


Figure 3-5 The M1 and M2 muffles with camera in CRETA lab.

3.3.2 The solidification window of PMP-YBCO

The nucleating temperature T_n with seed is between 1011°C - 1006°C and the solidification window is 1006°C - 980°C from susceptibility investigation. The growth process is modified as shown in figure 3-6. The sample is heated to an overheating temperature of 1040°C at $60^{\circ}\text{C}/\text{h}$ and kept 2hrs at this temperature, cooled down to 1014°C at $60^{\circ}/\text{h}$ then slowly cooled from 1014°C to 1003°C at $1^{\circ}/\text{h}$, from 1003°C to 990°C at $0.2^{\circ}\text{C}/\text{h}$ and from 990°C to 984°C at $1^{\circ}\text{C}/\text{h}$. Pictures of the growth at the surface surface are recorded by the camera every hour. The nucleation and growth steps on surface reveal the growth temperature window. Compared to susceptibility measurement, the practical nucleating temperature is found around 1000°C , the single domain growth is in the 1000°C - 980°C temperature range.

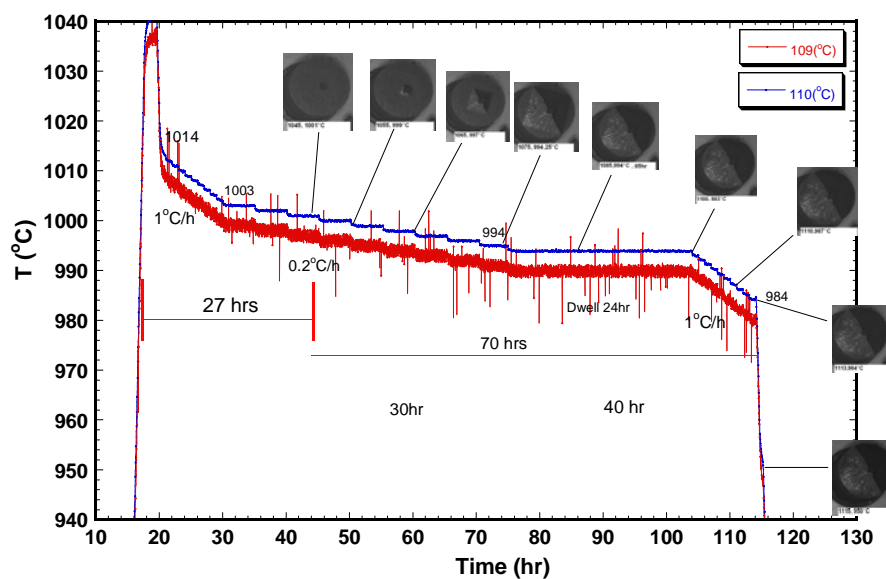


Figure 3-6 The surface growth of PMP-YBCO single domain is monitored with the video pictures in situ during the processing.

In furnace M1 and M2, all the plain PMP-YBCO single domains have a good textured on surface, but grew only a few millimetres in depth, as shown in figure 3-7. When the sample is cut along c-axis, the section reveals multiples grains with different directions as shown in figure 3-7b. The 123 crystal is not grown to the bottom along c-axis and melted phase, porosity and cracks are co-existed in the sample.

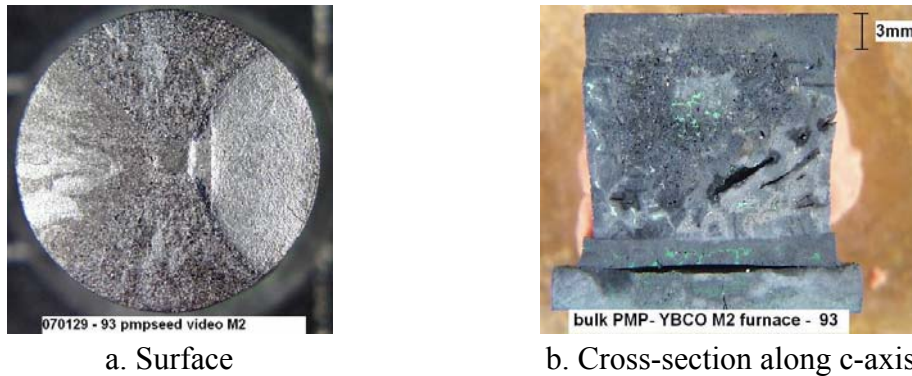


Figure 3-7 The morphology of PMP-YBCO single domain after processing in muffle furnace M2.

3.3.3 Batch fabrication of PMP-YBCO single domain

On the other hand, with the same PMP process, we have made the batch of PMP-YBCO single domain in diameter of 30mm at NIN (Xi'an, China). The ab plane of single domain is parallel to the surface, the growth depth is to 8-10mm, as shown in figure 3-8. This result shows the temperature distribution is different between the muffle furnace M2 and the NIN's furnace. In the single domain growth the driving force of the crystal comes from the undercooling degree. It is related to the temperature undercooling, temperature gradient undercooling and the constitutional undercooling. The undercooling from the furnace itself is only a temperature gradient undercooling. Therefore, based on the same composition and process, the reason why the single domain grows well in NIN's furnace is due to the temperature gradient undercooling. The temperature gradient is about $0.02^{\circ}\text{C}/\text{cm}$ in NIN's furnace which provides a little undercooling degree for growth. The successfully batch grown single domain in a batch means anyway the high temperature susceptibility measurement and video observation provided us with accurate process parameters.

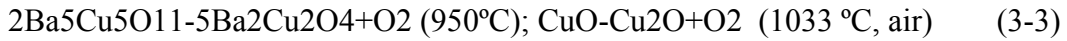


Figure 3-8 Superconductor PMP-YBCO single domain with $\Phi 30\text{mm} \times 15\text{mm}$ size prepared in one batch.

3.4 Oxygen diffusion effect to the growth

A weight loss phenomenon is found in the thermogravimetry measurement of plain and hole sample. Several influences are analyzed to cause the weight loss in PMP-YBCO sample: system errors, water gas vaporizing, carbon oxide CO_2 or oxygen O_2 loss. They are analyzed in detail in the following.

If there is a system errors in measurement to make losing weight in the heating region of $200\text{-}1060^\circ\text{C}$, so that there should be an increasing weight during the cooling region from $1060^\circ\text{C}\text{-}200^\circ\text{C}$. But this phenomenon doesn't happen. So, the losing weight is not depended on the system errors in themogravimetry measurement. If there is some water in sample, we can dry the sample at 100°C to make sure that most of the eventual water is gone. The hole PMP-YBCO sample is treated in 100°C drying before thermogravimetry measurement. Comparing the data (were are they) between drying and no drying, there is still a weight loss in dried sample. Thereby, the water is not the reason for weight loss. As to the carbon oxide spilled out, it has been confirmed that the carbon content in precursor powder is less than 800 ppm (0.08%wt), so the carbon oxide in the PMP-YBCO sample is less than 0.08%wt. But the weight loss is up to 8%wt far from the carbon oxide potentially released. So the carbon oxide is not considered to influence much the weight loss. From above, the system errors, water and carbon oxide are not the real cause of weight loss in PMP-YBCO sample. Furthermore, considering the oxygen O_2 spilling, there are several phase decompositions with regards to 011 and CuO [3.4] that are releasing oxygen as follows:



The oxygen is released from sample at high temperature. Supposed the 011 and CuO decomposed thoroughly, the calculated oxygen loss amounts to about 0.0903g/g. The experimental weight loss in the thermogravimetry curve of hole PMP-YBCO sample is 0.0804g/g. The experimental weight loss is consistent to the calculation value of oxygen released. So we can assume the weight loss in PMP-YBCO sample comes mostly from the oxygen loss.

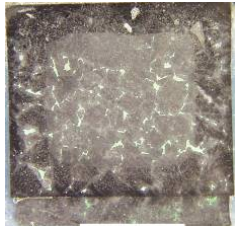
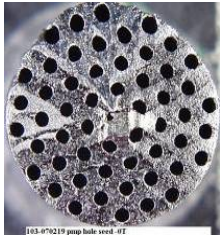
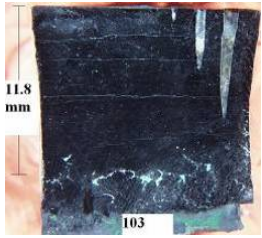
The measured thermogravimetry curves of plain and hole PMP-YBCO samples is shown in figure 3-9. They were processed the same way and their morphology is shown in table 3-1. The thin-walled sample is losing more weight than the plain sample. We assume this is a consequence of the reduced diffusion path of hole sample.

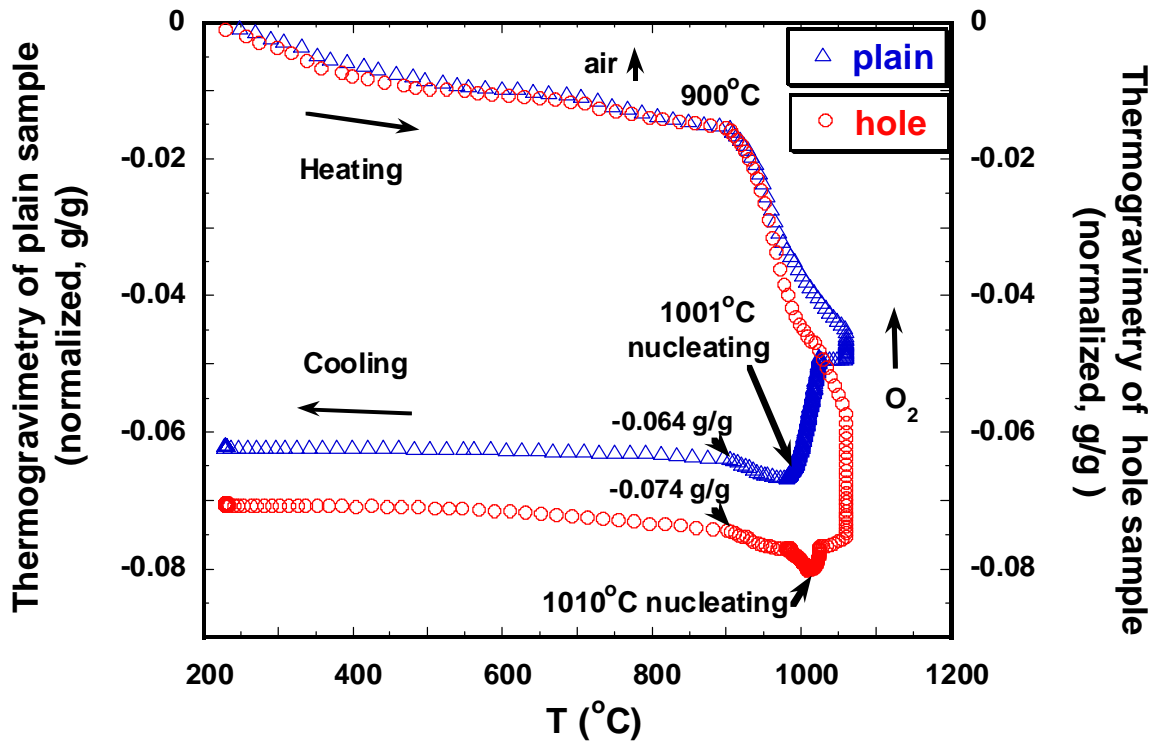
The specific surface area of plain sample and hole sample were calculated and gives the following results :

$$\begin{aligned} \text{Plain:} \quad & \sigma_{\text{plain}} = S/m = 72.22 \text{ mm}^2/\text{g} \\ \text{Hole:} \quad & \sigma_{\text{hole}} = S/m = 275.2 \text{ mm}^2/\text{g} \end{aligned} \quad (3-4)$$

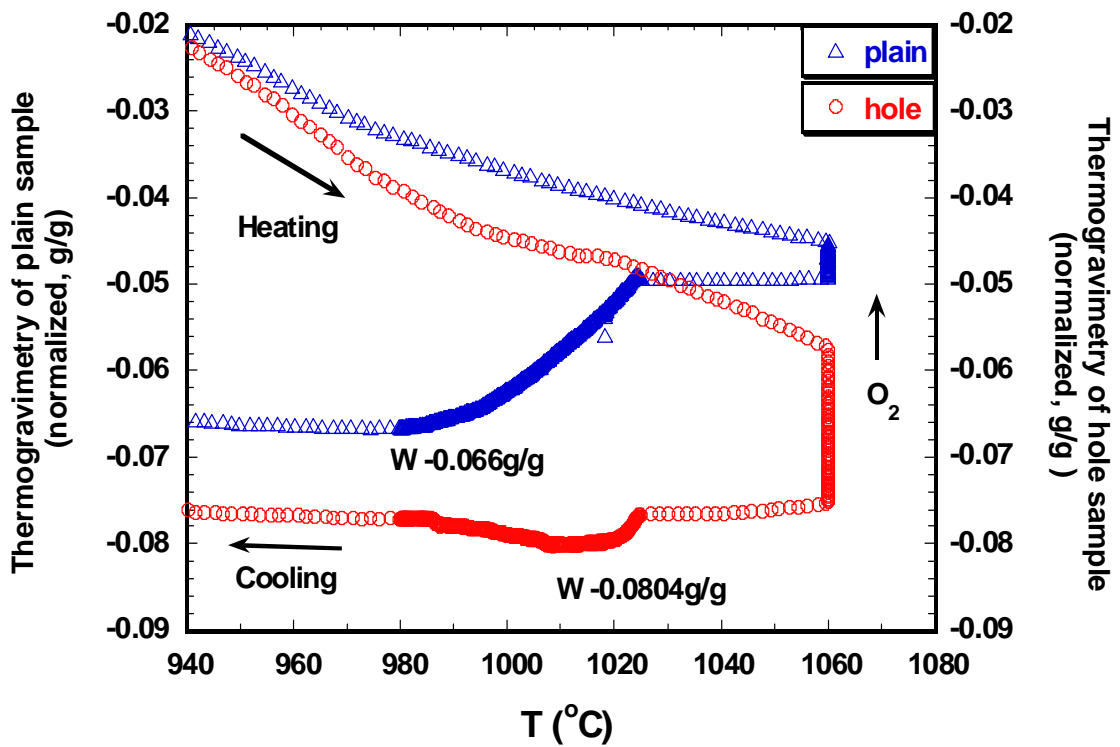
S is the surface area of sample, σ the specific surface area and m the mass of sample. The specific surface area of hole sample is 4 times than the one of plain sample. A larger surface ratio provides much reduced diffusion path for the oxygen out. . The gross weight loss per gram is 80mg/g in a hole sample and 66mg/g in a plain sample.

Table 3-1 Gross oxygen lost at high temperature and oxygen absorbed during the 123 growth of plain- and hole- sample. Morphology of plain- and hole- PMP-YBCO sample grown with Sm123 seed.

PMP-YBCO	Specific surface area σ (mm^2/g)	Weight loss mg/g	Oxygen absorbed mg/g	Surface	Section
Plain sample	72	66	2		
Hole sample	275	80	6.4		



a.



b.

Figure 3-9 Thermogravimetry of plain and hole PMP-YBCO samples. The oxygen released contribute to the weight loss in sample. The weight loss by a hole sample is larger than by a plain sample.

An interesting phenomenon is noticed: the weight starts to increase during solidification of the hole sample just after the nucleation has occurred as shown in figure 3-10. The weight increase of oxygen is 6.4mg/g in the hole sample and 2mg/g in the plain sample. Our assumption is that the weight increase comes from the “oxygen” entering the sample that is required for the 123 crystal growth to proceed. Also, the effect of oxygen partial pressure on the solidification has been shown in X.Chaud’s thesis and OCMG process, etc. and some authors have used the oxygen diffusion to control a directional solidification of the YBCO. Thus we can deduce that the oxygen diffusion plays a role for the 123 growth similarly to the Y diffusion used by Y Shiohara’s model. This is a key point in the present work: sufficient oxygen diffusion is a crucial step for YBCO solidification.

Moreover the role of the oxygen diffusion is confirmed by the comparison of both geometry plain and hole: the YBCO single domain is fully grown in the hole sample of size $\Phi 20\text{mm} \times 18\text{mm}$, whereas the grain is limited to the upper surface in the plain sample. The oxygen diffusion in the hole PMP-YBCO growth will be discussed in the section 3.5.

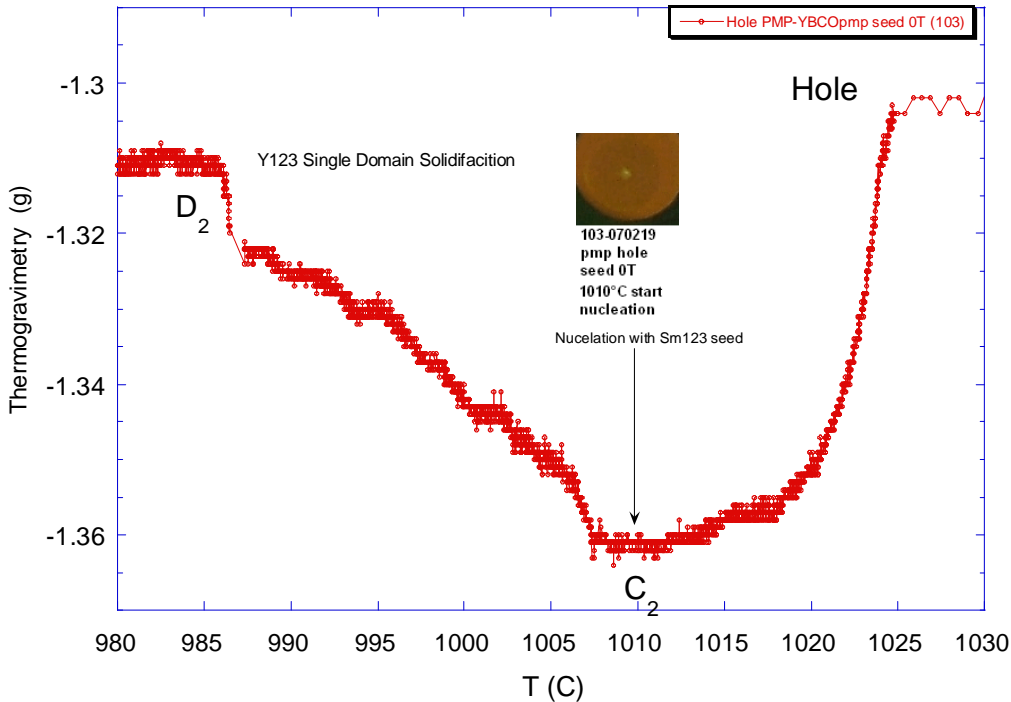


Figure 3-10 Thermogravimetry of hole PMP-YBCO sample. Weight increasing in solidification after nucleating. The photo shows Y123 nucleating start at 1010°C with seed Sm123.

3.5 Dynamics of the hole PMP-YBCO single domain growth

3.5.1 Growth of hole PMP-YBCO single domains

The preparation of the plain samples is described in section 3.1. The powder is uniaxially pressed into a $\Phi 20\text{mm} \times 18\text{mm}$ hole pellet (about 16 g). The hole PMP-YBCO bulk is prepared by the similar process as plain sample in the high temperature furnace with in situ video monitoring. Pictures of the surface are taken every hours. The whole growth process on surface is illustrated in figure 3-11. The hole sample is grown to a single domain on the surface and also in the depth, contrary to the plain sample.

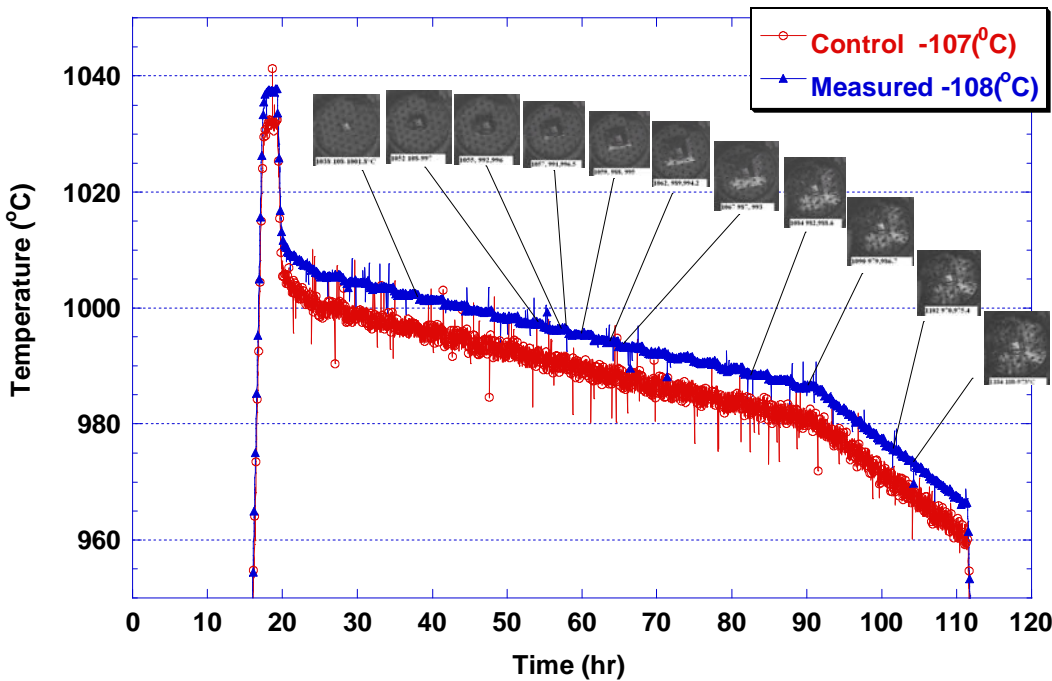


Figure 3-11 The process and observation of PMP-YBCO fabrication using a thin wall geometry.

3.5.2 Growth rate Ra

By measuring the size of the crystal on the video pictures taken every hour during the growth process of plain and hole sample (as shown in figure 3-6 and figure 3-11), we deduce the growth rate Ra of plain and hole samples as illustrated in figure 3-12. The experimental growth rate Ra versus undercooling degree is plotted in figure 3-13. The growth rate Ra of plain sample is estimated around 0.1-0.3mm/h, and the one of hole sample about 0.1-1mm/h . The maximum growth rate Ra of hole sample is 10 times than the one of plain sample.

According to the BCF theory (see chapter 1), the growth rate should be proportional to the undercooling ΔT or its square, i.e. $R \propto \Delta T$ or $R \propto \Delta T^2$. But here the growth rate R_a of hole PMP-YBCO increased with the undercooling increasing when $\Delta T < 18^\circ\text{C}$, it decrease after $\Delta T > 18^\circ\text{C}$. The growth rate R_a increased in the primary stage and then become decreased gradually. It is consistent with the result of MTG-YBCO single domain growth investigated by X. Chaud [3.5]. But it is inconsistent with the BCF theory. It is a confusing problem.

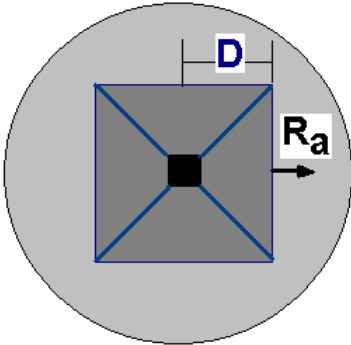


Figure 3-12 The growth width on ab plane and the growth rate along (001) direction of PMP-YBCO single domain.

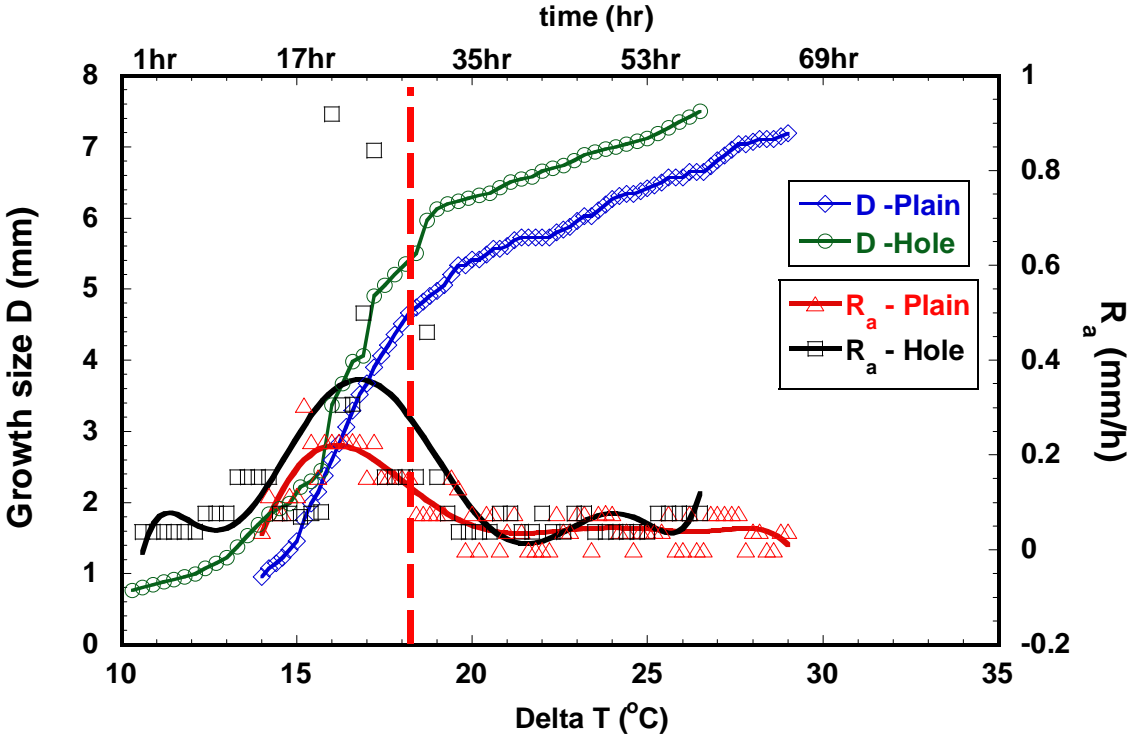


Figure 3-13 The growth size D and the growth rate Ra on ab plane of PMP-YBCO sample.

3.5.3 Experimental

The growth depth is very important for the single domain growth since it gives a larger volume of the crystal domain. The growth rate R_c along c-axis is essential for growth depth. We try to study the relationship between the c-axis growth rate R_c and the undercooling ΔT .

Using the in situ high temperature susceptibility measurement device without magnetic field, we performed thermogravimetric measurements during the hole PMP-YBCO fabrication process. The temperature is from room temperature to 1200°C, the resolution of the weighting machine is 0.1mg, a sketch of the TG instrument is shown in figure 3-14. It is different from the general thermogravimetry instrument in that sense that a large sample of 20-30 grams is considered while the general TG instrument can only contain 10 mg sample. Our thermogravimetric experiment reflects the real processing of our samples and are depending on the experimental conditions through the thermal and gaz diffusion since because of large sample it is affected by thermal and diffusion process.

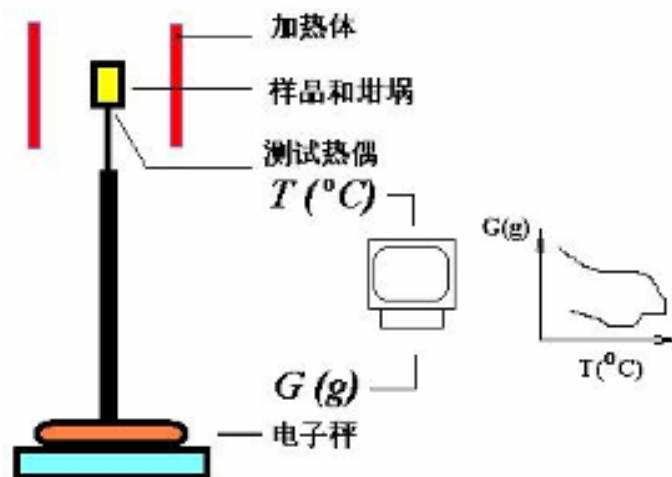


Figure 3-14 The sketch of the in situ thermogravimetry measurement of bulk sample.

In order to investigate the growth rate, the samples are quenched in air at different undercooling degrees at the following temperatures: 1005°C, 1000°C, 995°C, 990°C, 980°C, 970°C and 960°C. The process is illustrated in figure 3-15. The quench experiments are listed as sample Q1, Q2, Q3, Q4, Q5, Q6 and Q7.

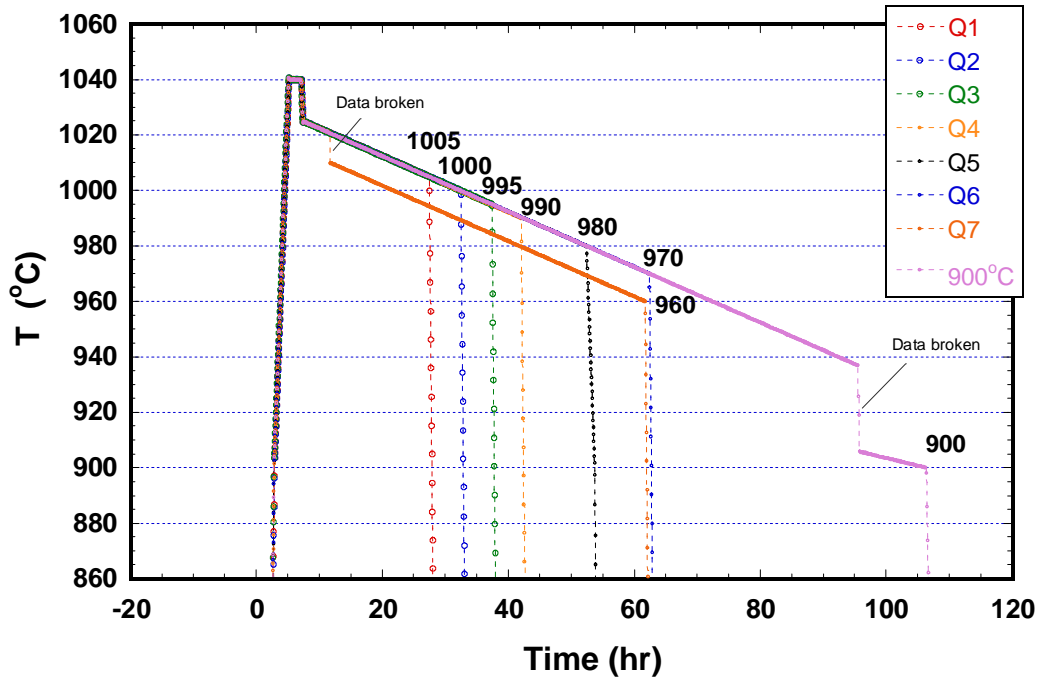


Figure 3-15 Quench process of the hole PMP-YBCO sample.

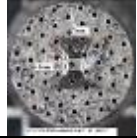
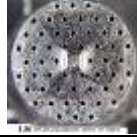
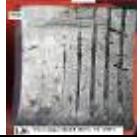
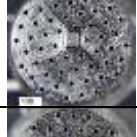
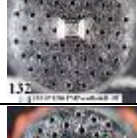
The quenched sample were vertically cut in their middle using a diamond wire saw and the sections were polished. The pictures of the as-grown square 123 single domain on surface and the laminar section were taken with a numerical camera using macrolens. Macrographs of the sections displaying the morphology of the quenched samples are shown in Table 3-2. (XXX I have not seen any microstructure !!! XXX) The grown length a and the grown depth h are measured. We calculate the growth rate R_a and R_c with the grown length difference Δa , Δh corresponding to the growth time Δt , as $R_a = \Delta a / \Delta t$, $R_c = \Delta h / \Delta t$. The undercooling ΔT is defined as the temperature difference between the nucleating temperature T_n (1010°C) and the quenched temperature T_{quench} , as:

$$\Delta T = T_n - T_{\text{quench}} = 1010^\circ\text{C} - T_{\text{quench}} \quad (3-5)$$

ΔT is the undercooling degree. The nucleating temperature T_n on surface of PMP-YBCO with seed Sm_{123} is about 1010°C as determined by the Faraday Balance in chapter 2. In our experiments, the sample is placed in an homogeneous temperature region, so that the thermal gradient is sufficiently small to consider that the sample is grown in isothermal condition. The temperature gradient undercooling is then neglected.

The calculated growth rate R_a in ab plane and R_c along the c -axis are listed in Table 3-2. The mass of oxygen absorbed into quenched sample is estimated from the in situ thermogravimetry measurements. We calculate the oxygen mass transport velocity VO_2 in different quenched samples, they are also listed in Table 3-2.

Table 3-2 It shows the morphology of hole PMP-YBCO single domain and lists the data of the undercooling ΔT , the growth rate R_a on aa plane, the growth rate R_c along c-axis and the velocity of oxygen mass transport V_{O_2} in the quenched hole PMP-YBCO single domain.

sample	T (°C)	ΔT (°C)	ab plane	section	R_a 10^{-5} (mm/s)	R_c 10^{-5} (mm/s)	V_{O_2} 10^{-5} (mg/s)
Q1	1005°C	5°C			18.1	9.4	
Q2	1000°C	10°C			15.3	6.7	43.7
Q3	995°C	15°C			5.5 *	13.3	80.0
Q4	990°C	20°C			5.5 *	11.1	42.2
Q5	980°C	30°C			-	10.3	36.2
Q6	970°C	40°C			-	4.2	28.0
Q7	960°C	50°C			-	2.5	15.0

3.5.4 Growth rates R_{ab} and R_c determined from quench experiments

In this experiment, the growth rate R_a of hole PMP-YBCO is found to increase along with the undercooling degree when $\Delta T < 10^\circ\text{C}$, then it decreases with increasing undercooling when $\Delta T > 10^\circ\text{C}$, as shown in figure 3-16. The growth law is the same as the one resulting from the in situ video measurement. The growth rate R_c of hole PMP-YBCO increased with the increasing undercooling degree when $\Delta T < 20^\circ\text{C}$, then it decreases when $\Delta T > 20^\circ\text{C}$.

In the experiment of A. Endo, as shown in figure 3-16, when the undercooling degree is below 20°C , the growth rate continue to increase with the undercooling ΔT . It is consistent with the BCF theory. In our experiment, both of the growth rate R_a and R_c are increasing with the undercooling degree at first, but they are then decreasing after the undercooling degree had reached a critical value as 18°C for R_a in the video experiment, as 10°C for R_a in

quench experiment and as 20°C for Rc in quench experiment. This phenomenon of the growth rate decreasing later seems to be inconsistent with the BCF theory.

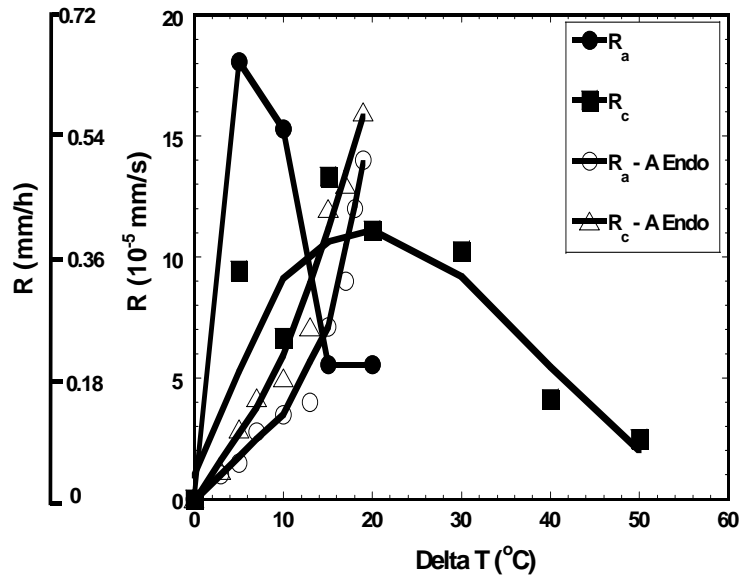


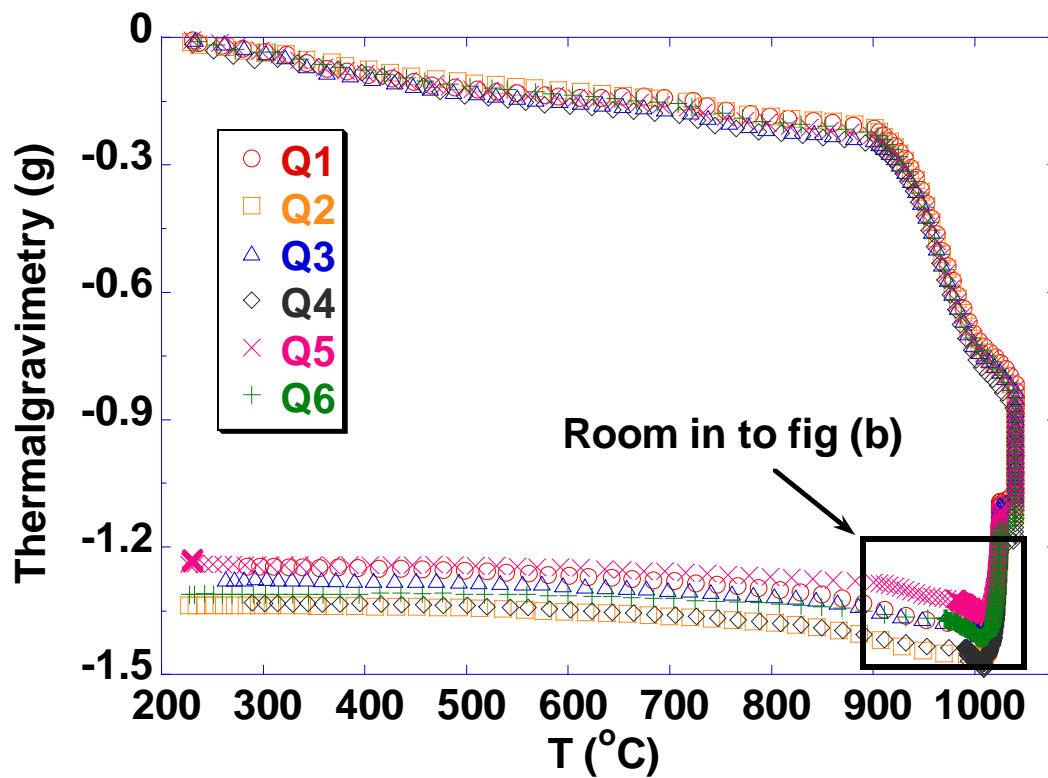
Figure 3-16 Dependence of ab plane growth rate Ra and c-axis growth rate Rc on the undercooling degree ΔT of hole sample comparing to the data from A. Endo.

3.5.5 Effect of oxygen diffusion on growth rate Rc

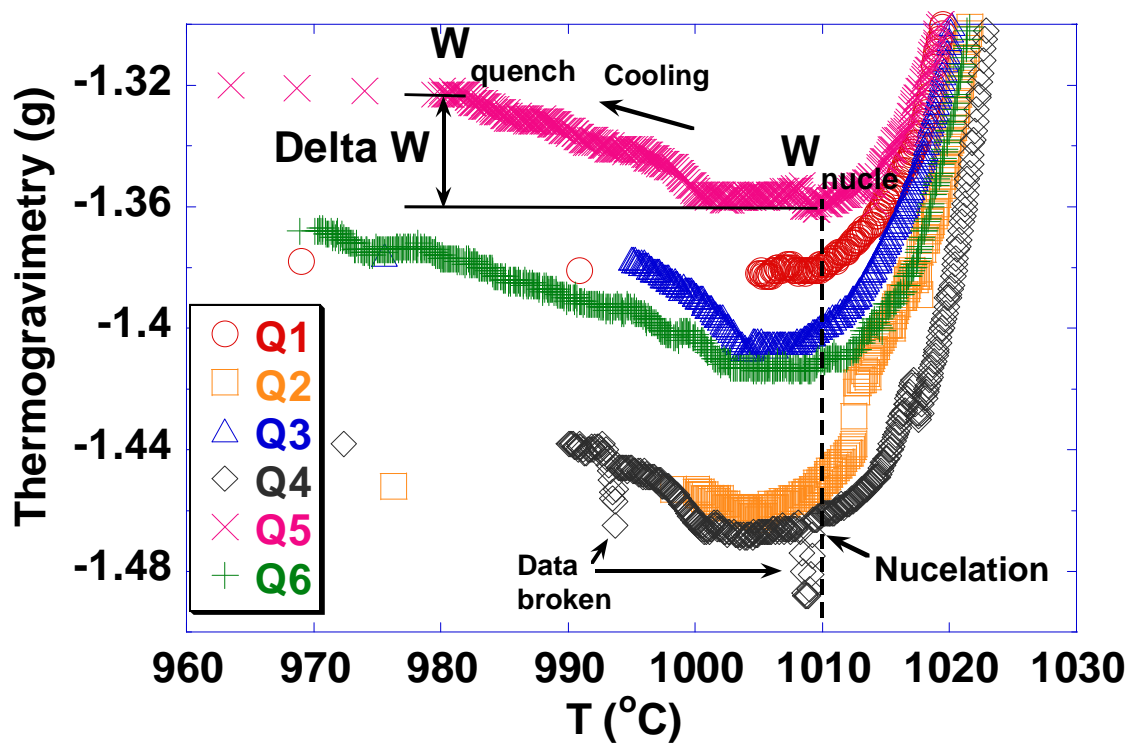
A mass loss is observed in the thermogravimetry curves of the hole PMP-YBCO samples before the Y123 crystal nucleation, then an increase of the mass is seen after nucleation. We have associated in the paragraph 3.4, these changes of mass to oxygen loss or uptake. As shown in figure 3-17, the quantity of oxygen related to the mass increase ΔW can be measured on the thermogravimetry curve. The interval time Δt can be estimated from the cooling rate. Therefore the oxygen mass transport velocity V_{O_2} absorbed into sample is calculated by the following equation:

$$V_{O_2} = \Delta W / \Delta t, \Delta W = W_{\text{quench}} - W_{\text{nucle}} \quad (3-6)$$

Here W_{quench} is the mass value at the quenched point and W_{nucle} the mass value at the nucleating point (figure 3-17b). V_{O_2} is the oxygen absorbed mass transport velocity during Y123 growth. The data are listed in Table 3-2.



a.



b.

Figure 3-17 Thermogravimetric curves of the quenched hole PMP-YBCO single domain samples. (a) Thermogravimetric curves of the entire process. (b) Thermogravimetric curves zoom in between 960°C to 1030°C.

We found some proportionality between the c-axis growth rate R_c and the oxygen mass transport velocity V_{O_2} as can be seen in figure 3-18. This result indicates the Y123 growth requires enough oxygen to proceed. In our experiment, even though the large thermal undercooling ΔT is applied, since the insufficient oxygen atom transport limits the 123 growth, the c-axis growth rate R_c cannot catch the undercooling ΔT speed. Therefore the growth rate R_c is controlled by the oxygen diffusion more than the thermal undercooling ΔT , as supported by the linear relationship:

$$R_c \propto V_{O_2} \quad (3-8)$$

In fact, according to the BCF theory, the growth rate is related not only to the undercooling ΔT but also to the supersaturation σ , as

$$R \propto \sigma, \text{ or } R \propto \sigma^2 \quad (3-9)$$

So we think the R_c is related to the oxygen supersaturation. Therefore, the growth mechanism of hole PMP-YBCO single domain should be considered to depend on both of the undercooling and the oxygen super-saturation σ .

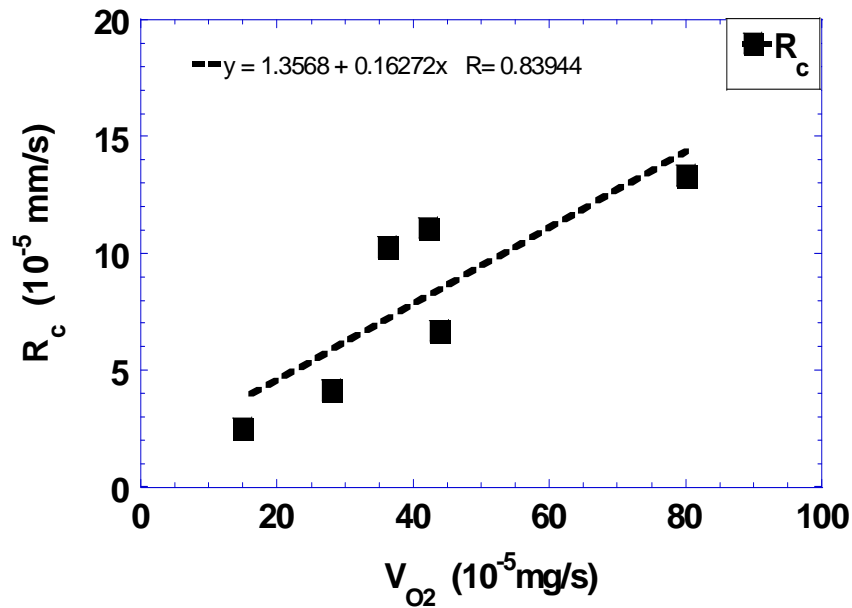


Figure 3-18 The c-axis growth rate R_c has a linear relationship to the oxygen mass transport velocity V_{D-O_2}

3.5.6 Hole PMP-YBCO Single domain growth in flowing air

Our experiment have revealed that the growth is much better in hole samples than iplain sample. We fabricated many hole samples in furnace M1. Despite a complete growth of the single domain at the surface of the sample, the growth in depth was limited to a few millimeters and not satisfying. Considering the oxygen loss in the process, we decided to fabricate some samples under flowing air to provide sufficient oxygen to the growth. We used

the same heat treatment to grow a hole sample in static air and another in flowing air after nucleation at 1010°C. To accentuate the static air feature was accentuated in furnace muffle M1 by caulking as shown in figure 3-19, whereas flowing air was provide by a feeder adjusted to the same furnace as sketched in figure 3-20.

A clear difference on the growth depth is observed: it reaches 16 mm down to the sample bottom for the sample prepared in flowing air and only 6mm for the sample in static air condition, as shown in figure 3-21. This result proves that sufficient oxygen is needed to promote the single domain growth. The growth rate is related to the oxygen supersaturation σ .



Figure 3-19 Muffle furnace M1 with the door closed keeping primary air atmosphere.

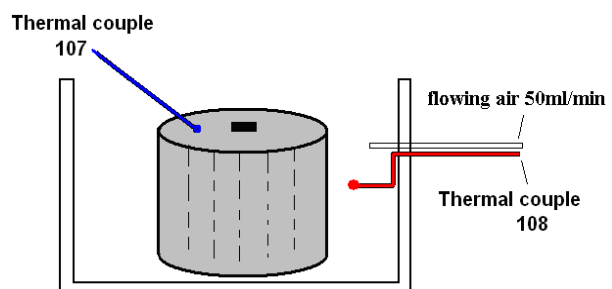
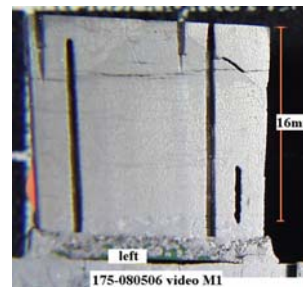


Figure 3-20 Sketch of muffle furnace M1 with a flowing air feeder.



a. No flowing air



b. In flowing air

Figure 3-21 Cross section of hole samples without and with flowing air during the crystal growth.

3.5.7 Constitutional undercooling in the growth

The crystal growth driving force comes from thermal and constitutional undercooling degree. To investigate the effect of constitutional undercooling on the growth of YBCO crystal, we designed the following experiment: one sample is quenched at 1000°C to check the growth depth in PMP-YBCO sample, another one is kept 30 hrs at 1000°C, then quenched. Both samples were subjected to the same process before 1000°C and their cross sections are shown in figure 3-22.

The growth depth in the first quenched sample at 1000°C is 2.9 mm. The other sample quenched after a 30 hrs dwell has grown to 6.5 mm in depth.

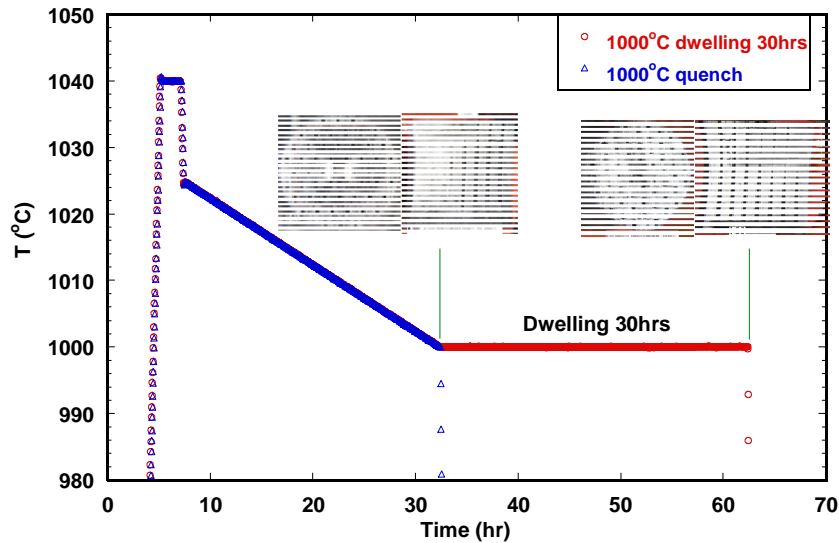


Figure 3-22 The process of the constitutional cooling for dwelling time 30hrs at 1000°C and normal process. The growth depth in constitutional cooling growing is 2 times than it in normal process.

3.5.8 Effect of reduced diffusion path on growth

The function of the holes in the hole sample is to reduced the length of the diffusion path. Since the diffusion time is dependent on the square of this length, such reduction will accelerate the oxygen diffusion. The specific surface area is also largely increased, which means more oxygen will diffuse faster in the bulk. We have shown in fig 3-13 that the thin wall geometry (hole sample) improves the growth rate R_a of YBCO crystal.

In this experiment, we drilled the samples with different number holes to change the ratio of surface area σ' and the length of the diffusion path.

The following samples were prepared: a plain sample (no hole), one hole ($\varnothing 0.6\text{mm}$), 12 holes ($\varnothing 0.6\text{mm}$), 55 holes ($\varnothing 0.6\text{mm}$), 55 holes ($\varnothing 1\text{mm}$). The samples are marked as A, B, C, D, E. The specific surface area is defined the area per gram, as

$$\sigma' = S/\text{mass} \text{ (mm}^2/\text{g)} \quad (3-10)$$

The specific surface area σ' of each samples is listed in table 3-3.

The samples are prepared in the same conditions using the same temperature profile and the in situ susceptibility furnace in its thermogravimetric version. Their morphology is shown in figure 3-23. The growth depth is measured from the growth traces on the sample side surface.

Single domains have clearly grown on the whole surface of the pellets, but the growth depth h is very different from one to another. When the specific surface area is larger and the diffusion length smaller, the growth is going deeper along c-axis. The growth depths are listed in table 3-3. The relationship of growth depth and the specific surface area is shown in figure 3-24. When the specific surface area σ' is larger than $100 \text{ mm}^2/\text{g}$, the growth h in c-axis reaches 15mm which corresponds to the height of the pellet and so the maximum value achievable in this experiment.

The oxygen uptake of each sample is calculated from their thermogravimetric measurement. The oxygen weight increase is larger in hole sample than in plain sample as shown in figure 3-10. It means that a large specific surface area and reduced diffusion path provide an effective tunnel for oxygen diffusion for the 123 crystal growth.

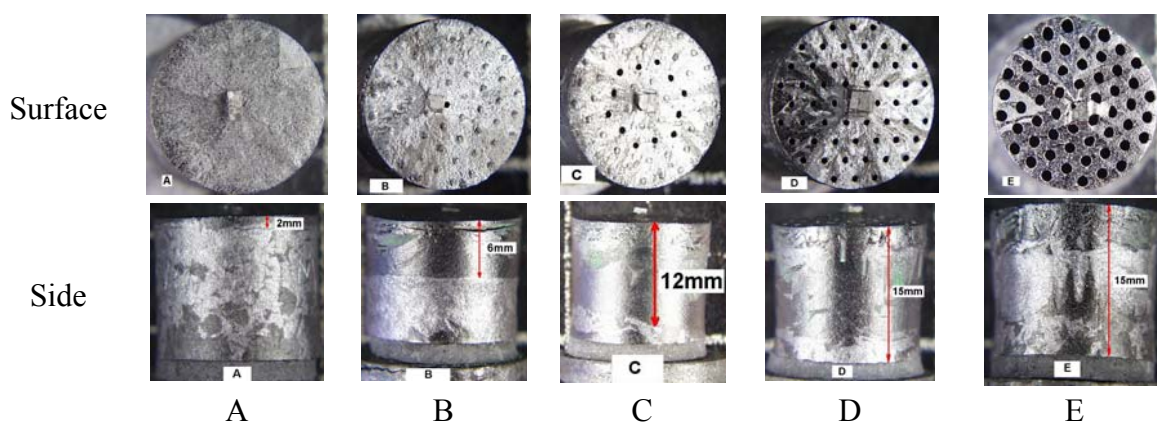


Figure 3-23 Morphology of surface and side of plain and hole PMP-YBCO samples A, B C, D and E with different distribution of holes yielding increasing specific surface area σ and diminishing diffusion path. The growth depth h in the sample is increased with the specific surface area σ increasing and the diffusion path reducing.

Table 3-3. The specific surface area σ and the growth depth h of samples A, B C, D and E.

Sample	Sample geometry	Specific surface area σ (mm^2/g)	Growth Depth h (mm)	Diffusion length (mm) (about half the wall thickness)
A	Plain- no holes	72	2	8 mm
B	$\text{Ø}0.6\text{mm}$ hole- 1	81	6	3.7 mm
C	$\text{Ø}0.6\text{mm}$ hole- 12	96	12	1.55 mm
D	$\text{Ø}0.6\text{mm}$ hole- 55	196	15	0.48 mm
E	$\text{Ø}1\text{mm}$ hole- 55	275	15	0.7 mm

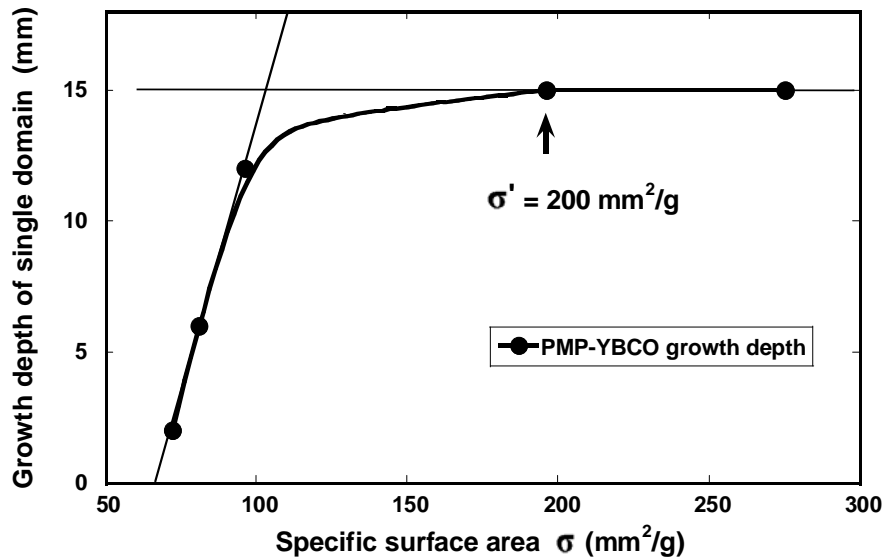


Figure 3-24 Growth depth versus the specific surface area σ of PMP-YBCO single domain. Note that 15 mm is the height of the pellet and so the maximum value achievable.

3.6 Growth mechanism of hole PMP-YBCO single domains

3.6.1 Faceted growth, Surface and nucleation of 123 crystals

We observed by SEM the microstructure on an ab-plane after cleavage as shown in figure 3-25. The plane looks rough at micrometer scale as shown in figure 3-25a. The whiter particles are the 211 secondary phase, the holes seen at the surface are also left by Y211 particles that were ripped from the surface during cleavage. As the magnification is increased (fig 3-25b, c and d), the surface appears as a succession of flat terraces. A few micrometer flat planes are observed clearly in figure 3-25d. It shows that the growth is faceted in PMP-YBCO single domain.

The faceted growth can be identified by the interface entropy of crystal which is related to the Jackson factor α . W. Kurz and D. J. Fisher compiled the growth morphologies and crystallization entropies of materials with interface entropy up to 100 as described in table 3-4 [3.6]. If the entropy or the Jackson factor α is above 5, the crystal growth in solution, vapour-solid and liquid-solid system is faceted. With a Jackson factor α above 5, Y123 crystals show faceted surface as expected.

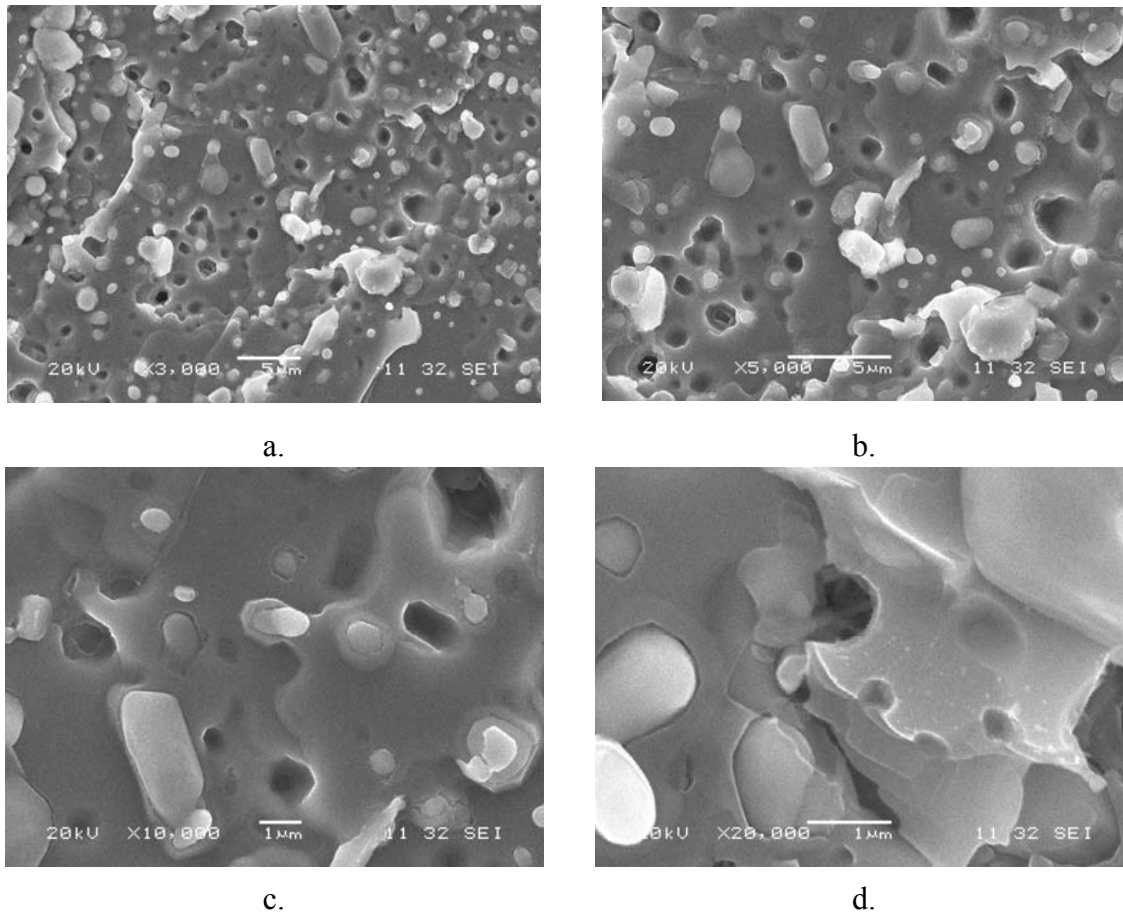


Figure 3-25 The faceted growth on ab plane in PMP-YBCO sample. From rough at low magnification, the ab plane surface becomes flat and smooth when the scale is down to the atomic size.

Table 3-4 Growth morphologies and crystallization entropies.

Dimensionless entropy ($\Delta S_f/R$)	Supersaturated substance	Phase	Morphology
~ 1	Metals	Melt	Non-faceted
~ 1	“Plastic” crystals	Melt	Non-faceted
2-3	Semiconductors	Solution	Non-faceted/faceted
2-3	Semimetals	Solution	Non-faceted/faceted
~ 6	Molecular crystals	Solution	Faceted
~ 10	Metals	Vapor	Faceted
~ 20	Complex molecules	Melt	Faceted
~ 100	Polymers	Melt	Faceted

As $\alpha > 5$, the 123 crystal surfaces are smooth and the nucleation is observed to result from a screw nucleation as discussed in section 3.1.

3.6.2 Yttrium diffusion

In 1996, Y Shiohara summarized the 123 growth characteristics from melt-solid system and considered the interface kinetic [3.6]. Based on the BCF theory, he analyzed the 123 crystal growth mechanism on the interface kinetic and solute diffusion. The crystal growth rate

R is in a parabolic law or liner relationship with the supersaturation σ or undercooling ΔT . The relationship between the growth rate R on ab plane and the yttrium supersaturation σ was investigated by Kanamori and Y. Shiohara using the SRL-CP method (a directional solidification technique). Their experimental result is in accordance with the law $R \propto \sigma^2$ when the yttrium supersaturation is sufficient small, $\sigma < \sigma_1$ [3.7]. Furthermore, A. Endo's research works have established that the Y123 growth rate is proportional to the undercooling degree ΔT or to its square when the undercooling degree is less than 20K ($\Delta T < 20K$) in the constant undercooling solidification method [3.8]. These two results show that the Y123 growth rate is related with the undercooling ΔT and supersaturation σ and are consistent with the BCF theory. The driving force of 123 crystal growth is due to the undercooling and supersaturation based on the screw nucleation.

As far as the Y123 growth dynamic is concerned, Izumi, Cima and Mori presented in 1992 the Yttrium diffusion growth model respectively [3.9, 3.10, 3.11]. They assumed the Y123 growth is controlled by the yttrium diffusion in liquid and the growth proceeds in an isothermal environment.

For a classical peritectic reaction, the growth would stop quickly since, once the 123 nucleation has happened, the 211 particles are wrapped by 123 phase formed by the peritectic reaction, and the yttrium would have to diffuse across an increasing layer of solid 123 phase for the reaction to pursue.

The results obtained with directional growth technique lead the authors to the conclusion that the necessary solute for the peritectic reaction is provided from 211 particles to the 123 growth front through a liquid. Based on this idea, they develop a model where the 211 particles dissolves ahead of the growth front to enrich the liquid in yttrium and where this dissolved yttrium is transported by diffusion through the liquid to the growing Y123 front. In such a model, the 123 crystal growth is necessarily controlled by the yttrium diffusion.

But in our experiment it is found that the growth rate R_c increasing when the undercooling $\Delta T > 15^\circ C$ and decreasing when $\Delta T > 20^\circ C$ in hole PMP-YBCO single domain. This relationship seems to be in conflict with the growth law in BCF theory. We also found that the oxygen diffusion which is not taken into account in the directional solidification is an important parameter.

3.6.3 Oxygen diffusion

By comparing 123 crystal growth in plain and hole samples, we have shown that the oxygen diffusion is also a controlling parameter of the 123 crystal growth. The c-axis growth

rate R_c was found to be more or less proportional to the oxygen diffusion velocity $R_c \propto V_{O_2}$. This fact reveals that in the vapor-solid system, the growth rate is related to the supersaturation σ as $R \propto \sigma$ or $R \propto \sigma^2$. Thus it is assumed that the c-axis growth rate R_c is proportional to the oxygen supersaturation σ as

$$R_c \propto \sigma \rightarrow R_c \propto V_{O_2} \quad (3-11)$$

Considering the oxygen mass transport in the 123 growth, an oxygen interfacial diffusion model is suggested to explain the oxygen transport in hole PMP-YBCO single domain growth. We regard the oxygen atom has three positions in the hole PMP-YBCO as shown in figure 3-28. The position 1 is in atmosphere (air), the position 2 is in the solution zone of sample and the position 3 is at 123 crystal growth interface. When Y123 is growing, the oxygen atom transport is probably along two paths: the oxygen atom travels from the air across the solution zone to arrive at the interface as $1 \rightarrow 2 \rightarrow 3$; or the oxygen atom travels along the interface to reach directly the growth front as $1 \rightarrow 3$.

If oxygen atom diffuses along the $1 \rightarrow 2 \rightarrow 3$ path, the oxygen atom should cross the melted zone. Thus the melted zone becomes a barrier of oxygen diffusion, which decreases the oxygen diffusion speed. Otherwise, if oxygen atom diffuses directly from air along the $1 \rightarrow 3$ path, it becomes easier to get to the interface for the 123 growth. Benefiting from the hole-shape, when the 123 crystal grows larger than 2 mm (the width between the holes), the 123 interface side will be exposed in air, the oxygen atom can diffuse to the interface directly. In this case the oxygen atom transport becomes an interfacial diffusion.

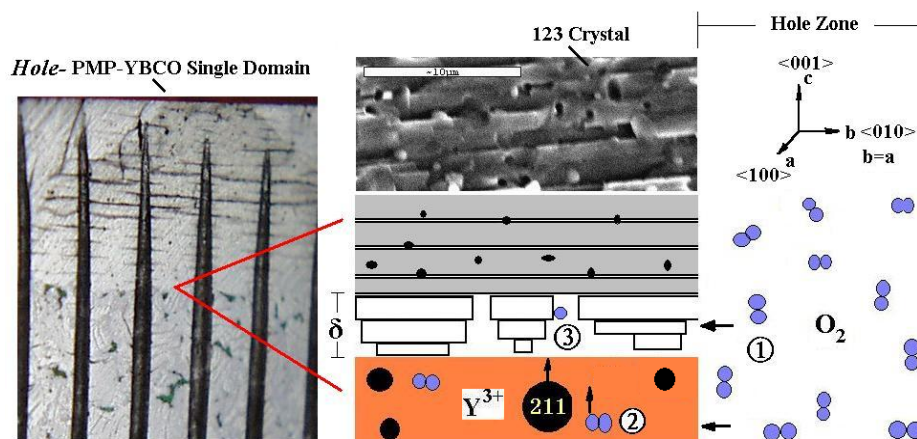


Figure 3-28. Sketch of oxygen diffusion paths in hole PMP-YBCO single domain growth.

3.6.4 Solution diffusion and growth system

Generally, the crystal growth depends on the thermodynamic driving force from the decreased free energies G of the system. In the vapour and the solution system, the driving

force of the crystal growth comes from the supersaturation σ . In the melt system, the driving force comes from the undercooling ΔT . In the view of atoms transport, the driving force is limited by the atom attachment on the interface and the latent heat transport [3.2, 3.7]. The Y123 single domain is grown from a semisolid environment. The Y123 crystal growth rate is much smaller than the heat flow velocity. It is assumed in an isothermal environment that the growth rate is mostly limited by the atom attachment rate. It is analyzed that the atom transport arriving at the interface includes the solute diffusion and interface diffusion process [3.12]. Furthermore, considering the diffusion mechanism implied by the Y123 crystal growth as discussed by Y. Nakamura and Y. Shiohara, the Y123 crystal growth is limited by the two-steps diffusion: the interface diffusion with the atom attachment to the interface and the solute diffusion from the environmental phase. As shown in figure 3-29, C_0 is the initial solution concentration, C_e is the equilibrium concentration in 123 crystal and C_i is the interfacial liquid concentration. The diffusion route is decided by the solution diffusion or interfacial diffusion depending on the relationship of C_i and C_0 .

If $C_i=C_0$, the growth rate is controlled by an interfacial diffusion.

If $C_i=C_e$, the growth rate is controlled by a solution diffusion.

If $C_e < C_i < C_0$, the growth rate is decided by the mixed control.

In fact, there are four elements diffusing, ie, Y, Ba, Cu and O in the 123 crystal growth. Since the yttrium solubility in Ba-Cu-O liquid is so small, only 0.006%mol [3.6], it limits the 123 growth rate to a low 10-5 mm/s. The 123 growth is controlled by the yttrium diffusion in liquid. Our experimental results indicate that oxygen diffusion is also dominating the growth rate of 123 crystal growth.

Therefore, the 123 growth depends on two types of diffusion: 1) the yttrium, barium and copper ions diffuse in melt liquid towards the Y123 growth interface from the solution diffusion and interfacial diffusion as in melt-solid system, as shown along with the line b in figure 3-29. 2) The oxygen diffusion depends on interfacial diffusion from air as in vapour-solid system, along with the line a in figure 3-29.

If the oxygen atom diffuses from the air and the yttrium diffusion from the melt, the 123 growth would be considered in two surrounding systems: 1) Vapour-solid system: as oxygen atom transports directly from air to interface. 2) Melt-solid system: as yttrium diffusion from liquid to interface, as well as the barium and copper ion diffusion.

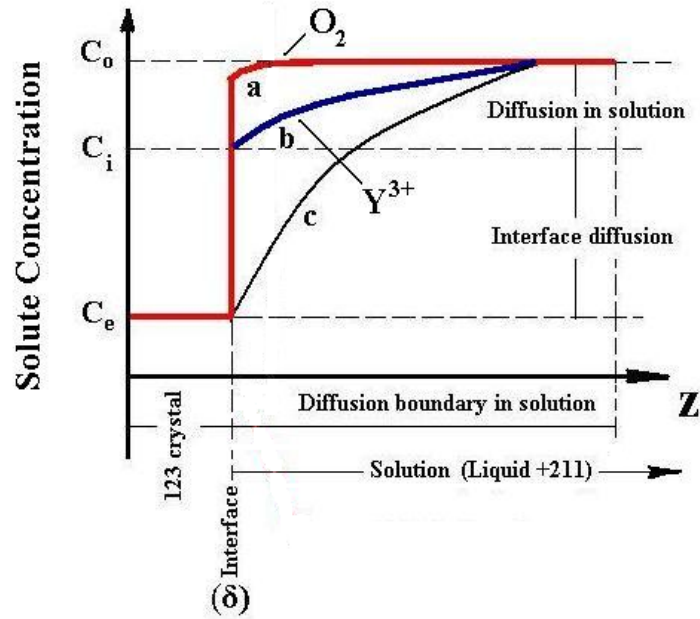


Figure 3-29 Illustration of the oxygen interfacial diffusion and the yttrium diffusion in solution.

3.7 Summary

1) We found that PMP-YBCO single domain fabrication starts with screw nucleation on (001) plane. The critical size of nuclei is $3\mu\text{m}$. Comparing the nucleating temperature with Sm123 Seed and without seed, we found a temperature window of 1011°C - 1006°C in which parasitic random nucleation should be prevented. The practical nucleation temperature is found at 1000°C , the single domain growth is found in 1000°C - 980°C by in situ high temperature video monitoring. We have successfully made a batch of 9 PMP-YBCO single domains with a 30 mm diameter using the information above.

2) In the dynamic studying of hole PMP-YBCO single domain growth, it is found the growth rate R_a and R_c are increasing with the undercooling degree at first, after the undercooling degree reached critical values of 18°C for R_a in the video experiment, of 10°C for R_a in quench experiment and of 20°C for R_c in quench experiment, the growth rate decreases. The growth rate R_a is about 0.1-0.7mm/h. By comparing plain and hole samples, we found that the oxygen diffusion is affecting the growth law. It is found the growth rate R_c is directly proportional to the oxygen diffusion velocity V_{O_2} . The oxygen diffusion dominates the growth of PMP-YBCO single-domain.

3) The 123 crystal growth of the hole PMP-YBCO in air depends on two growth systems: the melt-solid system and the vapour-solid system. In the melt-solid growth system, the growth rate is proportionnal to the square of the undercooling ΔT , as $R \propto \Delta T^2$. In the vapour-solid system, the growth rate is related to the oxygen mass transport velocity $R_c \propto V_{O_2}$.

There is two types of diffusions in the 123 crystal growth: 1) the yttrium, barium and copper ion diffuse in melt liquid transport towards the 123 growth interface from the solution diffusion and interfacial diffusion as in melt-solid system. 2) The oxygen diffusion depends on interfacial diffusion from air as in vapor-solid system. The oxygen interfacial diffusion in the hole PMP-YBCO becomes a dominating parameter in the 123 growth.

4) A large specific surface area with artificial holes provides an effective tunnel for oxygen diffusion in the 123 crystal growth by reducing the diffusion length. The full growth of a single domain on a $\Phi 20\text{mm} \times 18\text{mm}$ sample requires a specific area above $100 \text{ mm}^2/\text{g}$, or a diffusion length less than 0.5 mm.

5) The growth of 123 crystals is not only depending on the temperature undercooling but also the constitutional undercooling. The crystal growth driving force comes from the thermal undercooling ΔT_T and the constitutional undercooling ΔT_c , $\Delta T = \Delta T_T + \Delta T_c$.

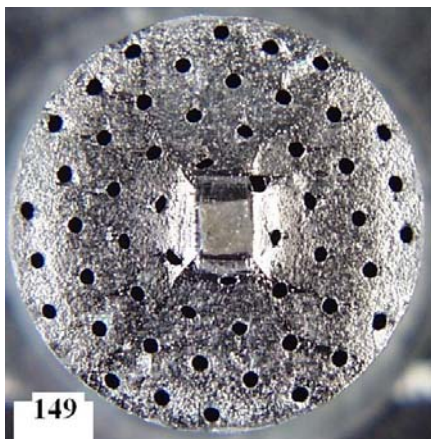
References

- [3.1] Kenneth A. Jackson, «Kinetic Processes- Crystal growth, Diffusion, and Phase Transitions in Materials», WILEY- VCH Verlag GmbH & Co. KGaA. 2004.
- [3.2] C.Klemenz, Physica C 265 1996 126.
- [3.3] B N SUN, Physica C, 157, (1989)181.
- [3.4] T B Lindemer, F A Washburn, C S MacDougall: Physica C, 196 (1992) p390.
- [3.5] Xavier Chaud, D.Isfort, E. Beaugnon, R. Tournier, 2000, Physica C 341-348 2413-2416.
- [3.6] Y.Shiohara, A.Endo, 1997 Materials Science and Engineering, R19 1-86.
- [3.7] Y Kanamori and Y Shiohara, 1996 J. Mater. Res., 11 2693.
- [3.8] A Endo, H S Chauhan, Y Nakamura, Y Shiohara, 1996 J Mater Res 11 1114.
- [3.9] T Izumi, Y Nakamura and Y Shiohara, 1993 J. Cryst. Growth, 128 757-761.
- [3.10] M J Cima, 1992 J.Appl.Phys., 72 179.
- [3.11] N Mori, 1992 J Jpn.Inst.Mat, 6 648.
- [3.12] Y Nakamura, Y Shiohara, J Mater. Res., 11, 1996, 2450.

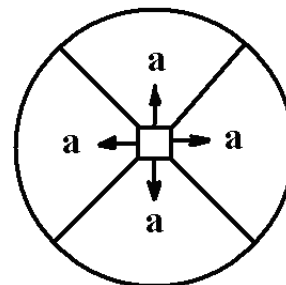
Chapter 4 Microstructure and properties of PMP-YBCO single domain

4.1 Microstructure of PMP-YBCO single domain

The microstructure of hole PMP-YBCO single domains has similar character as plain single domains. Figure 4-1a shows the surface morphology of square crystal domain grown from a Sm123 seed. The ab-plane of Y123 crystal is parallel to surface. The [110] sub-grain boundary of a/a grain section separates single domain into four sections, the growth sketch is shown in figure 4-1b. The 123 growth along a- direction near the Sm123 seed is observed as shown in figure 4-2. We observed steps which reflect the (100) and (010) borders of grown ab-planes. These steps come from the fact that the ab-planes are growing on top of each other by a screw nucleation mechanism as discussed in previous chapter 3.6. The 123 growth front clearly keeps the textured direction throughout the hole shape, as shown in figure 4-2b, c, d. The artificial holes have no influence on the 123 growth texture. In chapter 3, the hole shape has been shown to improve the oxygen diffusion and the 123 growth rate.



a. Surface morphology



b. Sketch of surface growth

Figure 4-1 Morphology on surface and sketch of the growth of the hole PMP-YBCO sample. Four sub-grain boundary are created by the a/a direction growth.

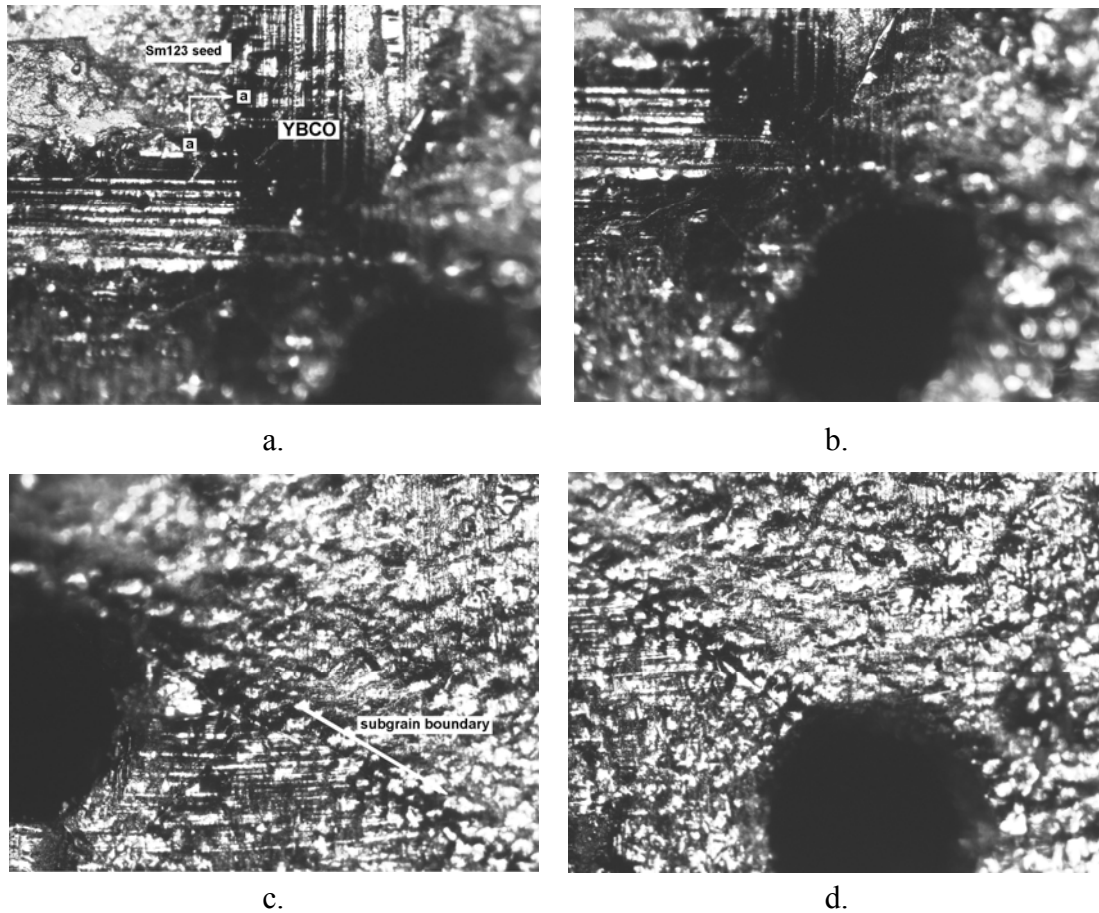


Figure 4-2 The growth morphology on the rough surface of a hole PMP-YBCO single domain viewed by optical microscopy. The sub-grain boundary of a/b- growth section is along [110] direction. The textured structure is not influenced by the hole shape.

We cut the sample along c-axis and polish it down to 1 μm . Their morphology is observed with an optical microscope under polarized light as shown in figure 4-3. It is observed that there is two inclined lines below the Sm123 seed appeared in figure 4-4. These lines are revealing the boundary of a pyramidal region below the seed depleted in Y211 particles. Further horizontal cuts at different depths show that this region is a square below the seed larger as the cut is deeper. We compare the amount of 211 particles at different places of the section. Six places are referred as to a,b,c,d,e,f as shown in figure 4-5. is the density of Y211 particles is much larger in part b than in any other parts. A dividing line separates the dense and the sparse distribution of Y211 particles. When the Y123 crystal grows in the ab-plane along the (100) and (010) direction, the growth interface encounters Y211 particles. The large 211 particles are pushed away ahead of the interface, the small ones are trapped within the Y123 crystal. This special character related to the Y211 distribution in a Y123 single domain is called the pushing-trapping effect [4.1].

The 211 particles distribution in the six parts of the section represented in figure 4-3 is observed by polarized optical microscopy as shown in figure 4-5. The Y211 particles are spherical or rod-like and their mean size is below $0.5\mu\text{m}$ as analyzed with Visilog 6.0 software.

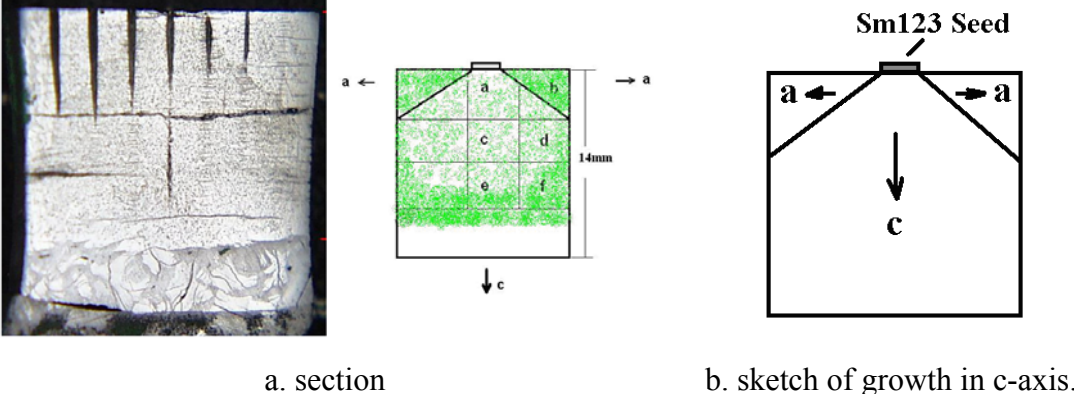


Figure 4-3 Section morphology and sketch of the single domain growth with seed. A pyramidal region depleted in Y211 particles is formed below the seed by the 211 pushing-trapping effect.

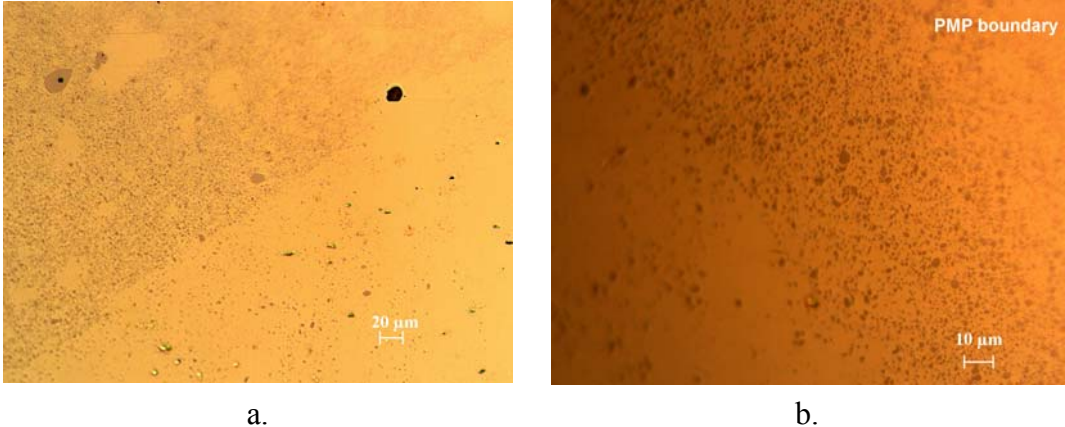
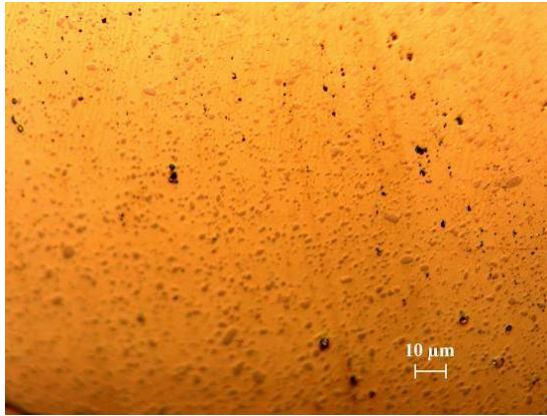
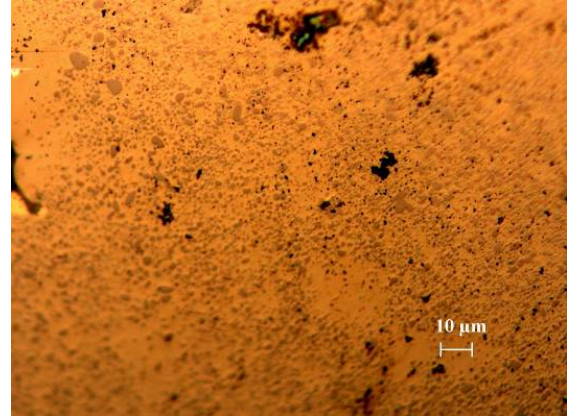


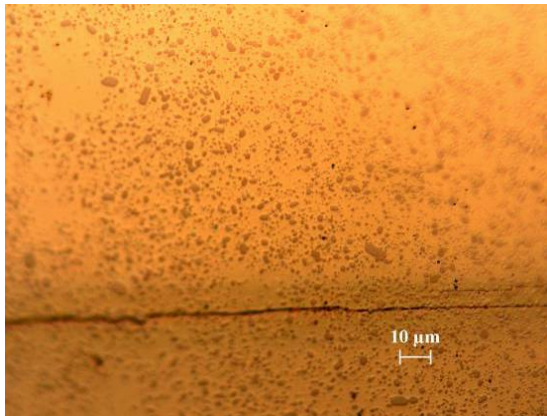
Figure 4-4 Green phase Y211 particles distribution due to pushing-trapping effect on the vertical section of a PMP –YBCO single domain.



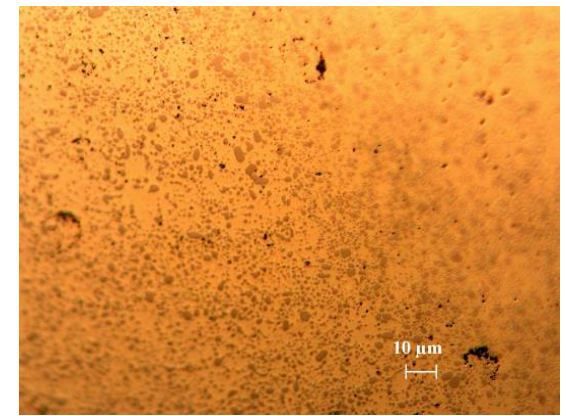
Part a



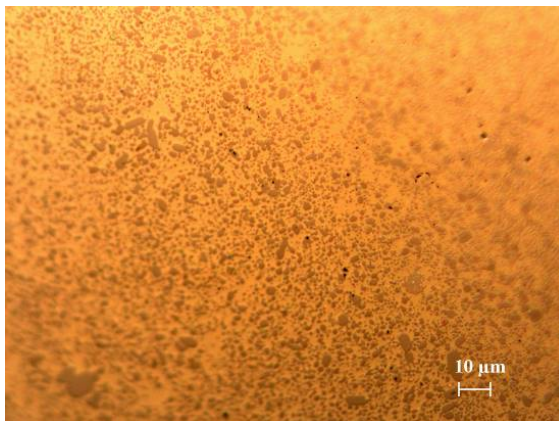
Part b



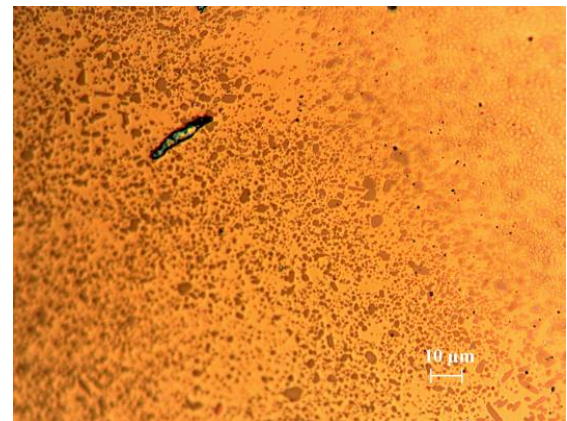
Part c



Part d



Part e



Part f

Figure 4-5 Morphology of PMP-YBCO sample with heating rate of 60°C/h.

The morphology near artificial hole is shown in figure 4-6, the ab-plane is parallel to the surface and so perpendicular to the pictured section. The c-axis is parallel to the axis of hole. The parallel black lines visible on the picture correspond to cracks propagating in the ab-plane which are formed mainly during T-O phase transition. When the 123 crystal is annealed in an oxygen atmosphere, new oxygen atoms enter into the crystal lattice inducing

the T-O phase transition (tetragonal to orthorhombic). This means the **a** axis elongates, the **c** axis and **b** axis shorten, which produce stresses inside the sample. The width between the cracks is around 300 μm .

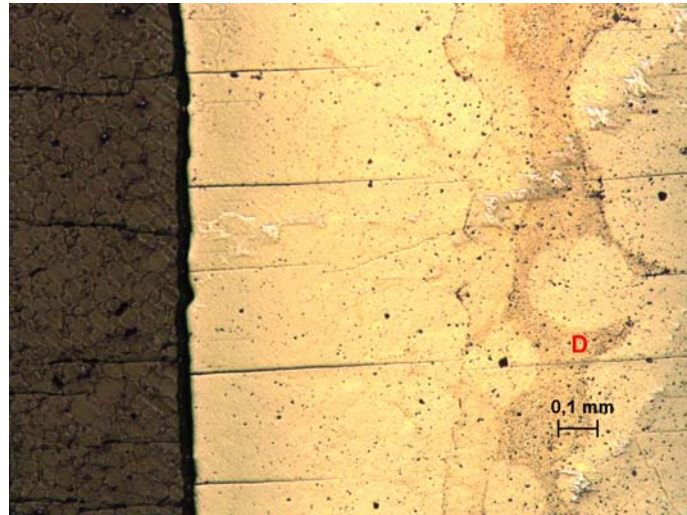
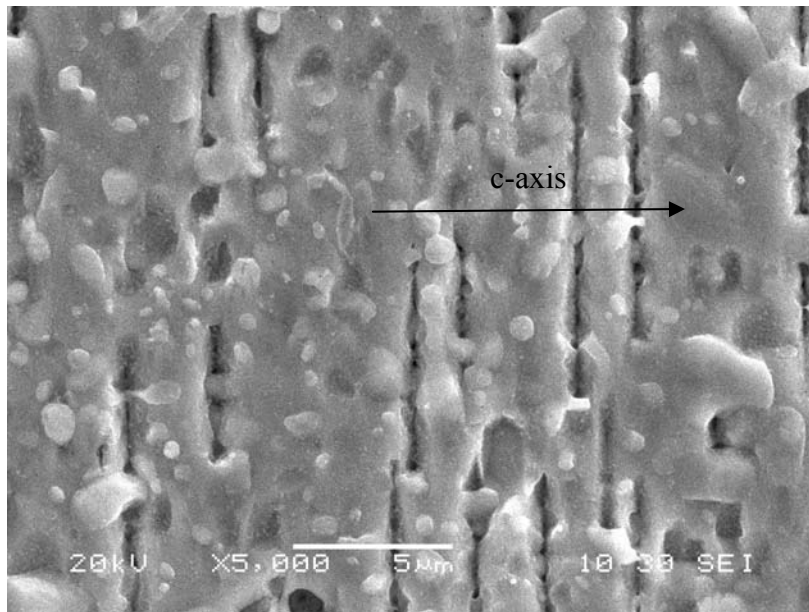
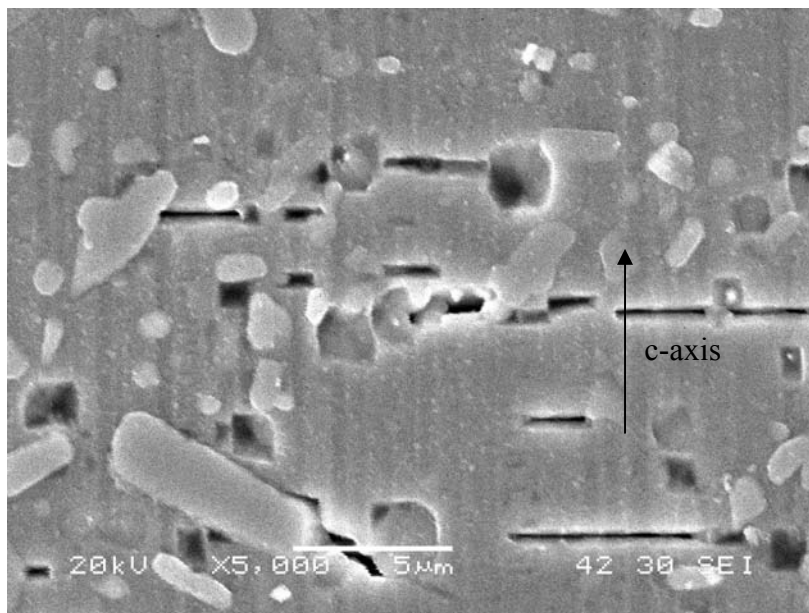


Figure 4-6 Morphology of PMP-YBCO sample near the hole. It shows the a/b cracks parallel to ab-planes due to T-O transition.

To go further, we used the scanning electron microscopy (SEM) to investigate the microstructure and the 211 particles distribution along c-axis as shown in figure 4-7a. It shows 123 crystal layers with a 2-5 μm width. Fine spherical 211 particles are homogeneously distributed in the 123 matrix with a mean size of about 300 nm. The round shape indicates the 211 particles are consumed and have not grown larger. If the 211 particles are coarsening, they will appear as rod-like shape as shown in MTG-YBCO sample (figure 4-7b). Comparing the 211 particles in PMP-YBCO and in MTG-YBCO sample, the size of the 211 particles of PMP-YBCO are much finer. This is because the PMP process uses 211, BaCuO₂, and CuO as precursors and forms the 123 phase directly by the peritectic reaction as $211+L \rightarrow 123$. The 211 particles are consumed and refined in the 123 grain growth. Therefore, the typical microstructure of fine 211 particles of about 300 nm and well connected thin 123 layer is achieved in PMP-YBCO sample.



a. PMP-YBCO



b. MTG-YBCO

Figure 4-7 Microstructure of PMP-YBCO (a) and MTG-YBCO (b) samples by SEM. (a) It shows the 123 crystal layer, ab-microcracks, a fine distribution of spherical and ellipsoidal Y211 particles with a mean size about $0.3\mu\text{m}$. (b) The 211 particles distributed in MTG-YBCO has a rod-like shape and a larger size around $1\text{-}5\mu\text{m}$.

The microstructure of ab plane of hole PMP-YBCO samples is observed by SEM and is shown in figure 4-8. It shows the faceted growth on ab plane. As discussed in chapter 3, the 123 crystal has a typical faceted growth character.

We can also observed in figure 4-8 the porosity distribution of a PMP-YBCO sample. In chapter 3 we discuss the weight loss phenomenon. The oxygen is released from sample as a consequence of the BaCuO_2 and CuO decomposition at high temperature. The pore is formed

by the remnant oxygen trapped within the sample. As shown in figure 4-8a,b, the mean porosity diameter is about $5\mu\text{m}$ in the hole sample. We calculate the porosity distribution density of the sample from the remnant oxygen in the sample from the thermogravimetry measurement and porosity observation. The porosity distribution is $\sim 8/(10\mu\text{m}^2)$ in hole sample. This is consistent with the experimental observation. It is proved that the porosity breaks the Y123 crystal connection as crack triggering site and prevents the current flowing so that makes the transport critical current decreased. Therefore the high quality YBCO single domain requires less porosity. Because of its large specific surface area, any gas released escapes more easily in a hole sample. In particular a hole sample releases more oxygen out, which results in a decrease of the pores number and diameter. The hole sample has drastically less pores than a plain sample (a picture for comparison is missing). More detailed analysis is referred in [Annex 5](#).

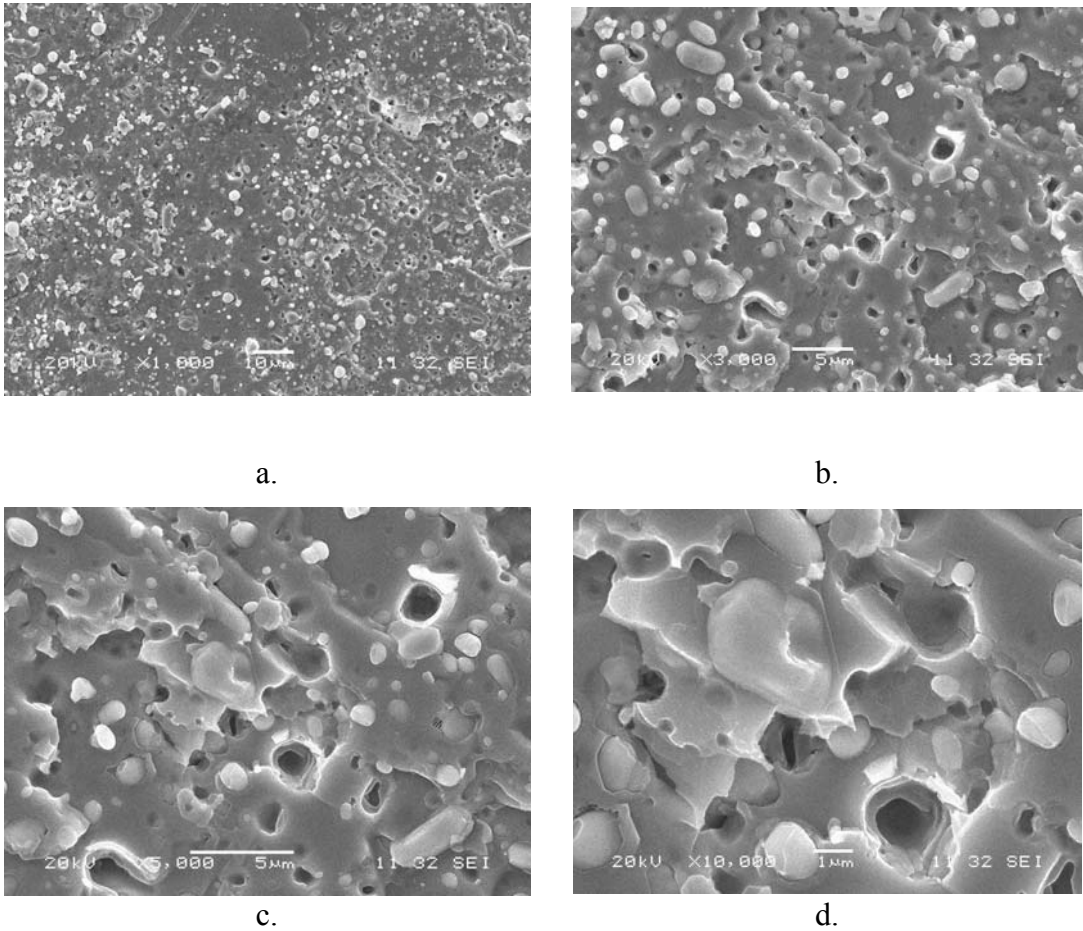


Figure 4-8 Microstructure on ab- plane of a hole PMP-YBCO single domain observed by SEM.

4.2 High pressure oxygen treatment and low pressure flowing oxygen treatment

An oxygen treatment is a necessary step to insure the tetragonal-to-orthorhombic (T-O) phase transition in YBCO crystal that will provide the superconducting phase. Generally, the YBCO sample is treated in flowing oxygen treatment at 300°C-500°C as a “classical oxygen treatment”. The dwelling time lasts about 100hr-300hr for a bulk sample. We will refer to this treatment as low pressure oxygen treatment (LO₂), as shown in figure 4-9. Recently, a high pressure oxygen treatment has been developed for reducing cracks and promoting an homogeneous oxygenation. What is even more essential on a point of view of applications, is that the treatment induce a faster oxygen diffusion, so that the time required for oxygenation is effectively shortened. This high pressure oxygen treatment is depicted in figure 4-10. Oxygen pressure is increased up to 16MPa at 750°C and dwelling 32 hours, the process is marked as HO₂. We treated some hole samples in the LO₂ and some in the HO₂ treatment. The superconducting transition temperature T_c and the trapped magnetic field B_{tr} were measured to compare the effect of the two treatments.

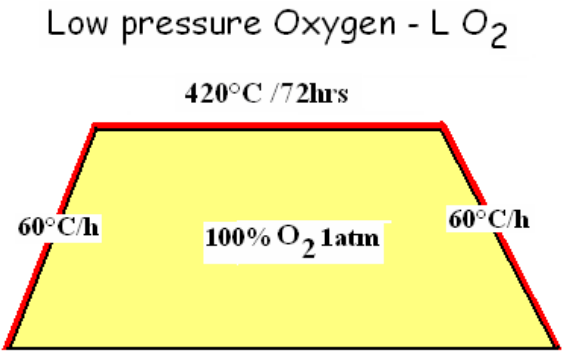


Figure 4-9 Flowing oxygen treatment.

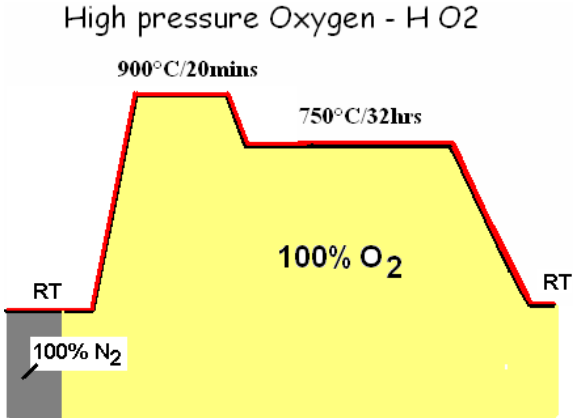


Figure 4-10 High pressure oxygen treatment

4.3 T_c and oxygen content

The superconducting critical transition temperature T_c in LO_2 treatment is measured by resistance measurement as shown in figure 4-11. The T_c in HO_2 treatment is measured by the susceptibility measurement (Tristan's chi prime or BS2). The system error of susceptibility measurement is eliminated by averaging the data from the range of increasing and the decreasing temperature. In both case the samples are cooled the same way in nitrogen vapour. This explains the difference between the cooling and heating stage.

The result is shown in figure 4-12. The critical transition temperatures T_c of the samples treated in HO_2 and LO_2 are respectively:

$$T_c=94.5K (HO_2), T_c = 91.5K (LO_2) \quad (4-1)$$

The critical transition temperature T_c in HO_2 is higher 3K than it in LO_2 . This result is consistent with the common view that the HO_2 treatment gives a more homogeneous and higher oxygen content. On the other hand we tested the oxygen content $7-\delta$ of the sample treated in the HO_2 and LO_2 to compare the effect of the oxygen treatment on the superconductivity.

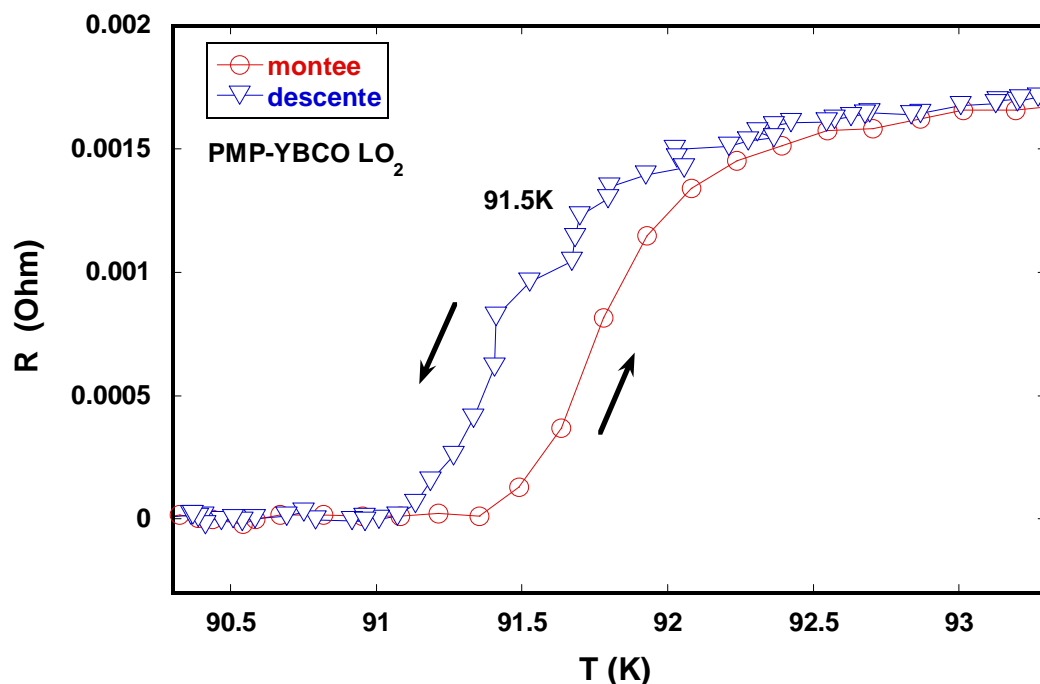


Figure 4-11 The superconducting critical transition temperature T_c in LO_2 treatment measured by resistance measurement.

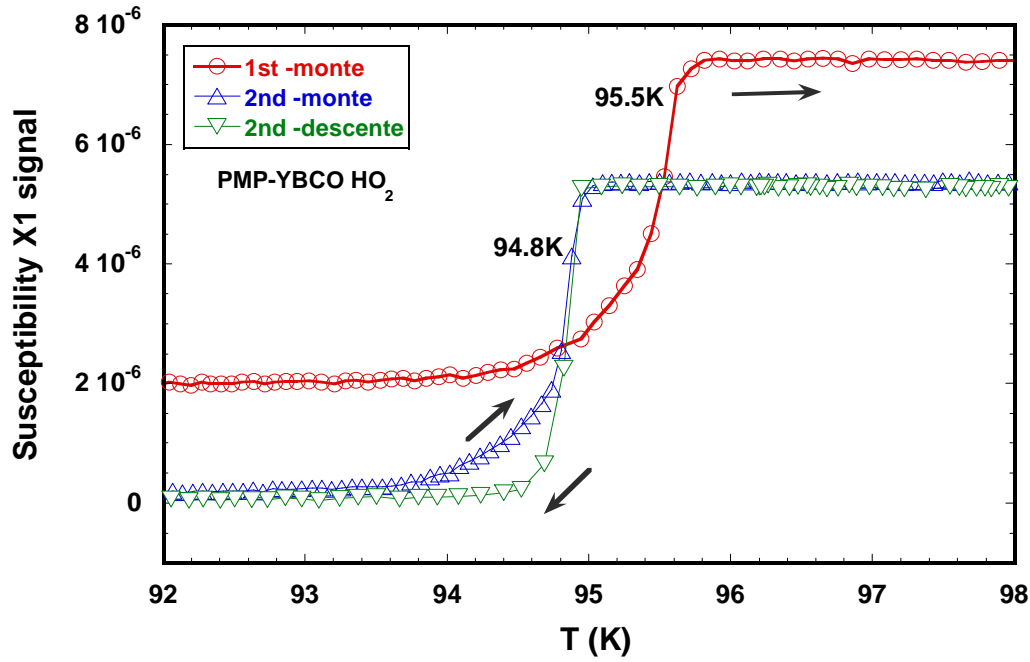


Figure 4-12 The superconducting critical transition temperature T_c in HO_2 treatment measured by the susceptibility method. The critical transition temperature T_c is up to 94-95K.

The oxygen content $7-\delta$ of the YBCO sample is calculated by the crystal lattice c as described in equation (4-3)[4.2]. The lattice constant c is estimated from the (006) peak of X-ray diffraction in YBCO sample. The c parameter can be obtained by the Bragg function in equation (4-4).

$$7-\delta = 74.49 - 5.787c \quad (4-3)$$

$$2d\sin\theta = \lambda \quad (4-4)$$

Here $7-\delta$ is the oxygen content in $\text{YBa}_2\text{Cu}_3\text{O}_{7-\delta}$, c is the c -axis cell parameter in \AA , d is the six times of c -axis cell parameter as $d=6c$, θ is the diffraction of angle, λ is the wave length of copper $\text{Cu } \kappa \alpha_1$, 1.451 \AA . The X-ray diffraction of PMP-YBCO sample in H O_2 and L O_2 treatment is tested as shown in figure 4-13. Both of the oxygen content is calculated as:

$$7-\delta = 6.796 \text{ (HO}_2\text{)} , 7-\delta = 6.737 \text{ (LO}_2\text{)} \quad (4-5)$$

The result shows the oxygen content $7-\delta$ in HO_2 treatment is more 0.059 than it treated in LO_2 treatment. Since the superconductivity is related to the oxygen constant, when the oxygen content is near $7-\delta=6.8\sim 6.9$, the superconducting transition temperature T_c is achieved to higher as 93~94K. Thus the high pressure oxygen treatment HO_2 increases the oxygen content and improves the superconducting transition temperature T_c .

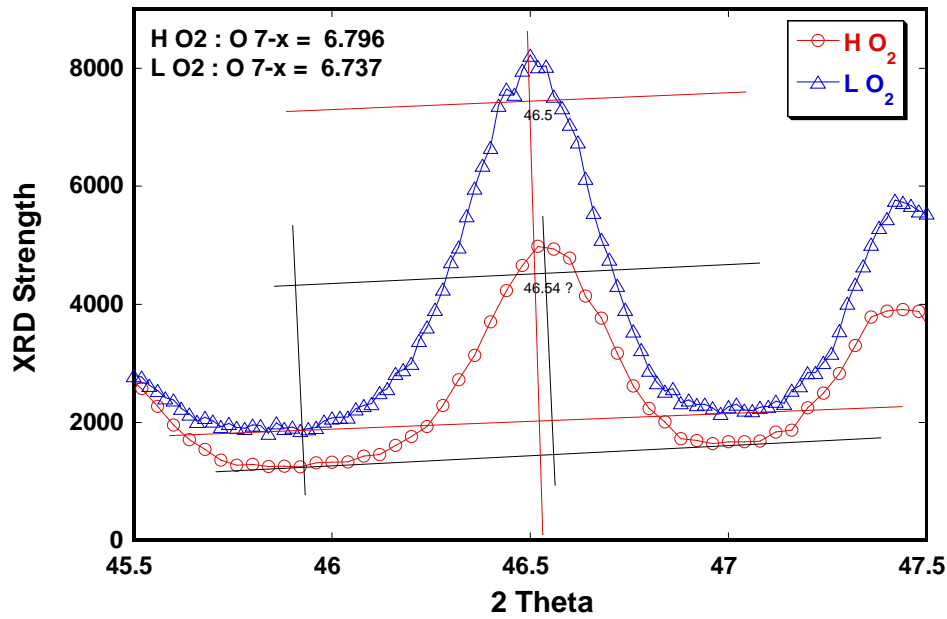
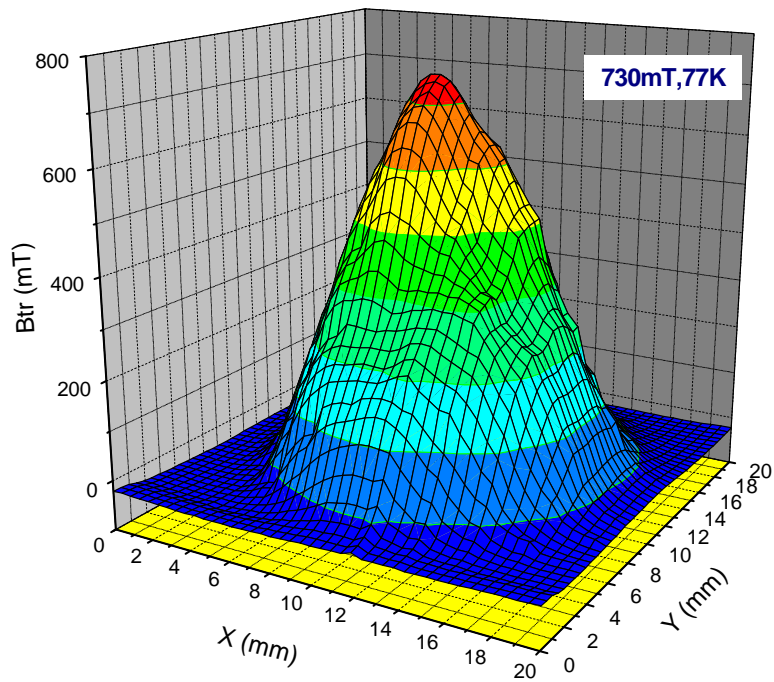


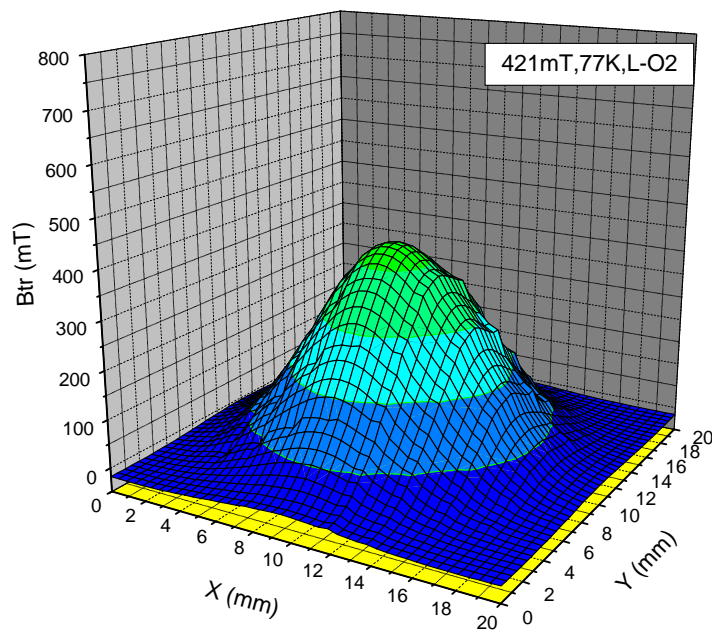
Figure 4-13 X-ray diffraction (006) peak of PMP-YBCO sample in H O₂ and L O₂ treatment.

4.4 Comparison of trapped magnetic field B_{tr} of PMP-YBCO treated in HO₂ and LO₂

The samples have been magnetised in a static magnetic field of 2T for 30 mn at 77K in field cooling process (FC). After waiting for 20 mn after removing the applied field to make sure the magnetization is stable, a Hall probe is used to scan the trapped magnetic field B_{tr} at a position 0.2mm above the sample surface. The measured trapped magnetic field B_{tr} distribution is shown in figure 4-14. For both samples, the distribution looks like a nice conical shape. This at least indicates that the current loop is flowing around all the sample and confirms their single domain character. The maximum B_{tr} of the single domain PMP-YBCO treated in HO₂ is 739mT, the one of the sample treated in LO₂ is much lower, 420mT. It indicates the high pressure oxygen treatment improves the magnetic trapped field B_{tr} .



a. B_{tr} (HO_2)



b. B_{tr} (LO_2)

Figure 4-14. Trapped magnetic field B_{tr} of hole PMP-YBCO in HO_2 and LO_2 treatment.

Since the sample has a different size, in order to compare their trapped magnetic field B_{tr} , a factor β is defined by normalizing the trapped magnetic field B_{tr} with the diameter,

which is suggested by Dr. Xavier. It is similar to the critical current density J_c according to the same unit $A\ cm^{-2}$, as

$$\beta = \mathbf{B}_{tr}/\mathbf{d} \quad \sim \mathbf{J}_c \quad (4-5)$$

B_{tr} is the trapped magnetic field, \mathbf{d} is the diameter of the sample. This factor β is proportional to the critical current density J_c of YBCO bulk.

We compare the best properties of B_{tr} at present, by referring to the best records of MPMG-YBCO single domain prepared in ISTECH (Japan), CNRS/CRETA (France) and our sample from NIN/Xi'an (China). The normalized factor β of the three samples is listed in table 4-2. The best record of trapped magnetic field is 1.6T of MPMG-YBCO prepared in ISTECH. Its normalized factor β is 48.5, the hole MTG-YBCO sample is 52.5 and the hole PMP-YBCO is 49.2. This result shows the PMP-YBCO have the same critical current level with the MPMG-YBCO sample. The same result is also confirmed by the critical current density measurement. So a higher trapped magnetic field B_{tr} above 1.6T could be expected in the hole PMP-YBCO single domain of similar diameter.

Table 4-2 The trapped field \mathbf{B}_{tr} and the normalized factor β of MPMG-, MTG-, PMP-YBCO single domain.

Research institute and author	Sample shape, process	\mathbf{B}_{tr}	\mathbf{d}	$\beta = \mathbf{B}_{tr}/\mathbf{d}$
Japan ISTECH, S Nariki	Plain, MPMG	1600mT	33mm	48.5
CNRS/CRETA, Xavier	Hole, MTG	840mT	16mm	52.5
NIN/SMRC, Cuiping	Hole, PMP	730mT	15mm	49.2

4.5 Trapped magnetic field B_{tr} and levitation force F of PMP-YBCO single domain

At 77K we measure the levitation force of $\Phi 30\text{mm}$ PMP-YBCO single domain. It is measured in zero field cooling process by approaching a 0.5T NdFeB magnet. Two samples with higher levitation force are selected to measure the trapped magnetic field B_{tr} later. We observe the morphology of the two samples under the microscopy at first. After polishing the samples PMP-YBCO1 and PMP-YBCO2 are found to have two crystal domains on surface as shown in figures 4-15a and b. The ab plane in the small domain is vertical to the ab plane in the larger domain. The textured direction in two domains is different. The domain boundary is formed between them resulting in breaking the current.

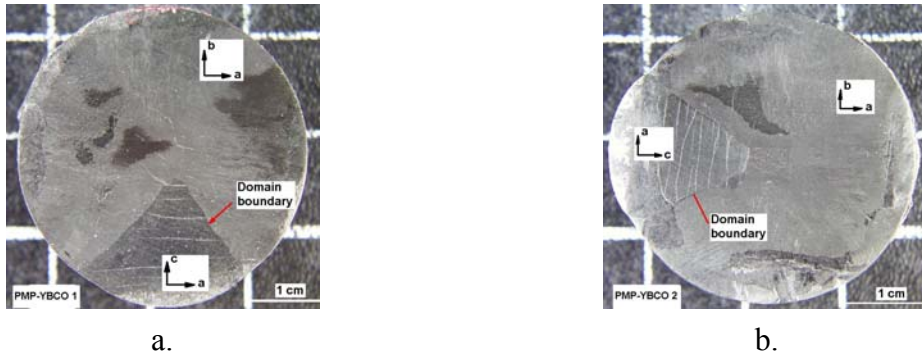


Figure 4-15 Polished surface of the bulk single domains PMP-YBCO1 and PMP-YBCO2 prepared in one batch.

At 77K, the magnetic levitation force of sample PMP-YBCO and PMP-YBCO2 are measured by the “Levitation force measurement standard”. The result is shown in figure 4-16. When the sample moves to the NdFeB magnet by the speed of 0.1mm/s, the levitation force is increased to 43N at the 2 mm position above magnet. The levitation force density is 6 N/cm² (77K, 0.5T). When the distance between the sample and the magnet is increased again, the levitation force is decreased. An attractive force appeared when the sample is near 10 mm far from the magnet. Both the repulsive and the attractive force between the sample and the magnet participate to the stable levitation between the superconductor and the magnet.

The levitation force density f is proportional to the critical current density J_c and the loop radius r of single domain, as $f \propto J_c \cdot r \cdot z \cdot dH/dz$. Here z is the height of single domain and the dH/dz is the magnetic field gradient. The levitation force density f can be up to $\sim 200\text{N/cm}^2$ in theory [4.3]. But the domain boundary, large angle grain boundary, cracks and porosity in the sample decrease the levitation force.

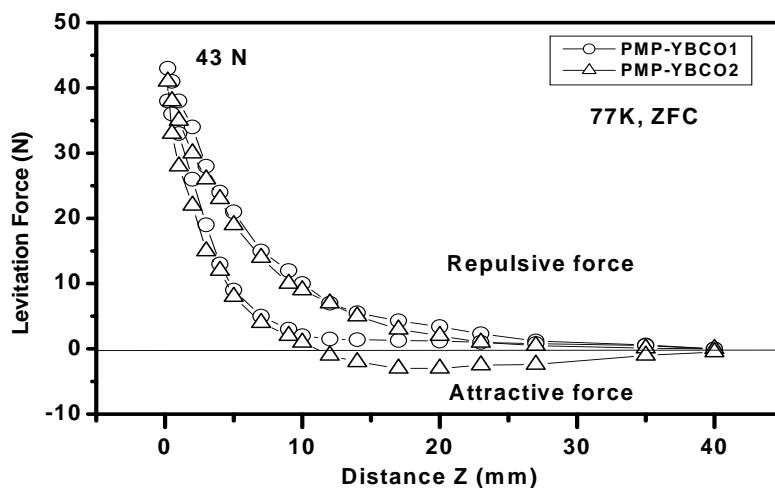


Figure 4-16 The levitation force F versus the distance z between the magnet NdFeB and superconductor. The maximum levitation force value is 43N (77K, 0.5T).

The samples PMP-YBCO1 and PMP-YBCO2 are magnetised in a static magnetic field of 2T. The magnetization process is the same as described above in section 4.4. The trapped magnetic field B_{tr} distribution at 0.2mm position above the sample surface is scanned with a Hall probe. The trapped magnetic field B_{tr} of the sample is shown in figure 4-17. The maximum B_{tr} of the single domain PMP-YBCO1 is 380mT (figure 4-17a) , B_{tr} of PMP-YBCO2 is 250mT (figure 4-17b). The trapped magnetic field B_{tr} is proportional to the critical current density J_c and the single domain size r , as $\mathbf{B}_{tr} \propto \mathbf{J}_c \cdot \mathbf{r}$. The trapped magnetic field B_{tr} distribution reveals the current distribution in the sample. The B_{tr} in the small domain of PMP-YBCO1 sample shows lower value of 40mT (low B_{tr}) . It is lower than it in large domain as 380mT. It shows that the anisotropic current distribution on ab and ac plane. As shown in figure 4-15b, there are several peaks of trapped magnetic field B_{tr} . It shows that there are more large boundaries preventing the transport current to pass. It makes the current flowing in local smaller domains as underlined by the occurrence of several peaks with smaller B_{tr} . The B_{tr} distribution reveals the crystal domain structure of the sample.

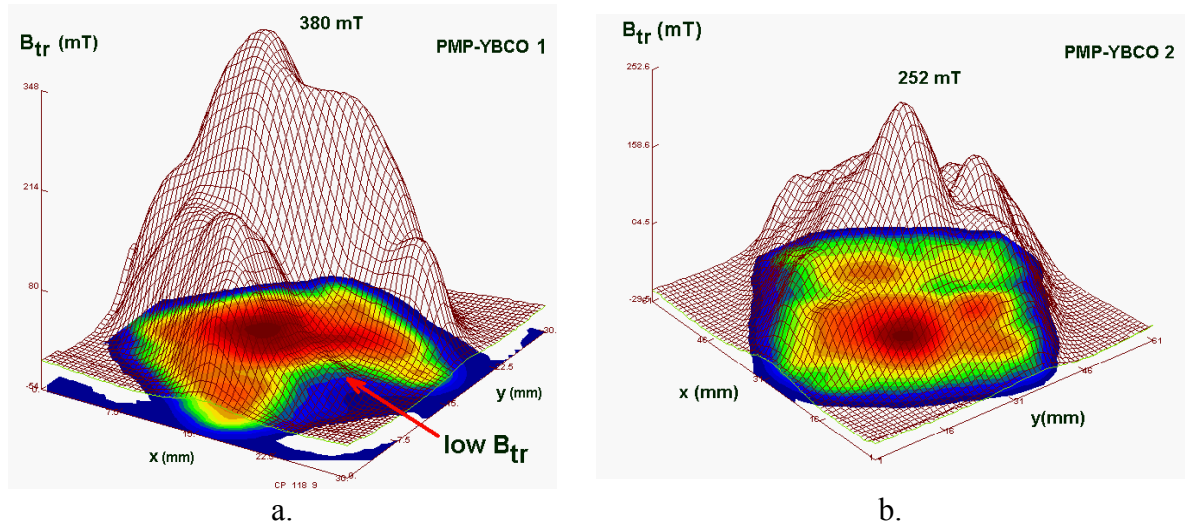


Figure 4-17 a.The trapped magnetic field \mathbf{B}_{tr} distribution of PMP-YBCO1 sample on surface at 77K, the maximum value is 380mT. b.The maximum trapped magnetic field \mathbf{B}_{tr} of PMP-YBCO2 is 252mT at 77K. The multi peak of \mathbf{B}_{tr} reveals the domain structure in single domain.

4.6 Magnetic critical current density J_{cm}

The de-pairing critical current j_c^{dep} in superconductor is the critical intrinsic current J_c . It is the practical property in YBCO superconductor application. The magnetization of the PMP-YBCO sample is measured by a VSM located at the CNRS. The instrument BS2 is of the “Extractor magnetometer” type. Its resolution is $5 \times 10^{-7} \text{A} \cdot \text{m}^2$. Based on the Bean model [4.4], the critical current density J_{cm} is calculated from its measured magnetization. As shown in

figure 4-18, the measured samples are cut into rectangular bars with size of $2 \times 2 \times 5 \text{ mm}^3$, then treated in the HO_2 treatment of 160bars pressure of oxygen at 750°C for 24 hours. The magnetization ΔM is measured with the applied field parallel to c-axis ($H//c$) or in the ab plane ($H//ab$).

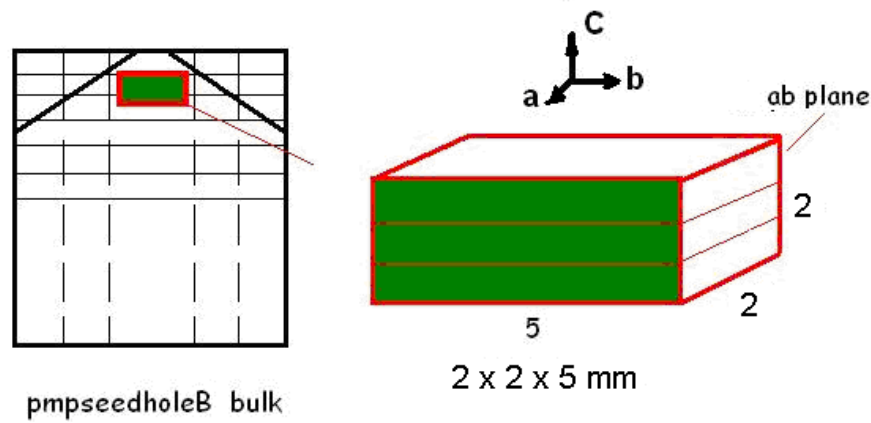


Figure 4-18 Sketch to indicate the position of the $2 \times 2 \times 5 \text{ mm}^3$ bars cut in the PMP-YBCO sample for magnetization measurement ΔM .

The magnetization curves of the hole PMP-YBCO sample measured for the applied field parallel to c-axis ($H//c$) or ab plane ($H//ab$) are shown in figure 4-19. The magnetization is larger when the applied field is parallel to the c-axis (with $H//c$) than when applied in the ab-plane (with $H//ab$). This anisotropic magnetization in YBCO material is related to the anisotropic structure and coherence length ($\xi_{ab}=2.7\text{nm}$, $\xi_c=0.3\text{nm}$). The magnetic critical current J_{cm} of the PMP-YBCO single domain samples is calculated by the Bean model from the magnetization. Figure 4-20 shows the dependence of the magnetic critical current J_{cm} on the applied field H . The critical current density J_{cm} of PMP-YBCO sample is as high as $1.2 \times 10^5 \text{ A.cm}^{-2}$ (77K, 0T) as a benefit from the refined 211 particles. It reaches the best record $J_{cm} \sim 10^5 \text{ Acm}^{-2}$ (77K, 0T) of MPMG-YBCO samples [4.5], as shown in figure 4-21.

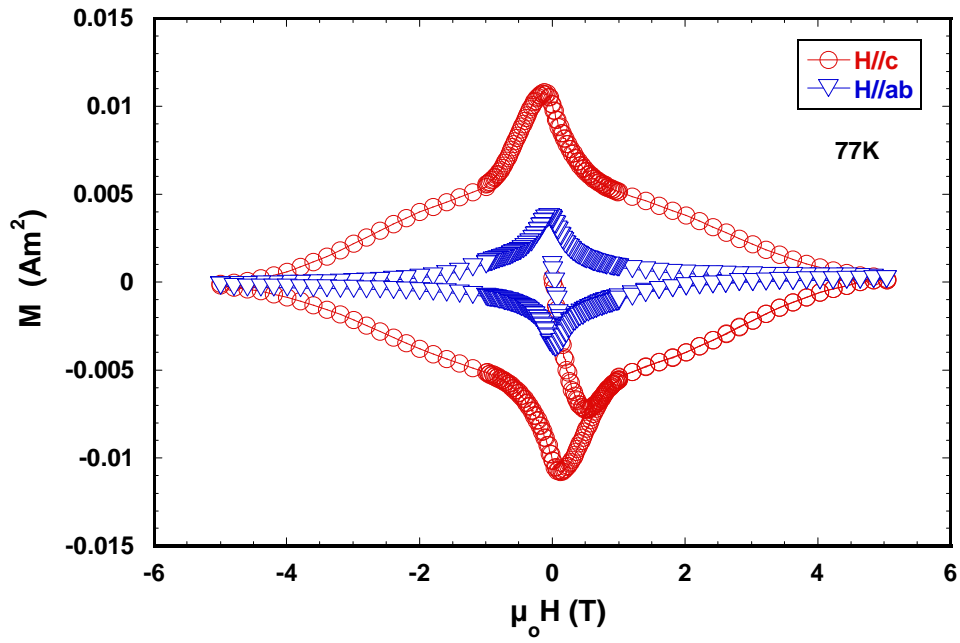


Figure 4-19 Hysteretic line of PMP-YBCO sample at 77K

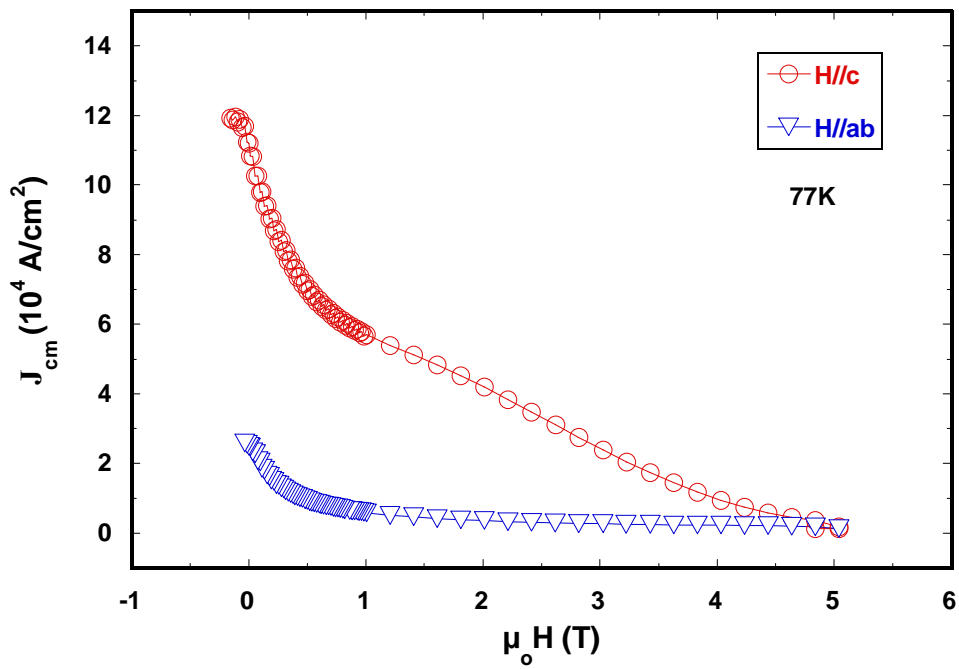


Figure 4-20 The critical current density J_{cm} of PMP-YBCO sample versus applied field

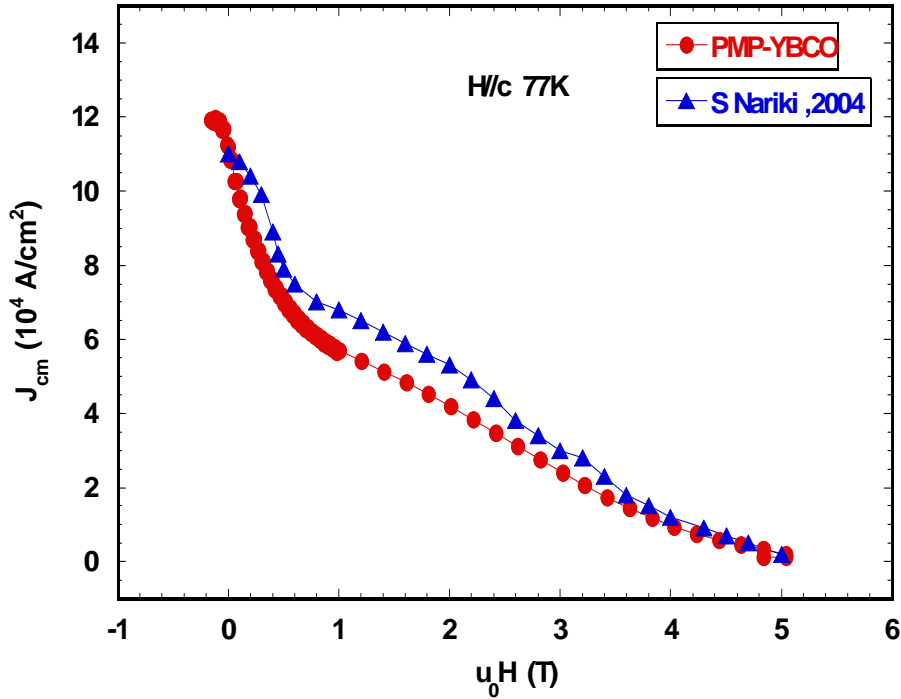


Figure 4-21 The critical current density J_{cm} curve of PMP-YBCO sample comparing to the best record of MPMG-YBCO sample prepared by S Nariki.

4.7 Flux pinning in PMP-YBCO single domain

4.7.1 Irreversibility line B_{irr}

The irreversibility field B_{irr} is the upper limit of the magnetic field for the existence of a critical current density J_c in the type II superconductor. Only below the irreversibility field B_{irr} , the flux is pinned as the vortex glass or Bragg glass/vortex lattice to enable a superconducting current J_c . Above the irreversibility field B_{irr} , the vortex glass changes into flux liquid, the flux could not be pinned anymore. In the vortex liquid state, the current is zero. The magnetic flowing current density J_{cm} is improved as the irreversibility field B_{irr} is increased.

The irreversibility magnetization line of the hole PMP-YBCO sample is obtained from the magnetization hysteresis curves measured at different temperatures as shown in figure 4-22. From the irreversibility magnetization ($M=0$) of each curves, the irreversibility field B_{irr} is deduced as shown in figure 4-23. When the temperature increases from 60K to 85K, the irreversibility field B_{irr} decreases from 12T to 2T. At 77K, the irreversibility field B_{irr} is about 4.5T in the hole PMP-YBCO sample. It means that the applications of the PMP-YBCO single domain are limited to magnetic fields below $B_{irr}=4.5T$ at 77K.

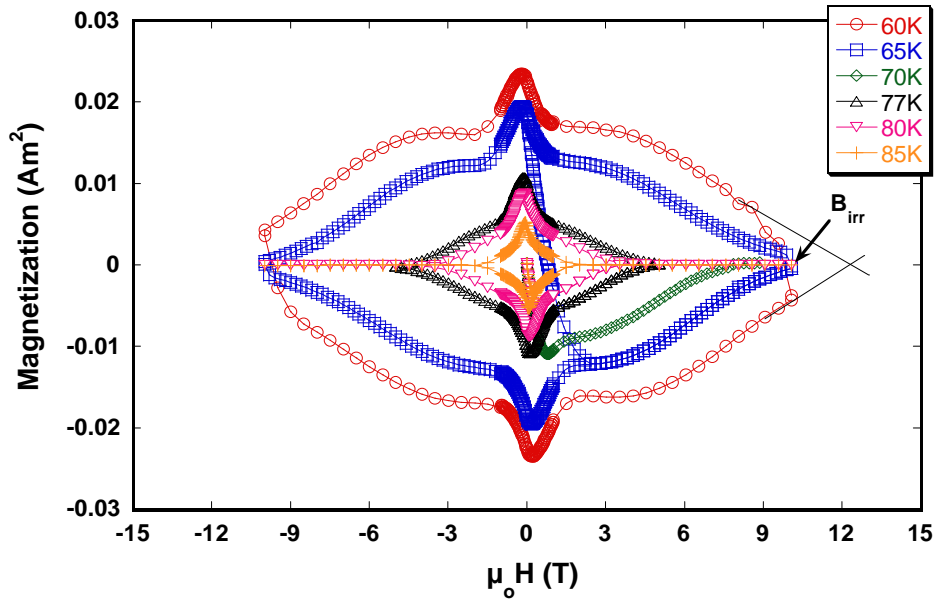


Figure 4-22. Magnetization line of PMP-YBCO single domain sample at different temperature.

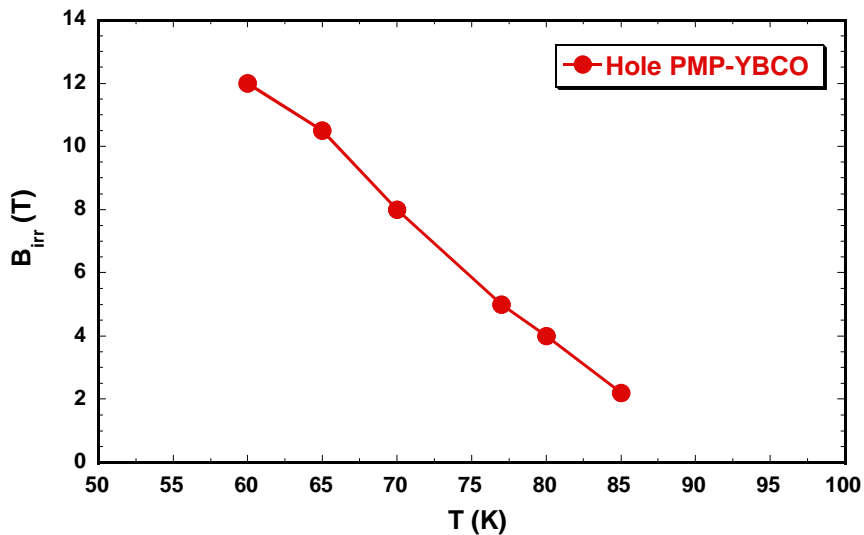


Figure 4-23. Dependence of the irreversibility line B_{irr} of a PMP-YBCO single domain sample on temperature. The irreversibility field B_{irr} is 4.5T at 77K.

4.7.2 Flux pinning and vortex phase diagram of PMP-YBCO

In order to understand the vortex motion for the application of PMP-YBCO, we compare the irreversibility line B_{irr} of PMP-YBCO to H. Kupfer's results as shown in figure 4-24 [4.6]. According to these results, when the oxygen content is as $\delta=0.03$ ($7-\delta=6.97$), the irreversibility field B_{irr} is 7T at 77K. Comparing our data of 4.5T at 77K which corresponds according to our calculation to $\delta=6.73$ for LO2 and $\delta=6.79$ for HO2, there is room for a significant increase of the PMP-YBCO irreversibility field B_{irr} . As the irreversibility field B_{irr} is the limiting field of vortex glass for stable flux pinning, it has also an influence on the

limitation of the trapped magnetic field value, \mathbf{B}_{tr} . At present, the best record of trapped field \mathbf{B}_{tr} is 1.6T for Ø33mm diameter MTG-YBCO samples [4.5]. And it is 0.7T for Ø15 mm PMP-YBCO samples. Therefore, the trapped field \mathbf{B}_{tr} of PMP-YBCO could be increased to higher values [4.7].

When the oxygen content is up to $\delta=0.003$ ($7-\delta=6.997$), the irreversibility field B_{irr} rises to the higher value according to Hans K pfer's result. It means that the irreversibility field B_{irr} corresponds to the oxygen content on which the superconducting transition temperature T_c is also depending. This phenomenon is regarded as to the **δT -pinning**, which is caused by the spatial scatter of the superconducting transition temperature T_c . A relationship between the irreversibility field B_{irr} and T_c is identified [4.8]: $\mathbf{B}_{irr}(\mathbf{T})= \mathbf{B}(0)(1-\mathbf{T}/\mathbf{T}_c)^n$.

Flux (or vortex) state in YBCO has a different behaviour in different temperature T or field H as shown in the vortex phase diagram presented in the figure 1.24. Thus the flux pinning of YBCO has a different mechanism in different region. Only to understand their different pinning mechanisms, we can find an effective way to increase the pinning force. In vortex glass phase, there is a strong pinning of the flux line lattice. In Bragg glass phase, there is a weak pinning state. However, at an application temperature of 77K for bulk YBCO, the pinning state for flux line is weak. Thus, at 77K the bulk YBCO traps less magnetic field, so that it is needed to improve the \mathbf{B}_{irr} line.

Generally, there are two fundamental pinning mechanisms describing the flux pinning [4.9]: 1) **δl -pinning**, it is about the scattering of the electron mean free path; 2) **δT -pinning**, The spatial scatter of the superconducting transition temperature T_c . When the superconductor is in the mixed state, a flux line contains one quantum of magnetic flux $\Phi_0=h/2e$, which composed of normal conducting core of radius ξ (**coherence length**) and a surrounding super-current, the flux line is pinned in the radius. This pinning belongs to the **δl -pinning**. In the PMP-YBCO sample the J_{cm} achieved value up to 10^5 A.cm⁻² (77K, 0T) as a benefit from the refined Y211 particles. It is related to the **δl -pinning** since the refined Y211 particles provide a higher density of Y211/Y123 interface acting a effective flux pinning centers. And the **δT -pinning** is related to the oxygen content which causes the electron density changing, making the spatial scatter of the superconducting transition temperature T_c . The oxygen content of PMP-YBCO is measured as $7-\delta=6.796$ ($\delta=0.204$), which is far from the oxygen content claimed by K pfer ($\delta<0.007$). The irreversibility field B_{irr} of PMP-YBCO at 77K is only half of the K pfer's result. In order to increase the irreversibility field B_{irr} of PMP-YBCO, the oxygen content should be increased. We consider the flux pinning in the PMP-YBCO sample mainly depends on the **δl -pinning** and **δT -pinning**, which is related to the refined 211 particles and to the oxygen content.

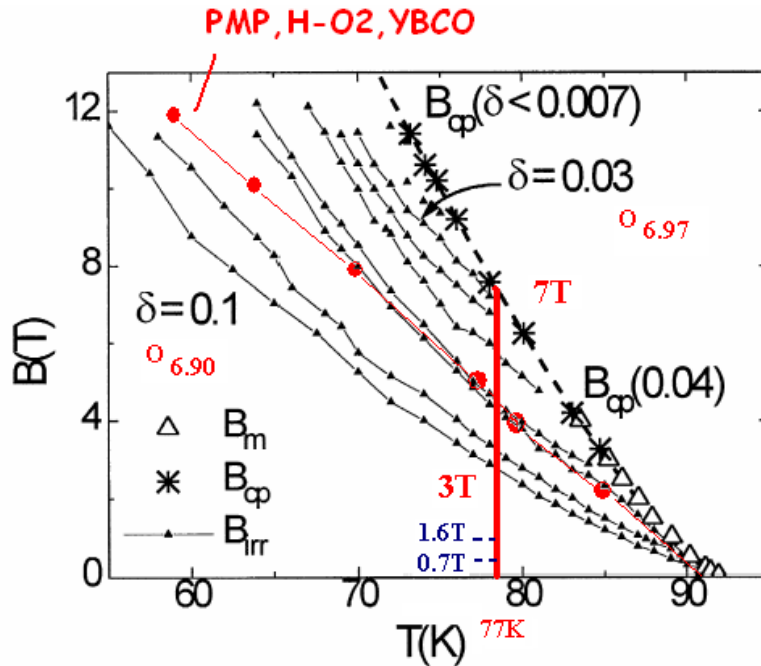
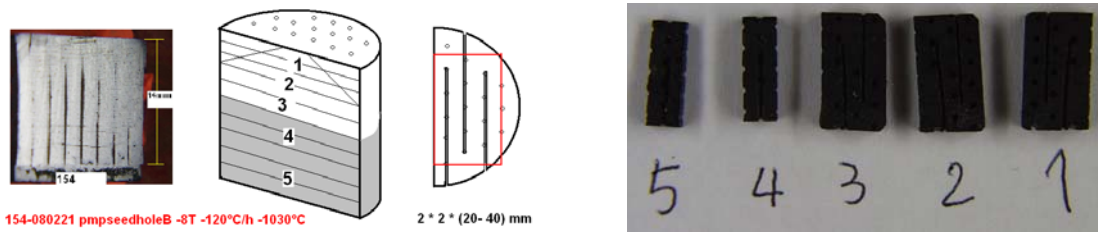


Figure 4-24 Irreversibility line of PMP-YBCO single domain sample compared to Hans Küpfer's results (smaller sample). The irreversibility magnetic field B_{irr} is 7T at 77K in Küpfer's line as the oxygen is 6.97 ($\delta=0.03$). The B_{irr} is 4.5T at 77K in PMP-YBCO sample for an oxygen content estimated at 6.79 with our calculation, at 6.88 according to Prikhna's measurement.

4.8 Transport critical current density J_{ct}

The transport critical current density J_{ct} is the practical parameter in the YBCO bulk applications. The transport critical current density J_{ctr} of a PMP-YBCO hole sample has been tested. As shown in figure 4-26a, the measured sample was cut from the centre part of the pellet below the seed. First, the sample was cut into $2 \times 2 \times (20-40)$ mm³ pieces (figure 4-26b). We checked the absence of macro-cracks in the sample. Some silver paste was painted on four points of the sample to prepare the four point resistive measurement, then the sample was heated in an atmosphere progressively enriched in O₂ to perform a dwell at 900°C for 30 mn under flowing oxygen so that the silver can diffuse into the sample. After gluing some silver wires on the painted points using the silver paste again, the sample was heated at 900°C again and then treated at 420°C for 72 hours in flowing oxygen, as shown in figure 4-26.



a. Sketch of position of cut pieces.

b. prepared samples.

Figure 4-25 Sketch of cutting sample for the transport critical current density J_{ct} measurement

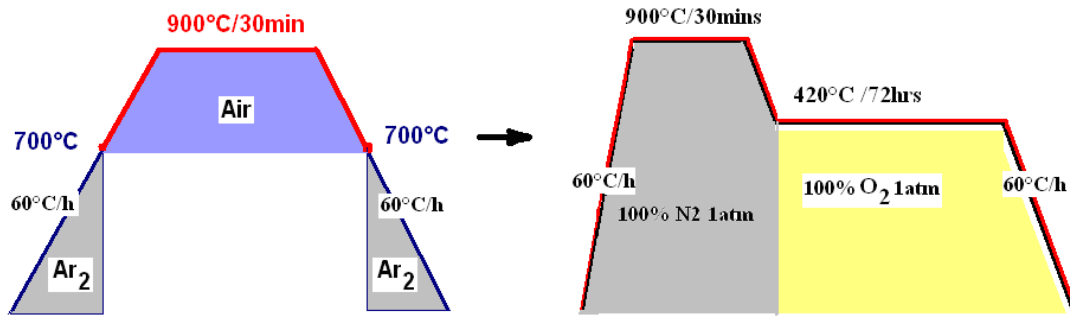
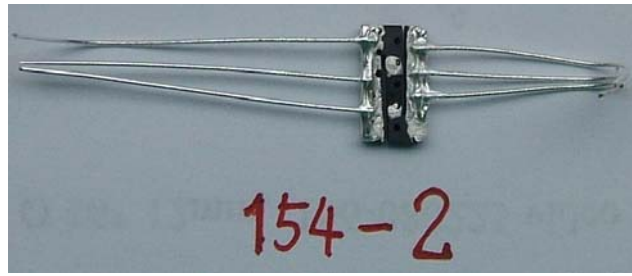
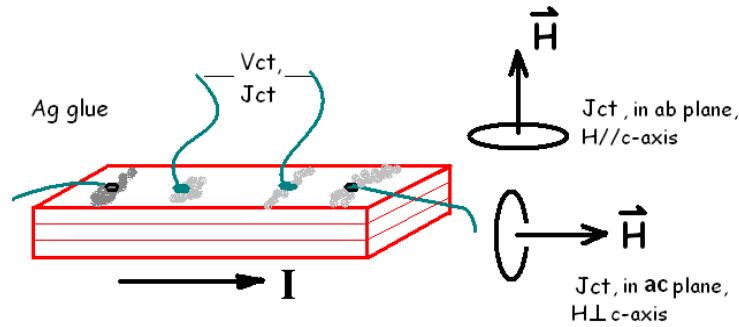


Figure 4-26 Heat treatment in two steps for preparing silver contact, fixing silver wires on YBCO samples and finally performing the oxygen annealing treatment for promoting the T-O transition

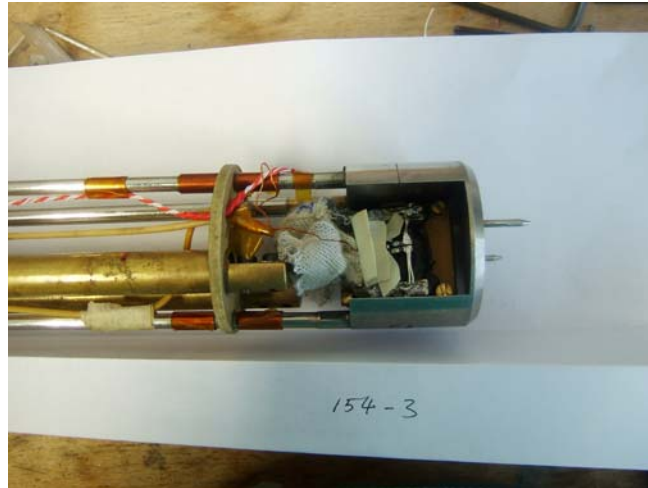
The prepared sample is shown in figure 4-27a. The superconducting critical transition temperature T_c is measured to be 91.5 K (figure 4-11). We measured the transport current I_c of the PMP-YBCO sample with an applied magnetic field $H//c$ and $H//ab$, as shown in figure 4-27b and c. The sample is fixed on a copper plate for thermal diffusion with a thin paper tape inbetween for electrical insulation. The silver wires are soldered to the adequate terminals. The support shown figure 4-27 c is then inserted into a variable temperature insert working with helium flow down to liquid He_2 for measurement. The insert stands in the room temperature bore of a superconducting coil so that a magnetic field up to 8T could be applied. The sample support can be rotated according to the desired magnetic field direction. We started to perform current measurement at 81K and then the temperature was decreased step by step. This is to avoid burning the sample. We start at a rather high temperature for which the critical current will be rather low. The critical current increases as the temperature decreases. To perform a measure at each temperature, the current is increased gradually until the superconductivity disappeared. We used a criterion of $10\mu V/cm$ to determine the J_c . The transport critical current density J_{ct} versus temperature is shown figure 4-28. At 78.5K, the J_{ctr} is $\sim 7.5 \times 10^3 A.cm^{-2}$. This is the first time the critical transport current density was measured on a sample length of 20-40mm of PMP-YBCO single domain. This result displays the real practical property of PMP-YBCO single domain for application.



a.



b.



c.

Figure 4-27 Picture of a sample for transport critical current measurement (a). Sketch of the connections on the samples and its position with regards to the applied magnetic field (b). Picture of the sample holder for the variable temperature insert used for measuring the transport critical current density J_{ct} at different temperatures from 300 K to 4.2 K (c).

Comparing the magnetic critical current density J_{cm} of PMP-YBCO samples which is up to $1.2 \times 10^5 \text{ A.cm}^{-2}$ (77K, 0T), the transport critical current density J_{ctr} is only $\sim 7.5 \times 10^3 \text{ A/cm}^2$ (at 78.5K). It is two order of magnitudes lower than J_{cm} . It reveals that there are cracks, pores and boundaries inside the PMP-YBCO sample breaking the current. The fact that the measured J_{cm} is already reaching up to 10^5 A.cm^{-2} (77K) means that the flux pinning function is enhanced by the refined 211 particles and the homogenous oxygen content in hole shape samples. However, the cracks, pores and grain boundaries reduce the transport critical current density J_{ct} . These problems related to the YBCO single domain fabrication stands in the way to application.

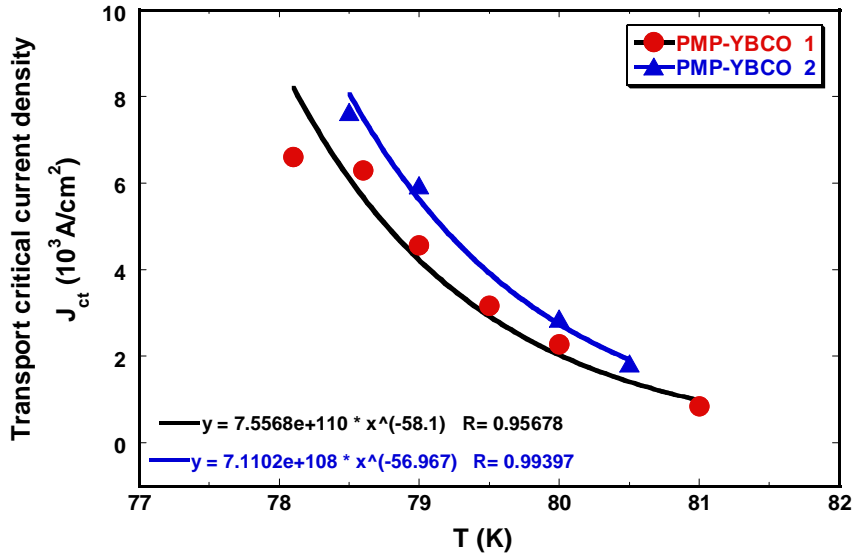


Figure 4-28 The transport critical current density J_{ct} versus temperature of hole PMP-YBCO.

The transport critical current density J_{ct} versus field is measured as shown in figure 4-29. When the applied field increases, the transport critical current density J_{ct} decreases. A relationship is obtained for the PMP-YBCO sample, as

$$J_{ct} = 0.8 \times 10^3 \cdot B^{-1} \quad (4-7)$$

From this equation, the J_{ct} will be reduced to 160 A/cm^2 when the applied field is 5T, which can be provided to the application of PMP-YBCO sample at higher applied field.

Considering the relationship between the levitation force, B_{tr} , J_{cm} , J_{ct} and the microstructure of PMP-YBCO single domain, the high magnetic critical current density J_{cm} is achieved as 10^5 A/cm^2 (77K). But the lower properties of J_{ct} shows the microstructure of PMP-YBCO influences the properties very much. As the cracks, pores and grain boundaries existed in the sample, for the PMP process, the microstructure should be improved in the fabrication.

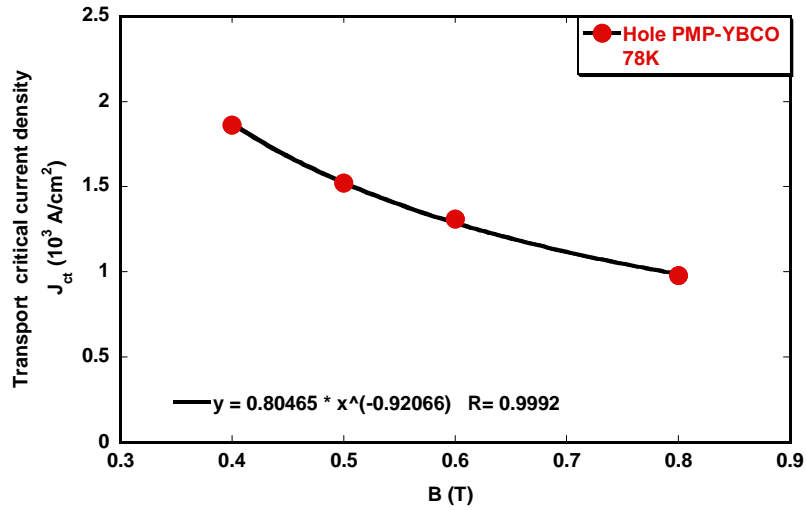


Figure 4-29. Dependence of the transport critical current density J_{ct} on magnetic field B of PMP-YBCO single domain sample at 78K.

4.9 Summary

- 1) The hole PMP-YBCO single domain has a typical structure. The Y211 particles push-trapping phenomenon is obvious. It presents the special character of PMP process, i.e. a homogenous distribution of fine and spherical Y211 particles. The hole shape has no influence on the 123 crystal textured growth and decreases the porosity size.
- 2) The high pressure oxygen treatment is proved to increase the oxygen constant $7-\delta$ of Y123 crystal. It improves the trapped magnetic field B_{tr} , the maximum value is 739mT in $\Phi 15$ mm hole PMP-YBCO single domain at 77K since refined Y211 particles are obtained. The magnetic critical current density J_{cm} is achieved as $\sim 1.2 \times 10^5 \text{ A/cm}^2$ (77K) in the PMP-YBCO single domain sample, which competes with the best record at present.
- 3) The irreversibility field B_{irr} of PMP-YBCO is 4.5T at 77K, it could be increased to a higher value. The flux pinning of PMP-YBCO sample is depending on the **δl -pinning** and **δT -pinning**, which are related to the refined Y211 particles and to the oxygen content respectively.
- 4) The transport critical current density J_{ct} is measured up to $\sim 7.5 \times 10^3 \text{ A.cm}^{-2}$ (78.5K). The transport critical current density J_{ct} is two order of magnitude lower than the magnetic critical current density J_{cm} . It reveals the detrimental effect of the cracks, pores and boundaries existing in the PMP-YBCO sample breaking the current.

References:

- [4.1] M P Delamare, H Walter, B Bringmann, A Leenders, H C Freyhardt, “Macrosegregation of Y₂BaCuO₅ particles in top-seeded melt textured monoliths”, Physica C 323 1999 107-114
- [4.2] T A vanderah, Journal of Crystal Growth 118 1992 385-395.
- [4.3] C P Zhang, Dissertation for Master, “A study on the Growth, Microstructure and Property of Bulk Single Domain YBCO & REBCO Superconductors”, Northwest Polytechnical University, July 2005.
- [4.4] C P Bean. Magnetization of Hard Superconductors. Physical Review Letters. 1962, 8(6): 250-253
- [4.5] S Nariki, 2004 Supercond.Sci.Technol. 17 S30.
- [4.6] H Kupfer, Physica C 332 2000 80-85.
- [4.7] V.S.Boyko, 2007 Physica C 466 56-60.
- [4.8] G Krabbes,G Fuchs, W –R Canders,H May, R Palka, “High Temperature Superconductor Bulk Materials”, WILEY-VCH VERLAG GmbH&Co.KGaA, 2006
- [4.9] Blatter G, Feigel’man M V, Geshkenbein V B, Larkin A I and Vinokur V M 1994 Rev.Mod.Phys. 66 1125.

Chapter 5 Effect of the heating rate on PMP-YBCO single domain

5.1 Experimental

When samples are heated using different heating rate, it is found that the PMP-YBCO samples undergo different phase transitions. For instance, the 123 formation may be avoided, and this may have technological impact for preparing 123 single domains. That is why this chapter focus on this aspect.

We continue to investigate the effect of heating rate on the 211 particles size and the magnetism critical current density J_{cm} . We measured the susceptibility of the samples in 8T field as the samples are prepared as hole PMP-YBCO bulk with seed. The samples marked as R1, R2, R3, R4, R5 are treated using the same process except changing different heating rate of 10°C/hr, 60°C/hr, 90°C/hr, 120°C/hr, 240°C/hr during 900°C-1060°C. The detail process is shown in figure 2-12. The microstructure of the samples is observed by optical microscopy and scanning electron microscopy. Their morphology is shown in the [table 5-1](#). The samples were oxygenated under high pressure of oxygen and small pieces were cut out their center part to performed magnetization measurements.

5.2 Effect on the phase transition

The effect of heating rate on the phase transition of PMP-YBCO is already discussed in section 2.3. As shown in [figure 5-1](#), when the heating rate is over 120°C/hr, the 123 phase does not form in samples. Therefore the 120°C/h becomes a critical heating rate of 123 phase formation for hole samples. The result reveals that each process parameter could change the phase transition in the PMP-YBCO single domain growth, such as heating rate or overheating temperature, etc. We select the 120°C/h heating rate to control the 123 phase formation in the process.

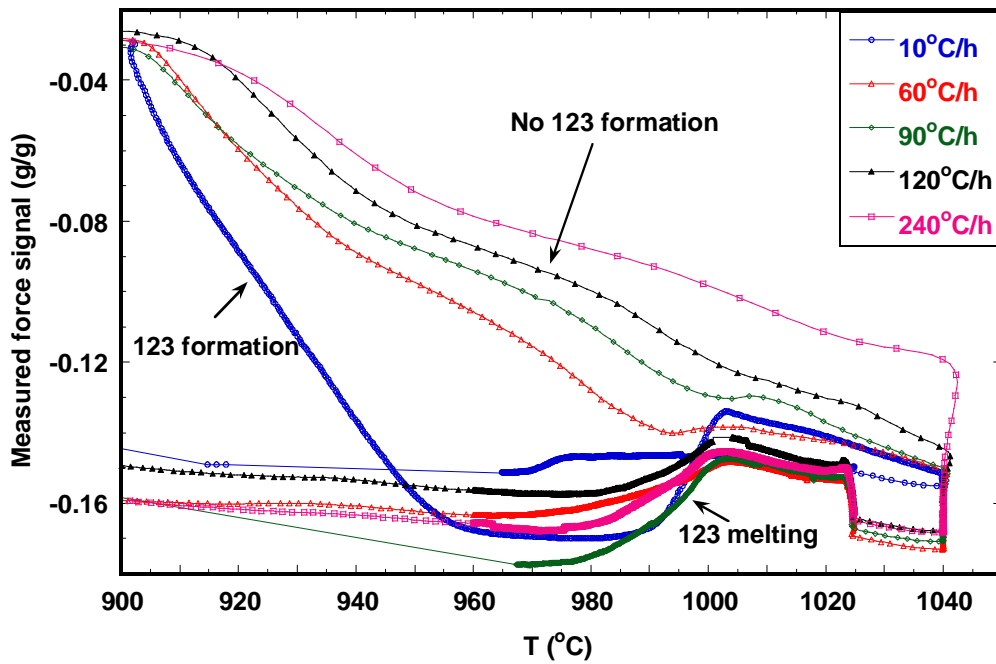


Figure 5-1 The susceptibility curve versus temperature of hole PMP-YBCO samples processed with different heating rates during the part of the heating step where 123 is supposed to form. It shows the effect of the heating rate during the phase transition that is changing the 123 phase formation.

5.3 Effect on the 211 particles

A centre piece of the samples is selected to be observed as represented by the gray part in figure 5-2. The microstructures observed by optical microscopy are shown in figure 5-3. The dark particles are the 211 (Y_2BaCO_5) phase. We use the Visilog 6.0 software to analyze the mean size of 211 particles. Corresponding to the following heating rates, 10°C/h, 60°C/h, 90°C/h, 120°C/h, 240°C/h, the mean size of 211 particles is measured as 0.37 μ m, 0.57 μ m, 0.53 μ m, 0.59 μ m, 0.37 μ m, respectively. The result shows that the heating rate influences the size of 211 particles, and that the mean size is much below 1 μ m. The refined 211 particles is the typical character of the PMP process which influence is also analyzed in section 4.1.

In the lower heating rate 10°C/h process, the 211 size is smaller (0.37 μ m) than it in the samples with 60°C/h, 90°C/h, 120°C/h heating rate (0.57 μ m, 0.53 μ m, 0.59 μ m). The result at 10°C/h is a bit unexpected. How to explain the phenomenon, it is supposed that the lower heating rate makes 123 phase formation resulting in refining the 211 particles first. When the sample is melted, the 123 crystal decomposed into 211 particles and the liquid phase. The 211 particles are refined secondly. During the 123 crystal solidification stage, 211 particles are consumed to form 123 crystal, resulting in the 211 particles refined again. This lower heating

rate makes 211 refined and get a critical current density J_{cm} up to $1.1 \times 10^5 \text{ Acm}^{-2}$ (77K). On the other hand, in the fast heating rate 240°C/h process, the 211 size is also smaller ($0.37\mu\text{m}$) than for the other heating rate samples. This phenomenon can be explained by the time spent in the heating stage is less in fast heating rate so that 211 coarsening can be avoided before solidification. A critical current density J_{cm} near 10^5 Acm^{-2} (77K) is also obtained. The five samples were observed by SEM and the corresponding microstructures are shown in figure 5-4. And we also get the same result as the 211 particle is round and the mean size is smaller than $1\mu\text{m}$. We conclude the results listed in [table 5-1](#).

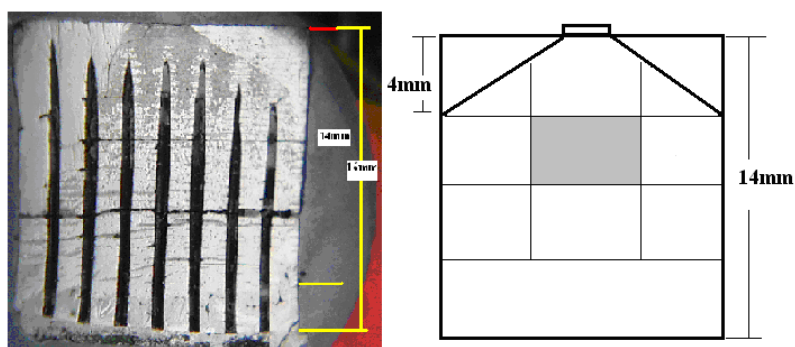
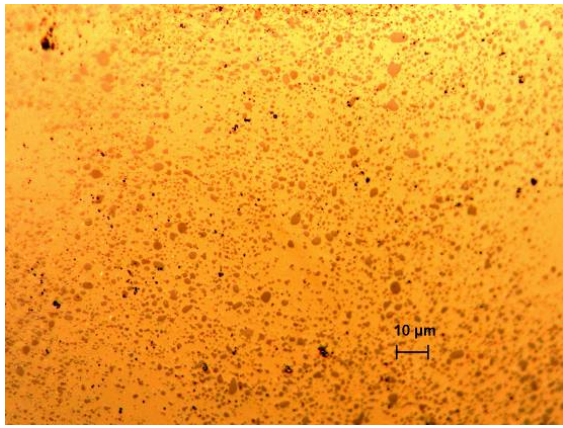
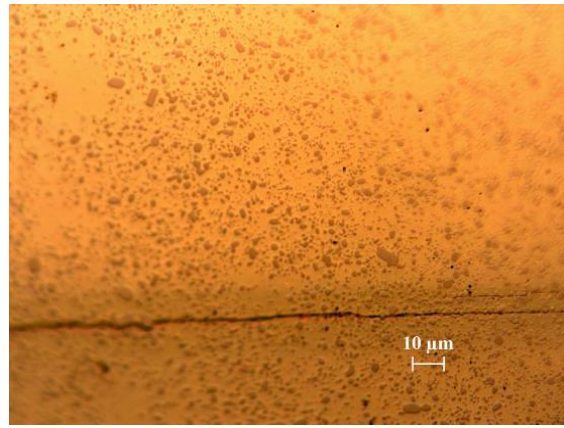


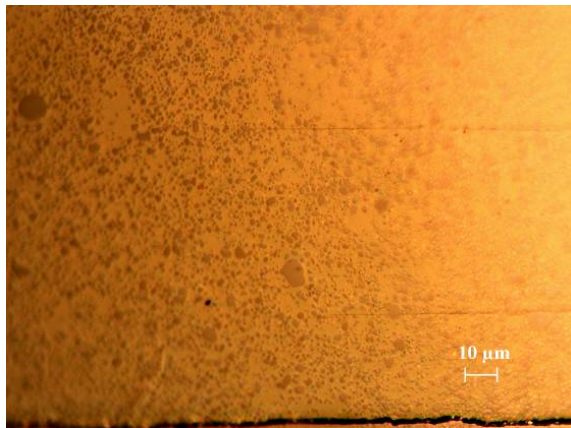
Figure 5-2 Sketch of hole- PMP-YBCO section for morphology observation (Gray part).



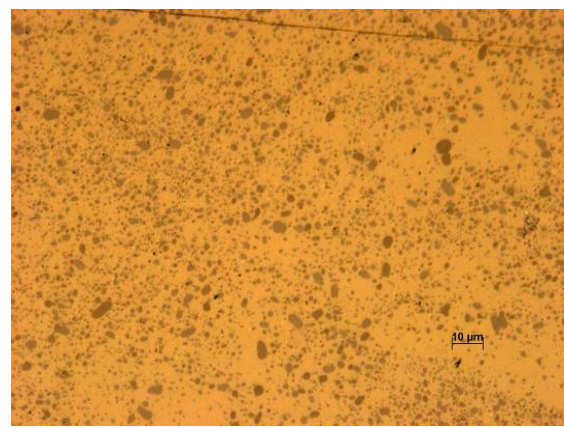
R1, 10°C/h, $d_{211} \sim 0.37 \mu\text{m}$



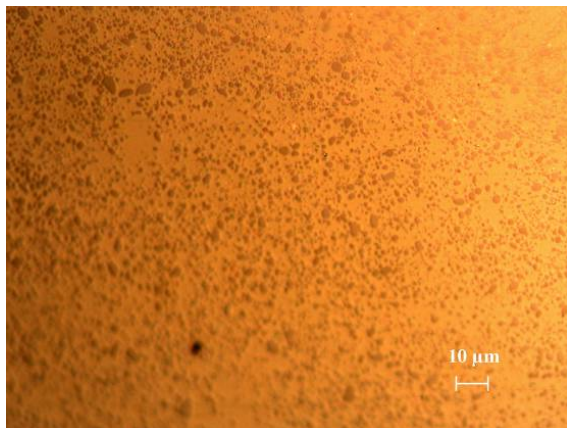
R2, 60°C/h, $d_{211} \sim 0.57 \mu\text{m}$



R3, 90°C/h, $d_{211} \sim 0.53 \mu\text{m}$

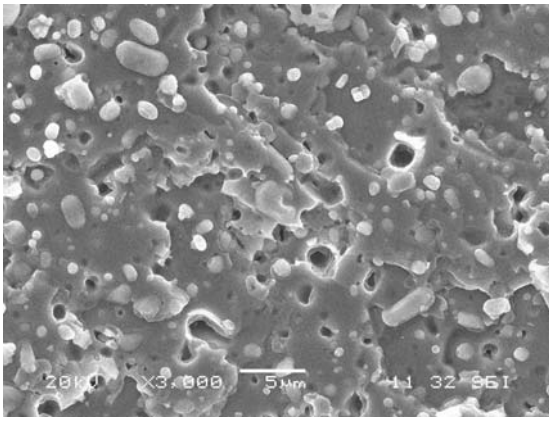


R4, 120°C/h, $d_{211} \sim 0.59 \mu\text{m}$

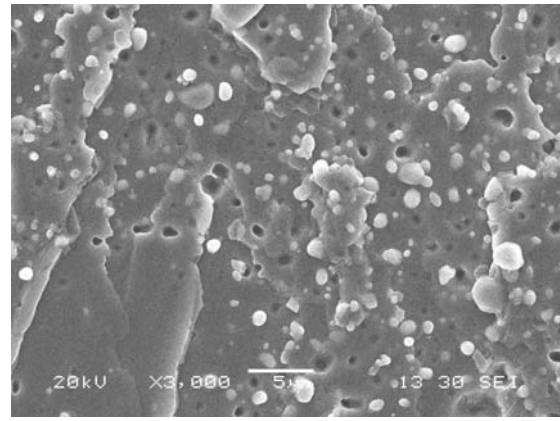


R5, 240°C/h, $d_{211} \sim 0.37 \mu\text{m}$

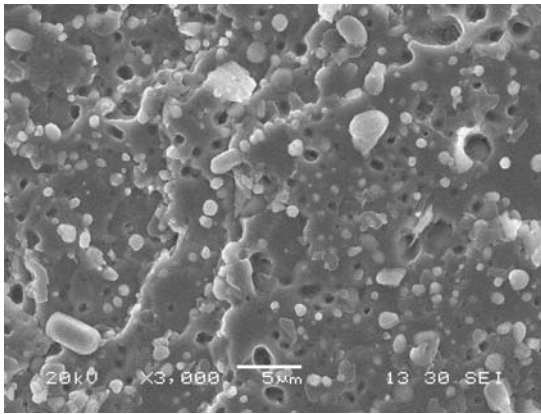
Figure 5-3 Y211 distribution in centre part of PMP-YBCO bulk corresponding to the different heating rate R1, R2, R3, R4, R5. The dark particles are the 211(Y_2BaCO_5) phase particles.



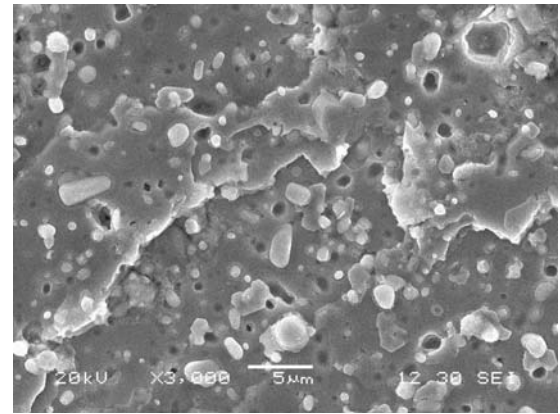
R1, 10°C/h



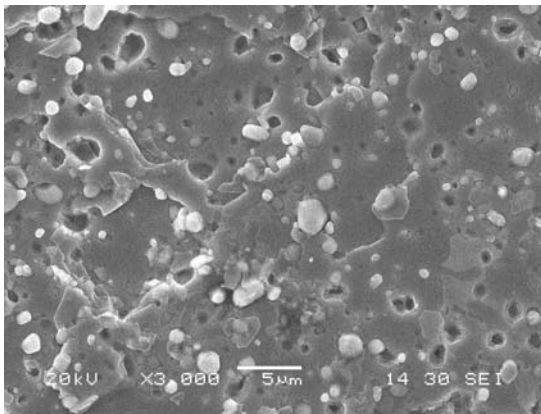
R2, 60°C/h



R3, 90°C/h



R4, 120°C/h



R5, 240°C/h

Figure 5-4 SEM observation in centre part of PMP-YBCO section with different heating rate of the sample R1, R2, R3, R4, R5. The 211 particles are mostly spherical and the mean size is less than 1 μ m. Some rather large rod-like particles are seen on pictures corresponding to R1, R3 and R4. The Y211 in R1 looks larger than any other samples and the Y211 density seems to vary, the sample R5 showing the lowest density. But are the pictures really representative of the entire sample.

5.4 Effect on the magnetism critical current density J_{cm}

Small size ($2 \times 2 \times 6 \text{ mm}^3$) samples were cut from the centre part of each five samples R1, R2, R3, R4, R5 for measuring the critical current density J_{cm} . The hysteretic magnetization were obtained at 77K using the VSM in CNRS (BS2) as described in section 4.7. The critical current density J_{cm} is calculated from the magnetization data using the Bean model. At first, we measure the superconducting transition temperature T_c to make sure a superconducting state is well obtained in the high pressure oxygen treatment. The result is shown in figure 5-5. All the T_c value is above 91.5K.

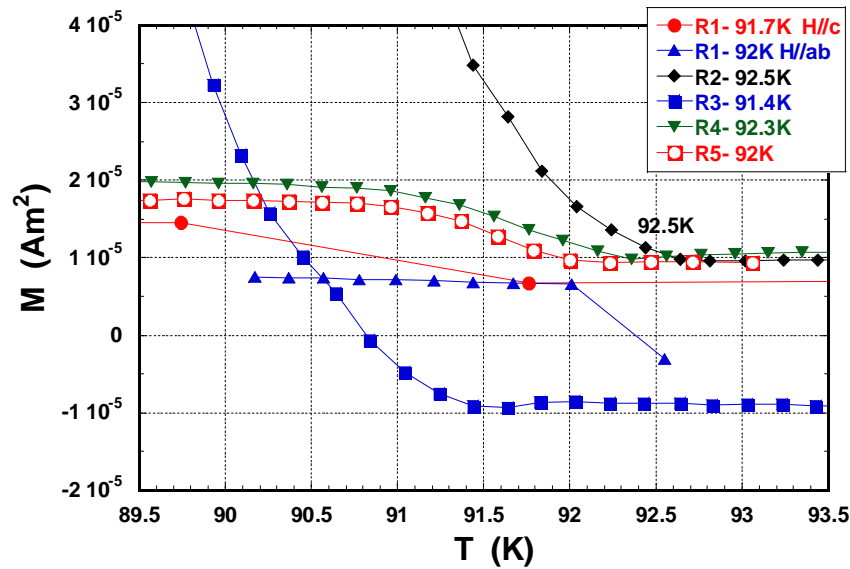
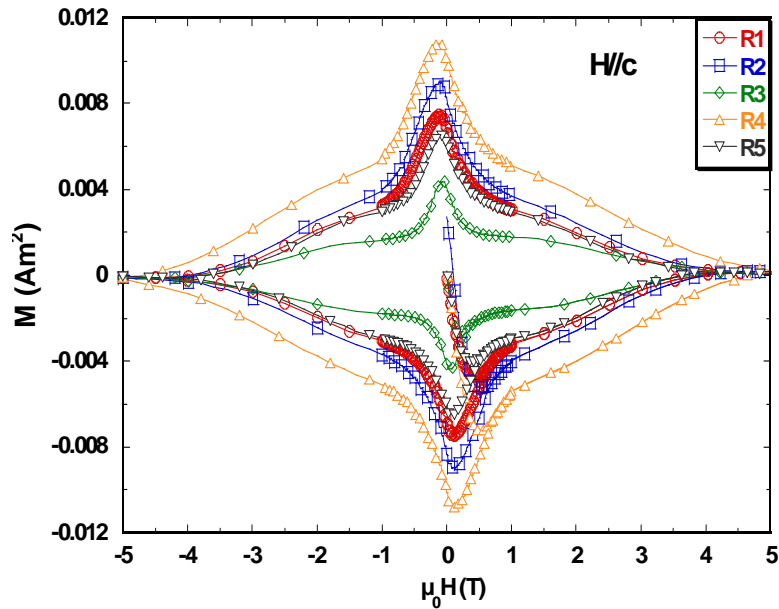


Figure 5-5 The critical superconducting transition temperature T_c of R1, R1, R2, R3, R4, R5, which the T_c is above 91.5K.

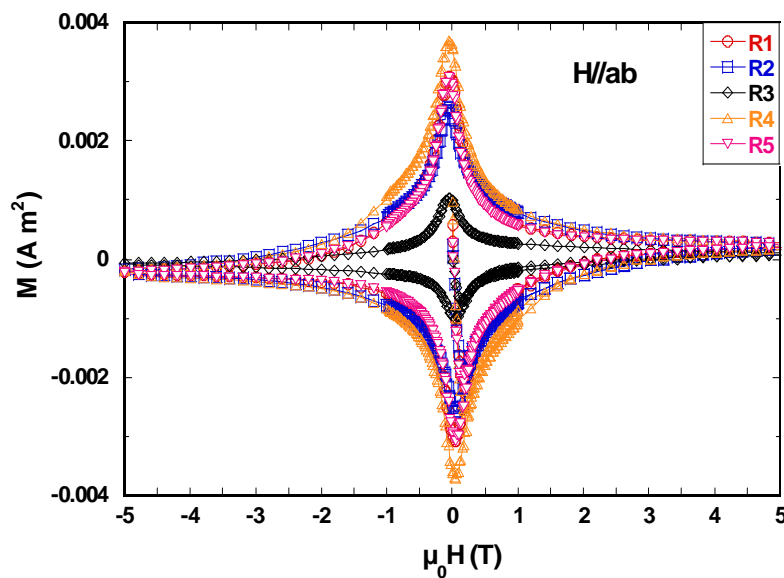
The measured hysteretic magnetization curves are shown in figure 5-6. Because of the anisotropy of 123 crystal, the magnetization is also displaying a strong anisotropy. The magnetization of PMP-YBCO sample at H//c is three times the one at H//ab. The critical current density J_{cm} versus applied field H is shown in figure 5-7. The current density J_{cm} at H//c is three times of the current density J_{cm} at H//ab. The maximum J_{cm} at H//c is 10^5 A/cm^2 (77K) in samples corresponding to the heating rates of 120°C/h , 10°C/h and 240°C/h , which can be compared to the best record $J_{cm} \sim 1.1 \times 10^5 \text{ A/cm}^2$ (77K) [5.1]. The fish-tail effect related to the δT -pinning [5.2] is obviously not present in these samples.

We have discussed the flux pinning of PMP-YBCO in chapter 4. H. Küpfer has shown that the irreversibility field B_{irr} is related to δT_c -pinning. The value of the irreversibility field B_{irr} is determined when the J_{cm} tends to zero and is found similar for the five samples. We assumed that the δT_c -pinning situation is the same in the five samples since the T_c is similar. So the critical current density J_{cm} could be compared to each other. The maximum value of

10^5A/cm^2 (77K) is measured in the samples with heating rate of 120°C/h , 10°C/h and 240°C/h , and the minimum value of $5 \times 10^5 \text{A/cm}^2$ (77K) is found in the sample with heating rate of 90°C/h , the maximum data is more than two times the minimum data. If the δT_c -pinning function is similar in the samples we analyze the difference of J_{cm} caused from the δI -pinning.

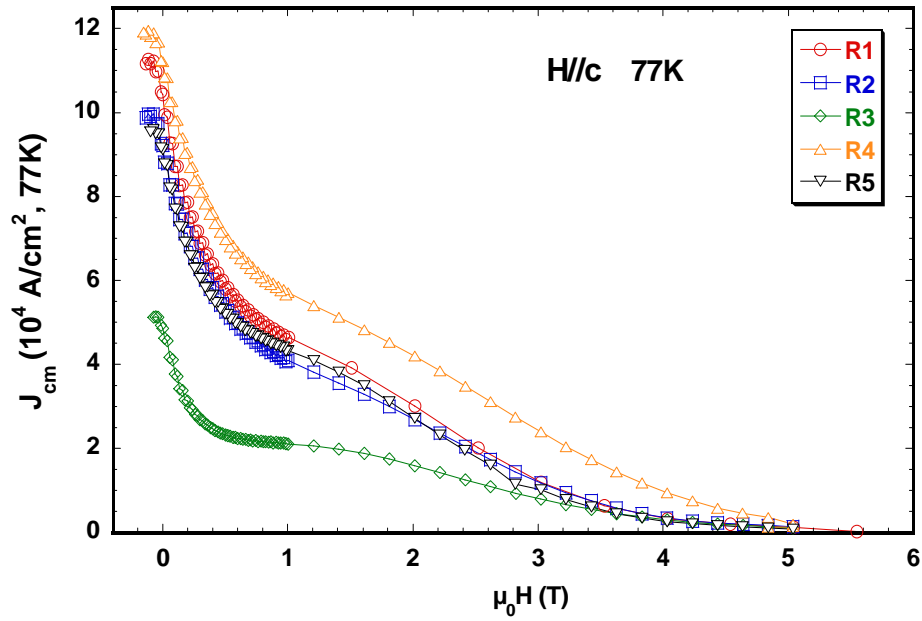


a. H//c

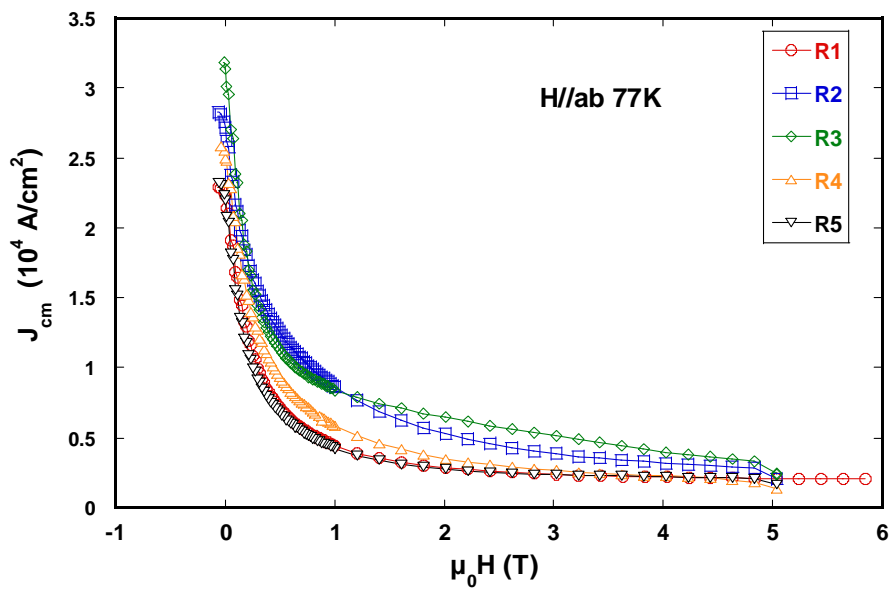


b. H//ab

Figure 5-6 Magnetization lines of PMP-YBCO samples R1, R2, R3, R4, R5 at 77K. The magnetization of PMP-YBCO sample at H//c is three times the one at H//ab. The color code have changed between H//c and H//ab. It is very confusing.



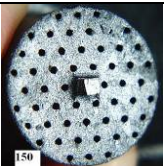
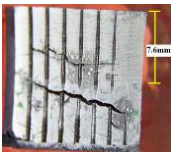
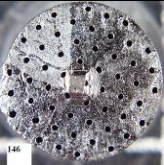
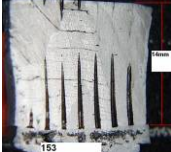
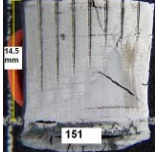
a. H//c



b. H//ab

Figure 5-7 The critical current density J_{cm} versus applied field of PMP-YBCO sample R1, R2, R3, R4, R5 at 77K. Why the data of R3 is as good as R2 whereas its magnetization is the worst ?

Table 5-1 The Morphology of surface and section of sample. The mean size of 211 particles, T_c and J_{cm} of PMP-YBCO sample R1, R2, R3, R4, R5 with different heating rates.

Sample	R_h (°C/h)	Surface	Section	d_{211} (μm)	T_c (K)	J_{cm} ($\text{A}/\text{cm}^2, 77\text{K}, 0\text{T}$)
R1	10°C/h			0.37	92	11.3×10^4
R2	60°C/h			0.57	92.5	4.63×10^4
R3	90°C/h			0.53	91.4	5.13×10^4
R4	120°C/h			0.59	92.3	12.0×10^4
R5	240°C/h			0.37	92	9.58×10^4

M. Murakami found the critical current density J_c increased by the 211 addition [5.3] and has proved that the 211/123 interface is a very effective pinning site in YBCO. If the size of 211 particle is small, the density of 211/123 interface will be increased. Thus the critical current density J_{cm} is inversely proportional to the mean size of 211 particles, as

$$J_{cm} \propto 1/d_{211} \quad (5-1)$$

d_{211} is the mean size of the 211 particles. The critical current density J_{cm} and the d_{211} data of the samples with different heating rates are listed in table 5-1. If we plot J_{cm} versus $1/d_{211}$ for our data, we found an imperfect linear relationship between J_{cm} and $1/d_{211}$ as shown in figure 5-8.

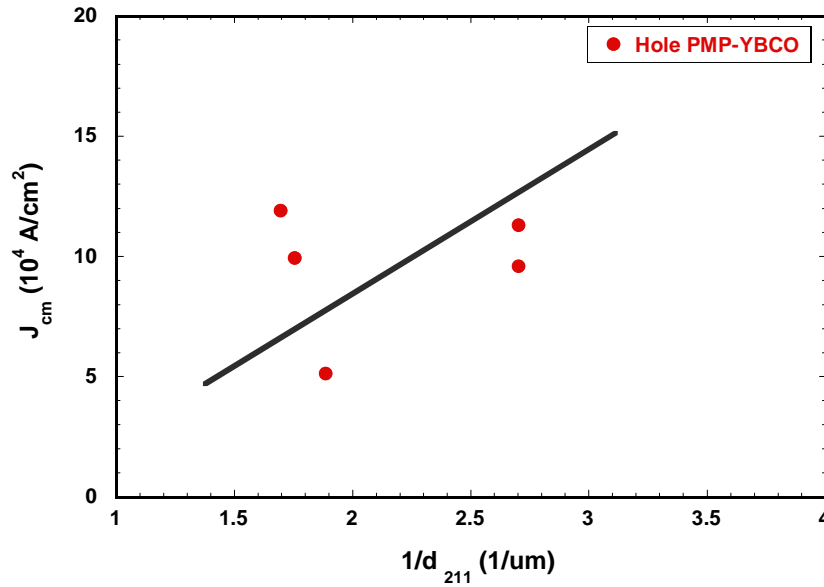


Figure 5-8 The critical current density J_{cm} versus the inverse proportion of the mean size of 211 ($1/d_{211}$). It has an imperfect linear relationship between J_{cm} and $1/d_{211}$.

Furthermore, whether the flux pinning of the PMP-YBCO is related to the δT_c -pinning, we continue to discuss it. In the section 4.7 we discuss the relationship of the irreversible field B_{irr} and the oxygen content. It is showed that the high oxygen constant rising the irreversibility B_{irr} line. So we think the flux pinning in PMP-YBCO sample depends also on the δT_c -pinning related to the oxygen content. The relationship of the critical current density J_{cm} (H//c or H//ab) and the superconducting transition temperature T_c is plotted in figure 5-9. When the T_c increase 0.5K larger, the J_{cm} (H//c) enhances 2 times. But this increasing is not happened at H//ab. The result implies that the flux pinning along c-axis is depended to the spatial electron density distribution which is different from ab plane. Considering the effect of T_c on the J_{cm} , we think the flux pinning in PMP-YBCO has both of the δI -pinning and the δT_c -pinning. The magnetic critical current density J_{cm} is related to both of the size of 211 particles and the transition temperature T_c .

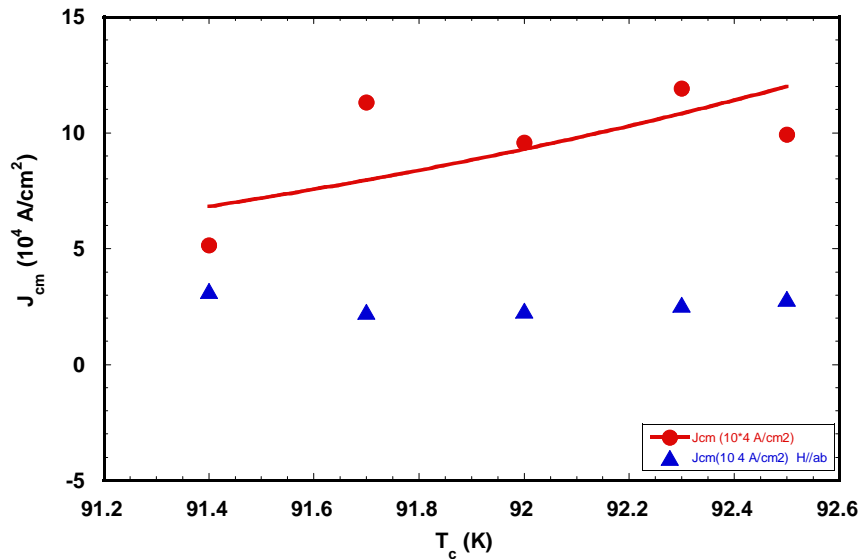


Figure 5-9 Dependence of the critical current density J_{cm} (H//c and H//ab) on superconducting transition temperature T_c .

5.5 Summary

- 1) The heating rate influences the 123 phase formation in the PMP-YBCO sample. It also influences the size of 211 particles. The faster or slower heating rate will refine the Y211 particles. The feasible heating rate is necessary to the PMP-YBCO single domain growth.
- 2) The heating rate influences the critical current density J_{cm} of the PMP-YBCO sample. The maximum J_{cm} at H//c is 1.2×10^5 A/cm 2 (77K) with heating rate of 120°C/h, 10°C/h or 240°C/h which is equivalent to the best record $J_{cm} \sim 1.1 \times 10^5$ A/cm 2 (77K). The flux pinning in PMP-YBCO sample is related not only to the 211/123 interface but also to the T_c , which of the δI -pinning and the δT_c -pinning.

References

- [5.1] S Nariki, 2004 *Supercond.Sci.Technol.* **17** S30.
 [5.2] M R Koblischka, 2000 *Supercond.Sci.Technol.*, **13** p738-744.
 [5.3] M Murakami, H Fujimoto, 1991 *Physica C*, **185-189** p321.

Chapter 6 Conclusion and prospect

Based on the investigation of the phase transitions, fabrication and properties of PMP-YBCO single domain samples, we obtain the following results:

1. The crystalline phase transition of PMP-YBCO bulk was investigated by the susceptibility measurement – high temperature Faraday Balance. The phase transitions happening during the PMP-YBCO bulk fabrication were revealed and identified. It includes: ① 123 formation and melting: $211+011+\text{CuO}\rightarrow 123$ ($900^{\circ}\text{C}-1000^{\circ}\text{C}$); $123\rightarrow 211+\text{L}$ ($1000^{\circ}\text{C}-1012^{\circ}\text{C}$). ② 011 melting: $\text{BaCuO}_2+\text{CuOL}$ ($900^{\circ}\text{C}-1020^{\circ}\text{C}$); ③ CuO decomposing and recomposing reaction: $\text{CuO}\rightarrow\text{Cu}_2\text{O}+\text{O}_2\uparrow$ ($1022^{\circ}\text{C}-1060^{\circ}\text{C}$, at 1060°C , $1060^{\circ}\text{C}-1025^{\circ}\text{C}$); $\text{Cu}_2\text{O}+\text{O}_2\rightarrow\text{CuO}$ (at 1025°C); ④ 123 solidification: $211+\text{L}\rightarrow 123$ ($1004^{\circ}\text{C}-980^{\circ}\text{C}$).
2. Comparing the nucleation temperature of bulk PMP-YBCO with Sm123 Seed and without seed, the nucleating temperature window is found to be in the $1011^{\circ}\text{C}-1006^{\circ}\text{C}$ temperature range as to prevent the random nucleation of secondary nuclei. The single domain growth window is in $1000^{\circ}\text{C}-980^{\circ}\text{C}$ investigated by the high temperature video in-situ. By the PMP process we have successfully grown several PMP-YBCO single domain samples with the following size $\Phi 30\text{mm}\times 15\text{mm}$ in one batch.
3. We have investigated the effect of geometry on the phase transitions and on the process. We used samples referred as hole sample which were pressed and/or machined with a network of regularly distributed holes. This results in a geometry with thin wall below 3 mm so that the length of the diffusion path for thermal or chemical diffusion is drastically reduced. The reduced diffusion path influences the phase transition of PMP-YBCO with artificial holes provides an effective tunnel for oxygen diffusion in the 123 crystal growth. When the specific surface area is larger than $100\text{mm}^2/\text{g}$, a PMP-YBCO single domain can be fully grown in a pellet with the following size: $\Phi 20\text{mm}\times 18\text{mm}$.
4. The heating rate influences the phase transition of PMP-YBCO bulk. The critical heating rate $120^{\circ}\text{C}/\text{h}$ is found to avoid the 123 formation in hole PMP-YBCO single domain samples. The heating rate also influences the size of 211 particles as well as the magnetic critical current density J_{cm} . The faster or the slower heating rate will refine the 211 particles. The feasible heating rate is necessary to be selected in the PMP-YBCO single domain growth
5. The effect of the overheating temperature T_0 on the nucleation temperature T_n in PMP-YBCO is studied. The 123 nucleation temperature T_n reduces as the overheating temperature T_0 increases. As the overheating temperature T_0 was increased from 1060°C

to 1150°C , the 123 nucleation temperature T_n reduced from 1004°C to 997°C. A high overheating temperature delayed the nucleation. This phenomenon is analyzed according with the Turnbull's heterogeneous nucleation theory.

6. In the dynamic study of growth of hole PMP-YBCO single domain samples which present the particularity of reduce diffusion path, a critical undercooling $\Delta T'$ is found in the PMP-YBCO single domain growth. It is 10~18K to the growth rate on ab plane and 20K to the growth rate along c-axis. When $\Delta T < \Delta T'$, the growth rate increases with the undercooling decreasing. When $\Delta T > \Delta T'$, the growth rate decreases with the undercooling increasing. It is found the phenomenon of the growth rate decreasing with an increasing undercooling is related to the oxygen diffusion. When the oxygen super-saturation and the diffusion velocity are lower, the growth rate is limited by the oxygen diffusion even though the thermal undercooling increases. It is found the growth rate R_c is directly proportional to the oxygen diffusion velocity V_{O_2} . The PMP-YBCO single domain growth is dominated by the oxygen diffusion. The growth rate R_a is $5\sim 18 \times 10^{-5}$ mm/s and the growth rate R_c is $4\sim 10 \times 10^{-5}$ mm/s, R_a is about two times of R_c .
7. The 123 crystal growth of the hole PMP-YBCO single domain depends on two growth systems: the melt-solid system and the vapour-solid system. In the melt-solid growth system, the growth rate is proportional to the square of the undercooling value ΔT , as $R \propto \Delta T^2$. In the vapour-solid system, the growth rate is related to the oxygen mass transport velocity $R_c \propto V_{O_2}$. And the 123 growth depends on two types diffusions: 1)The yttrium, barium and copper ions diffuse through the liquid melt to the 123 growth interface from the solution diffusion and interfacial diffusion as in melt-solid system. 2) The oxygen diffusion depends on interfacial diffusion from air as in vapor-solid system.
8. In the PMP-YBCO single domain growth, the growth of 123 crystal is not only depending on the thermal undercooling but also on the constitutional undercooling. The 123 crystal growth driving force comes from both of the thermal undercooling ΔT_T and the constitutional undercooling ΔT_c , $\Delta T = \Delta T_T + \Delta T_c$. At the same time it should consider the oxygen super-saturation and its diffusion.
9. The hole PMP-YBCO single domain has a typical morphology of square single domain. The distribution of the 211 particles below the seed is characteristic of the pushing-trapping phenomenon. Out of this region, it has the specific character of PMP process: a homogenous distribution of fine and spherical 211 particles as the. The hole shape has no influence on the 123 crystal textured growth, but helps to decrease the porosity diameter.
10. The high pressure oxygen treatment is proved to increase the oxygen constant $7-\delta$ of 123 crystal. It improves the trapped magnetic field B_{tr} of hole PMP-YBCO single domain to

739mT in diameter of $\Phi 15\text{mm}$ sample at 77K. The magnetism critical current density \mathbf{J}_{cm} is achieved as $\sim 1.2 \times 10^5 \text{A/cm}^2$ (77K, 0T) in the PMP-YBCO single domain which reaches the best record at present.

11. The irreversibility field \mathbf{B}_{irr} line of PMP-YBCO sample is below it of the sample with oxygen content $\delta < 0.003$, so the \mathbf{B}_{irr} of PMP-YBCO can be improved further. The flux pinning in PMP-YBCO sample is analyzed not only to the 211 particles but also to the superconducting transition temperature \mathbf{T}_c (oxygen constant), which of the $\delta\mathbf{l}$ -pinning and the $\delta\mathbf{T}_c$ -pinning.
12. The transport critical current density \mathbf{J}_{ct} is measured to $\sim 7.5 \times 10^3 \text{A/cm}^2$ (78.5K). It is lower two order magnitudes than the magnetism critical current density \mathbf{J}_{cm} . It reveals the cracks, pores and boundaries existed in the PMP-YBCO sample. To eliminate them is one of key problems in the PMP-YBCO single domain growth.

Prospects

For continuing study, we consider the more fruitful results will be obtained in the following three aspects researches:

1. Based on the susceptibility transition measurement, a quantified analysis system of studying phase transition can be installed in more detail to analyse the phase transition.
2. The flowing oxygen gas putting into furnace can improve the YBCO single domain growth, this method can be used to grow larger size single domain in hole-PMP-YBCO sample.
3. Optimising the high pressure oxygen treatment is necessary to make the oxygen content $\delta < 0.003$ obtained so as to increase the \mathbf{B}_{irr} line resulting in good \mathbf{B}_{tr} value.

Annex 1: Magnetic field character parameter and the temperature distribution measurement

1. Magnetic field distribution measurement and the character parameter

Each coil has its character parameter. Our magnetic coil is provided by the current as shown in the table 1. In most situations, we use 8T value as the current percent is 95.45%.

Table1. The current I value corresponding to the magnetic field B and the current percent (%)

Current I (A)	Magnetic field B (T)	I/Im (%)
114.54	8	95.45%
	7	83.52%
	6	71.58%
71.5875	5	59.65%
57.27	4	47.72%
	3	35.79%
	2	23.86%
	1	11.93%

Supposed the zero position is at the maximum magnetic field in coil. We measured the magnetic field distribution as shown in figure 2.

According to the calculating equations as followings:

$$(B \cdot dB/dz)_{8T} = (B \cdot dB/dz)_{0.2T} \cdot (8^2/0.199^2) = (B \cdot dB/dz)_{0.2T} \cdot 1616.12$$

$$(dB/dz)_{8T} = (dB/dz)_{0.2T} \cdot (8/0.199) = (B \cdot dB/dz)_{0.2T} \cdot 6.36$$

$$B_{8T} = (B \cdot dB/dz)_{8T} / (dB/dz)_{8T}$$

The magnetic field distribution of 8T is calculated from the 0.2T value, as shown in red line. The character of $B \cdot dB/dz$ is also calculated from the values of 0.2T.

We measured the magnetic force of metal Cr in at 8T field. The calculated force and the measured force is consistent each other very well as shown in figure 3. The maximum position is at the between $Z=+10\text{cm}$ and $Z=+11\text{cm}$. The detailed calculated magnetic field

distribution , magnetic field gradient and the magnetic force and the experimental values are listed in table 2.

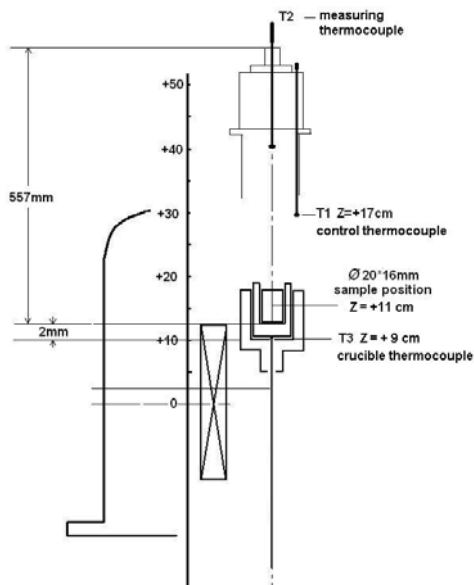


Figure 1. The sample, control thermocouple, measured thermocouples in the coil.

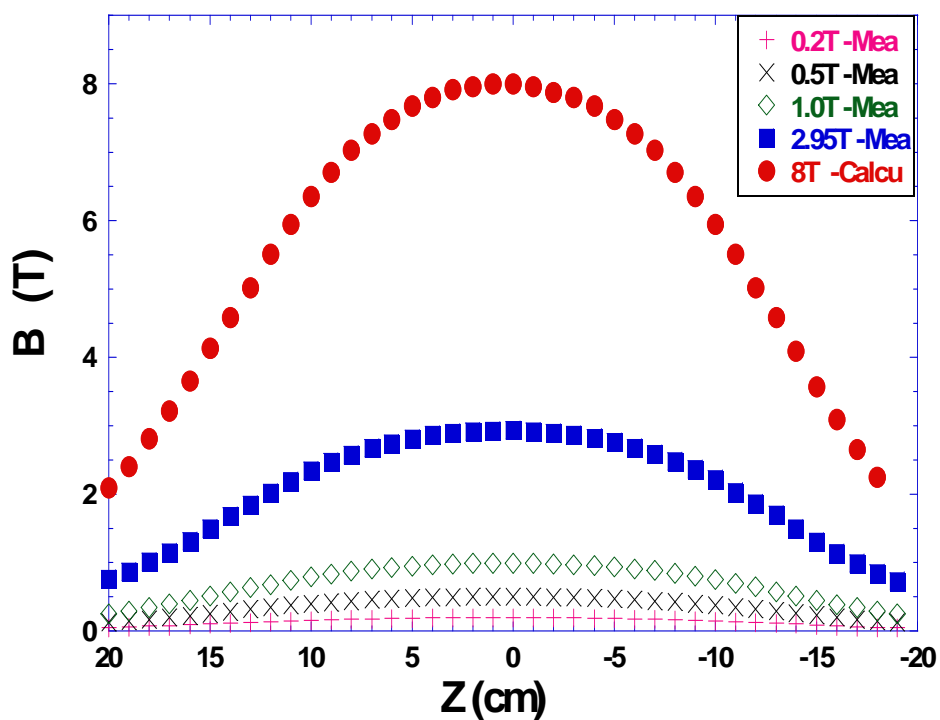


Figure 2 The magnetic field distribution B of 8T and 0.2T

Table 2 The measured data of magnetic field distribution, gradient of 0.2T, 0.8T and the calculated values. The magnetic force of metal Cr (26.035g) in magnetic field

Z (cm)	0.2T measured	0.8T calculated			Calculated Cr force F (g)	Measured Cr force F (g)	Calibrated 0.8T BdB/dz (T ² /m)
	B (T)	B (T)	dB/dz (T/m)	BdB/dz (T ² /m)			
18	0.07	2.8141	40.2	113.13	10.191		
17	0.08	3.2162	42.21	135.75	12.229		
16	0.091	3.6584	46.23	169.13	15.235		
15	0.103	4.1408	46.23	191.43	17.244		
14	0.114	4.583	46.23	211.87	19.085	20.501	
13	0.125	5.0252	46.23	232.32	20.928	22.423	
12	0.137	5.5077	46.23	254.62	22.936	23.636	
11	0.148	5.9499	42.21	251.15	22.624	23.747	263.618
10	0.158	6.3519	38.19	242.58	21.852	23.574	
9	0.167	6.7137	34.17	229.41	20.666	22.285	
8	0.175	7.0353	28.14	197.97	17.833	20.291	
7	0.181	7.2766	22.11	160.88	14.492	17.91	
6	0.186	7.4776	20.1	150.3	13.539	15.392	
5	0.191	7.6786	16.08	123.47	11.122	12.574	
4	0.194	7.7992	12.06	94.058	8.4728	10.101	
3	0.197	7.9198	8.04	63.675	5.7359	7.606	
2	0.198	7.96	4.02	31.999	2.8825	5.37	
1	0.199	8.0002	2.01	16.08	1.4485	3.109	
0	0.199	8.0002	-2.01	-16.08	-1.4485	0.763	
-1	0.198	7.96	-6.03	-47.999	-4.3238	-1.385	
-2	0.196	7.8796	-8.04	-63.352	-5.7068	-3.573	
-3	0.194	7.7992	-10.05	-78.382	-7.0607	-5.855	
-4	0.191	7.6786	-16.08	-123.47	-11.122	-8.381	
-5	0.186	7.4776	-20.1	-150.3	-13.539	-10.676	
-6	0.181	7.2766	-22.11	-160.88	-14.492	-13.381	
-7	0.175	7.0353	-28.14	-197.97	-17.833	-16.011	
-8	0.167	6.7137	-34.17	-229.41	-20.666	-18.851	
-9	0.158	6.3519	-38.19	-242.58	-21.852	-20.695	
-10	0.148	5.9499	-42.21	-251.15	-22.624		
-11	0.137	5.5077	-46.23	-254.62	-22.936		
-12	0.125	5.0252	-46.23	-232.32	-20.928		

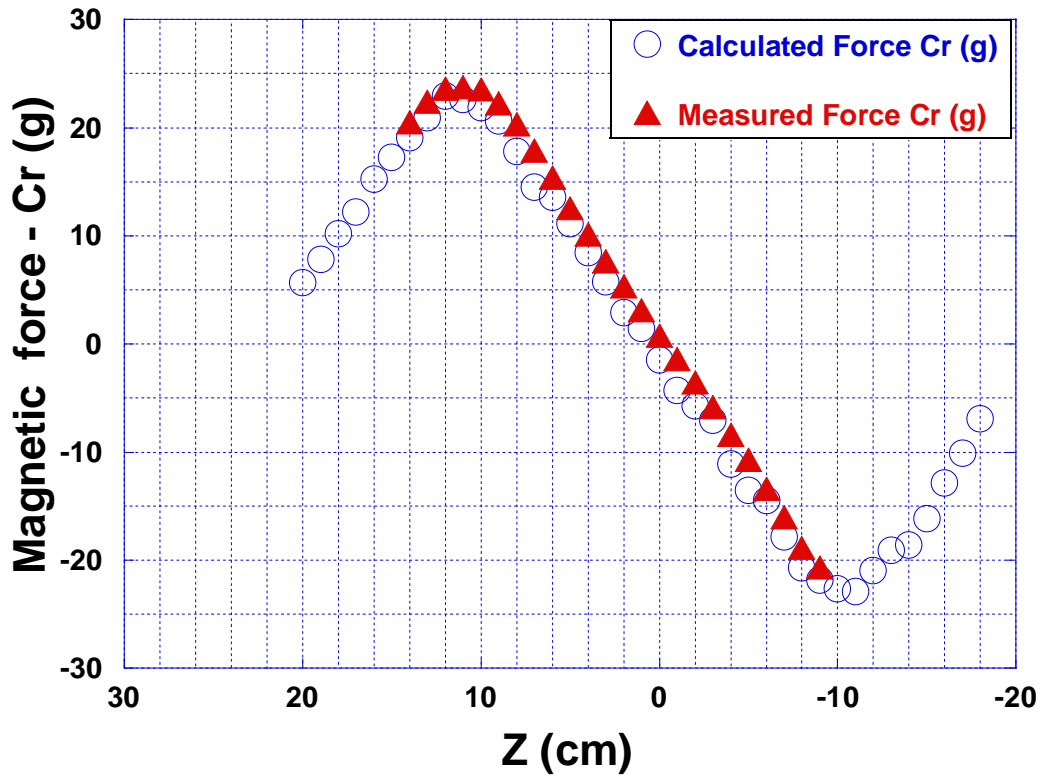


Figure 3 The measured data and the calculated data of magnetic force in 8T of metal Cr

Based the measured force value at $Z=+11$ cm, as listed in table 2, $F=23.747$ g, we calibrated the coil character parameter $\mathbf{B} \cdot d\mathbf{B}/dz$ as $263.618(\text{T}^2/\text{m})$, and the value $\mathbf{H} \cdot d\mathbf{H}/dz$ is transformed to be $263.618 \times 10^6 (\text{Oe}^2/\text{cm})$. The value is used in our experiments for susceptibility calculation.

2. Temperature distribution measurement

The sample placement is designed at the maximum magnetic force and the maximum heating position. We measured the temperature distribution in the coil as keeping the control temperature as $T_1=900^\circ\text{C}$, as shown in figure 4. In the end we found the right position for sample as shown in figure 5.

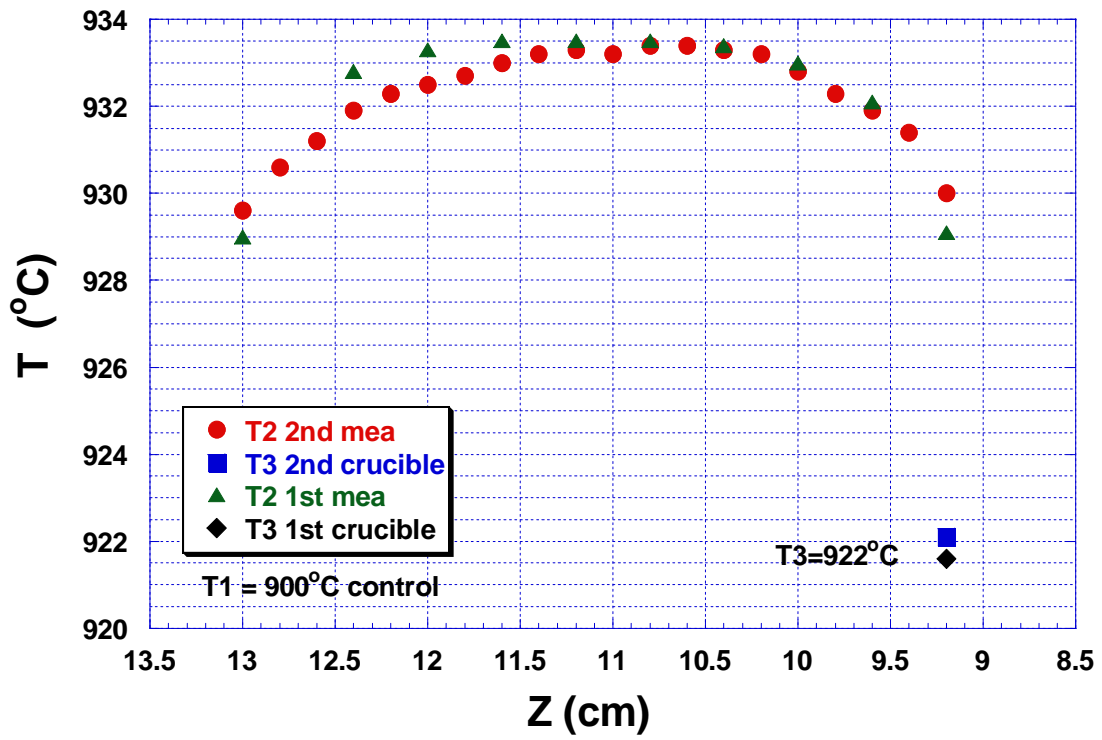


Figure 4 The measured temperature distribution in coil

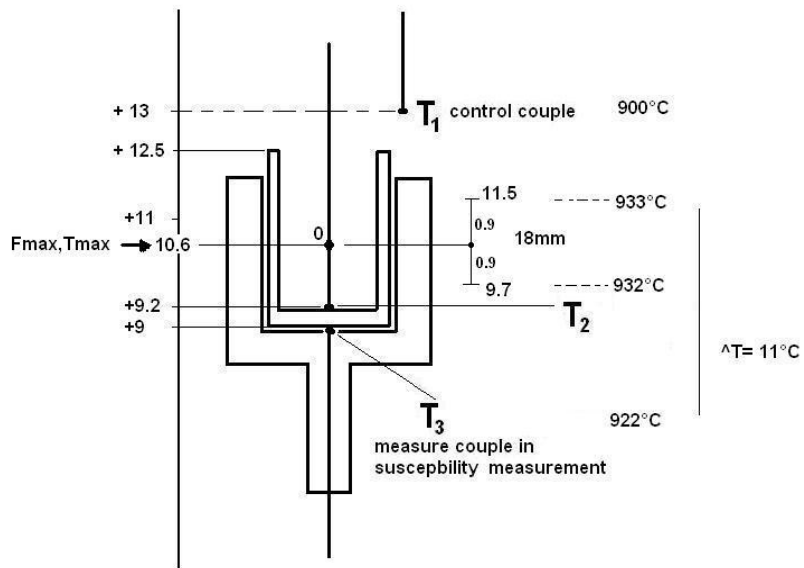


Figure 5 The sample position and the thermocouples position in the coil.

Annex 2 : Susceptibility and oxygen lost calculation of PMP-YBCO sample

1. Experimental measurement signals and susceptibility calculation

The magnetic susceptibility is derived from measuring the magnetic force by a weighting device exerted on the magnetic material placed in a known field gradient. The force is described as:

$$\mathbf{F} = \chi \cdot \mathbf{m} \cdot \mathbf{H} \cdot d\mathbf{H}/dz \quad (1)$$

Here \mathbf{F} is the force of the material in magnetic field, χ its susceptibility, \mathbf{m} its mass, \mathbf{H} the applied magnetic field strength and $d\mathbf{H}/dz$ is the magnetic field gradient. In our experiment, the measured $\mathbf{B} \cdot d\mathbf{B}/dz$ is $263.6 \text{ T}^2/\text{m}$ at the assumed sample position. $\mathbf{H} \cdot d\mathbf{H}/dz$ is obtained from $\mathbf{B} \cdot d\mathbf{B}/dz$. As,

$$\mathbf{H} \cdot d\mathbf{H}/dz = 263.6 \times 10^6 \text{ (Oe}^2/\text{cm)} \quad (2)$$

The sample susceptibility can be calculated from its measured magnetic force from equation (1), is

$$\chi = \mathbf{F} / (\mathbf{m} \cdot \mathbf{H} \cdot d\mathbf{H}/dz) \quad (3)$$

There is two superposed substrates under the sample which avoid bulk YBCO reacting with Al_2O_3 crucible. The substrate just below the sample is a layer of 123 and Yb123 mixture (about 4g with a 1:0.2 weight ratio). It is placed on an Y_2O_3 layer (about 2.5g), as shown in the figure 1. The sample with substrates in its alumina crucible is put into a vertical furnace.

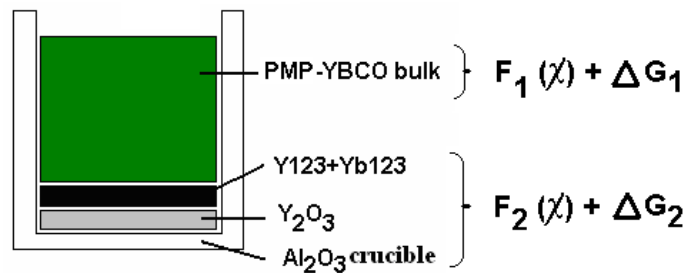


Figure 1. The placement of sample. The PMP-YBCO bulk is placed on the substrates 123/Yb123 and Y_2O_3 layers, three of them is in an Al_2O_3 crucible. $\mathbf{F}_1(\chi) + \Delta\mathbf{G}_1$ is contributed from the PMP-YBCO bulk; $\mathbf{F}_2(\chi) + \Delta\mathbf{G}_2$ is from substrates 123/Yb123, Y_2O_3 and crucible.

It is found that the substrates are necessary for growing PMP-YBCO single domains. We measured the susceptibility of the PMP-YBCO sample without substrates. But the 123 crystal was not growing during the cooling stage because of a serious reaction between the PMP-YBCO pellet and the alumina crucible as well as because of an important liquid phase loss. Therefore the measured susceptibility transition data of PMP-YBCO without substrates did not

display the real phase transition of the PMP-YBCO growth. So we used the configuration with substrates to study the phase transition of PMP-YBCO.

Attention has to be paid to the original force signal \mathbf{F} , it is as

$$\mathbf{F} = \mathbf{F}_i(\chi) + \Delta\mathbf{G}_i \quad (4)$$

where $\mathbf{F}_i(\chi)$ is the “magnetic force” measured by the balance and $\Delta\mathbf{G}_i$ the gravitational weight. We assumed that the reaction between PMP-YBCO and substrates is neglected. The measured force signal \mathbf{F} includes the magnetic force $\mathbf{F}_1(\chi)$ related to the susceptibility χ contribution of the PMP-YBCO bulk, the magnetic force $\mathbf{F}_2(\chi)$ related to the susceptibility of the substrates (Yb123+123, Y_2O_3) with the Al_2O_3 crucible, the weight $\Delta\mathbf{G}_1$ comes from the weight variation of PMP-YBCO bulk itself, the weight $\Delta\mathbf{G}_2$ of the weight lost of substrates (Yb123+123, Y_2O_3) with the Al_2O_3 crucible. The measured force could be described in equation (5), as well as shown in figure 1.

$$\mathbf{F} = \mathbf{F}_1(\chi) + \mathbf{F}_2(\chi) + \Delta\mathbf{G}_1 + \Delta\mathbf{G}_2 \quad (5)$$

After removing the force signal $\mathbf{F}_2(\chi)$, $\Delta\mathbf{G}_1$ and $\Delta\mathbf{G}_2$ from the total force signal (\mathbf{F}), the susceptibility of PMP-YBCO sample can be derived from $\mathbf{F}_1(\chi)$ using the equation (3). In order to remove the signals which are not contribution to the PMP-YBCO susceptibility from the overall signal, we performed four kinds of measurements. They are named sample A, B, C, D and listed in table 1.

For the four samples, substrates and crucibles used, we pay attention to keep the same mass in order to enable the comparison of data and the calculation needed to obtain the own susceptibility PMP-YBCO pellet. Samples A and B are tested in an 8T field for the susceptibility measurement. When there is no magnetic field, the magnetic field $B=0\text{T}$, the Faraday balance setup can be used as a sensitive thermogravimetric (TG) analyzer. Samples C and D are tested in zero field (0T) for their weight lost measurement.

Table 1. Mass comparison of samples A, B, C, D, substrates and crucibles, with or without magnetic field for magnetic force or TG measurement by the Faraday balance setup.

Sample		Mass (g)			
		PMP-YBCO	Yb123-123	Y_2O_3	Crucible
A	PMP-YBCO/ Yb123-123/ Y_2O_3 /Crucible, B=8T	20.0	4.0	2.5	48.0
B	Yb123-123/ Y_2O_3 / Crucible, B=8T	/	4.1	2.6	48.2
C	PMP-YBCO/Yb123-123/ Y_2O_3 /Crucible, B=0T	20.0	4.0	2.5	47.6
D	Yb123-123/ Y_2O_3 /Crucible, B=0T	/	4.0	2.5	48.0

Sample A is the PMP-YBCO bulk with 123/Yb123, Y_2O_3 substrates and alumina crucible measured in magnetic field (8T), as shown in figure 2. The measured signal F_A is described as

$$F_A = F_1(\chi) + F_2(\chi) + \Delta G_1 + \Delta G_2 \quad (6)$$

Sample B is only the substrates and crucible set measured in magnetic field (8T), as shown in figure 3. its force signal F_B is

$$F_B = F_2(\chi) + \Delta G_2 \quad (7)$$

Sample C is the PMP-YBCO pellet with the substrates/crucible set measured within zero field (0T), as shown in figure 4. The force signal F_C

$$F_C = \Delta G_1 + \Delta G_2 \quad (8)$$

Sample D is the substrates/crucible set measured with zero field (0T), as shown in figure 5.

$$F_D = \Delta G_2 \quad (9)$$

The magnetic force of PMP-YBCO sample can be obtained from (6), (7), (8), (9), as

$$F_1(\chi) = F_A - F_B - (F_C - F_D) \quad (10)$$

So that the susceptibility χ of PMP-YBCO is derived from equation (3) and (10), is

$$\chi = F / (\mathbf{m} \cdot \mathbf{H} \cdot d\mathbf{H}/dz) = F_1(\chi) / (\mathbf{m} \cdot \mathbf{H} \cdot d\mathbf{H}/dz) \quad (11)$$

It is calculated and plotted changing versus temperature in thesis. The arithmetical mean error is estimated $\delta\chi / \chi \approx 10^{-3}$.

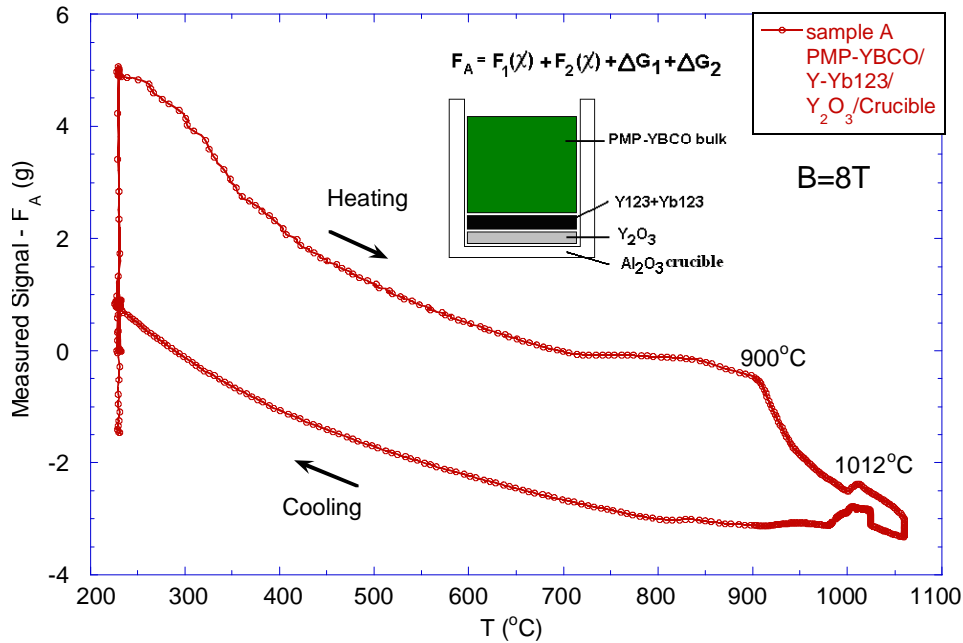


Figure 2. Measured signal F_A by the Faraday balance in 8T field. It includes the magnetic force $F_1(\chi)$ related to the PMP-YBCO pellet, $F_2(\chi)$ to the substrates and crucible, as well as the weight contribution ΔG_1 of the PMP-YBCO pellet and ΔG_2 of the substrates and crucible when their susceptibility changed and the weight lost in high temperature. Here we used the unit **gram** for magnetic signal, so that the magnetic force can be compared and calculated with weight.

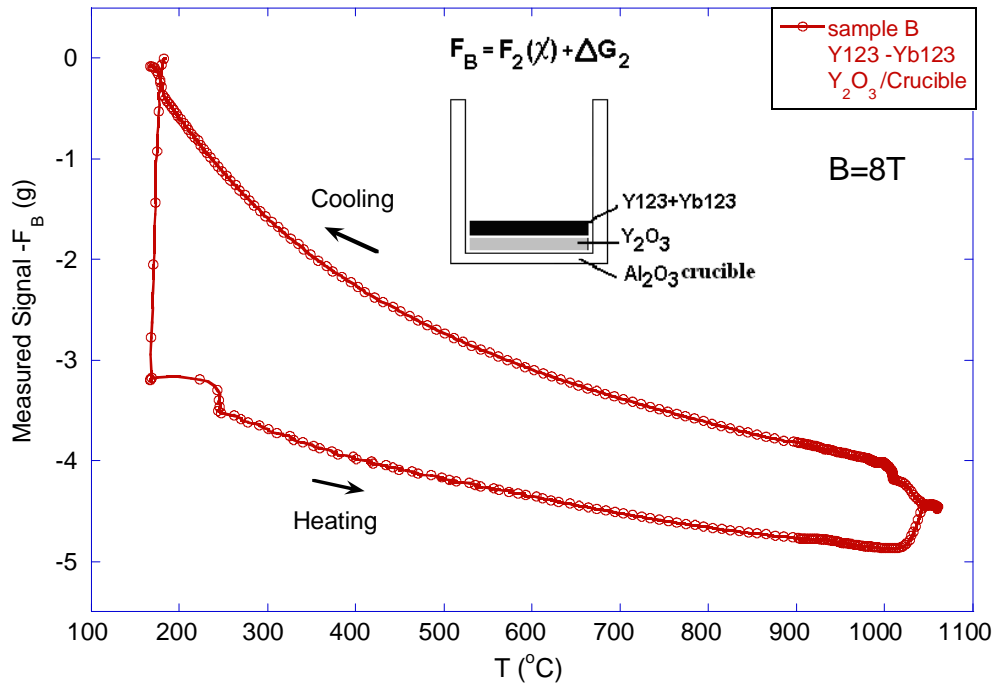


Figure 3. Signal of sample B (the substrates and crucible) measured by the Faraday balance in an 8 T field. The signal is the magnetic force $F_2(\mathbf{B})$ of the substrates and crucible, and the weight contribution (ΔG^*) of the substrates and crucible.

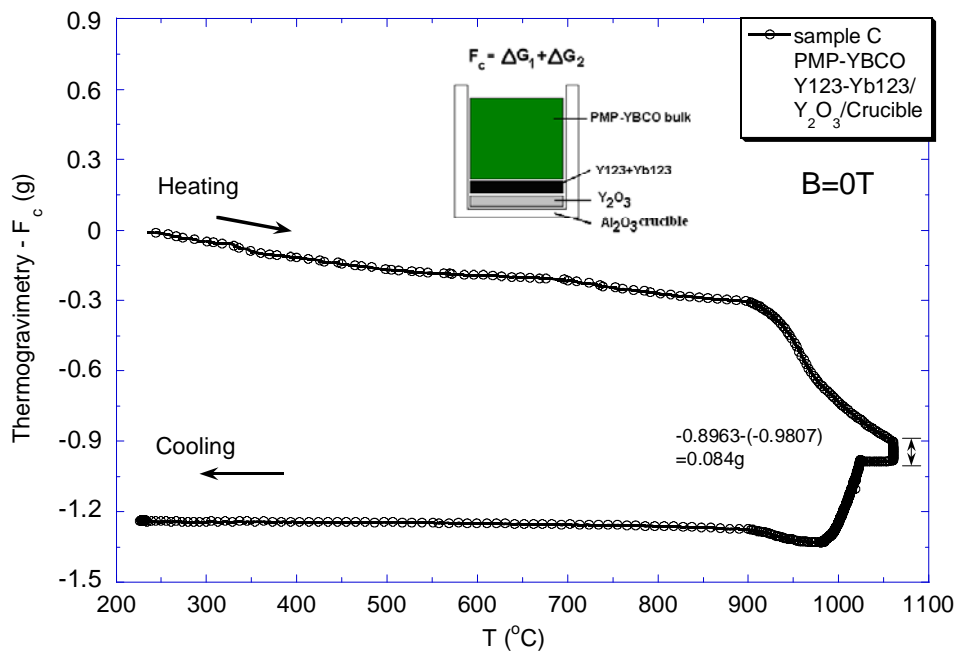


Figure 4. Thermogravimetry of sample C (the PMP-YBCO pellet with the substrates and crucible) measured by the Faraday balance in no magnetic field ($B=0T$). The force signal $\Delta G(C)$ includes the weight losses of the PMP-YBCO pellet, the substrates and crucible.

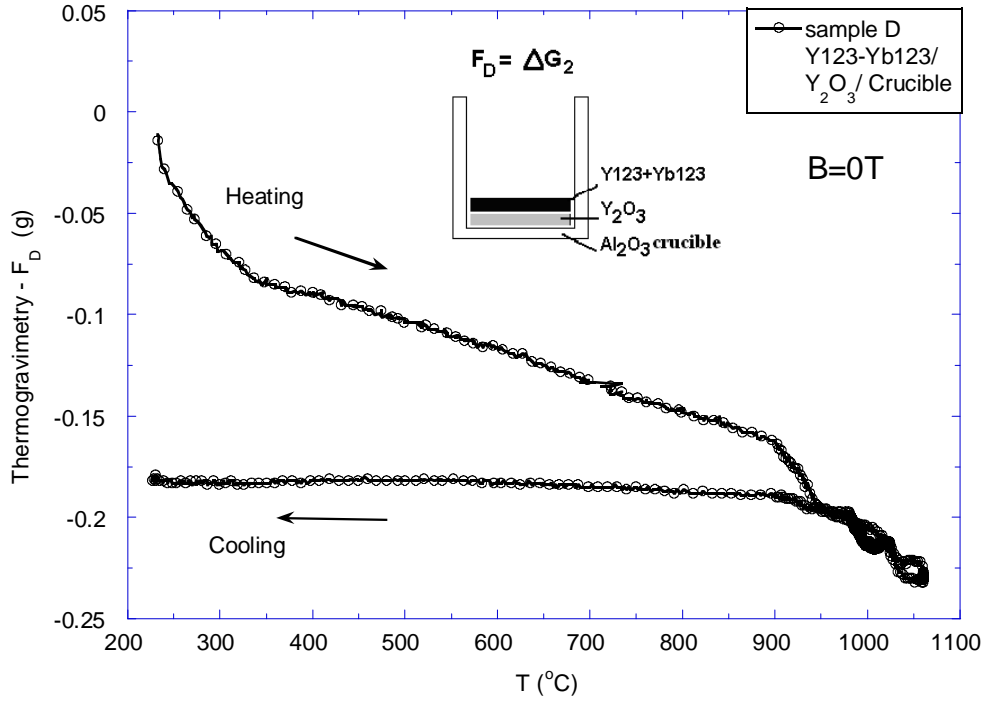


Figure 5. Thermogravimetry of sample D (the substrates and crucible) measured by the Faraday balance in no magnetic field ($B=0T$). The force signal $\Delta G(D)$ corresponds to the weight losses of the substrates and crucible.

2. Oxygen lost calculation from the thermogravimetry

The calculated susceptibility χ of the PMP-YBCO bulk versus temperature is shown in thesis figure 2-6. it is analyzed the $Cu^{2+}(L1)$ decomposes into $Cu^+(L2)$ and releases oxygen in $1012^{\circ}C-1060^{\circ}C$ and at $1060^{\circ}C$. The susceptibility and the thermogravimetry keep decreasing as shown in figure 6 and figure 7. In order to analyze the phase transition at $1060^{\circ}C$, we deal with the measured signal of PMP-YBCO bulk using equations (12) and (13), and plotting the resulting signal of F_A-F_B and F_C-F_D in figure 6 and figure 7. The equation (12) represents the measured force and weight lost signal. The equation (13) represents the weight lost signal of PMP-YBCO bulk.

$$F_A-F_B = F_1(\chi) + \Delta G_1 \quad (12)$$

$$F_C-F_D = \Delta G_1 \quad (13)$$

In figure 6, at $1060^{\circ}C$, the signal decreases $0.3347g$ in F_A-F_B line and the weight lost in F_C-F_D line is $0.0801g$.

Considering the $Cu^{2+}(L1)$ decomposing in high temperature, the reaction $Cu^{2+}(L1) \rightarrow Cu^+(L2) + O_2$, the magnetic Cu^{2+} ion transforms to nonmagnetic Cu^+ ion. It makes the susceptibility decreasing so that to decrease its magnetic force and with the oxygen lost. It is calculated the mol amounts n_{CuO} of CuO is $1/8$ times of oxygen mass. Named the released oxygen mass as ΔG_{CuO} , the mol amounts n of CuO is $n_{CuO} = (1/8) \Delta G_{CuO}$. Since the mol susceptibility χ_{CuO} of CuO is equal to the mol susceptibility of Cu^{2+} at $1060^{\circ}C$ and calculated in equation (11):

$$\chi_{CuO} = \chi_{Cu^{2+}} = \frac{C}{T} = \frac{0.45}{1060 + 273} = 337 \times 10^{-6} (emu / Oe \cdot mol) \quad (15)$$

C is the Curie constant of Cu^{2+} ion as 0.45. From the equation (11), (2) and (3), the magnetic force of CuO has a relationship of ΔG_{CuO} :

$$F_1(\chi) = \chi_{\text{CuO}} \cdot n_{\text{CuO}} \cdot H \frac{dH}{dz} = 11.1 \cdot \Delta G_{\text{CuO}} \quad (16)$$

Therefore,
$$F_1(\chi) + \Delta G_{\text{CuO}} = 12.1 \cdot \Delta G_{\text{CuO}} \quad (17)$$

Noticing the experimental released oxygen is:

$$\Delta G_{\text{CuO}} = 0.0801\text{g} \quad (18)$$

The total magnetic force with released oxygen from Cu^{2+} (L1) decomposition is:

$$F_1(\chi) + \Delta G_{\text{CuO}} = 0.9692\text{g} \quad (19)$$

Comparing both of the calculating data and the experimental data:

$$0.9692\text{g} > 0.3347\text{g} \quad (20)$$

Obviously, the calculated data is larger than the measured experimental data. The result suggests that there is other oxygen released in other reason except CuO decomposition, which is suggested as the oxygen dissolved in the sample. We name this dissolved oxygen as $\Delta G'$. Basing on the analysis, the released oxygen is dissolved in the sample, when the temperature is increasing the dissolved oxygen will release off. It contributes the oxygen lost $\Delta G'$.

So that we can add an equation (21) to the equation (12) and (13) as:

$$\Delta G_1 = \Delta G_{\text{CuO}} + \Delta G' \quad (21)$$

$\Delta G'$ comes from the dissolved oxygen in the PMP-YBCO sample.

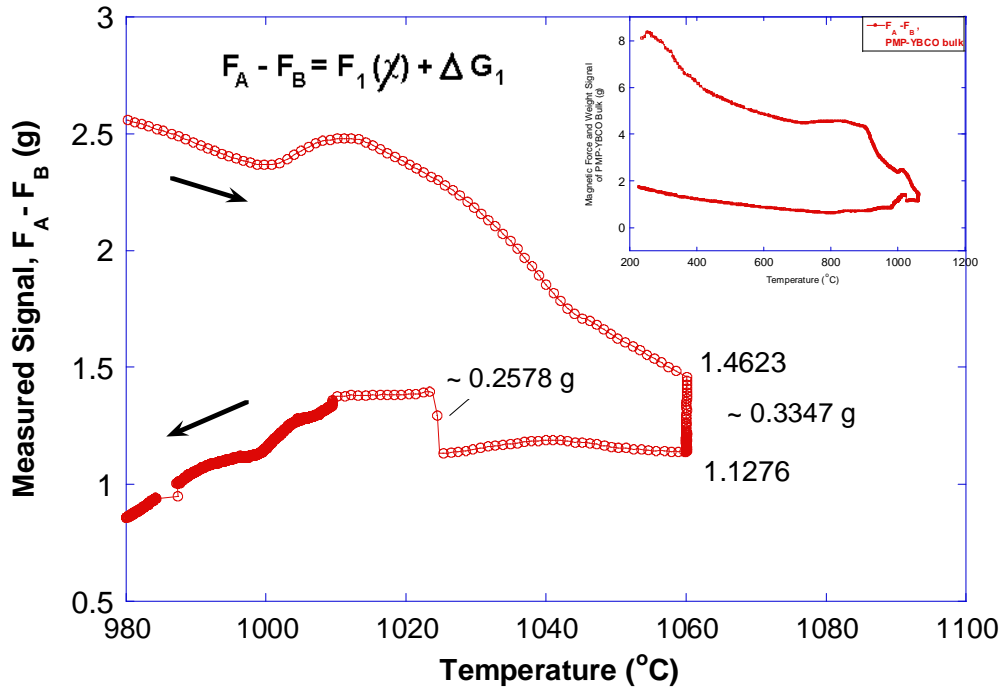


Figure 6 Measured signal of PMP-YBCO sample in 8T magnetic field including magnetic force and the weight lost signal. It is obtained by F_A minus F_B . At 1060 $^{\circ}\text{C}$, the decreased signal is 0.3347g.

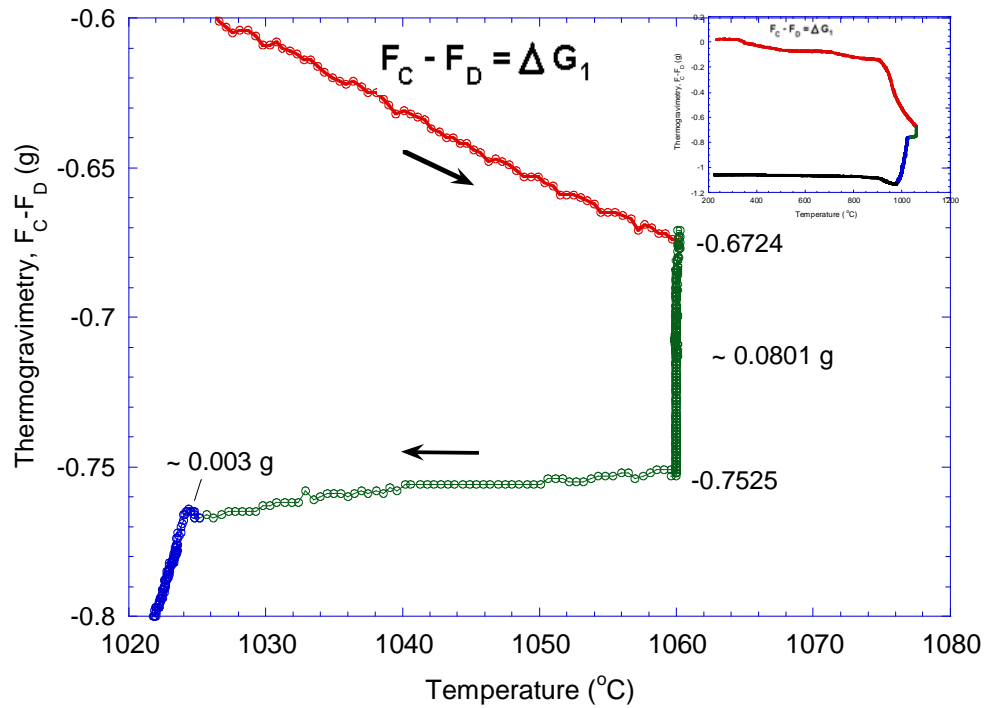


Figure 7 TG signal of PMP-YBCO sample. it is noticed the weight decreased 0.0801g at 1060°C.

Cooling stage

At 1025°C. From 1025°C the cooling rate is changed and the sample is cooled down slowly at 1°C/h. The susceptibility is found to increase around 1025°C in a few degree range. As the reaction happened $\text{Cu}^+(\text{L2}) + \text{O}_2 \rightarrow \text{Cu}^{2+}(\text{L1})$, the nonmagnetic Cu^+ ion transforms into the magnetic Cu^{2+} ion with a susceptibility increase as a result. And the same phenomenon of susceptibility rising is also found in MTG process, which is explained of the “oxygen uptake” as the Cu_2O transform to CuO .

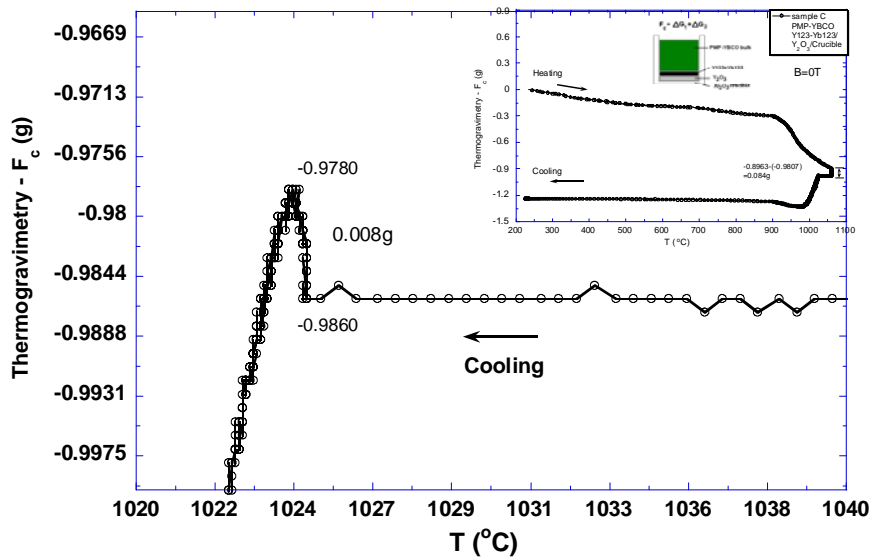


Figure 8 Thermogravimetry of PMP-YBCO at 1020°C-1040°C

As analyzing above, at 1025°C, the experimental absorbed oxygen is:

$$\Delta G_{CuO} = 0.008g \quad (22)$$

So the total magnetic force with absorbed oxygen from $Cu^+(L2)+O_2 \rightarrow Cu^{2+}(L1)$ reaction is:

$$F_1(\chi) + \Delta G_{CuO} = 0.0968g \quad (23)$$

As the experimental data is 0.2578g as shown in figure 6, comparing the calculating data and the experimental data:

$$0.0968g \ll 0.2578g \quad (24)$$

This result indicates that there is other oxygen as dissolved in the sample contributing the reaction, as same equation as (21):

$$\Delta G_1 = \Delta G_{CuO} + \Delta G'$$

$\Delta G'$ comes from the dissolved oxygen in the PMP-YBCO sample.

Annex 3 : Effect of changing heating rate on the measured signal

We investigated the effect of changing heating rate on the measured signal of PMP-YBCO. For example, the sample PMP-YBCO used in this paper. Comparing the effect of temperature and the heating or cooling rate on the measured signal, as the following figure 1, the influence of temperature on measured signal is much more than the influence of heating rate changing on it, although the influence of heating/cooling rate on measured signal can not be ignored.

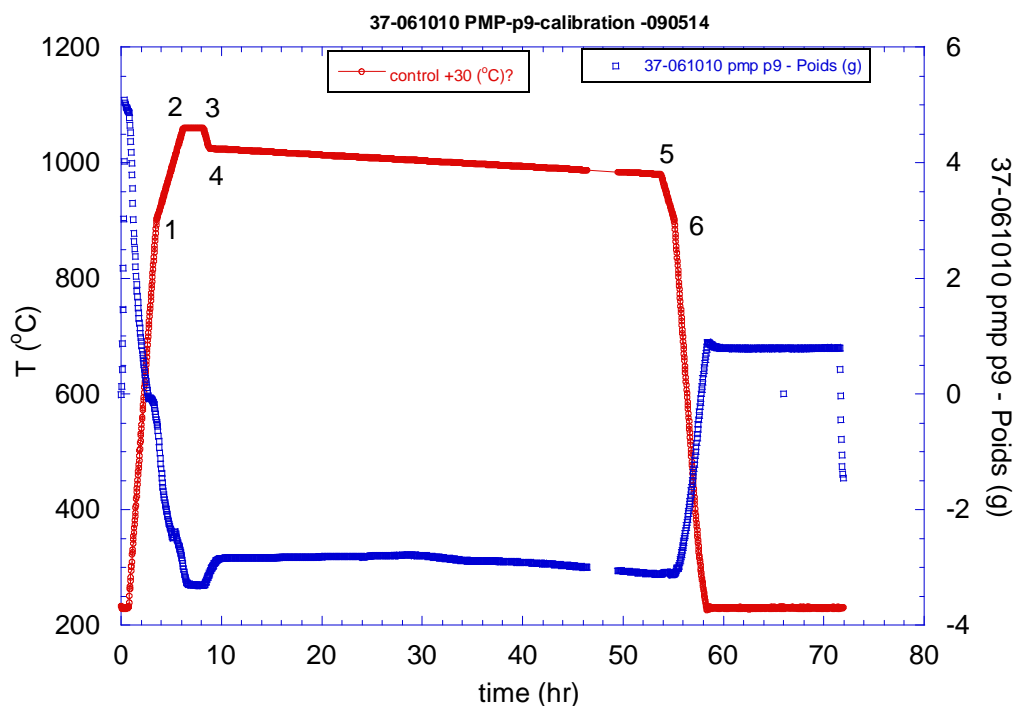


Figure 1 It is the measured signal line and process in whole time

We can compare both inflexion at heating/cooling rate changing. Figure 2 to figure 4 are in detailed. It is the change of 240°C/h – 60°C/h at 900°C. The inflection of signal line at 900°C is small, but at 730°C, 1000°C, 1012°C with the same heating rate, the inflection is obvious. The measured signal is mainly changed by the temperature from 200°C to 1060°C, as shown in figure 2.

When the temperature changes from 1060°C to 1025°C, the cooling rate from 60°C/h to 1°C/h, the signal goes to the equilibrium using 1 hour to balance the effect of the changing cooling rate on the signal, as shown in figure 3.

As shown in figure 4, it is obvious that the temperature making the inflection at 1004 °C instead of the cooling rate changing, since the cooling rate not changing.

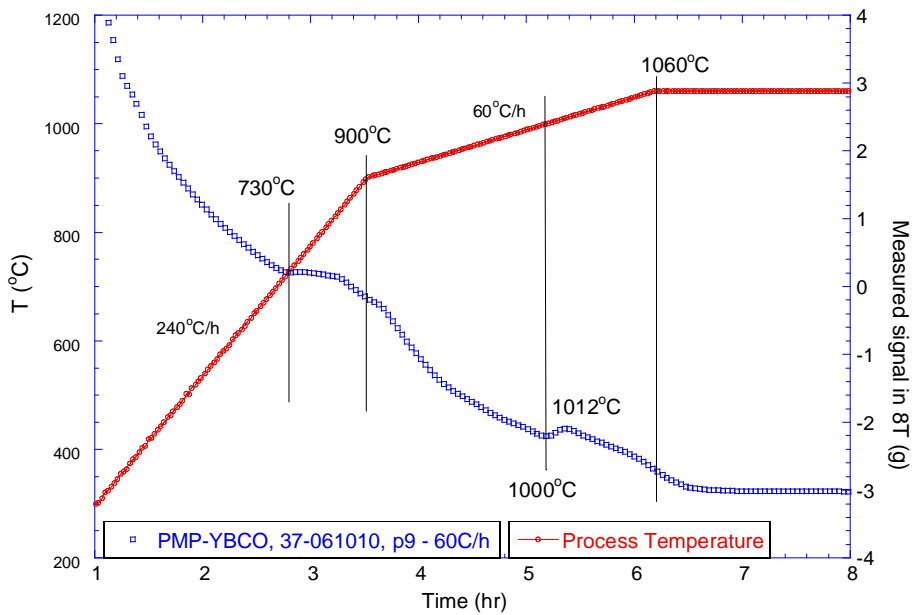


Figure 2: The inflection of signal line at the change of 240°C/h – 60°C/h at 900°C.

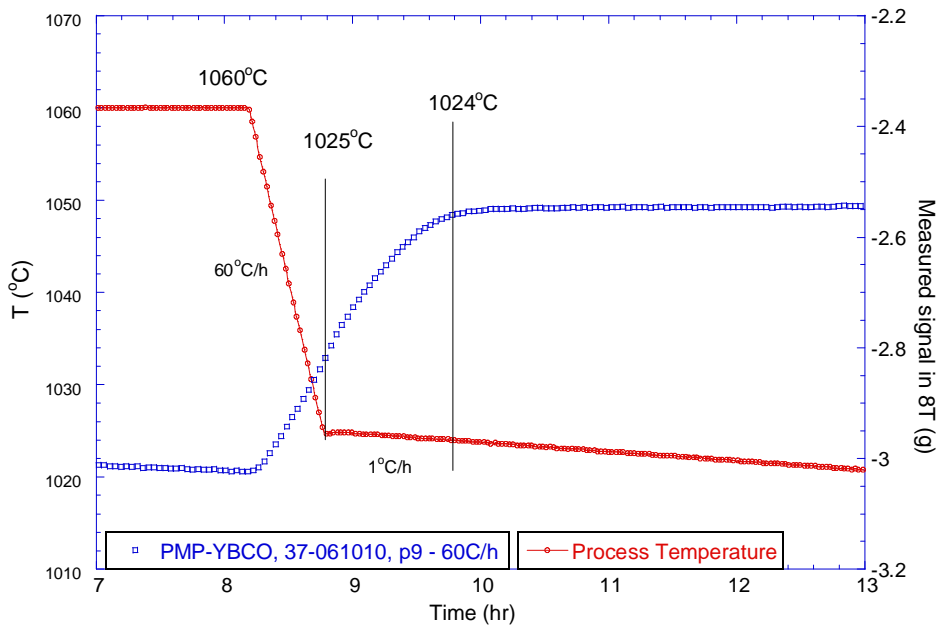


Figure 3: The inflection of signal line at the change from 1060°C to 1025°C, cooling rate from 60°C/h to 1°C/h.

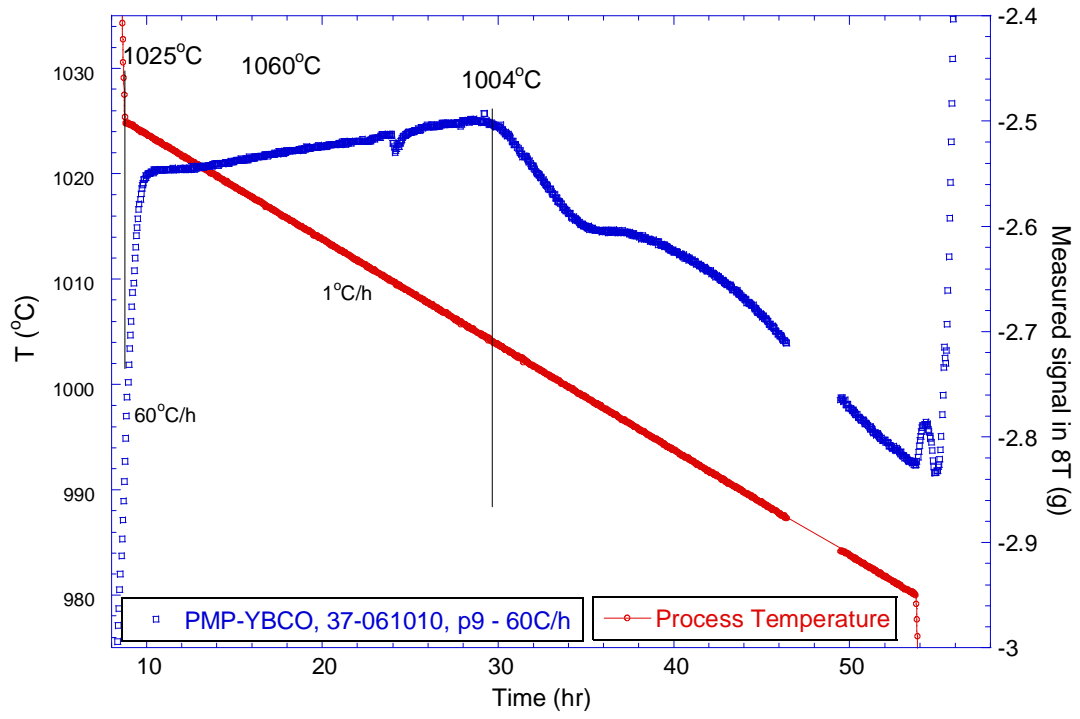
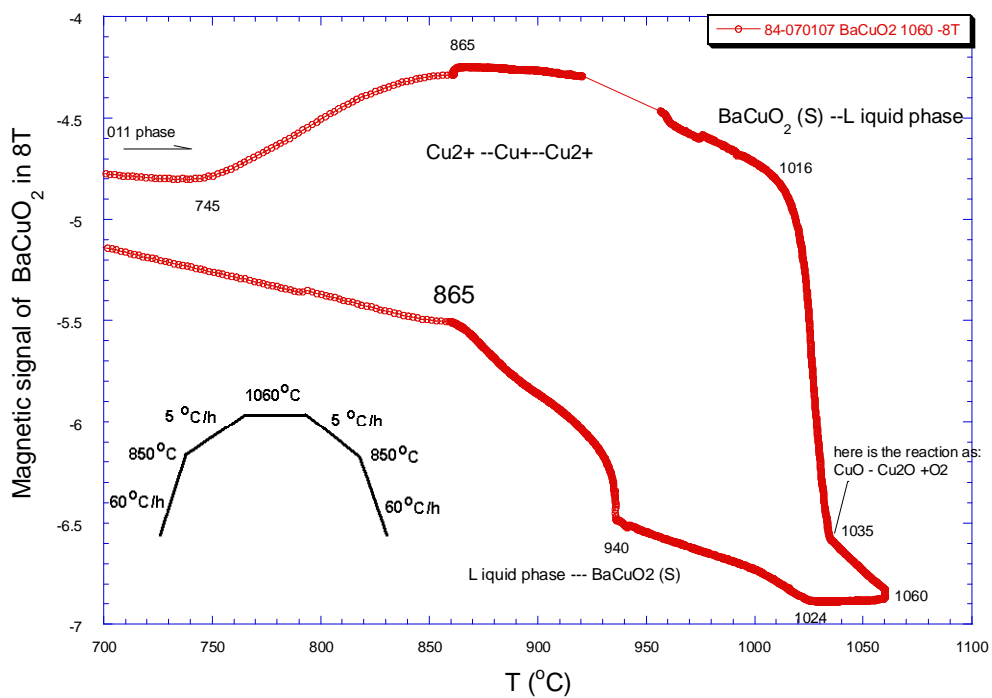


Figure 4: The inflection of signal line at at 1004 °C.

Annex 4 : The susceptibility measured signal of 011 phase

The susceptibility transition of 011 phase is investigated as shown in following figure. The figure is the 011 phase tested magnetic signal line in 8T. It shows the reaction at 865°C, 1006°C, 1035°C in heating and 1024°C in cooling. According the Bao-CuO phase diagram, above 890°C, the 011 begin to melt to liquid phase. From the susceptibility transition of 011, the melting range is supposed at 865-1016, after 1016, the 011 phase is melted as liquid phase.

Otherwise, it needs more experiments such as quench and X-ray diffraction to identifying it further. However, the 011 phase transition affects much more on the reaction inflexion of PMP-YBCO, such as 900°C.



The susceptibility transition line as magnetic signal of 011 phase is tested in 8T.

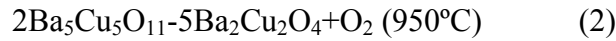
Annex 5 : Porosity Calculation

A selection for explanation of porosity in sample from paper will be published: Effect of Specific Surface Area on Growth and Porosity of Oxide Superconducting Ceramic YBCO Single Domain

C P Zhang^{1,2,4}, X Chaud³, H T Cao¹, E Beaugnon^{3,4}, L Zhou^{1,2}

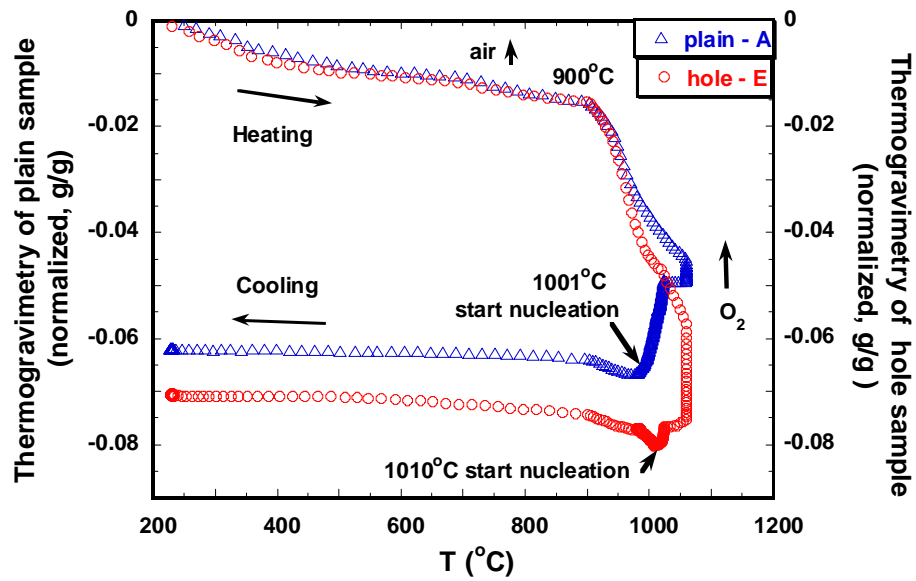
Porosity distribution

The oxygen released from sample based on the BaCuO₂ and CuO decomposition in high temperature [A.5.1], as:

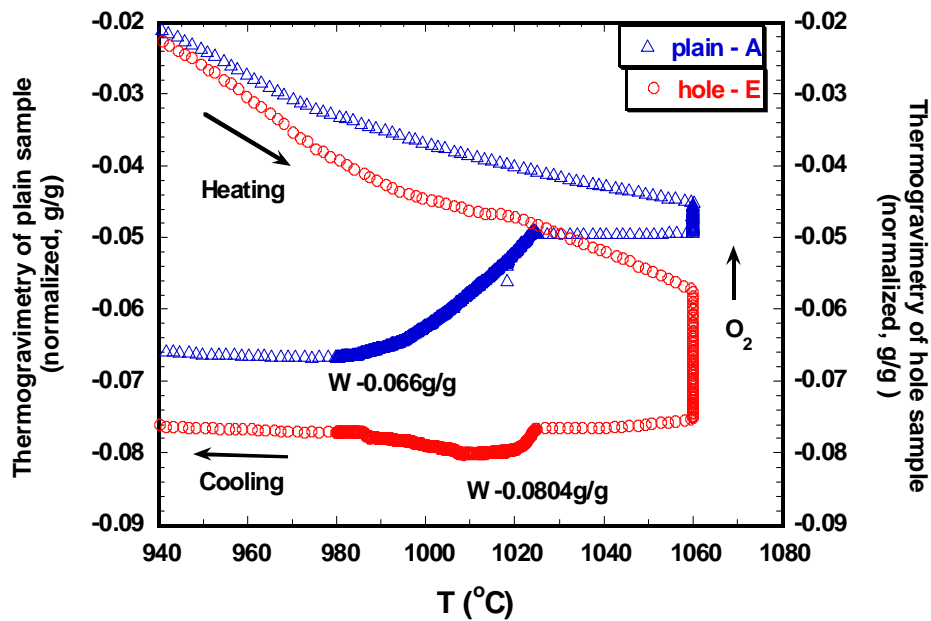


So the pore is formed by the remnant oxygen within the sample as well as the air inside. As the oxygen released, a weight lost phenomenon is happened in the thermogravimetry measurement (figure 3). Corresponding to the plain sample A and the hole 55 sample E. Secondly it is related to the oxygen emitting out from the BaCuO and CuO decomposing. The weight lost is normalized by the sample's mass, and the weight lost in hole sample is much more than that in plain sample. The maximum weight lost in plain sample A is 66mg/g and it is 80mg/g in hole sample E (figure 3b). It means a large quantity of remnant oxygen pocked in the plain sample.

The microstructure of the plain and the hole sample is shown in figure 4 and figure 5 which observed by SEM. The mean porosity diameter in plain sample is observed as 80 μm , and it is about 5 μm in the hole sample. This result indicates the large quantity of oxygen pocked in the plain sample resulting in larger pore diameter. We calculate the porosity distribution density of the sample based on the thermogravimetry measurement and porosity observation. The calculation is processed as counting the pore numbers N in the sample then divided by the expanding sample's area S . The expanding sample's area is supposed as the same sample's volume expanding to an area with the thickness of one pore diameter. At first we calculate the oxygen mass of one pore m . Second to calculate the remnant oxygen mass ΔW in the sample. Then the pore numbers N in sample can be obtained ($N=\Delta W/m$). So the porosity distribution density can be calculated as N/S and listed in table 2. The porosity distribution is $1/(100\mu\text{m})^2$ in plain sample and $\sim 8/(10\mu\text{m})^2$ in hole sample. The porosity distribution is consistent with the experimental observation.



a.



b.

Figure 3. Thermogravimetric curve of plain and hole PMP-YBCO sample A and E. The air and the oxygen released out make the weight lost in sample. a. Thermogravimetric curve in whole process. The weight lost in hole sample E is larger than it in plain sample A. b. Room-in of the thermogravimetric curve from 940°C to 1080 °C. The maximum weight lost is 0.066g/g in sample A and it is 0.0804g/g in sample E.

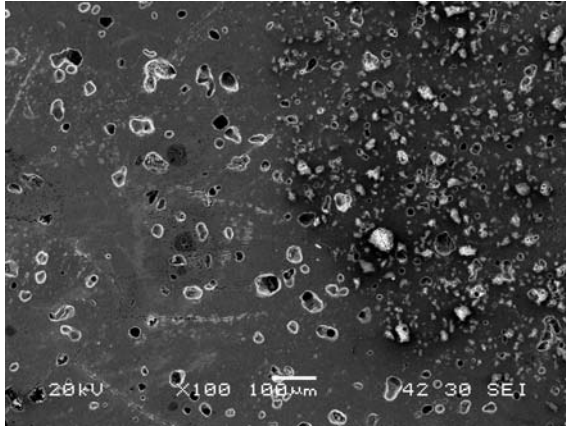


Figure 4. Microstructure of the plain sample (SEM).
The mean porosity diameter is as $80\mu\text{m}$ ($\times 100$).

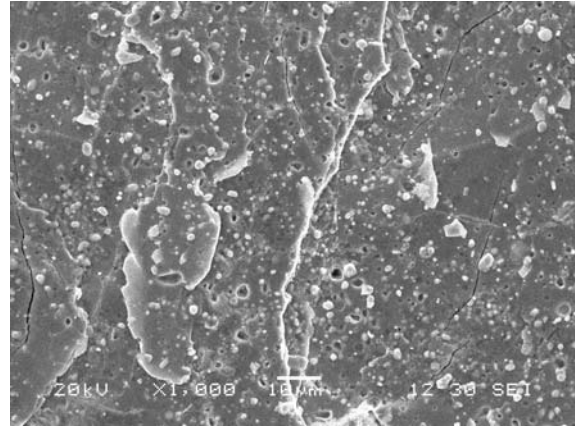


Figure 5. SEM of the hole sample. The mean porosity diameter is as $5\mu\text{m}$ which is smaller than it in the plain sample ($\times 1000$).

Table 2. The porosity distribution calculated in the plain sample A and the hole sample E.

Sample	A	E
Observed pore diameter, $d(\mu\text{m})$	80	5
Oxygen mass of one pore, $m=(4\pi/3)(d/2)^3\rho$, (g)	8.8×10^{-8}	2.16×10^{-11}
Measured normalized maximum weight lost, W (g)	0.0666	0.0804
Mass of remnant oxygen in the sample, $\Delta W= W_{\text{max}}-W$, (g/g)	0.0243	0.0099
Porosity numbers of 1 gram, $(n/g)=\Delta W/m$, (/g)	2.76×10^5	4.58×10^8
Mass of the sample, M (g)	18.762	15.003
Porosity numbers of the sample, $N=(n/g)\cdot M$	5.18×10^6	6.87×10^9
Assumed surface area of sample, $S_A=(\pi r^2\times h')/d$, $S_E=[(\pi r^2-\pi r'^2)\times h']/d$, (mm^2)	6.28×10^4	8.66×10^4
Porosity density per area, N/S	$\sim 1/(100\mu\text{m})^2$	$\sim 8/(10\mu\text{m})^2$

(* Oxygen density ρ at 1000°C is 0.33 g/L . The calculated normalized maximum weight lost W_{max} is 0.0903g/g including the air lost 0.015g/g . The sample's height h' is 16mm . The sample's radius r is 10mm and the hole's radius r' is 0.5mm)

References:

[A.5.1] T B Lindemer, F A Washburn, C S MacDougall: Physica C, 196 (1992) 390.

Published Papers and Conferences

1. C P Zhang, X Chaud , E Beaugnon and L Zhou. Bulk YBCO growth monitored by in situ high-temperature magnetic susceptibility. J. Phys.: Conf. Ser. 97 012040 (7pp) 2008, doi: [10.1088/1742-6596/97/1/012040](https://doi.org/10.1088/1742-6596/97/1/012040). (SCI No. ISSN1742-6596)
2. C P Zhang, Xu Xiaoyan, Feng Yong, Wang Jingrong, Zhou Lian. "Insetting Multi-Seeds for YBCO Single Domian Depth Growth". Chinese Journal of Low Temperature Physics. 2009, 31(4): 301-305 (In Chinese)
3. C P Zhang, X Chaud , E Beaugnon, X Y Xu and L Zhou. "Properties of superconductor YBCO single domain prepared by top seed powder melting process". Journal of Functional Materials. 2009, 10(40): 1454-1456 (In Chinese)
4. C P Zhang, X Chaud , E Beaugnon, X.Y.Xu and L Zhou. Effect of Specific Surface Area on Growth and Porosity of Oxide Superconducting Ceramic YBCO Single Domain. Key Engineering Materials. Accepted, be published in May, 2010.
5. C P Zhang, Xavier Chaud, Eric Beaugnon, Cao Haitao, Lian Zhou. "A new approaches for in-situ studying the phase trasnition of paramagnetic materials – high-temperature Faraday Balance". Materials Science and Processing. Accepted, be published in 2010 (In Chinese)
6. C P Zhang, X Chaud , E Beaugnon and L Zhou. Crystalline Phase Transition of Bulk PMP-YBCO Superconductor Investigated by High Temperature Faraday Balance. Physica C. To be published.
7. C P Zhang, X Chaud , E Beaugnon and L Zhou. Effect of Oxygen Diffusion on c-axis Growth Rate R_c in PMP-YBCO Single Domain. Physica C. To be published.

Patent:

"A method of fabricating superconductor DyBaCuO single domain", Patent NO.:

ZL200510132722.3. Zhou Lian, Feng Yong, Zhang cuiping, Xu Xaioyan, Xiong xiaomei, Yu Zeming.

Conferences:

- 1) February 2007, France, took part in "le séminaire Macodev". Gave a presentation: "Contribution of in situ high temperature magnetic susceptibility to the growth of large YBCO single-domains".
- 2) September 2007, Belgium, Brussels, took part in the EUCAS2007. Gave a poster: "Bulk YBCO Growth Monitored By In Situ High-Temperature Magnetic Susceptibility".

- 3) September 2008, France, Grenoble CNRS, took part in the conference for material with France-China. Gave a presentation: “Crystalline Phase Transition of MTG- and PMP-YBCO Superconductor Bulk Investigated by Faraday Balance & Thermogravimetry”.
- 4) August 2009, China, Herbin, took part in the “international conference of ceramic- CICC-6”, gave a presentation: “Effect of Specific Surface Area on Growth and Porosity of Oxide Superconducting Ceramic YBCO Single Domain”.

Résumé- Une série de résultats fructueux ont été obtenus au cours de notre étude sur la fabrication de supraconducteur YBCO monodomaine à partir d'un procédé par fusion de poudre (PMP). Premièrement, grâce à une balance de Faraday à haute température, nous avons révélé les transitions de phase dynamiques pendant la croissance de monodomaine YBCO par le procédé PMP, ce qui est un travail de recherche original dans ce domaine. Ces résultats sur les transitions de phase ont contribué à une meilleure compréhension de la fabrication des monodomaine PMP-YBCO. Deuxièmement, nous avons étudié la dynamique de croissance des monodomaines PMP-YBCO. L'effet de la diffusion de l'oxygène sur le taux de croissance des monodomaines YBCO est démontré. De la relation entre les taux de croissance et l'étude de la surfusion, nous déduisons que la croissance de cristaux d'YBCO dépend de deux types de diffusion. L'une a trait au transport des ions yttrium, baryum et cuivre vers l'interface de croissance de la phase 123 à travers la phase liquide fondue par diffusion en solution et interfaciale comme dans un système liquide fondu-solide. L'autre concerne la diffusion de l'oxygène qui repose sur la diffusion interfaciale à partir de l'air comme dans un système vapeur-solide. Enfin, nous avons été les premiers à fabriquer par lot avec succès des monodomaines YBCO par procédé PMP de taille $\Phi 30\text{mm} \times 15\text{mm}$. Un champ magnétique important de 739 mT a pu être piégé par un monodomaine YBCO à parois minces de $\Phi 15\text{mm}$. Une mesure magnétique record de la densité de courant critique $J_{cm} \sim 1,2 \times 10^5 \text{A/cm}^2$ (77K) a été atteinte. Les résultats obtenus nous donnent plus de confiance pour fabriquer des échantillons YBCO monodomaine de haute qualité.

Mots clefs : Supraconductivité, $\text{YBa}_2\text{Cu}_3\text{O}_x$, Monodomaine, Croissance cristalline, Oxygénation, Applications

Abstract - A series of fruitful results were achieved in the course of our study on the fabrication of superconductor YBCO single domain by Powder Melting Process (PMP). First, by the high temperature Faraday Balance, we revealed the dynamic phase transition in the growth of YBCO single domain in PMP process, which is an original research work in this field. The clear phase transition results build a fundamental understanding for fabricating YBCO single domain by the PMP process. Second, we studied the growth dynamics of PMP-YBCO single domain. The effect of oxygen diffusion is underlined on the growth rate of YBCO single domain. From the relationship of growth rate and the undercooling study, we deduce that the YBCO crystal growth depends on two types of diffusion. One relates to the yttrium, barium and copper ions transport to the 123 growth interface through the melt liquid by solution diffusion and interfacial diffusion as in melt-solid system. The other one concerns the oxygen diffusion which relies on interfacial diffusion from air as in vapor-solid system. Finally, we were first to successfully fabricate the $\Phi 30\text{mm} \times 15\text{mm}$ YBCO single domain in batch with PMP process. A large trapped magnetic field value of $B_{tr}=739\text{mT}$ was obtained in a $\Phi 15\text{mm}$ hole YBCO single domain. A record magnetic critical current density $J_{cm} \sim 1.2 \times 10^5 \text{A/cm}^2$ (77K) was achieved. The obtained results give us more confidence to fabricate high quality YBCO single domain samples.

Keywords: Superconductivity, $\text{YBa}_2\text{Cu}_3\text{O}_x$, Single domain, Crystal growth, Oxygen annealing, Applications